POLITECNICO DI MILANO

School of Industrial and Information Engineering

Department of Chemistry, Materials and Chemical Engineering "Giulio Natta"

Master of Science in Materials Engineering and Nanotechnology



POLITECNICO
MILANO 1863

New Developments in 3D Printing of Composites: Photocurable Resins for UV-Assisted Processes

Master Thesis of:

Giada ZOCCHI

Matr. 835729

Supervisor: Prof. Marinella LEVI

Co-Supervisor: Dr. Marta INVERNIZZI

Academic Year: 2015-2016



This work is licensed under the Creative Commons Attribution-NonCommercial-ShareAlike 4.0 International License. To view a copy of this license, visit http://creativecommons.org/licenses/by-nc-sa/4.0/ or send a letter to Creative Commons, 444 Castro Street, Suite 900, Mountain View, California, 94041, USA.

“I pescatori sanno che il mare è pericoloso e le tempeste terribili,
ma non hanno mai considerato quei pericoli
ragioni sufficienti per rimanere a terra.”

Vincent Van Gogh

TABLE OF CONTENTS

Table of Contents ..... **i**

List of Figures ..... **v**

List of Graphs ..... **xi**

List of Tables ..... **xv**

List of Acronyms ..... **xix**

Abstract ..... **xxiii**

Estratto in lingua italiana ..... **xxv**

Foreword and Structure of the thesis ..... **xxxi**

Section 1. State of the art: The 3D printing world **1**

1.1 Introduction to 3D Printing **3**

1.1.1 What is 3D Printing? 3

1.1.2 A brief history of 3D printing 5

1.1.3 The Pros and Cons of 3D Printing 9

1.1.3.1 3D Printing benefits 9

1.1.3.2 3D Printing limits 11

1.2 3D Printing Technology **13**

1.2.1 How does 3D printing work? 13

1.2.1.1 3D modeling 14

1.2.1.2 .STL file export 15

1.2.1.3 Slicing 16

1.2.1.4 .Gcode file export 17

1.2.1.5 3D print 18

1.2.1.6 Post-processing and finishing 18

1.2.2 3D printing processes 20

1.2.2.1 Stereolithography (SL) 22

1.2.2.2 Digital Light Processing (DLP) 23

1.2.2.3 Material Jetting (MJ) 23

1.2.2.4 Selective Laser Sintering (SLS) 24

1.2.2.5 Inkjet Powder Printing (IPP) 26
1.2.2.6 Electron Beam Melting (EBM) 27
1.2.2.7 Fused Deposition Modelling (FDM) 28
1.2.3 From FDM to LDM 29
1.2.3.1 Advantages of LDM 30
1.2.3.2 Disadvantages of LDM 31
1.3 Extrudable Materials 33
1.3.1 Materials for FDM 33
1.3.2 Materials for LDM 36
1.3.2.1 Ceramics 36
1.3.2.2 Polymeric resin 38
1.3.2.3 Functional materials: composites 38
1.4 Photopolymer Systems 41
1.4.1 Photopolymer compounds 41
1.4.1.1 Photocurable monomers 42
1.4.1.2 Photoinitiators 43
1.4.2 Polymerization mechanism 45
1.4.2.1 Free radical polymerization 45
1.4.2.2 Cationic polymerization 46
1.4.2.3 Cationic vs Free radical 46
Section 2. Experimental work: Formulation, processing and characterization of printable solutions 49
2.1 Polymer Composites Formulation 51
2.1.1 Chemicals 51
2.1.1.1 Materials for matrix composition 51
2.1.1.2 Organic and inorganic fibers 54
2.1.1.3 Solvents 56
2.1.2 Polymeric matrix formulation 57
2.1.2.1 Preparation of the photocurable mixtures 57
2.1.2.2 Preparation of the dual-curable epoxy mixtures 58
2.1.2.3 Addition of plasticizers 60
2.1.2.4 Addition of silica 61
2.1.3 Fiber reinforced composites formulation 63
2.2 UV-Assisted 3D Printing Process 65
2.2.1 UV-3D printer asssembly 65
2.2.1.1 Extrusion system 66

2.2.1.2 UV- irradiation system....68
2.2.2 UV-3D printing process: from modeling to printing....70
2.2.2.1 3D modeling and Gcodes generation....70
2.2.2.2 Pre-printing stages....70
2.2.2.3 UV-3D printing process start....73
2.2.3 Printing parameters: printability windows....74
2.2.3.1 Spiral Cylinder Model (SCM)....76
2.3 Characterization Techniques....79
2.3.1 UV-light sources....79
2.3.2 Curing process investigation....81
2.3.2.1 UV-vis spectroscopy....81
2.3.2.2 Calorimetric analysis....82
2.3.2.3 Fourier Transform Infrared Spectroscopy (*FTIR*)....85
2.3.2.4 "Drop on glass" test....87
2.3.2.5 Gel Percentage measurement....87
2.3.3 Rheological investigation....90
2.3.4 Mechanical properties investigation....92
2.3.4.1 Dynamic Mechanical Analysis (*DMA*)....92
2.3.4.2 Tensile test....94
2.3.5 Morphology investigation....99
Section 3. Results and discussion....101
3.1 Polymer Composites Formulation....103
3.1.1 Polymer for UV-curing....103
3.1.1.1 Curing process investigation....103
3.1.1.2 Rheology investigation....122
3.1.2 Polymer for Dual-curing....125
3.1.2.1 Curing process investigation....126
3.1.2.2 Rheology investigation....132
3.1.3 Short fiber reinforced composites....134
3.1.3.1 Curing process investigation....134
3.1.3.2 Rheology investigation....138
3.2 UV-Assisted 3D Printing process....141
3.2.1 First approch to UV-3D printer: UV system optimization....141
3.2.2 Printability windows....145
3.2.2.1 SCM printing: material selection....149
3.2.2.2 SCM printing: process parameters optimization....153

3.2.3 Efficiency of the UV-3D printing process 159
3.3 Mechanical response 165
3.3.1 Dual-curable matrix 165
3.3.1.1 DMA analysis 165
3.3.1.2 Uniaxial tensile test 166
3.3.2 Fiber reinforced composites 170
3.3.2.1 DMA analysis 171
3.3.2.2 Uniaxial tensile test 174
3.3.2.3 Fractured surface inspection 182
Conclusions and outlooks 185
Appendix 189
Bibliography 193
Acknowledgements 203

LIST OF FIGURES

Figura 1 Risultati ottenuti dai test "goccia su vetrino" di materiali compositi……xxviii

Figura 2 UV-3D printer adopted for the printing of all the samples fabricated in this thesis work…… xxviii

Figura 3 Modello 3D dell'oggetto cilindrico a sbalzi utilizzato per la definizione degli ottimali parametri di stampa. A destra è mostato un esempio di oggetto stampato……xxix

Figura 4 Campioni a cella unitaria triangolare stampati in composito rinforzato con fibre corte di vetro (FILL 100-40% v/v)……xxx

Figure 1.1.1 Conceptual comparison of Subtractive and Additive Manufacturing [4]. *4*

Figure 1.1.2 SLA-1, the first 3D printer invented by Chuck Hull in 1983. These machine was introduced in 1987 as 3D System' first commercial RP system and after rigorous testing the first was sold in 1988..... *5*

Figure 1.1.3 Adrian Bowyer and Vik Olliver with a RepRap printer (parent) and a clone (child) produced using the original one [16]. *7*

Figure 1.1.4 On the left: significant events in the development of 3D printing..... *7*

Figure 1.1.5 Estimated 3D printer sales per year from 2007 to 2015. Source: Wohler's Report 2015; Gartner... *8*

Figure 1.1.6 Idea of complexity for free: with AM technology it is possible to obtain very complex geometries at no additional costs [8]. *9*

Figure 1.2.1 A printing cycle: from the 3D digital model to the physical object.(Godoj et all, 2006)..... *13*

Figure 1.2.2 Standford Bunny 3D model downloaded from Thingiverse [19]..... *15*

Figure 1.2.3 .STL file of the 3D model shown in the Figure 1.2.2. Different resolutions are reported. *16*

Figure 1.2.4 Slicing of the Standford Bunny model. *17*

Figure 1.2.5 3D printing to create physical object: from the layer be layer deposition to the final object. *18*

Figure 1.2.6 Reproduction of "Milo's Venus" made with FDM printer at +Lab. It is finished with abrasives and chrome painting [25]..... *19*

Figure 1.2.7 Additive Manufacturing processes infograph by 3DHub..... *20*

Figure 1.2.9 Schematic stereolitography apparatus (SLA) [15]..... *22*

Figure 1.2.10 Digital Light Processing schematization [15]..... *23*

Figure 1.2.11 PolyJet process schematization [30]. 24

Figure 1.2.12 Selective laser sintering process schematixation [15]..... 25

Figure 1.2.13 Binder Jetting process [15]..... 26

Figure 1.2.14 EBM process shematization [18]..... 27

Figure 1.2.15 FDM process schematization [6]..... 28

Figure 1.3.1 Stratasys's Periodic Table of 3D Printable Thermoplastic polymers. 33

Figure 1.3.2 12-meters tall Big Delta, Shamballa Technological Village [43]. 37

Figure 1.3.3 Pyromania by Francesco Pacelli 3D printed with clay [41]..... 37

Figure 1.4.1 General presentation of photoinitiated polymerization [77]..... 41

Figure 1.4.2 Monomers used in photoinitiated cationic polymerization [78]..... 42

Figure 1.4.3 Onium Salt Photoinitiators for Cationic Polymerization [77]. 43

Figure 1.4.4 Free radical polymerization mechanism [82]. 45

Figure 1.4.5 Scheme of photoinitiated cationic mechanism [77]..... 46

Figure 2.1.1 From the left: materials and instrumentation employed to prepare photocurable solutions. 58

Figure 2.1.2 Mortar used to reduce the anhydrides to powder. 59

Figure 2.1.3 Instrument used to mechanically mix the silica into the liquid solution: a) Control agitator; b) Glass spatula. 61

Figure 2.1.4 Homogenization of composite blend (Bamboo) by means of two metal spatulas. 63

Figure 2.2.1 LDM UV-3D printer used to process the materials developed in this thesis. 65

Figure 2.2.2 From FDM to LDM-printer: a) Conventional FDM 3Drag 1.2 benchop printer (Futura elettronica); b) Syringe extruder for liquid deposition designed by Natale, 2014 [29]..... 66

Figure 2.2.3 LDM extrusion apparatus components designed by Dr. Natale [29]..... 67

Figure 2.2.4 Exstrusion mechanism: gear system movement and pushing of the material in the syringe [29]..... 68

Figure 2.2.5 3D model of the supports for optical fiber. 69

Figure 2.2.6 Supporters mounted on the transverse bar of the LDM-3D printer. 69

Figure 2.2.7 Syringe preparation: a) Materials and instruments used; b) Filling of the syringe; c) Nozzle screwing; d) Shielding of the syringe. 71

Figure 2.2.8 Syringe assembly to the LDM UV-3D printer: a) Insertion of the syringe holder; b) Piston insertion. 71

Figure 2.2.9 z-Home calibration: a) Endstop mechanism; b) Alignment of the nozzle's tip on the printing plate. *72*

Figure 2.2.10 Repetier-Host interface: uploading and start commands. *73*

Figure 2.2.11 Layer height [25]. *74*

Figure 2.2.12 Shell thickness: zoom of a model whose shell thickness is set to 2. The red and green lines represent the two perimeters that will be printed with a 1 mm nozzle. *74*

Figure 2.2.13 Example of two different fill density percentage: 75% (upper), 25% (bottom). *75*

Figure 2.2.14 Model used to test the capability of LDM UV-3D printing in producing complex geometries: a) Frontal projection; b) 3D model designed with SolidWorks software [25]. *76*

Figure 2.2.15 Spiral conical model: a) Image of the entire object; b) Close-up on some layer to show the spiral fashion. *77*

Figure 2.3.1 UV chamber: control panel and reflector [88]. *79*

Figure 2.3.2 Camag UV Lamp 4 [89]. *80*

Figure 2.3.3 LC8 Lamp: control panel and connected optical fiber guides [90]. *80*

Figure 2.3.4 LCL1 Laser: control panel and the two optical fibers [91]. *80*

Figure 2.3.5 UV-vis spectrophotometry apparatus: a) Evolution 600 UV-vis spectrophotometer; b) Quartz cuvette and cuvette's holder. *81*

Figure 2.3.6 Apparatus for the calorimetric analysis: a) DSC/823e instrument and the mercury lamp with two optical fiber; b) Sample holder with the reference crugible; c) Chamber of the analysis. *83*

Figure 2.3.7 Press to close the aluminium pans for DSC analysis. *84*

Figure 2.3.8 FTIR instrument: a) Thermo Nicolet Nexus 670 spectrometer; b) Chamber for sample analysis. .. *85*

Figure 2.3.9 FTIR-sample: a) NaCl crystal disk, used as support for liquid solution, in the sample holder; b) Apparatus used to prepare the KBr disk for the analysis of powder. *86*

Figure 2.3.10 Example of two drops of solution deposited on a slide to perform the "Drop on Glass" test. *87*

Figure 2.3.11 Apparatus for Gel Percentage measurement: a) Sample immersed in acetone; b) Instrumentation used to filter the residual solvent. *88*

Figure 2.3.12 a) Bohlin rheometer used for the characterization of the epoxy matrix. b) Rheometrics rheometer employed in the composite dispersions characterization. c) Deposition of the mixture on the bottom plate. d) Sandwiching of the material between the plates. *90*

Figure 2.3.13 DMA/SDTA861 instrument used for the Dynamic Mechanical Analysis of cast and 3D printed rectangular samples. *92*

Figure 2.3.14 a) Mould for the preparation of DMA casted sample; b) 3D model (generated with Grasshopper software) for the printing of the DMA sample. *93*

Figure 2.3.15 Apparatus for tensile test: a) Zwick-Roell Z010 instrument; b) Longstroke extensometer closed on a sample. *94*

Figure 2.3.16 Tensile test specmen preparation: a) Mould used to cast the dumbbell specimen; b) 3D model in Cura. *95*

Figure 2.3.17 3D model of the RDFO specimen. In the upper right the diagram designed with Grasshopper. ... *96*

Figure 2.3.18 UV-3D printing process: printing of a glass fiber-reinforced RDFO sample. In the foreground an already printed sample. *96*

Figure 2.3.19 3D model of the lightweight cellular specimen. *97*

Figure 2.3.20 Specimens prepared for tensile test: a) casted pt-ES3MA dumbbell samples; b) casted pt-ES3MAOX200-11 dumbbell samples; c) RDFO (100% infill) UV-3D printed sample made of pt-ES3MAOX200-11 and SFR-composites; d) Lightweight cellular UV-3D printed samples made of FILL100-25 composite ink. . *98*

Figure 2.3.21 Optical microscope used for the morphological investigation: a) Olympus BX-60 microscope; b) Leica DMI 3000..... *99*

Figure 3.1.1 Aluminium crucible containing the samples, post p-DSC analysis: p-DVES3 solutions (1,4,5,7); p-DVES2 solutions (2,3,6,9); p-DVEI1 solutions (8,10-12). Samples UV-exposed for 3 min at 100% irradiation intensity: 1,3,11. SamplesUV- exposed for 1 min at 100% irradiation intensity: 2,5,8. SamplesUV- exposed for 3 min at 50% irradiation intensity: 4,6,10. SamplesUV- exposed for 1 min at 50% irradiation intensity: 7,9,12. *112*

Figure 3.1.2 UV-shielding vial with the reacted materials. In particular this picture shows the p-DVEI solutions with 1% wt and 0,5% wt of photoinitiator. *112*

Figure 3.1.3 Photolytically initiated crosslinking reaction of the cycloaliphatic diepoxide [79]..... *117*

Figure 3.1.4 Particular of a p-ES3 casted sample: a) piece of sample before the gel percentage test; b) sample after the immersion in acetone. *121*

Figure 3.1.5 Vial containing the pt-ES3PA solution. The white PA precipitate can be easily seen after leading the solution at room temperature for a couple of hours. *125*

Figure 3.1.6 Drops irradiated with LC-L1V3 laser (relative intensity 1-0.5%) for increasing time intervals... *126*

Figure 3.1.7 Scheme of the thermally activated reaction. *130*

Figure 3.1.8 SFR composites drops: the drops containing glass fiber were exposed to UV light for 2 sec while those with carbon and bamboo fibers for 4sec in order to make them solid. *135*

Figure 3.2.1 Results of the "drop on glass" test (p-ES3 solution): on the left, the drops irradiated at the maximun intensity (100%) for 2 sec, varying the distance UV-source-drop from 2 cm up to 8 cm. On the right,

the drops irradiated at halved intensity (50%) for 2 sec, varying the distance UV-source-drop from 2 cm up to 8 cm. *142*

Figure 3.2.2 Results of the "drop on glass" test (p-ES3 solution). Irradiation conditions: 2sec at a constant distance of 4 cm from the UV-source, varying the light intensity from 100% to 10%. *143*

Figure 3.2.3 Results of the "drop on glass" test (p-ES3OX200-13 solution). Irradiation conditions: 2sec at a constant distance of 4 cm from the UV-source, varying the light intensity from 100% to 10%. *144*

Figure 3.2.4 SCM printed with p-ES3OX200 at increasing OX200 weight concentration. On the left the 3D model is presented. Formulations with the silica content less than 9 %wt are not good to be UV-3D printed. The two with higher filler concentration are instead correct to be printed. All the presented samples are printed setting the UV-laser at the maximun available intensity. *150*

Figure 3.2.5 SCM printed with pt-ES3MAOX200 at increasing OX200 weight concentration. On the left the 3D model is presented. Formulations with the silica content less than 9 %wt are not good to be UV-3D printed. The two with higher filler concentration are instead correct to be printed. All the presented samples are printed setting the UV-laser at the maximun available intensity but they are not yet thermal-treated. *150*

Figure 3.2.6 SCM printed with SFR-composites inks: PX35-10, BAMBOO-10, FILL100-10, FILL100-50. Only the last two formulations are suitable to fabricate the SCM. The first two remain to soft during the UV-3D printing process. All the presented samples are not thermal-treated. *152*

Figure 3.2.7 Optical microscopic images (20x magnification) of a) FILL100-10; b) FILL100-50. ..... *162*

Figure 3.2.8 Optical microscopic images (20x magnification) of a) FILL200-10; b) FILL200-50. ..... *162*

Figure 3.2.9 Optical microscopic images of a) BAMBOO-10 (20x); b) PX35-10 (10x). *163*

Figure 3.3.1 Microscopic image (100x magnification) of banboo fibers embedded in the duel-cure polymeric matrix. *175*

Figure 3.3.2 Microscopic images of fractured surfaces: a) FILL 100-10 (magnification 100x), b)) FILL 100-50 (magnification 200x). *183*

Figure 3.3.3 Microscopic images of fractured surfaces: a) FILL 200-10 (magnification 200x), b) FILL 200-10 (magnification 100x). *183*

Figure 3.3.4 Microscopic images of fractured surfaces: a) PX35-10 (magnification 20x), b) BAMBOO-10 (magnification 10x). *184*

Figure 1A Drops on glass of pt-ES3PA irradiated with laser at 365nm for different time intervals……189

LIST OF GRAPHS

Graph 3.1.1 UV-vis absorption spectra of the photoinitiators used for the cationic UV-curing formulations: sulfonium salt (PI-S) and iodonium salt (PI-I). *104*

Graph 3.1.2 Photo-DSC exotherms for the photo-polymerization of p-EI3, p-ES3, p-DVEI3 and p-DVES3 solutions at 25°C. time of exposure 3 min, light intensity percentage 100%. *107*

Graph 3.1.3 Photo-DSC exotherms for the photo-polymerization of p-DVES solutions at 3, 2, 1, 0.5% wt of sulfonium initiator. Test conditions: temperature 25°C, time of exposure 3 min, light intensity percentage 100%. *109*

Graph 3.1.4 Photo-DSC exotherms for the photo-polymerization of p-DVEI solutions at 3, 2, 1, 0.5% wt of iodonium initiator. Test conditions: temperature 25°C, time of exposure 3 min, light intensity percentage 100%. *110*

Graph 3.1.5 Photo-DSC exotherms for the photo-polymerization of p-EI3 solution at 25°C at varying relative light intensity from 1 to 0.05. ..... *113*

Graph 3.1.6 Epoxy monomer conversion of p-ES3 solution photocured at 25°C with various relative intensities. The corresponding ΔHexo are listed in Table 3.1.7. ..... *115*

Graph 3.1.7 Crosslinking conversion percentage against time of UV exposure. The samples used for the photocalorimetric analysis were irradiated at light intensity of 1300mW/cm^2. ..... *116*

Graph 3.1.8 FTIR analysis: a) Sspectra of p-ES3 pre-irradiation (blue), after UV exposure for 15 sec (purple) and in dark (green and light blue). The spectrum after a thermal treatment is also reported (red). b) Magnification of the epoxy band. *118*

Graph 3.1.9 Conversion determined by the evaluation of the FTIR spectra. Squares-continuous line: irradiation for 15 sec (yellow), dark curing for 2h (green), thermal treatment for 2h (orange). Triangles-dashed line: irradiation for 1 sec (yellow), dark curing for 1h (green). *119*

Graph 3.1.10 FTIR spectrum of the residual acetone used for the immersion of p-ES3 casted samples (1) in the gel percentage test. *121*

Graph 3.1.11 Viscosity curves of p-ES3OX200 formulations at increasing filler concentrations. *123*

Graph 3.1.12 FTIR spectrum of maleic anhydride. *128*

Graph 3.1.13 FTIR analysis: a) Sspectra of pt-ES3MA pre-irradiation (blue), after UV exposure for 15 sec (light blue) and in dark (red and light green). The spectrum after a thermal treatment is also reported (dark green). b) Magnification of the maleic band. *129*

Graph 3.1.14 Conversion determined by the evaluation of the FTIR spectra of the p-ES3MA dual-curable solution. Conversion associated to three curing stages are shown: irradiation for 15 sec (yellow line), dark curing for 1h (green line), and thermal treatment for 1h (orange line). *130*

Graph 3.1.15 FTIR spectra of the residual solvent used for the immersion of the samples in the gel percentage measurement. Green line represents the spectrum of the solvent in which the most cured sample was immersed; red line is about the residual of the less cured sample. *132*

Graph 3.1.16 Viscosity curves of pt-ES3MAOX200 formulations at increasing filler concentrations. *133*

Graph 3.1.17 Photo-DSC results for SFR-composites inks: a) Exothermic curves; b) Enthalpy values. *137*

Graph 3.1.18 Viscosity curves of SFR composite formulations at increasing fibers volume fraction: a) FILL 100; b) FILL 200. ..... *138*

Graph 3.1.19 Viscosity curves of carbon (PX35) and bamboo (BAMBOO) SFR-composites. *139*

Graph 3.2.1 Shear stress as function of shear rate for UV-curable inks at increasing silica content. The corresponding printability windows are also presented as the region within the dashed lines (the window related to a partcilar material is identified with the same color used for its rheological curve). *147*

Graph 3.2.2 Shear stress as function of shear rate for dual-curable inks at increasing silica content. The correspondind printability windows are also presented as the region within the dashed lines (the window related to a partcilar material is identified with the same color used for its rheological curve). *147*

Graph 3.2.3 Shear stress as function of shear rate for SFR-composites at increasing fiber volume content. The correspondind printability windows are also presented as the region within the dashed lines (the window related to a partcilar material is identified with the same color used for its rheological curve). a) FILL 100; b) FILL200; c) BAMBOO and PX35 ..... *148*

Graph 3.2.4 Consistency indexes K as function of filler OX200 concentration; the values are obtained by the power-law approximation for the viscosity curves shown in the Graph 3.1.11 for the p-ES3OX200 and in the Graph 3.1.16 for the pt-ES3MAOX200. The lower limit K value was reported as red line. *151*

Graph 3.2.5 Consistency indexes K as function of fiber (glass, carbon and bamboo) concentration; the values are obtained by the power-law approximation for the SFR-composites viscosity curves shown in the Graph 3.1.17. The lower limit K value was reported as red line. *153*

Graph 3.2.6 FTIR spectrun of residual acetone, used in the gel percentage test. *160*

Graph 3.3.1 Representative stress-strain curves of UV-3D printed and cast samples made of dual-cure material. *167*

Graph 3.3.2 Average values of a) elastic modulus, b) ultimate tensile strength and c) deformation at break. *168*

Graph 3.3.3 Storage modulus obtain by DMA analysis. The value of 25.56 GPa and 4.65 GPa, related to FILL 100-40 and Fill 200-50, respectively, are strange results. As they not follow the incresing trend, they will be not considered as valid data and are not reported in this graph *172*

Graph 3.3.4 Representative stress-strain curves of RDFO-type UV-3D printed sample made of SFR-composites (10% v/v of fibers) The red line refers to sample made of dual-cure polymeric matrix. *176*

Graph 3.3.5 Average values of a) elastic modulus, b) ultimate tensile strength and c) deformation at break for composite specimens. *177*

Graph 3.3.6 Elastic modulus obtain by performing tensile tests (points) and DMA analysis (triangle) on SFR-composites. The data about the matrix are also reported for comparison. In this graph the error bars are not reported for a better visualization of the data. The exact standard variation from the mean values are already shown in the Grapgh 3.3.3 and Graph 3.3.5 (a) for DMA and tensile test, respectively..... *180*

Graph 3.3.7 Stress-strain curve resulting from the tensile test of a FILL 100-40 sample with triangular infill. 181

Graph 1A UV-vis spectra of solution of BA, GLY, ESBO plasticizers diluted (0.001%) in methanol……..…..190.

LIST OF TABLES

Tabella 1 Risultati ottenuti dall'analisi di percento-gel effettuata sul materiale dual-cure (pt-ES3MA) e UV-curabile (p-ES). Le misure sono state effettuate sia su campioni castati che stampati usando la tecnologia UV-LDM.....xxvii

Tabella 2 Moduli elastici dei materiali compositi fibrorinforzati: sono riportati sia i valori sperimentali che quelli previsti dal modello Halpin-Tsai……xxx

Table 2.1.1 Chemical structures of reactans. 53

Table 2.1.2 Chemical and physical properties of the reactants. Data was collected from the SDS of the each material. 54

Table 2.1.3 Fibers technical data, collected from the SDS of each material [84]–[87]. *55*

Table 2.1.4 Technical data of solvents used during the experimental work. 56

Table 2.1.5 Weights of reagents to obtain solutions at different percentages of photoinitiator. 58

Table 2.1.6 Reagents quantities in dual-cure formulations. 60

Table 2.1.7 Weights of materials to prepare four different plasticized solutions. 60

Table 2.1.8 Amount of fumed silica OX200 added in different concentration by weigth to 5g of unfilled system in order to modify its viscosity. 62

Table 2.1.9 Percentages (% v/v) and corresponding weighst of fibers dispersed in 5g of polymeric matrix. 64

Table 2.2.1 Printing parameters set in Cura software. 77

Table 3.1.1 Drops resulting from the "drop on glass" test. Each drop was irradiated with UV-light using theUV Lamp 4..... 106

Table 3.1.2 p-DSC analysis results for the photopolymeriation of the p-EI3, p-ES3, p-DVEI3 and p-DVES3 solution. The data derive from the elaboration of the exotherm curves shown in the graph 3.1.2..... 107

Table 3.1.3 p-DSC analysis results for the photopolymeriation of the p-DVES solutions at different initiator concentrations: 3, 2, 1, 0.5% wt. The data derive from the elaboration of the exotherms shown in the graph 3.1.3..... 109

Table 3.1.4 p-DSC analysis results for the photopolymeriation of the p-DVEI solutions at different initiator concentrations: 3, 2, 1, 0.5% wt. The data derive from the elaboration of the exotherms shown in the graph 3.1.4. ..... *110*

Table 3.1.5 ΔHexo values resulting from the p-DSC analysis performed at 100% irradiation intensity and varying the time of exposure from 3 to 1 min. *111*

Table 3.1.6 ΔHexo values resulting from the p-DSC analysis performed at 50% irradiation intensity and varying the time of exposure from 3 to 1 min. *111*

Table 3.1.7 p-DSC analysis results for the photopolymeriation of the p-ES3 at varying UV light intensity. The data derive from the elaboration of the exotherm curves shown in the graph 3.15. ..... *114*

Table 3.1.8 Gel percentage test results: the initial and final weight of p-ES3 samples are reported with the corresponding calculated gel percentage. *120*

Table 3.1.9 Power-law index n and consistency index K, relative to the p-ES3OX200 formulations at different silica concentration. *124*

Table 3.1.10 Photo-DSC/DSC analysis results of dual-cure solutions: pt-ES3MA, pt-ES3MA-ESBO5. ..... *127*

Table 3.1.11 Gel percentage test results: mean and standars deviation values are reported. The images represent the samples appearence after the test with also the residual concentrated solvent stored in vials. *131*

Table 3.1.12 Power-law index n and consistency index K, relative to the tp-ES3MAOX200 formulations at different silica concentration. *133*

Table 3.1.13 p-DSC analysis results for the photopolymeriation of different SFR-composites inks. The data about the polymeric matrix are also reported for comparison. *136*

Table 3.1.14 Power-law index n and consistency index K, relative to the SFR-composite formulations. *140*

Table 3.2.1 UV-3D-printing parameters set to print the SCM_1 shown in the figure on the right. *154*

Table 3.2.2 UV-3D-printing parameters set to print the SCM_2 shown in the figure on the right. *155*

Table 3.2.3 UV-3D-printing parameters set to print the SCM_3 shown in the figure on the right. *156*

Table 3.2.4 UV-3D-printing parameters set to print the SCM_4 shown in the figure on the right. *157*

Table 3.2.5 UV-3D-printing parameters set to print the SCM_5 shown in the figure on the right. *158*

Table 3.2.6 Gel percentage results (mean and standars deviation values are reported) obtained by performing the test on printed samples. In the last column, the data previously obtained for cast samples are reported. *160*

Table 3.2.7 Gel percentage results (mean and standars deviation values are reported) obtained by performing the test on SFR-composites printed samples. *161*

Table 3.3.1 Storage modulus E' and temperature at the tan(δ) peak as obtained from DMA, and T_g as measured via DSC of crosslinked dual-cure epoxy resin processed by casting and by UV-3D-printing. *166*

Table 3.3.2 Storage modulus E' and temperature at the tan(δ) peak as obtained from DMA analyses performed on UV-3D printed samples of SFR-composites..... 172

Table 3.3.3 Values of parameters used for fitting the Halpin-Tsai equation..... 175

Table 3.3.4 Elastic modulus of SFR-composites: the measured values and the predicted ones are reported for comparison..... 179

Table 3.3.5 Mechanical properties of FILL 100-40 (triangular infill): the measured values and the predicted ones are reported for comparison..... 182

Table 1A Glass transition temperature related to the drops shown on the Figure 1……..189

Table 2A Glass transition temperature of dual-cure mixture with plasticizer at 5%wt……190

Table 3A Mechanical properties of dual-cure formulation containing the maleic anhydride. The results obtained for the material with and without the addition of ESBO plasticizer are reported. The uniaxial tensile tests are performed on both sample at a speed of 0.3 mm/s with a pre-load of 3N……191

LIST OF ACRONYMS

A

ABS	*Acrylonitrile-Butadiene-Styrene*
AC	*Acetone*
ACN	*Acetonitrile*
AM	*Additive Manufacturing*
ARALDITE CY 179 BD	*Bis-cycloaliphatic diepoxy monomer*
ASTM	*America Society for Testing and Materials International*

B

BA	*Benzyl Alcohol*

C

CAD	*Computer-Aided Design*
CAM	*Computer-Aided Manufacturing*
CSG	*Construction of Solid Geometry*

D

DF	*Digital Fabrication*
DIY	*Do It Yourself*
DMA	*Dynamic Mechanical Analysis*
DPL	*Digital light processing*
DSC	*Differential Scanning Calorimetry*

E

EBM	*Electron Beam Melting*
ESBO	*Epoxidized SoyBean Oil*

F

FDM	*Fused Deposition Modeling*
FFF	*Free Form Fabrication*

FILL 100	*Glass fiber 100 µm*
FILL 200F	*Glass fiber 200 µm*
FTIR	*Fourier Transform Infrared Spectroscopy*

G

GLY	*Glycerol*

I

IPP	*Inkjet Powder Printing*
ISO	*International Organization for Standardization*

L

LDM	*Liquid Deposition Modelling*
LS	*Laser Sintering*

M

Me-OH	*Methanol*
MA	*Maleic Anhydride*
MIT	*Massachusetts Institute of Technology*
MJ	*Material Jetting*
MJM	*MultiJet Modeling*

N

NURBS	*Non Uniform Rational B-Splines*

O

OM	*Optical Microscopy*
OX200	*Fumes silica*

P

PA	*PolyAmide or Phtalic Anhydride*
p-DSC	*Photo-Differential Scanning Calorimetry*
p-DVES	*Photo-Divinyl Ether resin with Sulfonium initiator*

p-DVEI	*Photo-Divinyl Ether resin with Iodonium initiator*
p-EI	*Photo-Epoxy resin with Iodonium initiator*
p-ES	*Photo-Epoxy resin with Sulfonium initiator*
PI-I	*Bis(4-methylphenyl)iodonium hexafluorophosphate*
PI-S	*TriarylSulfonium hexafluorophosphate salts*
PJ	*PolyJet*
PLA	*PolyLactic Acid*
PVA	*PolyVinyl Alcohol*
PX35	*Carbon fibers*
pt-ES3MA	*Dual-cure solution containinh Maleic Anhydride*
pt-ES3PA	*Dual-cure solution containinh Phthalic Anhydride*

R

RDFO	*Random Discontinuous Fiber Orientation*
RE	*Reverse Engineering*
RP	*Rapid Prototyping*

S

SCM	*Spiral Cylinder Model*
SFR	*Short Fiber Reinforcement*
SL	*Stereolithography*
SLA	*Stereolithography Apparatus*
SLS	*Selective Laser Sintering*
STL	*Standard Triangulation Language*

T

3DP	*Three Dimensional Printing*
TEGDVE	*Tri(Ethylene Glycol)Divinyl Ether*
TPU	*Thermoplastic PolyUrethane*

W

WASP	*World's Advanced Saving Project*

ABSTRACT

The aim of this work is the development of new polymer-based composites specially optimized for use in LDM UV-3D printing technology.

Initially UV-curable cationic systems were formulated and their photopolymerization process was investigated. Due to the low conversion efficiency of these systems, the adoption of a dual-cure technique has been necessary. Maleic anhydride was added to the cationic epoxy formulation; gel percentage and FTIR spectroscopy analyses confirmed the effective improvement of conversion. Silica was then added to the dual-cure material to increase its viscosity. Through rheological studies, optimal extrusion condition and printability windows for the developed dispersions were obtained. The formulation with 11% wt of silica was adopted as matrix material for SFR-composites development. Glass, carbon, and bamboo SFR-composite inks were prepared. Drop on glass and photocalorimetric analyses demonstrated that a rapid curing reaction could be achieved only in case of transparent glass fibers. Carbon and bamboo fibers slowed the kinetics of the photopolymerization reaction, due to their chemical nature that shields UV rays. In order to UV-3D print the developed inks, a LDM low cost machine was equipped with a UV-laser. The optimal printing parameters were founded by performing several printing trials, using as specially designed 3D model (SCM). The final part of this work was dedicated to the investigation of the mechanical response of UV-3D printed samples. The resulting mechanical properties demonstrated that the LDM technology is still far from replacing the traditional composite manufacturing techniques. However, tensile tests performed on triangular unit cell composites demonstrated the possibility offered by the UV-3D printing to control the mechanical response by varying the infill percentage and structure design.

The main advantages of LDM remain its lower cost, its ability to fabricate complex geometries and the possibility to print a wide range of materials. If the mechanical properties of the printed components can be improved, this technology could become more than an alternative to traditional manufacturing processes.

ESTRATTO IN LINGUA ITALIANA

Negli ultimi anni la stampa 3D, nonostante alcune attuali limitazioni, ha indubbiamente attirato su di sé un forte interesse. Non per nulla alcuni sostengono che tale tecnologia potrebbe addirittura portare au una "nuova rivoluzione industriale" visti gli impatti tecnici, economici e sociali che potrebbe avere.
La stampa 3D può infatti avere un potenziale impatto dirompente sul modo di progettare, produrre, distribuire e vendere i prodotti. L'utilizzo di una stampante 3D è già comune tra designer, ingegneri ed architetti i quali progettano prodotti e creano prototipi. Tale tecnologia di manifattura additiva si sta ritagliando sempre di più uno spazio anche nella produzione diretta di utensili e prodotti finiti per diversi utenti. Grazie a queste nuove applicazioni la stampa 3D potrebbe consentire livelli di personalizzazione di massa senza precedenti oltre a rendere piu veloci e meno costose le catene del valore. L'ingresso di tale tecnologia nel mercato della manifattura e della prototipazione (si può parlare di Prototipazione Rapida), oltre a portare ad innovazioni di prodotto/servizio, potrebbe avere un forte impatto anche nell'industria che si occupa della produzione dei materiali.
Insieme all'insorgere di nuove tecnologie di produzione additiva, anche i materiali appositamente pensati per la stampa 3D sono in continua evoluzione e sperimentazione. Ad oggi è disponibile una vasta gamma di materiali forniti in diversi stati: polveri, filamenti, granuli, resine, etc.
Le più recenti ricerche si stanno focalizzando sullo sviluppo di materiali resistenti che possano conferire elevate proprietà meccaniche ai pezzi stampati; è questo il caso dei materiali compositi. Oltre ai già commercializzati filamenti in ABS rinforzati con carbonio, nuove soluzioni liquide iniziano ad essere sviluppate. Una delle compagnie in prima linea in questo campo è Voxel8, con prodotti basati su materiali sviluppati presso i laboratori di Harvard dal team della ricercatrice Jennifer Lewis. La tecnologia scelta da Voxel8, chiamata *3D Direct Write,* permette di estrudere una 'pasta viscosa' a temperatura ambiente utilizzando sistemi pneumatici e/o volumetrici. Il co-fondatore della compagnia D. Oliver afferma: "*Siamo riusciti a far uscire in modo efficace questa pasta dalle siringhe. L'innovazione risiede nella scienza dei materiali dietro ai materiali che stai stampando. Non è cosa da poco ottenere un inchiostro con le specifiche corrette. Deve essere controllabile attraverso un erogatore, ma non deve essere liquido quando lo metti su una base, e deve essere stampato e solido a temperatura ambiente."*
Altri gruppi di ricerca sono focalizzati sullo sviluppo di sistemi di estrusione per la deposizioni di inchiostri a pasta viscosa tra cui i materiali compositi. Al +LAB, il laboratorio di stampa 3D presente al Politecnico di Milano, presso cui la ricerca qui presentata è stata condotta, la Prof.ssa Marinella Levi e il Dr. Natale lavorano ormai da qualche anno, sullo sviluppo della tecnologia LDM (*Liquid Deposition Modelling*), progettando e costruendo sistemi di estrusione per la deposizione di liquidi.

Tale metodo offre la possibilità di stampare materiali compositi attraverso l'introduzione di fibre strutturali corte o continue, direttamente durante la fase di estrusione.

In questo scenario si colloca il lavoro sperimentale presentato in questa tesi che ha come principale scopo quello di sviluppare materiali compositi fibrorinforzati, appositamente ottimizzati per la stampa LDM UV-assistita. Il lavoro sperimentale si è concentrato sul raggiungimento dei seguenti obiettivi:

- Sviluppo e caratterizzazione di nuovi sistemi cationici da adottare come matrice nella formulazione di inchiostri compositi per la stampa LDM UV-assistita.

- Valutazione degli effetti prodotti da diverse fibre aggiunte alla matrice polimerica in frazioni crescenti (10% v/v - 50%v/v), sulla stampabilità dei corrispettivi inchiostri.

- Assemblaggio di un sistema di irraggiamento UV su una stampante 3D low-cost per LDM.

- Definizione delle finestre di stampabilità in funzione dei materiali e dei parametri di stampa adottati.

- Valutazione dell'abilità del processo LDM UV-assistato di riprodurre forme complesse.

- Stampa e caratterizzazione meccanica dei materiali compositi precedentemente sviluppati.

La tesi è divisa in tre macro sezioni. La prima è dedicata all'introduzione teorica al mondo della stampa 3D: partendo dai vantaggi e svantaggi di tale metodo produttivo, si passa alla descrizione del principio comune di funzionamento delle tecnologie di manifattura additiva, fino ad arrivare alla presentazione della tecnologia di LDM. Quest'ultima è descritta nel dettaglio del suo principio di funzionamento e dei materiali da essa processati. Infine, si presenta una breve descrizione dei sistemi polimerici UV-sensibili sia in termini di materiali che di meccanismi di reazione, ponendo maggiore attenzione ai sistemi di polimerizzazione cationica.
Nella seconda parte di questa tesi è presentato l'intero lavoro sperimentale: i materiali utilizzati, i metodi di preparazione, la descrizione del processo di stampa (dall'assemblaggio della stampante con un sistema di irraggiamento UV alla stampa vera e propria di provini), ed infine sono descritte le varie tecniche di caratterizzazione.
La terza parte è dedicata alla presentazione e discussione dei risultati ottenuti. Le conclusione e i possibili sviluppi futuri sono infine riportati.

Inizialmente diverse formulazione cationiche sono state sviluppate utilizzando rispettivamente una resina epossidica cicloalifatica e un divinil etere con aggiunta di diverse concentrazioni di

fotoiniziatore, quali un solfonio e uno iodonio. A causa di problemi di instabilità chimica del sistema a base etere, il lavoro è stato portato avanti utilizzando unicamente la formulazione epossidica. La bassa efficienza di conversione di tale resina, risultante dall'analisi fotocalorimetrica, dalla spettroscopia FTIR e dalle misure di percento-gel, ha portato all'adozione di una tecnica di polimerizzazione in due stadi. Il sistema cationico UV-curabile è stato modificato con l'aggiunta di anidride maleica in modo da completarne la polimerizzazione per via termica. Studi di spettroscopia FTIR e misure di percento-gel sono state effettuate su tale sistema *dual-curable* e i risultati ottenuti hanno dimostrato l'efficacia di tale scelta (*Tabella 1*).

Material type	***Gel percentage Print [%]***	***Gel percentage Cast [%]***
UV-curable	74.06 ± 5.02	78.05 ± 4.73
Dual-curable	100.00 ± 0.00	99.90 ± 0.02

Tabella 1 Risultati ottenuti dall'analisi di percento-gel effettuata sul materiale dual-cure (pt-ES3MA) e UV-curabile (p-ES). Le misure sono state effettuate sia su campioni castati che stampati usando la tecnologia UV-LDM.

Questa formulazione dual-cure è stata quindi viscosizzata con l'aggiunta di silice pirogenica in differenti concentrazioni, al fine di ottenere inchiostri ad elevata viscosità. Attraverso una caratterizzazione reologica è stato possibile definire, sulla base della velocità di deformazione a taglio dei materiali all'ugello, applicando la legge di potenza e il modello di flusso capillare, le ottimali condizioni di estrusione e le finestre di stampabilità per le dispersioni ottenute. La soluzione migliore da adottare come materiale per la matrice di compositi fibrorinforzati è risultata essere la dispersione contenente 11% in peso di silice. A questo materiale sono state aggiunte differenti frazioni volumetriche (10% v/v - 50% v/v) di fibre corte di vetro (FILL 100 e FILL 200), carbonio (PX35), e bambù. L'analisi fotocalorimetrica e i test di "goccia su vetrino" effettuati sulle formulazioni in composito precedentemente ottenute, hanno dimostrato che una rapida reazione di polimerizzazione poteva essere raggiunta solo in caso di inchiostri rinforzati con fibre di vetro bianco-trasparente. Le fibre di carbonio e bambù, avendo una struttura chimica in grado di assorbire parte della radiazione UV incidente, rallentano la cinetica di fotopolimerizzazione della matrice dual-curable (*Figura 1*).

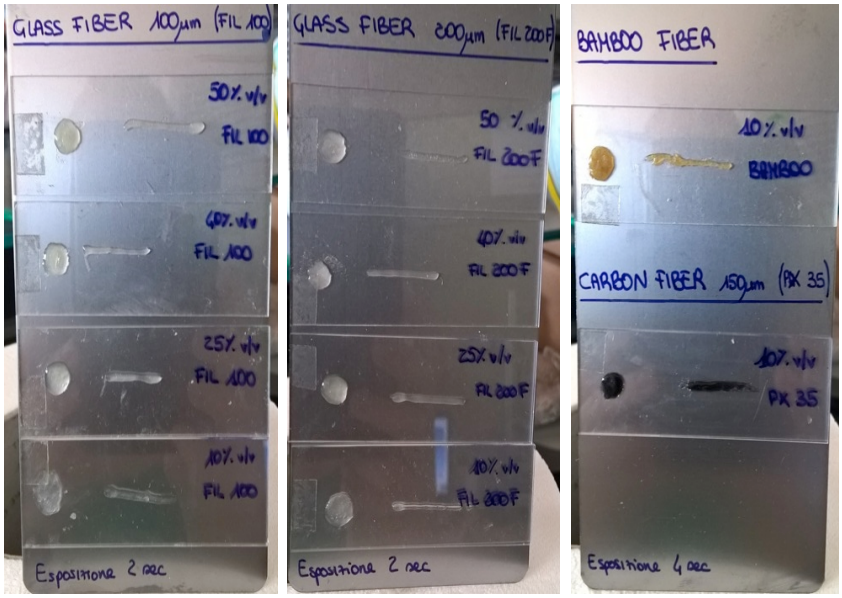

Figura 1 Risultati ottenuti dai test "goccia su vetrino" di materiali compositi.

Dopo aver ottimizzate le varie formulazioni, si è proceduto all'assemblaggio di una stampante low-cost per LDM. Tale macchina è stata equipaggiata di un sistema di irraggiamento UV costituito da un laser (emissione centrata a 365nm) con due fibre ottiche (*Figura 2*).

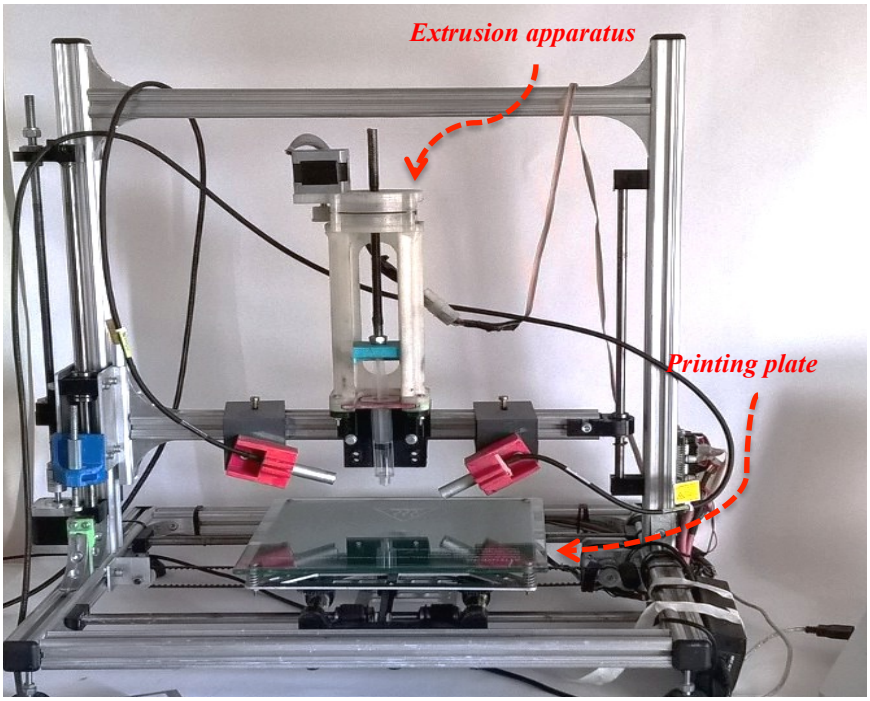

Figura 2 UV-3D printer adopted for the printing of all the samples fabricated in this thesis work.

Terminato l'asssemblaggio diverse prove di stampa sono state eseguite al fine di trovare i parametri ottimali per la stampa di oggetti con geometrie anche complesse. A tale scopo, è stato progettato un apposito modello 3D con sbalzi a diverse inclinazioni (*Figura 3*).

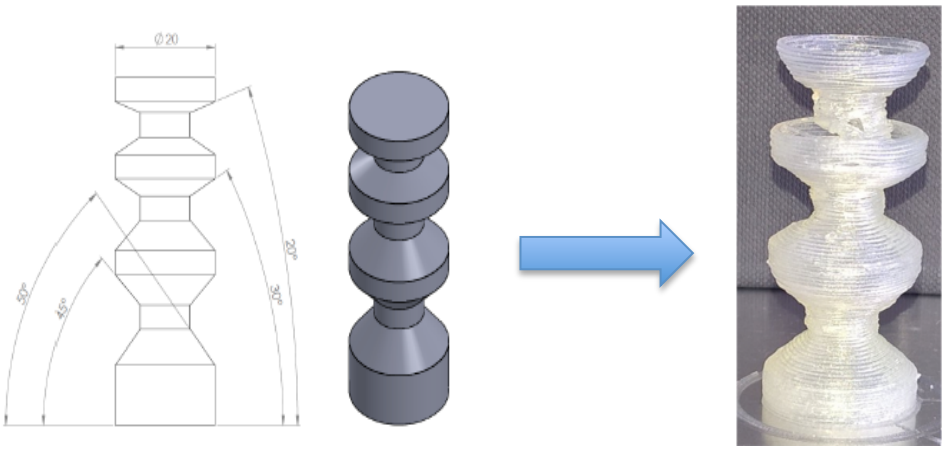

Figura 3 Modello 3D dell'oggetto cilindrico a sbalzi utilizzato per la definizione degli ottimali parametri di stampa. A destra è mostato un esempio di oggetto stampato.

I parametri ottimali per la stampa del sistema dual-curable sono risultati essere i seguenti: altezza layer 0.5 mm, velocità di stampa da 5 a 7 mm/sec, flusso 95-100% e intensità relativa della radiazione UV variabile da 0.9 a 1 (densità di poteza massima misurata 1300 mW/cm^2).

Oltre all'ottimizzazione del materiale e dei parametri relativi al processo, la parte finale del lavoro sperimentale è stata dedicata alla valutazione delle proprietà meccaniche di campioni fabbricati tramite la stampante 3D UV-assistita. L'analisi meccanica (prove di DMA e di trazione uniassiale) dei campioni stampati in materiale composito fibrorinforzato (campioni rettangolari con grado di riempimento del 100%) ha dimostrato che la tecnologia LDM non è ancora pronta a sostituire le tradizionali tecniche di produzione. Infatti le proprietà degli stampati sono risultate inferiori rispetto a quanto teoricamente previsto secondo il modello Halpin –Tsai (*Tabella 2*).

	E_{exp} [GPa]	$E_{Halpin\text{-}Tsai}$ [GPa]
pt-ES3MAOX20011 print (rect)	3.44 ± 0.53	-
FILL 100-10	3.58 ± 0.28	6.78
FILL 100-25	4.42 ± 0.40	12.60
FILL 100-40	5.06 ± 0.37	19.69

FILL 100-50	5.28 ± 0.67	25.33
FILL 200-10	3.32 ± 0.27	7.94
FILL 200-25	4.08 ± 0.41	15.44
FILL 200-40	5.06 ± 0.32	23.99
FILL 200-50	5.40± 0.36	30.40
BAMBOO-10	2.98 ± 0.15	4.77
PX35-10	3.83 ± 0.39	12.35

Tabella 2 Moduli elastici dei materiali compositi fibrorinforzati: sono riportati sia i valori sperimentali che quelli previsti dal modello Halpin-Tsai.

Tuttavia, prove di trazione uniassiale di compositi a cella unitaria triangolare (*Figura 4*) hanno dimostrano la possibilità offerta dalla stampa UV-3D di controllare la risposta meccanica semplicemente variando la percentuale di riempimento e la geometria delle strutture.

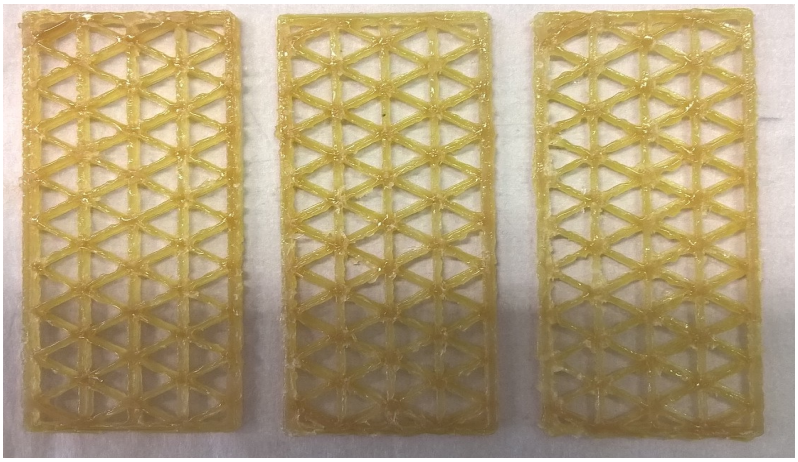

Figura 4 Campioni a cella unitaria triangolare stampati in composito rinforzato con fibre corte di vetro (FILL 100-40% v/v)

In generale, questa tesi dimostra che i principali vantaggi della stampa LDM rimangono il suo basso costo, la sua capacità di fabbricare geometrie anche molto complesse e la possibilità di stampare una vasta gamma di materiali. Se le proprietà meccaniche dei componenti ottenuti tramite processi di stampa 3D possono essere migliorate, questa tecnologia potrebbe diventare più di un'alternativa ai processi di produzione tradizionali.

FOREWORD AND STRUCTURE OF THE THESIS

During the last years, 3D printing, despite some current limitations, has undoubtedly attracted on itself a strong interest. Some argue that such technology could even lead to a "new industrial revolution" in the manufacturing world, having regard to the technical, economic and social implications that might have. The 3D printer can indeed have a disruptive potential impact on the way to design, produce, distribute and sell products.

Its use is common among designers, architects and engineers who design products and create prototypes. 3D printing is emerging also in the direct production of tools, molds and final products. Thanks to these new applications, 3D printing could enable unprecedented levels of mass customization in addition to make less expensive the supply chains.

The introduction of this technology, as well as lead to product/service innovations, could even have a stronger impact in materials production industry.

The materials available for 3D printing have come a long way since the early days of the technology. Similarly to printing techniques, even the materials used are in continuous evolution and experimentation. There is now a wide variety of different material types that are supplied in different states, such as powder, filament, pellets, granules, resin.

The most recent research is focusing on the development of stronger materials with increased mechanical properties, i.e. the composites. In addition to the well-known ABS filaments reinforced with carbon, some companies that deal with the production of 3D printing materials begin to develop composites based on liquid resins. One of the companies at the forefront of this field is Voxel8, with products based on the materials on which the Harvard researcher Jennifer Lewis works. The Voxel8's *3D Direct Write* printing technology allows to deposit a "viscous paste" at room temperature using pneumatic or volumetric systems.

As J. Lewis groups, also other teams of research are concentrated on the possibility to develop extusion systems for liquid deposition of composite materials. At +LAB (Politecnico of Milan), the laboratory where this thesis work was conducted, Professor Levi and Dr.Natale are focusing on the design and building of a liquid deposition system called LDM. This method offers the possibility to print composite materials through the introduction of short or continuous fibres, directly during the extrusion phase.

Within this framework, the experimental work presented in this thesis aims to investigate the possibility to formulate new polymer-based composite materials specially optimized for use in LDM UV-3D printing technology. The objectives to be achieved are as follows:

- Development and characterization of new photopolymer systems for use as matrix material in SFR-composite inks to be processed with UV-3D printing technology.

- Evaluation of the effects produced by different type and content of short reinforcing fibers on the processability of the corresponding inks.

- Assembly of a UV-radiation system on a low cost 3D printer for the deposition of liquid photocurable materials.

- Definition of the printability windows as function of materials and printing parameters.

- Evaluation of LDM UV-3D printing ability to reproduce complex geometries.

- Printing and mechanical characterization of composite specimens.

In particular, the structure of the thesis in which all the experimetal research is presented, is organized as follows:

- ***Section 1: State of the art: The 3D printing world***

The innovative world of the 3D printing technology, as additive manufacture, is presented.
An overview of the additive fabrication method, working principles, available processes and materials is provided. Finally, the attention focuses on a particular class of materials: the photopolymers.

- ***Section 2: Experimental work: Formulation, processing and characterization of printable solutions***

The whole experimental work conducted during the thesis experience is here presented. At the beginning, the adopted raw materials and the developed formulations for use in UV-3D printing application are descibed. Then, the UV-Assisted 3D Printing Process was presented: the UV-3D printer assembly and the stages of printing process are reported. Finally the characterization technique with the analytical methods employed to analyze the developed systems are presented.

- ***Section3: Results and discussion***

Firstly, the characterization of developed printable compositions is presented. In partcicular, the results of the analyses conducted on UV-curable systems, dual-curable materials and those related to the short fiber reinforced composites are shown.
Then, the study of the UV-Assisted 3D printing process in terms of parameters optimization and efficiency investigation is reported.
Finally, the mechanical response of the 3D printed materials is presented and discussed.

The present work concludes with a summary of the main collected results and a list of the main problems encountered during the experimental work. Future outlooks on the materials investigation carried out in this thesis experience are finally presented.

Section 1. STATE OF THE ART: THE 3D PRINTING WORLD

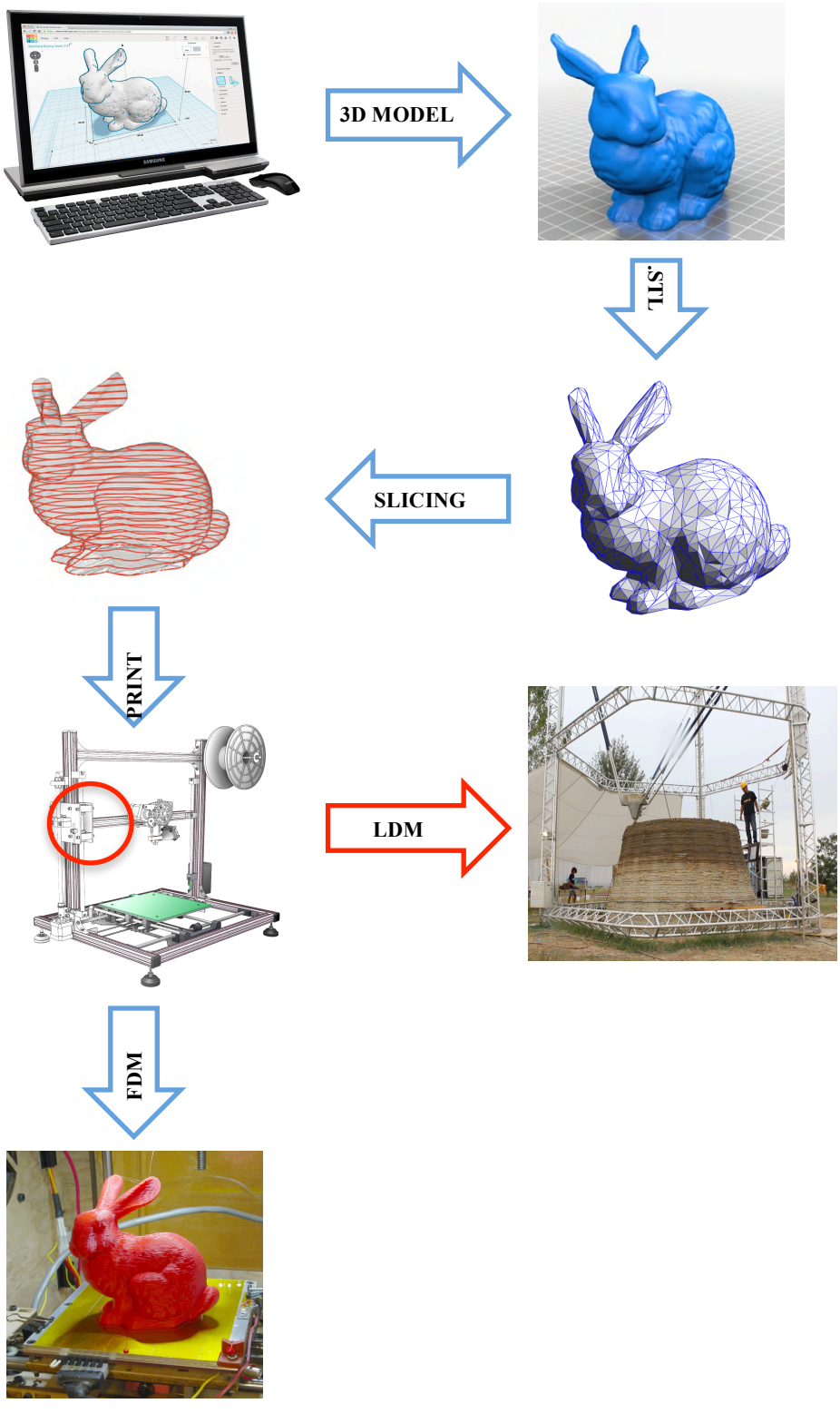

1.1 Introduction to 3D Printing

1.1.1 What is 3D Printing?

3D printing is a process that allows to fabricate a physical object from the three-dimensional digital model of the object itself, by adding layer by layer a material. Hence the term "*Digital Fabrication"* (DF) by which 3D printing technology is also identified. In a simplified version, 3D printing could be thought of as the process of building something with Lego® blocks automatically [1], [2].

Since the early eighties, different 3D printing advanced technologies have been developed, but all of them are based on the same principle of building up parts, additively, in layers at the mm and sub mm scale. Hence the term "*Additive Manufacturing*" (AM) that brings together all these tecnologies [3].
This is the key because 3D printing is considered a totally innovative manufacturing method compared to any other traditional existing manufacturing techniques, which are all based on the inverse principle of material subtraction. Indeed, all the traditional techniques require the subtraction of material from a large block, both to fabricate the end product itself and to produce a tool for casting or moulding processes. This implies the use of a combination of different machines and processes (e.g., forging, milling, bending, stamping, cutting, welding, gluing and assemby), thus imposing several limitations in terms of cost, time and material waste[1].
On the contrary, 3D printing, allowing the direct production of objects by means of a single layer by layer deposition process, reduces costs, waste and duration of the whole manufacturing cycle (*Figure 1.1.1*).

[1] The subtractive manufacturing processes can result in up to 90% of the original block of material being wasted.

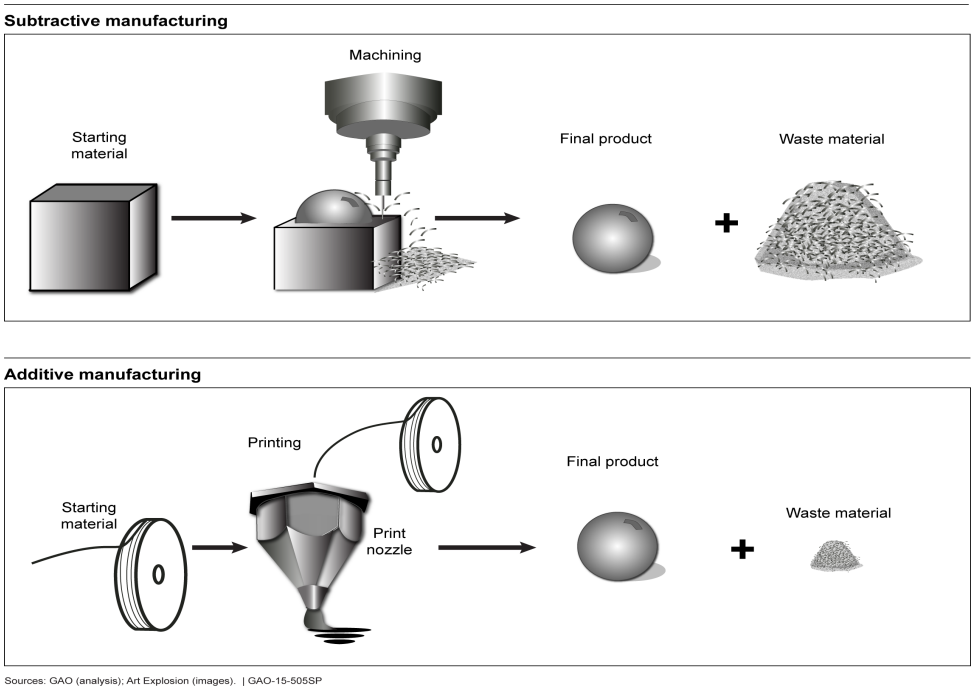

Figure 1.1.1 Conceptual comparison of Subtractive and Additive Manufacturing [4].

Moreover, 3D printing technology encourages and drives innovation with unprecedented freedom of design and, as a consequence, the "*Design for Manufacture and Assembly*" evolves into "*Design for Function*", where the only limitation is the imagination of the designer and its ability to implement appropriate design principles. AM technologies, being tool-less and enabling the creation of components with intricate geometries and complex functions at no additional cost, shall be adopted in different application fields: engineering, car manufacturing, aircraft manufacturing, shipbuilding industry, shoes manufacturing, product designer, dental, prosthetics, medical fields, etc [5]–[7].

3D printing, due to its ability in reproducing objects that emulate very well the appearence and functionalities of the finished products, was initially developed in the prototyping industry, we can talk about *Rapid Prototyping* (RP). In the following decades, having regard to its potential, 3D printing has started to be used also in the manufacturing industry for the fabrication of products and tools for end-users. In this case we can refer to the additive processes as *Rapid Manufacturing* and *Rapid Tooling*, respectively. In recent years, the development of cheaper and more accessible 3D printers has allowed the 3D printing technology to go beyond the industrial world, opening up to the wider audience of individual users, the so-called *makers*.

In the following paragraph, a brief overview on the development of AM technologies will be presented.

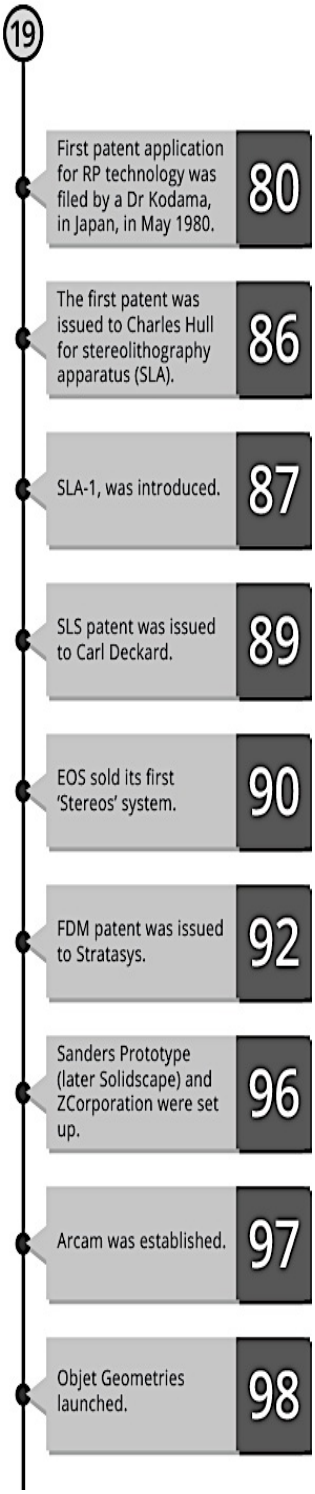

1.1.2 A brief history of 3D printing

Although 3D printing is commonly considered the daughter of present technological development, it has actually been developed over 30 years ago.

The first 3D printing technologies made their first appearance in the industrial world in the early 1980's with the aim of supporting companies in the development of prototypes.

Dr. Kodama, in Japan, filed the very first patent application for RP technology in May 1980. Unfortunately, the full patent specification was not filed before the one year deadline after the application and, hence, the origins of the 3D printing can be traced back to 1986, when Charles Hull filed the first patent for *Stereolithography* apparatus (SLA). Hull, who invented the first SLA machine in 1983 (*Figure 1.1.2*), defined SLA as "*a method and apparatus for making solid objects by successively "printing" thin layers of a curable material,e.g., a UV curable material, one on top of the other*" [9]. Then Hull co-founded the '3D Systems', one of the most prolific company operating in the 3D printing sector today [10].

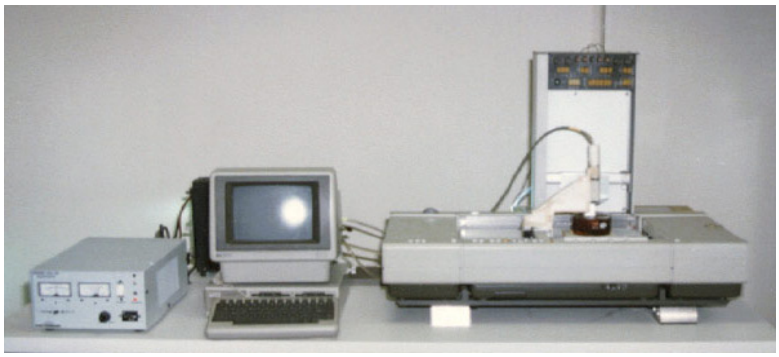

Figure 1.1.2 SLA-1, the first 3D printer invented by Chuck Hull in 1983. These machine was introduced in 1987 as 3D System' first commercial RP system and after rigorous testing the first was sold in 1988.

In the same period, others were working on the developed of new systems for RP: in 1987, Carl Deckard filed a patent for the *Selective Laser Sintering* (SLS) process [11].

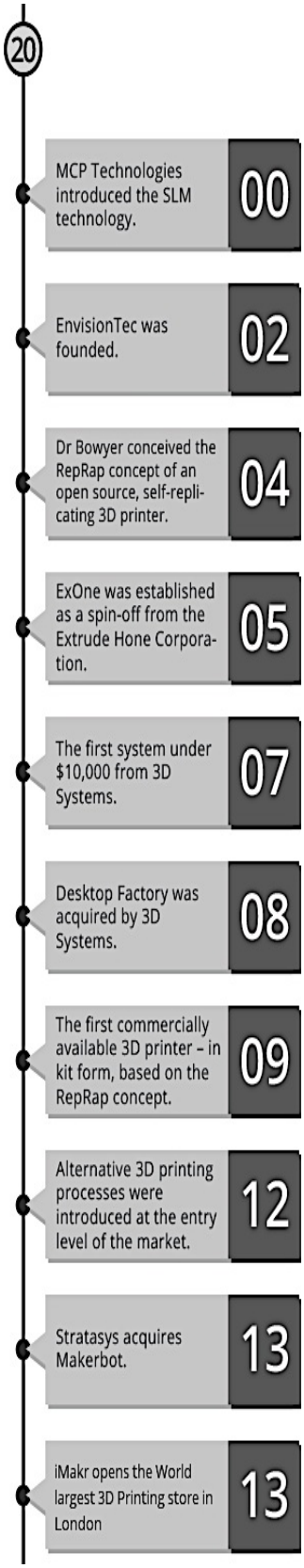

In 1989, Scott Crump, a co-founder of Stratasys Inc., filed a patent for *Fused Deposition modeling* (FDM) [12], [13].

Throughout the 1990's and early 2000's new technologies continued to be introduced, still completely focused on industrial applications: EOS, founded by Hans Langer, focused on *Laser Sintering* (LS) processes [14]; Emanuel Sachs et al. developed the *Three Dimensional Printing* (3DP), etc.

During the mid nineties, the 3D printing market started to show signs of a significant diversification. On one side, there were the very expensive systems that continued to be optimized for the production of highly engineered and complex components with high value. On the other side, office- and user-friendly, cost-effective systems began to be developed but they were all still mainly used in industrial applications.

For the development of the first small printers (desktop machines), suitable for personal use, we had to wait until 2007, year that marked the real turning point for accessible 3D printing technology, when the *RepRap phenomenon* took root.

Actually, the idea that it was possible to move from professional 3D printer to something new, smaller and more accessible, was expressed for the first time in 2004 by Adrian Bowyer. He imagined the concept of self-replicating machines, which were able to print their own components, and so simply and easily that anyone would be able to build them. From this idea came the RepRap Project (*Figure 1.1.3*).

But it was not until 2009 that the first desktop 3D printer was born. This is indeed the period in which the FDM patent expired.

In this year *MakerBot Industries*, a company of open-source hardware for 3D printer, started selling DIY[2] kits that allowed buyers to build their own printers.

[2] Do It Yourself: it is an activity of manual construction, modification or repair of objects without the aid of experts or professionals.



Figure 1.1.4 On the left: significant events in the development of 3D printing.

The interesting dichotomy is that, while the RepRap phenomenon has given rise to a whole new sector of commercial, entry-level 3D printers, the *ethos* of the RepRap community is all about Open Source developments [15].

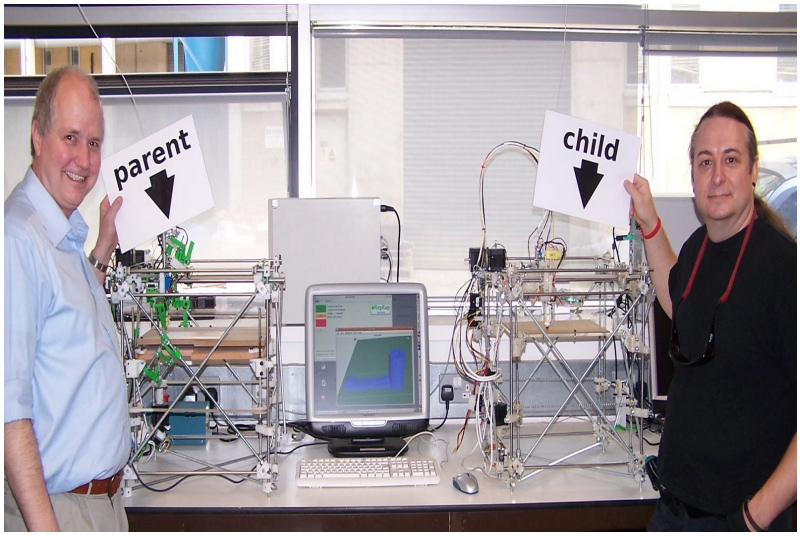

Figure 1.1.3 Adrian Bowyer and Vik Olliver with a RepRap printer (parent) and a clone (child) produced using the original one [16].

As more and more manufacturers followed, machines once cost $200,000 suddenly became available for below $2000, and the consumer 3D printing market took off in 2009 [6].

3D printer sales have been growing ever since (*Figure 1.1.5)*, and as additive manufacturing patents are continuing to expire, more innovations can be expected in the years to come. Today there are roughly 300,000 consumer 3D printers in the world and this figure is doubling every year.

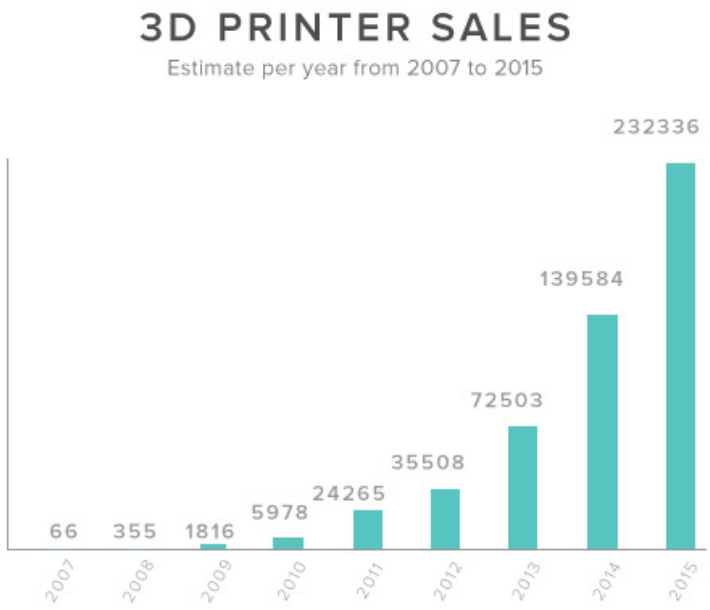

Figure 1.1.5 Estimated 3D printer sales per year from 2007 to 2015. Source: Wohler's Report 2015; Gartner

3D printing, being a very rapidly developing tecnology, comes with its set of inherent benefits, but also lags behind traditional manufacturing processes in some aspects.

The following paragraph presents the pro and cons of this technology.

1.1.3 The Pros and Cons of 3D Printing

1.1.3.1 3D Printing benefits

3D printing, whether at an industrial, local or personal level, brings a host of benefits that traditional manufacturing methods simply cannot [5].

- **Complexity is free**

One of the main benefits introduced by the 3D printing in the world of design and manufacturing is the ability to get products that involve levels of complexity that simply could not be produced physically in any other way. In particular, extremely complex and detailed products can be 3D printed at the same cost of a simple design product, which follows all the traditional rules of conventional manufacturing (*Figure 1.1.6*).
This has made a significant impact on industrial applications, especially in aerospace sector, where parts with complex geometry are required, often with properties like lightness and strongness.

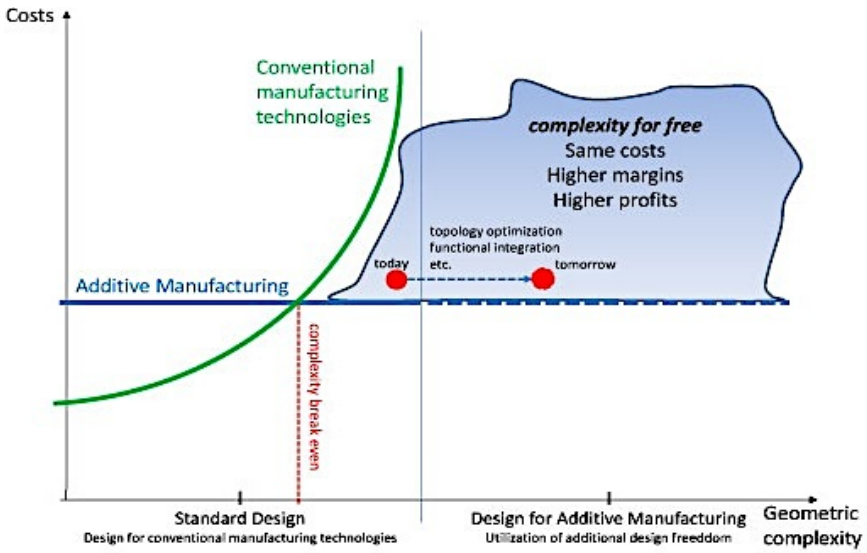

Figure 1.1.6 Idea of complexity for free: with AM technology it is possible to obtain very complex geometries at no additional costs [8].

- **Customization is free**

3D printing allows high degree of customization without increasing production costs.

This is the opposite of mass production, which involves the repetition and standardization limiting the possibility for customization.
With digital manufacturing the elements that affect the traditional production costs, e.g., the costs related to the production and modification of the molds, become free: every item can be customized to meet user's specific needs without additional manufacturing costs. This because the product differentiation, according to individual needs and requirements, not necessitate to change the equipment; the printer remains the same, it is sufficient to change only the 3D digital model.

- **Tool-less**

For industrial manufacturing, one of the most cost-, time- and labour-intensive stages of the product development process is the production of the tools. For low and medium volume applications, industrial 3D printing allows to eliminate tool production and all the support activities required during the traditional manufacturing of products, such as mold fabrication, assembly, etc. In fact on the same scale, 3D printing technologies, through the *in layers* fabrication, allow the production of self-assembled objects. This means shorter chain of supply and reduction of costs and time involved.

- **Speed and ease of prototyping, the faster and less risky route to market**

Since there is no expensive tooling required to create objects through 3D printing, it is particularly a cost effective method for designers or entrepreneurs who are looking to do market testing or small production runs.
Furthermore, due to the benefits listed above, 3D printing can be considered a way much less risky for those who are trying to find out a product idea to enter the manufacturing market.

- **Less waste**

3D printing is emerging in the manufacturing market also as an energy-efficient technology: there is a very little waste of raw materials. When you create an object by adopting an additive manufacturing technology, only as much material that is needed to create that particular object is used. In fact, the material is deposited only where it is needed to create the desirable geometry, thus obtaing lighter objects. Moreover, in some cases additional parts like supports could be necessary to hold up the entire structures if they are very protruding. In these cases, the support's material is not wasted but it can be recycled and repurposed into more 3D printed objects.

1.1.3.2 3D Printing limits

Despite all the benefits of manufacturing through additive methods, 3D printing, especially if thought as a process to be adopted for the large-scale production, presents some limits. Below, the most relevant ones are listed.

- **Higher cost for large scale productions**

3D printing cannot offer economies of scale; it is not yet competitive with conventional manufacturing processes when it comes to large scale productions. In general, AM processes are not cheaper for the production of a thousand pieces rather than just one. However, it is expected that the more the price of printers and raw materials continue to decrease, the more the range of efficient production increases.

- **Longer fabrication process**

The duration of the 3D printing process is one of the main limits of this technique: the production of a single printed 3D object requires more time than that would be needed if the same piece were produced through traditional technological process.

- **Low quality control**

3D printing is a very capable method of creating objects at a precision of around 20-100 microns but it is very difficult to run an effective quality control on the production process. Since each 3D printed piece can consist of thousands of layers of material it is difficult to know in advance which layers may have imperfections and how this might affect the final functionality.

- **Limited strength and endurance**

In some 3D printing technologies the strength of the printed object is not uniform due to the layer-by-layer fabrication process. As such, parts that have been 3D printed are often weaker than their traditionally manufactured counterparts, e.g., those obtained by casting. Also repeatability needs to be improved; parts made on different machines might have slightly varying properties. However, as technical improvements continue to be made on 3D printing processes, these limits will likely to vanish in the near future.

1.2 3D Printing Technology

1.2.1 How does 3D printing work?

The starting point for any 3D printing process is a 3D digital model of the object that you want to fabricate. By means of a dedicated software, this model is then sliced into thin cross-sectional layers and the corresponding file is sent to the 3D printer which works by adding layers of material on top of each other until the original digital model becomes a physical object [17].
The different phases of an entire printing cycle are shown in the *Figure 1.2.1*, and described more in detail hereinafter.

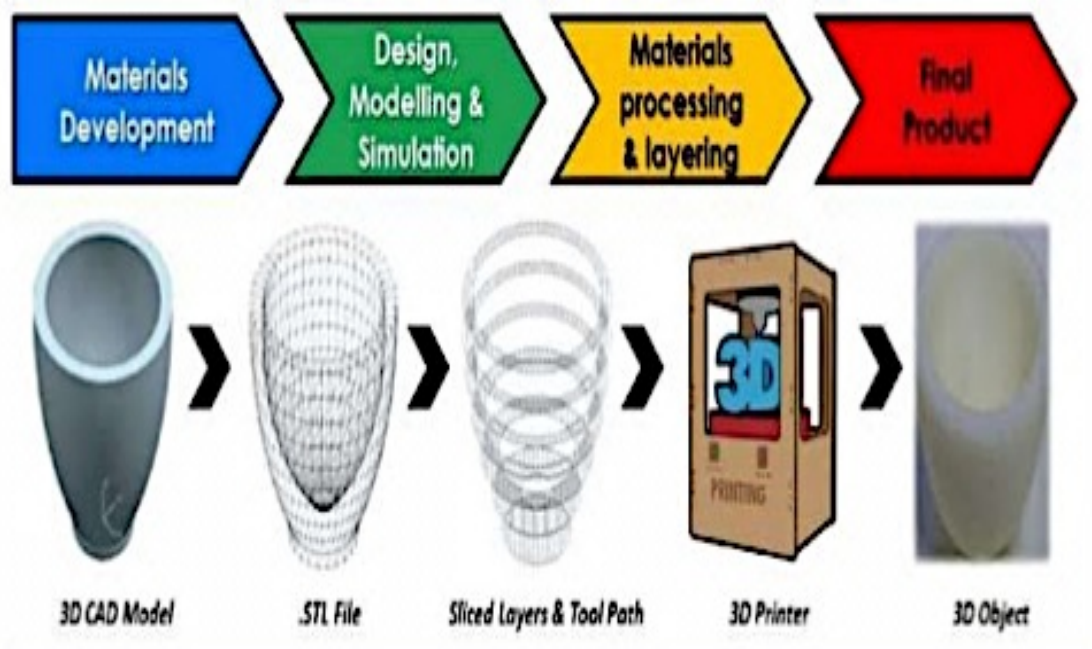

Figure 1.2.1 A printing cycle: from the 3D digital model to the physical object.(Godoj et all, 2006)

1.2.1.1 3D modeling

The preliminary stage in a printing cycle includes the 3D model design of the object you want to fabricate; this can be obtain by adopting different alternatives as described below.

- **Modeling through CAD software**

You can use special three-dimensional modeling software that can generate 3D objects working on solid or surface construction, i.e., the CAD[3] software.
There are different types of CAD software; the difference lies in the way in which the modeling itself takes place: solid, sculptural, parametric [18].

The 3D '*solid'* modeling software are based on the CSG[4] technology which offers the possibility of having pre-established forms, such as cylinders, cubes, pyramids, spheres, etc, through which you will define more complex objects through their union or modification.
The most famous programs with freeware license that use the solid modeling method are: Google *SketchUp, Autodesk 123D, Tinkercad* and *Blender*. Among the programs with paid license there are: *Solidworks, Pro Engineering, Solid Edge, AutoCAD, 3D Studio Max, Rhinoceros* and *Cinema 4D*.

The '*sculptural'* 3D modeling software allow you to create objects by carving basic three-dimensional shapes. Usually the basic shapes are freehand carved, this allows to get more graceful and natural surfaces. In fact, this type of 3D modeling is appropriate to draw figures, faces, natural or organic objects.
The most popular software of this type are: *ZBrush, Sculptris, FreeForm, Mudbox, 3D-Coat*.

Then there are the '*parametric'* 3D modeling software. These allow you to draw three-dimensional objects using writing programs containing the objects parameters. Different forms can be combined between them, defining in an extremely precise way each minimum variation of surface or volume due to the setting of the parameters. Examples of parametric modeling software are: *Grasshopper* and *OpenSCAD*.

[3] The abbreviation "CAD" means "*Computer-Aided Design*". The Computer Aided Design systems have as goal the creation of models, generally 3D, of an object.
[4] The abbreviation "CGS" means "*Construction Geometry of Solids*".

- **Download existing 3D models**

As an alternative to the design you can download models from some online libraries, where the community shares projects for free. The most visited are: *Thingiverse, GrabCAD, 123D Design.*

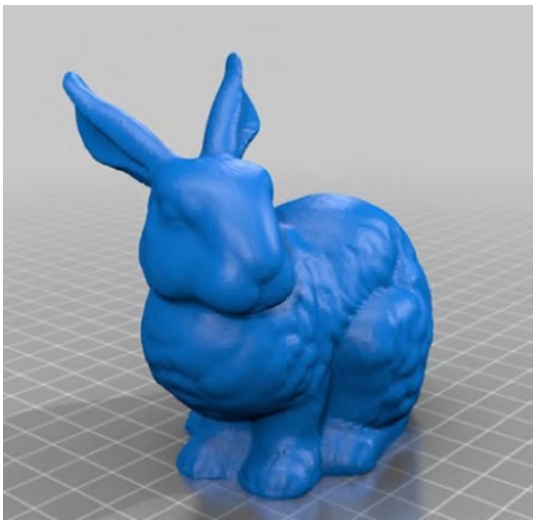

Figure 1.2.2 Standford Bunny 3D model downloaded from Thingiverse [19].

- **Reverse Engineering**

Lastly you can get the 3D model by performing a reverse engineering operation (RE), which is a process of digitization of a reference physical object. The RE consist of two phases:
- The first, called '*data acquisition'*, is based on the discretization of the objects in contiguous points in the space, a "cloud of points" which roughly describe the object's shape.
- The second phase, called '*transformation'*, consists in the elaboration of the "cloud of points" in mathematically definable surfaces. These areas, known as NURBS surfaces (Non Uniform Rational B-Splines), geometrically and rationally approximate the mesh obtained from the point cloud [20].

1.2.1.2 .STL file export

Once obtained the digital model, this is converted into a format compatible with the 3D printer management software. The graphic standard currently employed is the .STL[5] that divides the surfaces

[5] The .STL is the acronym for "Standard Triangulation Language" or "Solid Layer to" or "Stereo Lithography interface". This file format was introduced by the American company "3D System" in 1987.

into a network (mesh) of triangular elements to obtain a simplified representation of the internal and external surfaces of the object through triangular facets (*Figure 1.2.3*) [21].

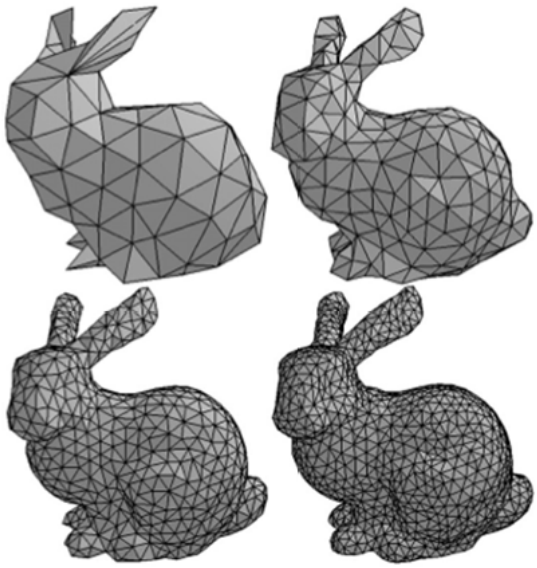

Figure 1.2.3 .STL file of the 3D model shown in the Figure 1.2.2. Different resolutions are reported.

The .STL file contains all the data related to the surface: X, Y and Z coordinates are repeated for each of the three vertices of the triangle, a vector describes the orientation of the normal to the surface. A total of 12 numbers are stored for each faceted architecture. In the .STL file there are no color, material, texture, substructures or other properties information [20].

1.2.1.3 Slicing

Slicing is the intermediate step between modeling and 3D printing, and it consists in the subdivision of the digital objects in layers.
Once the file .STL has been generated, it is loaded into a slicer-CAM[6] software (the most common in the market now are *Slic3r, Cure, Simplify 3D, Kisslicer).* These software allow to orient the object for optimal construction, to generate the supports for the overhanging parts and, finally, to convert it in a set of plans whose normal is parallel to the direction of printing (*Figure 1.2.4*) [22].

[6] CAM states for "*Computer-Aided Manufacturing*". The CAM software is commonly called "Slicer".



Figure 1.2.4 Slicing of the Standford Bunny model.

In particular, the slicing software converts the 3D models into a series of commands, which allow the 3D printer to figure out what to do and how it should move in order to build layer by layer the desired object.

The first goal during the slicing process is to set up and optimize some print features of the model, such as layer height, shell thickness, fill density, support type, print speed, etc. In fact each of these parameters, described in detail in the paragraph § *2.2.3*, can influence both during and after the release, the appearance and the behavior of the printed object. The ultimate goal of the slicing process is to export the 3D files in a recognizable format and readable by the printer.

1.2.1.4 .Gcode file export

As seen above, the slicer software converts the digital model into instructions to give to the 3D printer, setting all printing parameters. The printer receives all of these instructions thanks to a specific code, called *Gcode*.

The file contains the tool-path and the set parameters with all the information needed to guide the machine in the physical generation of the piece: feedrates, filling path, each position in X, Y and Z, the parameters of temperature and so on. This file contains the functions of a numerical control programming language.

For example, the *G* code is used for the positioning of the device and the execution of the work, the *M* code handles the machine; the T code indicates the code related to the Tool. *S* and *F* correspond to tool-Speed and tool-Feed, respectively.

After the generation, the Gcode is sent to the 3D printer through USB connection or directly by plugging a SD card containing the file in the machine.

1.2.1.5 3D print

The Gcode is interpreted by the machine and translated into consequential operations until the complete realization layer by layer of the physical object (*Figure 1.2.5*).

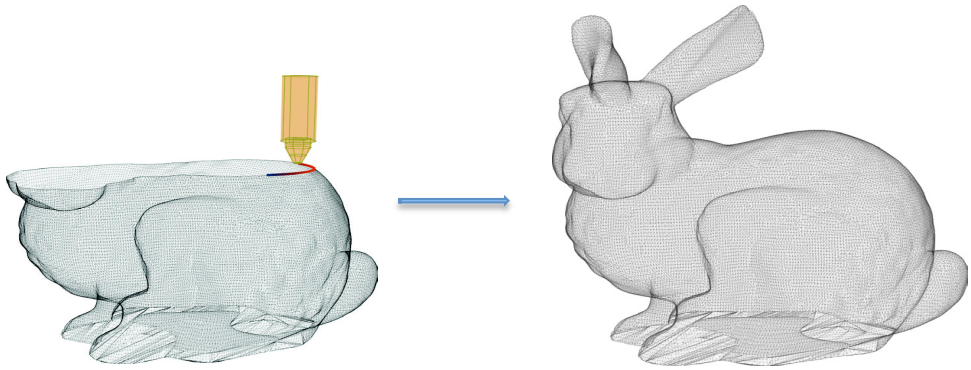

Layer by layer material deposition *Physical object*

Figure 1.2.5 3D printing to create physical object: from the layer be layer deposition to the final object.

If you do not have a printer you can take advantage of some online service to which you can send the .stl file and obtain the physical object, having the possibility to choose the type of material and color. Some sites that do this after service are: *Shapeways, Ponoko, Sculpteo, I.Materialise, ZoomRP, Redeye, Vectorialism* [23].

1.2.1.6 Post-processing and finishing

When the machine will have completed all the steps, the finished part will be removed from the printing plate, and you will proceed with the removal of the supports (if any) and with the execution of any post-treatments in order to improve the mechanical and / or aesthetical characteristics of the object, if required.

The methods to achieve the desired surface finish can be different. Dr. Federico Riva in his thesis "Superficie in attesa: processi per la finitura superficiale della stampa 3D FDM" [24], catalogs them in the following ways:

- *Subtractive and remodeling finishing*: provide for the removal of material using mechanical, chemical or thermal processes.

- *Intrinsic finishing*: derived from the material and printing parameters.

- *Additive Finishing*: made with weld material (e.g., painting (*Figure 1.2.6*)).



Figure 1.2.6 Reproduction of "Milo's Venus" made with FDM printer at +Lab. It is finished with abrasives and chrome painting [25].

1.2.2 3D printing processes

As already explained, all AM technologies create physical objects from digital designs layer by layer, but each using its own proprietary method. For many years, the additive manufacturing industry lacked categories for grouping AM technologies, which made it challenging when communicating information in both technical and non-technical settings. In February 2012 all the technologies have been grouped into categories by the "Committee F42" of "ASTM international". These process categories enable one to discuss a category of machines, rather than needing to explain an extensive list of commercial variations of a process methodology. In the publication, "*Standard Terminology for Additive Manufacturing Technologies*", the several processes are grouped according to the following standard terminology:

Binder jetting: an additive manufacturing process in which a liquid bonding agent is selectively deposited to join powder materials.

Directed energy deposition: an additive manufacturing process in which focused thermal energy is used to fuse materials by melting as they are being deposited.

Material extrusion: an additive manufacturing process in which material is selectively dispensed through a nozzle or orifice.

Material jetting: an additive manufacturing process in which droplets of build material are selectively deposited.

Powder bed fusion: an additive manufacturing process in which thermal energy selectively fuses regions of a powder bed.

Sheet lamination: an additive manufacturing process in which sheets of material are bonded to form an object.

Vat photopolymerization: an additive manufacturing process in which liquid photopolymer in a vat is selectively cured by light-activated polymerization [26].

Starting from the above high level grouping, the 3DHubs has created a very useful infographic highlighting all the main technologies, guiding through the printing process (the exact technology acronysms are reported), material options and ending with the key industry players (*Figure 1.2.7-zoomed image in the following insert*).

ADDITIVE MANUFACTURING TECHNOLOGIES

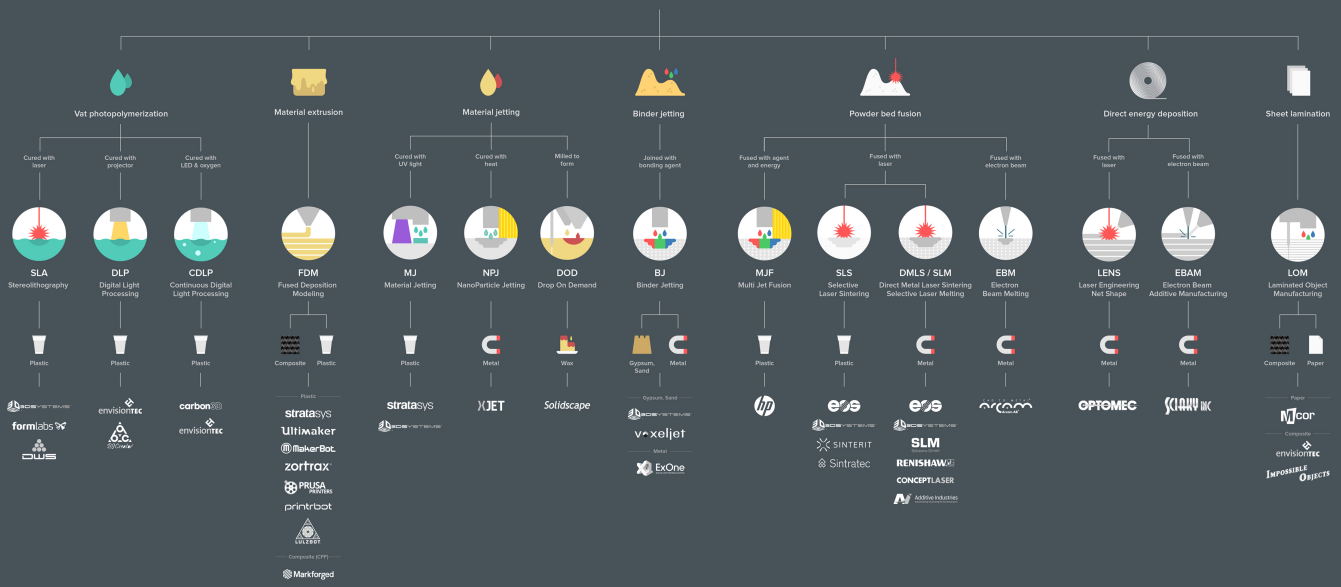

Find out more at **www.3dhubs.com/what-is-3d-printing**

3D HUBS

Moreover, the AM processes can be further reordered following different approaches. The most common one is to classify them according to baseline technology, like whether the process uses lasers, printer technology, extrusion technology, etc. Other approaches are to collect processes together according to the raw material input. This can be done on the basis of its physical state before processing (solid, liquid, powder) or according to the type of material (metal, thermoplastic polymer, photopolymer, clay, etc) [5], [27], [28].

Following the approach based on the physical state of raw materials, the different processes presented in the *Figure 1.2.7* can be reorganized as shown in the *Figure 1.2.8,* below.

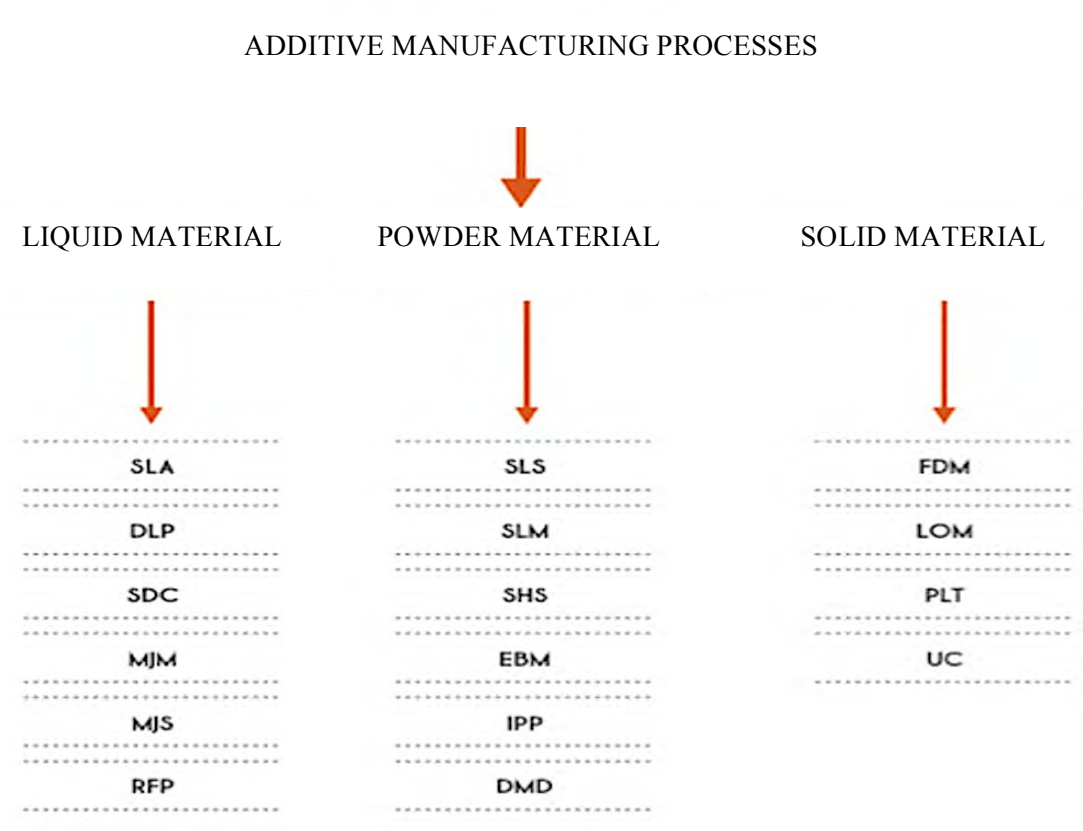

Figure 1.2.8 Classification of the 3D printing processes on the basis of the physical state of the processed material [29].

In the following paragraph, some of the processes in the two figures above will be analyzed in detail.

1.2.2.1 Stereolithography (SL)

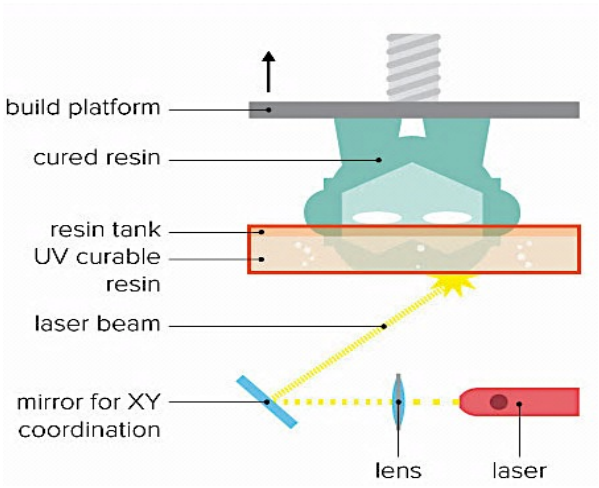

Figure 1.2.9 Schematic stereolitography apparatus (SLA) [15].

Stereolithography (SL) is widely recognized as the first 3D printing process; it was certainly the first to be commercialised (SLA1 by *3DSystem* ,1987). It is a laser-based process that works with photopolymer liquid resins. 3D printed objects are created from a liquid resin by using a light source to solidify the liquid material.

To create a 3D printed object, a build platform is submerged into a translucent tank filled with liquid resin. Once the build platform is fully covered by the resin, a laser beam maps each layer of the object through the bottom of the tank, thus solidifying the material. The beam is directed along the x-y axes across the surface of the resin according to the 3D data supplied to the machine (the .STL file), whereby the resin hardens precisely where the laser hits the surface.

After a layer has been completed, the platform lifts up (in the z axis) and lets a new layer of resin flow beneath the object once again. This process is repeated layer by layer until the desired object has been completed (*Figure 1.2.9*).

SL is considered one of the most precise 3D printing process to fabricated very accurate and complex design, with an excellent surface finish.

However limiting factors include the required post-processing steps and the stability of the materials over time, which can become more brittle. In fact, in many cases, the 3D printed objects need to be cleaned, subjected to intense light radiation in an oven-like machine to fully harden the resin and, if any, the support structures for some overhanging or undercutting part should be manually removed.

Materials available for SLA are limited to resins, but new varieties have appeared recently providing strength or flexibility to the final objects.

1.2.2.2 Digital Light Processing (DLP)

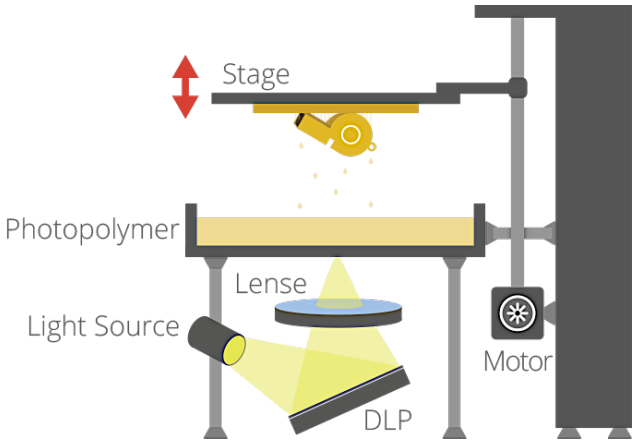

Figure 1.2.10 Digital Light Processing schematization [15].

Digital light processing (DLP), developed in 1987 by "Texas Instruments", is a process similar to stereolithography because also in this case photopolymers are used. The major difference is in the light source; in fact, DLP uses a more conventional light source (an arc lamp) and a projector (DLP projector) (*Figure 1.2.10*).

Like SL, DLP produces highly accurate parts with excellent resolution, but in its similarities the same requirements for support structures and post-curing are also included. However, one advantage of DLP over SL is that only a shallow tub of resin is required to facilitate the process, which generally results in less waste and lower running costs.

1.2.2.3 Material Jetting (MJ)

Material Jetting processes, such as Stratasys PolyJet (PJ) and 3D Systems MultiJet Modeling (MJM), are 3D printing processes in which tiny droplets of liquid photopolymer material are selectively deposited onto a build tray and instantly cured using UV light.

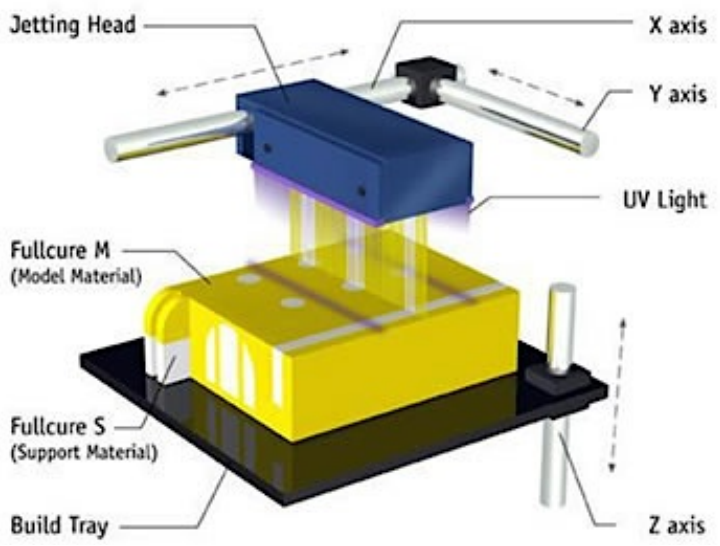

Figure 1.2.11 PolyJet process schematization [30].

The liquid materials (M *model* material and S removable gel-like *support* material, in the *Figure 1.2.11)* are selectively jetted through multiple jet heads and, as the process is repeated, these thin layers accumulate on the build tray to create a precise object.

The nature of this technology allows the simultaneous deposition of a range of materials, which means that a single part can be produced from multiple materials with different characteristics and properties. The available materials are liquid photopolymers that can provide to the final objects various properties including toughness, transparency or rubber-like flexibility.

Material jetting is a very precise 3D printing method (up to 16 μm layers can be printed), usually used for rapid tooling and prototyping, which can produce accurate parts with a very smooth finish.

1.2.2.4 Selective Laser Sintering (SLS)

SLS printing is a process patented in 1980 by Carl Deckard. It refers to a laser based 3D printing process that works with powdered materials.

A laser is traced across a powder bed of tightly compacted powdered material, according to the 3D data fed to the machine, in the x-y axes.

As the laser interacts with the surface of the powdered material it sinters, or fuses, the particles to each other forming a solid.

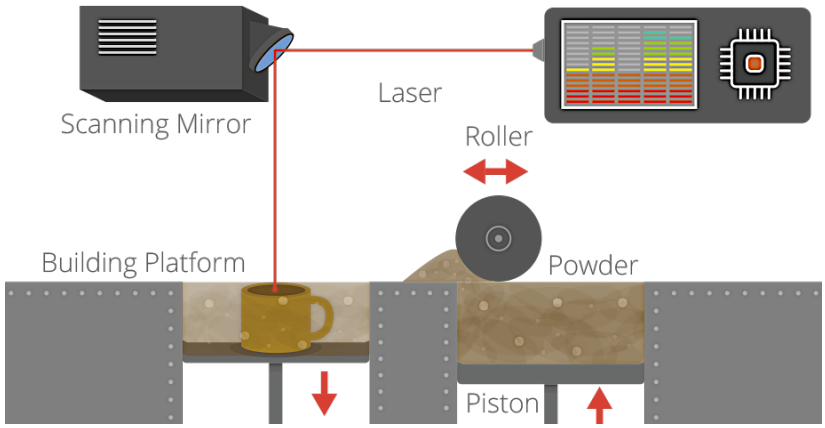

Figure 1.2.12 Selective laser sintering process schematixation [15].

Once a layer has been solidified, the print bed (printing platform) moves down slightly as the other bed containing the powder moves up; a roller smoothes the powder atop the surface of the already solid layer prior to the next pass of the laser for the subsequent layer to be formed and fused with the previous one. This process is repeated, and the laser melts successive layers one by one until the desired object has been completed.

Once the netire object is finished, the excess powder can be removed to leave the 'printed' parts (*Figure 1.2.12*).

SLS is widely used to produce functional prototypes and parts as well as some end products. The biggest advantage of laser sintering is the almost complete design freedom; excess unmelted powder acts as a support for overhangs and undercuts, thus allowing the manufacturing of complex and intricate shapes with no additional support needed.

However, on the downside, because of the high temperatures required for laser sintering, cooling times can be considerable. Furthermore, porosity has been an historical issue with this process, and while there have been significant improvements towards fully dense parts, some applications still necessitate infiltration with another material to improve mechanical characteristics.

Laser sintering can process plastic (generally, polyamides polystyrenes and thermoplastic elastomers) and metal, although metal sintering requires a higher-powered laser and increased in-process temperatures. Parts produced with this process are much stronger than with SL or DLP, although generally the surface finishing and accuracy are not so good.

1.2.2.5 Inkjet Powder Printing (IPP)

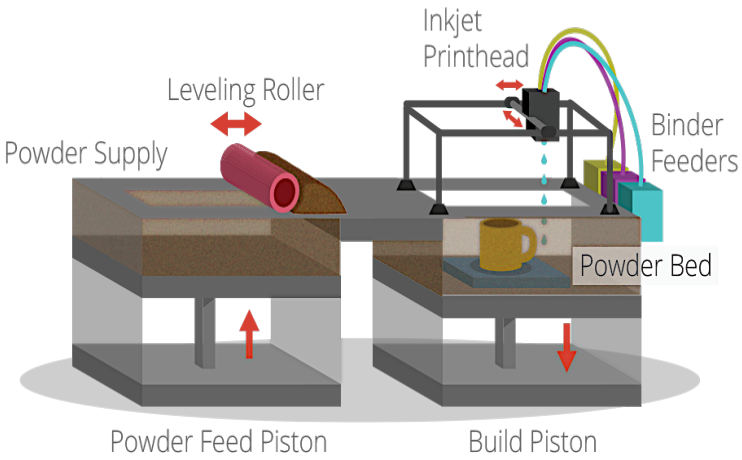

Figure 1.2.13 Binder Jetting process [15].

The inkjet powder printing technology has been developed at MIT with the name of "3DP", acronym of Three Dimensional Printing. It is similar to SLS because the printer uses thin layers of powdered material to build up an object, but instead of using a laser that sinters the layer together, these printers use a binding agent extruded from printhead to bind the powder together. The binder, which can be added also with some colors, is selectively sprayed into the powder bed in order to create the first layer of the required object. Once the first layer has been fused with the binding agent, the printing bed moves down slightly and a thin layer of new powder is spread atop the object (*Figure 1.2.13*). This process repeats until the desired object has been fully formed. After it is removed from the print bed, the object is cleaned from excess powder and coated with an adhesive glue to give it strength and to make it resistant to discoloration.

IPP is used in industrial 3D printing and the most diffused material is the sandstone. It is relatively affordable compared to SLS as the printing process requires less energy, but the printed objects are less strong.

The ability to print in full color has made sandstone popular for architectural models and lifelike sculptures.

1.2.2.6 Electron Beam Melting (EBM)

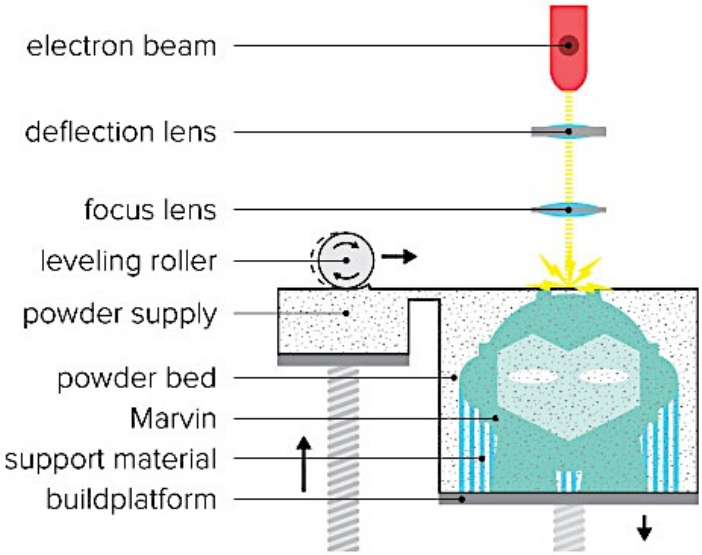

Figure 1.2.14 EBM process shematization [18].

The Electron Beam Melting 3D printing technique is a process developed by Swedish company Arcam. This is a metal printing technology which exploits the energy of a electron beam to selectively melt the metal powder. The presence of an electron beam as heat source leads the process to necessarily work under vacuum conditions.

During the printing process, a layer of metal powder is distributed onto a build platform, which is melted by an electron beam. The build platform is then lowered, coated with new layer of metal powder on top and the process is repeated until the object is fully realized.

EBM requires support structures, which anchors the object and overhanging structures to the build platform and enables heat transfer away from the melted powder (*Figure 1.2.14*).

Materials processed with EBM include various metals and alloys including steel, titanium, aluminum, cobalt-chrome and nickel.

Metal printing is considered the “holy grail” of additive manufacturing; it is widely used in the aerospace, aircraft, automotive and healthcare industry for a range of high-tech, low-volume use cases from prototyping to final production. 3D printed metal parts allow for monolithic construction (reducing the quantity of components), miniaturization and mass reduction. EBM have evolved to a stage where these prints are comparable to traditionally manufactured parts in terms of chemical composition, mechanical properties as well as microstructure.

1.2.2.7 Fused Deposition Modelling (FDM)

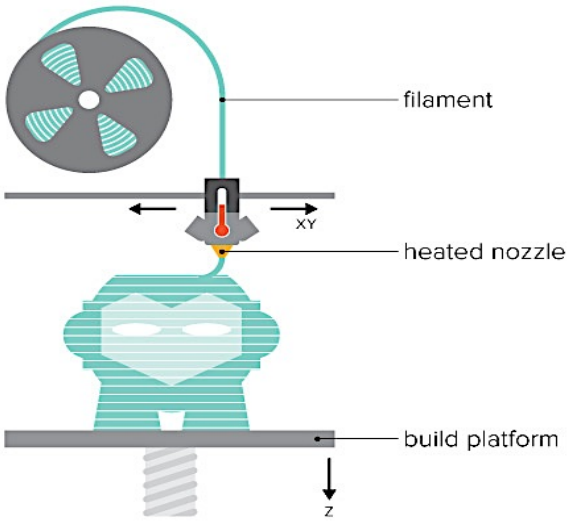

Figure 1.2.15 FDM process schematization [6].

The FDM printing process is a *material extrusion* type technology.

FDM is a trade name, registered by Stratasys, the company that originally developed it. Stratasys' FDM technology has been around since the early 1990's and today is an industrial grade 3D printing process. However, the entry-level 3D printers that have emerged since 2009, largely utilize a similar process referred to as Freeform Fabrication (FFF), but in a more basic form due to patents still held by Stratasys. The earliest RepRap machines and all subsequent open source and commercial evolutions employ anyway an extrusion methodology.

The process starts from a solid thermoplastic filament that is guided from a reel attached to the 3D printer to a heated nozzle that melts the material.

Once in a melted state, the material can be extruded and deposited on a horizontal plate called "Build Platform" by moving the print head or plate, or by combining the movements of the two elements in the spatial dimensions xy, in order to trace the layer section. In contact with the surface, the filament cools and rapidly solidifies, providing the foundation for the next layer.

At the end of the first layer the machine acts on the z axis lifting the extruder or in some variants, lowering the printing plate, and the deposition of the next layer start. This system is repeated several times until the three-dimensional object is completed (*Figure 1.2.15*).

As the cheapest 3D printing technology on the market, FDM also offers a wide variety of plastic-based materials in a wide variety of colors including ABS, PLA, nylon and even more attractive material blends including carbon-, glass-, kevlar- reinforced composites [31], bronze or wood. FDM is a great choice for quick and low-cost prototyping and can be used for a wide variety of applications.

1.2.3 From FDM to LDM

"The LDM 3D printing (Liquid Deposition Modeling) is a technology that uses liquid material at room temperature. According to this model the liquid is extruded in a controlled way layer by layer on the printing bed until the construction of the item is completed."
This is the definition of the new *material extrusion* process given in M. Levi's "Make or make not. There is no try. What to Print in 3D and Why" [32].

LDM can be thought of as the low-cost liquid evolution of the FDM: the two technologies possess the same electronic and mechanical elements that manage the handling dynamics of the extruder head. In both technologies, the material that has to be deposited is pushed inside a variable length channel that terminates with the printing nozzle, whose diameter can vary from some hundreds of microns up to the order of centimeters. The nozzle area, together with the speed at which the material is pushed and its density determine the flow rate and hence the speed and the deposition flux.

In the FDM technique the raw material is a thermoplastic polymer in the form of solid filament with a diameter of 1.75mm or 3mm, which is pushed by means of a gear inside the extruder block. Here, the material is induced to phase change, from solid to liquid state, by means of the heat generated by an electrical resistance. Once in the liquid state the polymer is able to escape from the nozzle, and the layer by layer deposition process can start, as previously explain *(§ 1.2.2.7*).
In the LDM process, the raw material can be any possible liquid at room temperature, with a variable viscosity. Generally, medium-high viscosity materials are used. These are loaded in an apposite extrusion system and, pushed by a suitable pressure, are forced to exit from the nozzle and to be deposited on the print plate. In particular, the extrusion mechanism can exploit different principles to generate the required pressure to force the material deposition: from the atmospheric pressure down to that induced by means of pneumatic systems which typically work with compressed air or mechanically.

In order to 3D print correctly liquid materials, Dr. Natale has designed and realised at +LAB specific extruders which allow to employ the required pressure for the material extrusion, checking the whole process in the best way [32], [29].
According to the Pascal's law (1653, *"Sur l'equilibre des liqueurs"*) that states [33]: *"The pressure exerted at any point of a confined fluid is transmitted in every other point of the fluid with the same intensity, regardless of the direction",* Natale initially designed a syringe extruder that, thanks to a specific modular slot, can be equipped with common luer lock from 1 to 100 ml plastic syringes. This,

mounted on a RepRap FDM printer, is exactly the same system adopted in this experimental work. Further details about the whole machine will be presented in details in the next section (*§ 2.2*).
Moreover, due to the impossibility for this system to process highly viscous-like materials and due to the poor material quantities that can be contained in such a syringe, a more performing extrusion method has been implemented using a cochlea system. By applying the Archimede's screw principle, it is possible to continuosly feed the extruder assuring a uniform and constant pressure [32].
In July 2014, Natale in collaboration with Massimo Moretti (*Wasp Projects*), developed at +LAB, two different extrusion systems with a screw system: the first one foresees a hopper system with a gravity refill while the second one has a refill system that uses a pressured tank.

1.2.3.1 Advantages of LDM

Compared to the FDM technology, the LDM presents many advantages:

- Several different materials can be processed: resins, ceramics, clays and silicones.

- LDM offers the possibility to add some particle of fibers to the liquid inks in order to print composites solutions.

- The extrusion modular nature allows also to obtain high-definition prints using nozzle diameters of the order of microns.

- LDM, working at room temperature, allows to avoid all the problems related to the high temperature required in FDM systems.

- Depending on the material, it is possible to avoid or reduce the formal withdrawal typical of thermoplastic.

- Using LDM it is possible to perform self-standing prints only by suitably modulating the mechanical system and the light stimulus in case of photocurable material.

1.2.3.2 Disadvantages of LDM

The LDM technique presents some drawbacks:

- The LDM extrusion system should be optimized according to the viscosity and the type of material you want to process.

- Especially in the case of a syringe extruder, the presence of possible bubbles in the ink can cause the printing failure due to the lack of material in some of the printing points.

- The inks should be chemically optimized to be adapted to this technology. Generally, they should be added with some fillers to increase their viscosity.

In the next chapter, the most common materials that can be processed through LDM systems are presented.

1.3 Extrudable Materials

1.3.1 Materials for FDM

Currently on the market there are several types of FDM 3D printers, which differ in shape and size, and are able to build objects with a resolution from 50 microns to the order of centimeters. The raw material for FDM is always a thermoplastic polymer in the form of filament with diameter varying from 1.75 to 3mm.

Based on the Mendeleev's *Periodic Table of Elements*, which organise into a logical order the known chemical elements according to their atomic weight and properties, Tangram Technology has published the '*Tangram Technology Periodic Table of Thermoplastics'*. In fact, it argues that much like Mendeleev's period table, polymers also have a strong relationship between their structure and properties. Following this idea, Stratasys has tried to create a periodic table which identifies how many different thermoplastic polymeric materials today's 3D printing technologies are currently able to process.

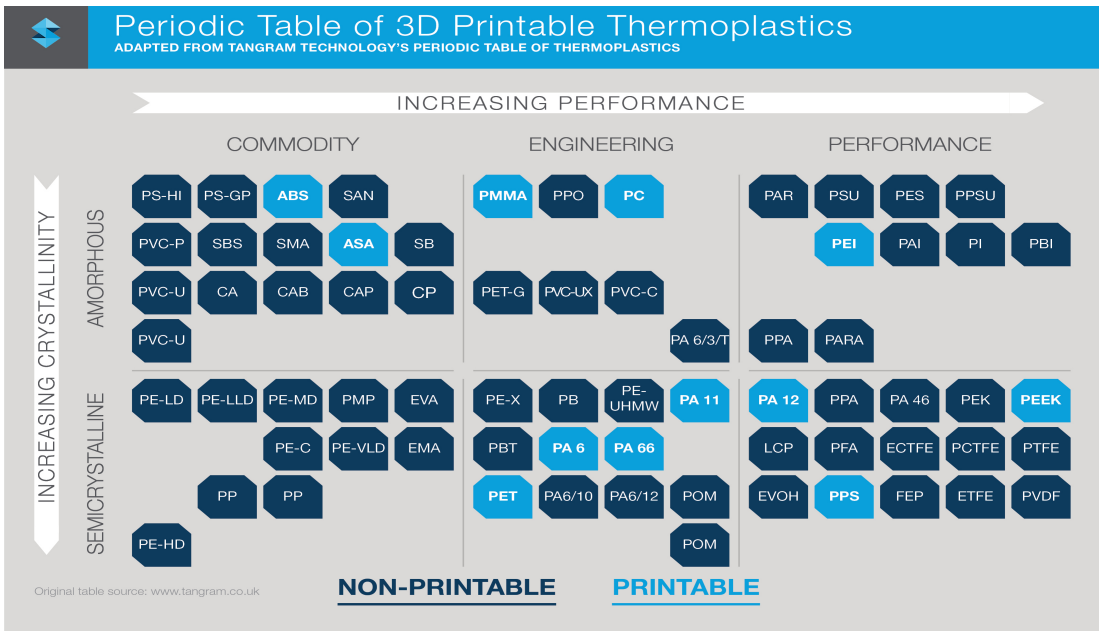

Figure 1.3.1 Stratasys's Periodic Table of 3D Printable Thermoplastic polymers.

The Stratasys's Periodic Table (*Figure 1.3.1)* reports only some of the most used material because, as Tangram Technology comments, "the true diversity of all the polymer types makes it impossible to include all their variations in one simple table" [34], [35].
Being one of the currently most used materials in 3D printing FDM technology, PLA should definitely be added in the Tangram table.

Below, the polymers commonly employed in FDM are described:

- ***PLA*** (polylactic acid): it is a polymer derived from cornstarch and thus biodegradable. Currently it is the print material for excellence as it is simple to process due to its low melting point (from 160° C to 220° C). It does not enact bad smells or toxic fumes during melting. Once cooled presents very small formal retreats; however, is a very fragile material, so it is not very suited to the construction of structural parts. Due to its biopolymeric nature, its mechanical properties could undergo changes over time due to several factors such as light and moisture [36].

- ***ABS*** (acrylonitrile-butadiene-styrene): it is a thermoplastic derived from petroleum processing. It is well known as the building material of the famous brick "LEGO®". During the extrusion, it produces a slight smell of burning plastic and produces toxic fumes hence it is recommended to have good ventilation during printing. Its melting temperature may vary between 220° C and 260° C. It's clear that printed parts are more heat resistant than those built in PLA. The molded ABS tends to not adhere to the printing plate thus particular expedients should be adopted, such as the heated surface or by using the so-called blue-tape.
ABS is very affected by the drastic temperature change and the withdrawals are often common problems in some geometries [37], [38].

PLA and ABS are available in different colors and may have different optical, mechanical and thermal properties depending on the manufacturer. Moreover, these materials may be mixed with particles to obtain filaments similar to wood, ceramics, aluminum, silver, or can be reinforced with glass, carbon fiber or Kevlar in order to increase their mechanical properties [39], [40] .

- ***PVA*** (Polyvinyl alcohol): it is generally used in 3D printers equipped with a double-extruder which allow the selection of two different materials: one for the fabrication of the final object and one for the support. In fact, PVA, being a water-soluble polymer, is often used in support printing of complex 3D parts. However, its strong hygroscopicity makes it particularly hard to use in high moisture content environments. Its melting temperature is about 190° C [37].

- ***PA***: polyamide, commonly known as Nylon, is used in printing of parts that require high mechanical properties such as strength at break and a low friction. Generally, it is used in the construction of components such as hinges and joints. The working temperature of PA is around 240° C, characteristic that makes it suitable to be used for build parts subjected at high temperatures. The processability of PA is very hard as it presents significant shrinkage effects and tends to absorb moisture if not stored properly.

- ***TPU*** (Thermoplastic Polyurethane): it is a thermoplastic elastomer used to produce elastics of various kinds, gaskets, soft parts of toys, garments and clothing accessories, medical parts and sheets to create large flexible packaging.
Because of its particular flexibility, in some cases it is very hard to extrude it.

As the demand for high-performance materials is increasing, the filament manufacturers are constantly looking for new formulation, trying to fit all existing thermoplastic polymers for use in printing.

1.3.2 Materials for LDM

The 3D printing of fluid materials is nowadays a big topic of research in additive manufacturing world. Thermoplastics are easier to 3D print because they set at room temperature after heating. This allows to avoid so many problems related to the material collapsing in case of overhanging structrures. Instead, when you're layering through LDM process the wet materials, there are some limitations due to geometries, collapses, drying, shrinkage, so the material extruded assumes a key role for obtaining acceptable final results [41].

In order to 3D print liquid materials, it is necessary to develop specific formulations that once extruded are characterized by a consistency and mechanical properties such that the material does not "liquefy" on the printing plate and, at the same time, the already printed piece does not collapse under the weight of subsequent layers [32].

The LDM offers the possibility to directly print different materials including polymeric resins, dispersions such as some ceramic materials, composites materials etc.

1.3.2.1 Ceramics

Among all the printable ceramic materials, the clays are the most used. The consistency of the clays can be optimized to make them 3D printable just working on weight ratios between the material itself, the water and, if any, some rheology modifiers [41], [42].

One of the most important pioneers of clay print is Massimo Moretti, who in 2012 created WASP (World's Advanced Saving Project). This is a project focused on developing 3D printing and that finds its roots in the world of Open-source.

The aim of WASP is to build 'zero-mile' homes, using materials found on the surrounding area, such as clay materials. To this end, it has built a 12-meters tall Big Delta, shown in the next figure (*Figure 1.3.2*).

The difficulties above mentioned, related to the deposition of a wet material (such as clay) are in these projects so crucial that, as a consequence, the need to find solutions increases. Focusing on this stimulating research direction, in the last months Wasp and the artist Francesco Pacelli began to work together. This collaboration aims to deepen the knowledge of LDM process, widening the number of potential extrudable ceramics materials and setting the correct mixtures and printing parameters to obtain functional 3D printed ceramic pieces. During last months, Wasp designed a smart LDM extruder based on a compressed air tank that feeds an endless screw in order to deposit clay selectively through a stepper motor. The mechanics of deltawasp machines is perfect for clay deposition because

it does not have a moving bed, so the print remains still while the extruder is moving layer by layer, avoiding dangerous shakes that could compromise the stability of the final printed part.



Figure 1.3.2 12-meters tall Big Delta, Shamballa Technological Village [43].

From the WASP-Pacelli collaboration, special shapes were also born, which highlight the potential of the LDM technique also in the art of fashion design. An example is reported below (*Figure 1.3.3*).



Figure 1.3.3 Pyromania by Francesco Pacelli 3D printed with clay [41].

1.3.2.2 Polymeric resin

The other class of materials that can be 3D printed via LDM are the polymeric resin, such as epoxides, acrylic, silicones [44].
As regards these materials, at the end of the extrusion it is necessary to generate specific physical or chemical stimuli able to provoke a change in the state from liquid to solid.
The activator stimuli can be of different nature: some materials react when irradiated with a heat source (*thermosetting resins)*, others tend to react if exposed to a light radiation (*photopolymer resins*). In all these cases the reactions bring the material to a solid state, with the formation of permanent bonds, usually irreversible. The solidification stage is very important for these materials as it prevents the material to flow, fixing the desired shape [32].
As LDM is in continuous evolution, different inks based on polymeric resins are being developed but generally they are quite all formulated as a matrix material for reinforced composites [45]–[50]. In this field, the most used are polyester, phenolic, epoxy and polyimide resins. These are characterized by a low viscosity at room temperature, which facilitates the impregnation of the fibers. Once polymerized, they also offer a good resistance to chemical agents. In contrast, the technological limitation about the use of these materials lies in the requirement of a chemical reaction during printing process in order to harden the initial liquid inks. In fact, it is well known that the hardening reaction control is very hard.
Recently, several studies have been conducted on the possibility of formulating printable inks that can be subjected to a double activator stimulus: the material is activated both via luminous stimulus and thermally, in a sequential way. In this case we can talk about dual-curing inks [51], [52].

The experimental work presented in this thesis is focused on the development of polymeric inks based on photopolymer resins; further information on these materials are given in the next chapter.

1.3.2.3 Functional materials: composites

The ability to integrate both form and function within printed objects is the next frontier in 3D printing. In recent years, several research groups are working on the formulation of functional materials that can be 3D printed. Among them the Harvard lab, led by researcher Jennifer Lewis, is the most productive. The principal activities of the *Lewis Group* involve 3D printing of soft functional materials for use in printed electronics, optical materials, lightweight structures, and microvascular architectures for cell culture and tissue engineering [48], [53]–[59].
This research group has developed a range of materials in "viscous paste" appearance, which can be processed at room temperature using pneumatic or volumetric systems, very similar to that designed

by Dr. Natale. In Lewis's articles it talks about '*Direct Ink Writing'*. This term describes fabrication methods that employ a computer-controlled translation stage, which moves a pattern-generating device, that is, an ink-deposition nozzle, to create materials with controlled architecture and composition. It is very similar to the method at the base of LDM.
Among the many types of functional inks developed at Harvard, many are reinforced with metal particles or short fibers of various types, for example carbon, synthetic wood, etc.
In fact, in recent years, the research is focusing on the development of composite materials for the production of high performing 3D printed objects.

Composites constitute a class of reinforced materials, in which at least one component (often in the form of fibers) has mechanical characteristics highly superior to the other.
In general, a composite can be defined as the union, by adhesion or cohesion, of two or more components, different in shape and chemical composition, insoluble in one another and separated by an interface [60], [61].
A composite is generally provided with a continuous phase (called *matrix),* and a discontinuous one (the *reinforcement*). For the first, polymeric materials (thermoplastic or thermosetting including photopolymer resins) are commonly employed (see § *1.3.2.2*) while the reinforcements can be micro-, nano-particles or fibers, both short and long.
The nature of the phases is a dominant feature in imparting the "composite" character to a formulation of different materials. But it is not the only variable. To obtain a composite with high mechanical resistance is essential to ensure good adhesion between the matrix and the reinforcement. Only in this way an efficient transfer of external loads can occur. The adhesion is usually promoted by the use of a third component, applied in a very thin layer on the surface of the fibers, that makes it compatible inorganic surface of the fibers (or particles) with the organic one [62].

Nowadays, the most common composites polymeric inks are reinforced with glass, carbon and aramid fibers. Thanks to its low cost and high strength, glass fiber is the most used fiber reinforcement; it is commercially available in different forms, such as short fibers, long filament and woven roving [52], [63]–[68].
Carbon fibers are used for the manufacture of high performance composite and they are characterized by a high modulus and high strength. The main disadvantages in the use of carbon are the high cost and the tendency to provoke brittle fractures [45], [50], [52], [69]–[73].
Aramid fibers, introduced in 1971 by Dupont with the name *Kevlar*, are characterized by a high toughness. Module, strength and cost are intermediate between those of glass and carbon fibers. The

main disadvantage in the use of these fibers is linked to the modest resistance to compression and degradation due to prolonged exposure to ultraviolet radiation.

Another type of fiber reinforcement is given by bio-based materials like bamboo, hemp, cotton and flax. [64], [74]–[76]

1.4 Photopolymer Systems

1.4.1 Photopolymer compounds

Since many years, photoinitiated polymerization is an important chemical process well established in many industrial fields. The use of photoinitiated polymers is continuosly growing not only in conventional areas such as coatings, inks but also in optoelectronics, stereolitography, microelectronics, in the field of bioengineering and, in general, for the fabrication of 3D objects. Photoinitiated polymerization is a process that is initiated by light and both the initiating species and the growing chain ends are radicals or cations.

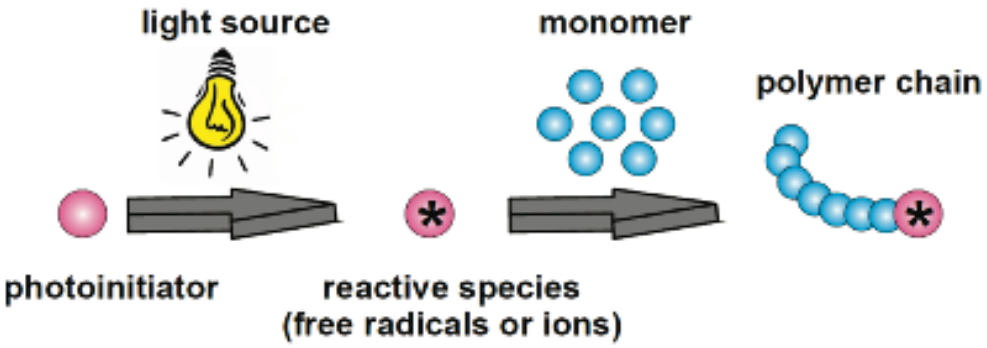

Figure 1.4.1 General presentation of photoinitiated polymerization [77].

As shown in the figure above (*Figure 1.4.1*), the role that light plays in the polymerization (although it gives the name to the whole process), is restricted only to the very first step of the process: the absorption which allows to the formation of the reactive species with the generation of an amount of energy needed to initiate the crosslinking process. Then, the major role is played by the photocurable system: monomers and photoinitiators. In this perspective, the proper selection of the photocurable system is the key for the development of an efficient formulation.

Depending on the polymerization mechanism, it can be possible to classify the photocurable blends in two major categories: the free radical photopolymerizable resins (in which the route is initiated by a

free radical) and the cationic photopolymerizable ones (in which the route is initiated by a cationic species).

1.4.1.1 Photocurable monomers

First of all, while free radical polymerization is limited to monomers with olefinic double bonds, compounds of quite different chemical nature (e.g., compounds containing epoxide or vinyl ether groups) can be polymerized *via* photoinitiated cationic polymerization.

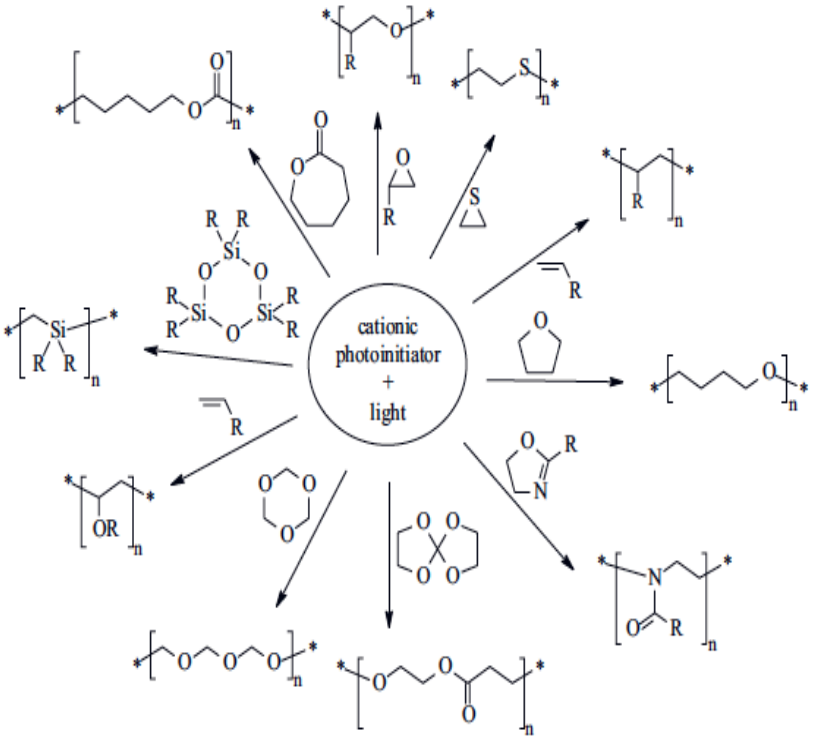

Figure 1.4.2 Monomers used in photoinitiated cationic polymerization [78].

The most important class of monomers which can be subjected to cationic photopolymerization are epoxides, vinyl ethers, propenyl ethers, siloxanes, oxetanes, cyclic acetals and formals, cyclic sulfides, lactones and lactams [78].

As shown in the figure above (*Figure 1.4.2*), cationic systems can include both unsaturated monomers (that undergo chain polymerization through the carbon-carbon double bonds) and cyclic monomers (that undergo ring-opening polymerization).

1.4.1.2 Photoinitiators

This is the molecule that when exposed to a specific radiation, (the exposure wavelength needs to match the absorption region of the selected photoinitiator) decomposes in reactive fragments that allow the polymerization reaction initiation. It affects the cure speed, the yellowing and the mechanical behavior of the photocurable system.

In case of free radical system, there are two types of photoinitators: a two-component system where the radical is generated through abstraction of a hydrogen atom from a donor compound (also called co-initiator), and a single-component system where two radicals are generated by cleavage. Benzophenone, Xanthones, and Quinones are examples of abstraction type photoinitiators, coupled with donor compounds like aliphatic amines; Benzoin ethers, Acetophenones, Benzoyl Oximes, and Acylphosphines are common cleavage-type photoinitiators [77].

In the last decades there was a rapid growth in the research of new photoinitiators for cationic routes; some examples are reported in the following figure.

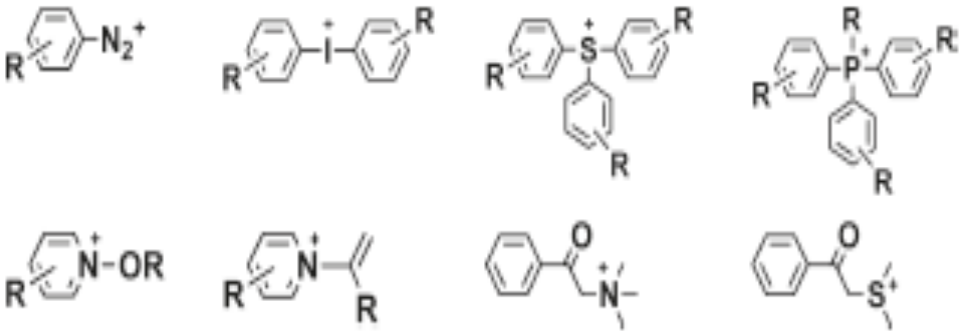

Figure 1.4.3 Onium Salt Photoinitiators for Cationic Polymerization [77].

The most efficient photoinitiators belong to the -onium salts family; these are the most used due to their thermal stability, good solubility in most of the available monomers, and high efficiency in generating the reactive species.

Iodonium and sulfonium are the most common onium salts used. These contain two and three arene groups for iodonium and sulfonium respectively.

The effective light-absorption component of these salts is the cationic portion: the structure of the cation has an important role in controlling photosensitivity, the quantum yield and the thermal stability of the salt. However, also the anionic part plays an important role. A crucial characteristic related to

the performance of the photoinitiator is that the counter anion is non-nucleophilic and it is responsible for the character of the propagating ion pair, having a direct impact on the kinetics of polymerization and whether termination can occur. As will be explained later, since the Bronsted acid generated during the initiation stage is considered the real active initiator for the polymerization process, there is a termination way where the couter ion of the acid could act as the nucleophile instead of a functional groups on the oligomer.
The most common counter anions, in order of decreasing reactivity, are: SbF6–, AsF6–, PF6–, BF4–. The larger the negativity of the charged anion, the more the weakness of its bonds, and the more active the propagating cationic species during the polymerization.

The onium type photoinitiators used in industry exhibit similar absorption characteristics; they generally absorb light at short wavelength, in the UV region. For example, diaryliodonium and triarylsulfonium salts (cationic photoinitiators) are the most effective for initiating wavelength between 210 and 350 nm. This can represent a technological problem, because there are no low-cost and simultaneously enough powerful UV light sources in that range [79]. In fact, in the photocurable materials industry, medium pressure mercury lamps are used, which emit most of energy at about 365 nm and only a little fraction in the absorption range of commercial onium photoinitiators. This means that there is a mismatch between the absorption characteristics of the commercial photoinitiators and the emission characteristics of the light sources, which lowers the photoinitiator activity.
To overcome the problem of poor absorption at wavelengths above 350 nm, the photocurable system can be optimized adding some photo-sensitizers, which can help to expand the spectral region over which omium salts are effective [80], [81].

1.4.2 Polymerization mechanism

As already said, photopolymerization can occur according to two different mechanisms which are the radical and the cationic.

1.4.2.1 Free radical polymerization

Photocurable materials that are subjected to the free-radical mechanism follow the chain-growth polymerization type, which includes three basic steps: initiation, chain propagation, and chain termination. The three steps are depicted in the scheme below (*Figure 1.4.4*), where R• represents the radical that is formed upon interaction with radiation during initiation, and M is a monomer. The formed active monomer is then propagated to create growing polymeric chain radicals. The propagation step involves reactions of the chain radicals with reactive double bonds of the prepolymers or oligomers. The termination reaction usually proceeds through combination, in which two chain radicals are joined together, or through disproportionation, which occurs when an atom (typically hydrogen) is transferred from one radical chain to another resulting in two polymeric chains.

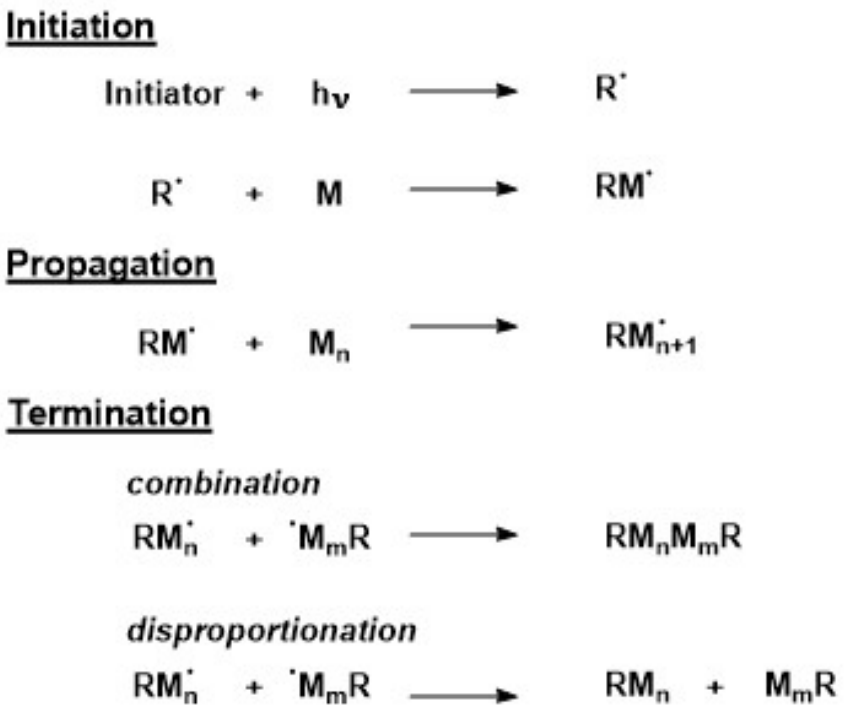

Figure 1.4.4 Free radical polymerization mechanism [82].

1.4.2.2 Cationic polymerization

The mechanism for cationic photopolymerization starts with the photodecomposition of the onium salt. This is quite complex, so here a simplified scheme is represented for a diaryliodonium salt.

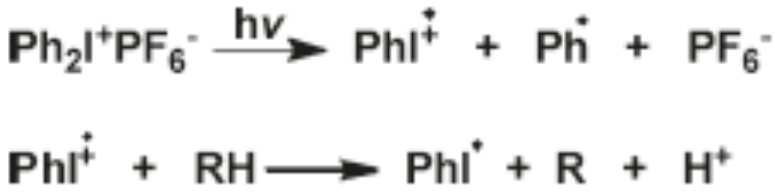

Figure 1.4.5 Scheme of photoinitiated cationic mechanism [77].

The first step consists in the photoexcitation of the salt and then the decay of the resulting excited singlet state with both homolytic and heterolytic cleavages; cation radical, aryl radical and unaltered counter anion are formed simultaneously. The radical species are very reactive and, when react with monomer molecules give protonic acid, H+, which is considered the effective initiator for the polymerization [78].

1.4.2.3 Cationic vs Free radical

Although free radical photopolymerization still dominates most industrial applications, in this thesis work the attention will be focused on cationic mechanism because of the several advantages offered by the cationic mode compared to the free radical one [77], [78], [83].

- The monomers that are prone to cationic polymerization exhibit low volatility and negligible toxicity and have good rheological properties.

- The cationic photopolymerization is inhibited only by moisture but not by molecular oxygen. This provides a significant practical advantage for industrial processes since this property eliminates the need for an inert curing atmosphere in order to achieve rapid cure rates.

- In contrast to the free-radical photopolymerization, which exhibits rapid termination (radical-radical termination reactions) when the light source is turn off, the cationic polymerization mechanisms are characterized by a low termination rate that permits the polymerization to proceed in the dark even

after irradiation, until nearly all of the monomer has been consumed. This dark-curing behavior permits the polymerization to progressively penetrate into areas that are inaccessible to the radiation source.

Section 2. EXPERIMENTAL WORK: FORMULATION, PROCESSING AND CHARACTERIZATION OF PRINTABLE SOLUTIONS

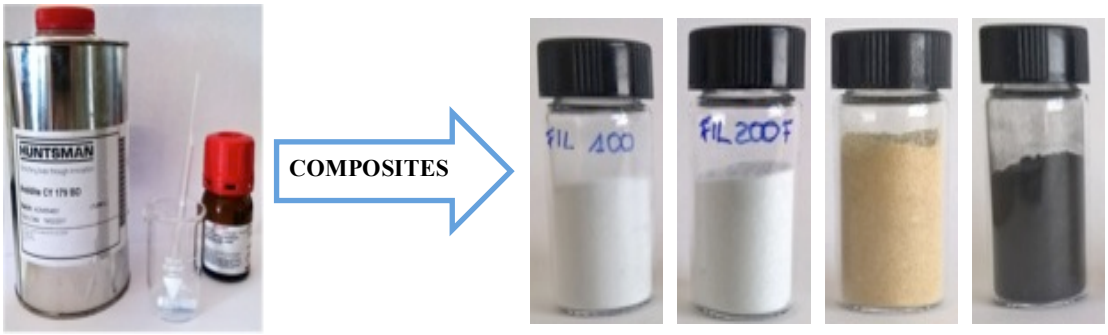

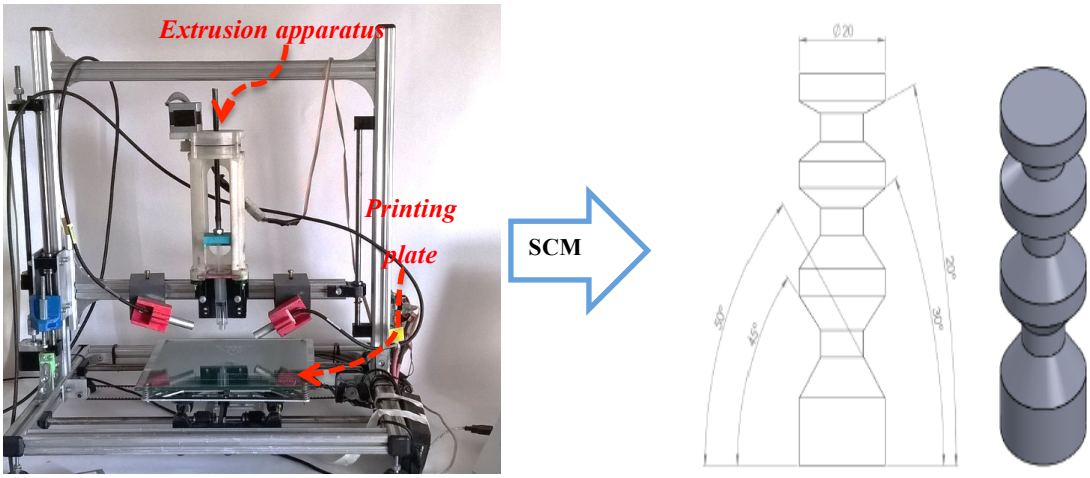

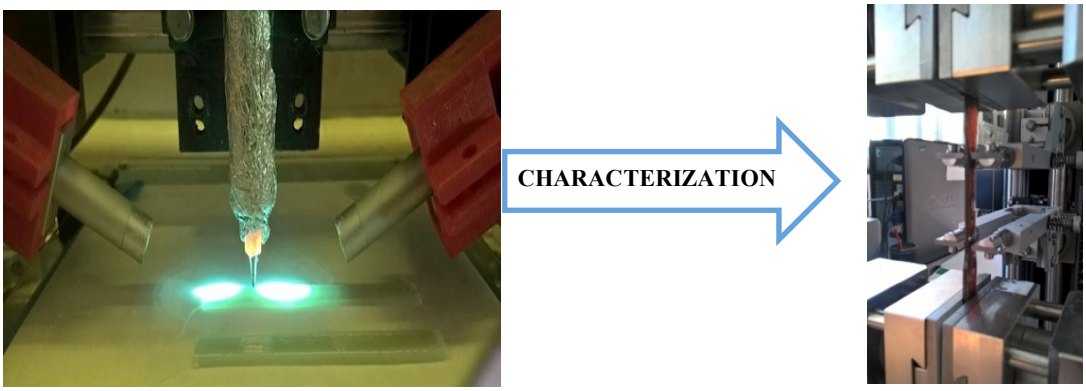

2.1 Polymer Composites Formulation

2.1.1 Chemicals

2.1.1.1 Materials for matrix composition

Photoinitiated polymers play a key role in the development of this experimental work. Photopolymers belong to the family of materials that change their properties when exposed to ultraviolet radiation. At the beginning of the work, two different resins were considered: one with an epoxy as functional group and one with an ether. The bis-cycloaliphatic diepoxy monomer (*ARALDITE CY 179 BD*), was kindly provided by Huntsman and the tri(ethylene glycol)divinyl ether, 98% pure (*TEGDVE*) was purchased from Sigma Aldrich, Italy.

Sulfonium and iodonium salts were used as photoinitiators. The first is a mixture of triarylsulfonium hexafluorophosphate salts (*PI-S*) in a 50% w/w solution of propylene carbonate and the second is the bis(4-methylphenyl)iodonium hexafluorophosphate (*PI-I*). As thermal curing agents the phthalic (*PA*) and maleic anhydride (*MA*), ≥ 99% pure, were employed. Both the initiators and the hardeners were purchased from Sigma-Aldrich. Some plasticizers were also used: glycerol (*GLY*), benzyl alcohol (*BA*), 99.75% pure, and epoxidized soybean oil (*ESBO*). The first were bought from Sigma while the oil was taken from Dollmar S.p.A.

Fumed silica (*OX200*, surface area of 200 m^2/g and average particle size 0.2-0.3 μm), used as rheological filler, was purchased by Sigma Aldrich, Italy.

In the following tables (*Table 2.1.1* and *Table 2.1.2*), the chemical structures and the main properties of the reactants are reported.

Monomers	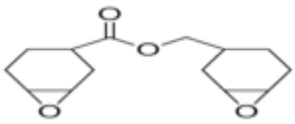	3,4-epoxycyclohexylmethyl-3',4'-epoxycyclohexane carboxylate (ARALDITE CY 179 BD)
	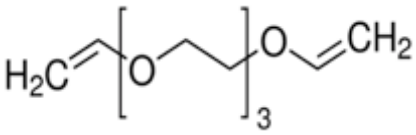	Tri(ethylene glycol)divinyl ether (TEGDVE)
Photoinitiators	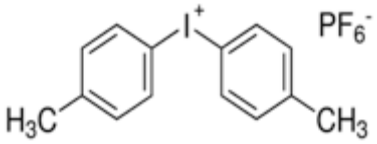	Bis(4-methylphenyl)iodonium hexafluorophosphate (PI-I)
	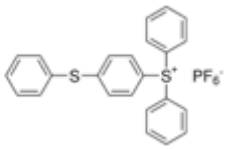 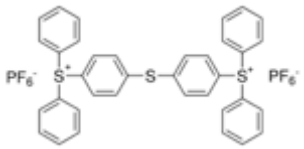	Triarylsulfonium hexafluorophosphate salts (PI-S)
Hardeners	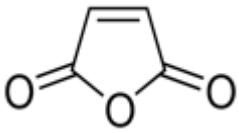	Maleic anhydride (MA)
	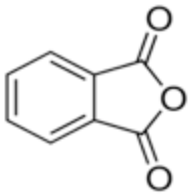	Phthalic anhydride (PA)
Plasticizers	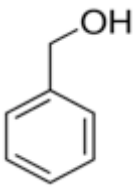	Benzyl alcohol (BA)

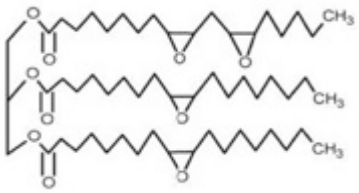	Epoxidized soyabean oil (ESBO)
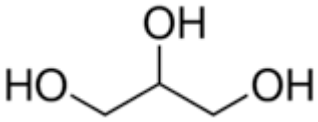	Glycerol (GLY)

Table 2.1.1 Chemical structures of reactans.

Chemicals	**Mw [g/mol]**	**ρ at 25°C [g/cm^3]**	**η at 25°C [mPa s]**	**Tm [°C]**	**Tb [°C]**	**Appearence**
ARALDITE CY 179 BD	140 g/Eq	1.17	378	-35	170	Transparent-off white liquid
TEGDVE	202.25	n.a	n.a.	n.a.	120/126	Colorless liquid
PI-I	454.13	n.a.	n.a.	n.a.	n.a.	White solid powder
PI-S	n.a.	1.32	n.a	n.a	n.a	Colorless liquid
MA	98.06	1.48	n.a	52/54	200	White solid flakes
PA	148.12	1.53	n.a	131	284	White solid flakes

BA	108.14	1.05	n.a	-16	203	Colorless liquid
ESBO	n.a	0.997	18000-3200	n.a	>250	Yellow to amber liquid
GLY	92.09	1.25	n.a.	20	182	Colorless liquid
OX 200	60.09	2.65	n.a	n.a	n.a	Mesoporous white powder

Table 2.1.2 Chemical and physical properties of the reactants. Data was collected from the SDS of the each material.

2.1.1.2 Organic and inorganic fibers

The dispersed phase of composite materials studied in this experimental work, consisted of both inorganic and organic fillers. For the first class of additives, the glass and carbon short fibers were considered, while the bamboo was used as organic reinforcement.

Two types of short glass fibers, both provided by Italdry srl, were tested: the FILL 100 and the FILL 200F. The FILs were both made from glass wires manufactured by continuous process (ISO 2078:1993); the FILL 200F was also added with a silane lubricant to improve the smoothness. Due to a possible moisture content (0.08 %), these fibers were dried in a vacuum oven at 100° C for 24 h before use.

Carbon fibers, 95% pure (PX35), obtained by a synthesis process using the polyacrylonitrile fibers as precursor, were kindly provided by Zoltek Carbon Fibers. They were used as received.

Bamboo organic fibers were provided by Sunstrand LLC. Also these fibers were dried in a vacum oven for 24 h at 100 °C before use.

In the table below (*Table 2.1.3*), the technical data about all the fibers employed in this work are reported.

Fibers	**ρ at 25°C [g/cm^3]**	**Fiber diameter [µm]**	**Fiber length [µm]**	**Appearence**
FILL 100	1.35	13	100	
FILL 200F	0.72	13	200	
PX35	1.81	7.2	150	
BAMBOO	0.6 - 1.4[7]	n.a.	n.a.	

Table 2.1.3 Fibers technical data, collected from the SDS of each material [84]–[87].

[7] To calculate the exact weight of bamboo added to the matrix in order to obtain a 8% v/v, the average density value was considered ρ_{avg} = 1 g/cm^3.

2.1.1.3 Solvents

During the experimental work some solvents were used: acetone (AC), acetonitrile (ACN) and methanol (Me-OH). All were purchased from Sigma-Aldrich and used as received without any further purification or dilution. In *Table 2.1.4*, the characteristics of all the solvents are reported.

Solvents	**Assay [%]**	**Mw [g/mol]**	**ρ at 25°C [g/mL]**	**Tm [°C]**	**Tb [°C]**	**Chemical structure**
AC	99.5	28.08	0.791	-114	56	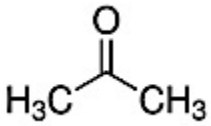
ACN	99.8	41.05	0.786	- 48	81	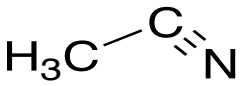
Me-OH	99.8	32.04	0.791	-98	64.7	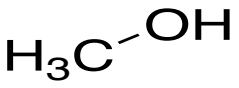

Table 2.1.4 Technical data of solvents used during the experimental work.

2.1.2 Polymeric matrix formulation

The polymeric matrix of the new composite materials consists of a dual-cure formulation. This was achieved by the development and optimization of photocurable mixtures to which the hardeners have been added to thermally complete the curing process.
The preparation procedures of each mixture are reported in the next paragraphs.

2.1.2.1 Preparation of the photocurable mixtures

Different photocurable formulations were developed. Four formulation lines can be distinguished on the base of the monomer and the photoinitiator used. The mixtures based on the epoxy monomer with the addition of sulfonium initiator will be indicated as *p-ES* in the following, and those with iodonium salt will be called *p-EI*. The formulations based on the divinyl ether monomer with the addition of sulfonium and iodonium will be indicated as *p-DVES and as p-DVEI,* respectively.
The formulations were obtained by mixing the photoinitiator and the resin in such proportions as to obtain different concentrations by weight of the photoinitiator: 3% wt, 2% wt, 1% wt, 0.5% wt. Each sample will be identified by the acronym indicating the type of monomer and photoinitiator used, followed by a number indicating the initiator concentration as weight %; for example, *p-ES3* states for *Photocurable* mixture of *Epoxy* resin with *3% wt* of *Sulfonium* initiator.

Each mixture was prepared using the following procedure:

- Put a magnetic stir bar in a glass beaker and tare.
- Pour the resin in the glass beaker and weigh.
- Calculate the quantity of initiator required to obtain the desired concentration by weight, (if necessary round up).
- Add the photoinitiator dropwise with a Pasteur pipette.
- Cover the beaker with aluminium foils in order to prevent accidental UV-activation.
- Stirr for 30 min at room temperature (23°C) to obtain homogeneous solution.
- Pour the solution in UV-shielded vials to be stored until use.



Figure 2.1.1 From the left: materials and instrumentation employed to prepare photocurable solutions.

The above figure (*Figure 2.1.1*) shows the materials and instrumentation used to prepare the epoxy based formulation.

In the following table (*Table 2.1.5*), the different weighings made to obtain mixtures at different concentrations of initiator are reported.

PHOTOCURABLE FORMULATIONS	Resin [g]	Initiator 3%wt [g]	Initiator 2% wt [g]	Initiator 1% wt [g]	Initiator 0.5% wt [g]
p-ES / p-EI	5.000	0.155	0.102	0.051	-
p-DVES / p-DVEI	5.000	0.155	0.102	0.051	0.025

Table 2.1.5 Weights of reagents to obtain solutions at different percentages of photoinitiator.

2.1.2.2 Preparation of the dual-curable epoxy mixtures

The dual-cure formulations were obtained by adding an hardener to the stock solution made of 3% wt of PI-S in ARALDITE CY 179 BD, called *p-ES3* (see §2.1.2.1). Two different solutions were prepared: one containing the phthalic anhydride, indicated as *pt-ES3PA* in the following, and another one with the maleic anhydride, called *pt-ES3MA*.

The amount of hardener added to the solution was calculated in order to have a final mixture in which only 25% by weight of the resin thermally polymerizes. The calculations (*Eq. 2.1*) were executed on the base of ARALDITE CY179 BD equivalent weight, 140 g/Eq, value taken from the reagent's data sheet.

$$Hardener's\ mass\ [g] = \left\{ \frac{\left[\frac{total\ mass\ of\ epoxy\ resin[g]*0.25}{140\left[\frac{g}{Eq}\right]}\right]}{2\left[\frac{Eq}{mol}\right]} \right\} * Mw\left[\frac{g}{mol}\right] \qquad (2.1)$$

If we consider the 25% wt of epoxy resin in *p-ES3* (2.5g considering a total amount of 10g), we can obtain the number of the corresponding equivalents by dividing the mass by 140g/Eq. The obtained result is then divided by the number of monomer functionality (2 Eq/mol) in order to obtain the number of monomer moles. Knowing that the monomer's and the anhydride's functionalities are the same, the total amount of hardener to be added to the UV-curable formulation is obtained moltiplying the number of moles by the molecular weight *Mw* of the specific anhydride[8].

The mixture's preparation procedure consisted in several steps:

- Put a magnetic stir bar in a glass beaker and tare.
- Pour the resin in the glass beaker and weigh.
- Reduce the anhydride's white flakes to powder using a mortar, (*Figure 2.1.2*).
- Gradually add the powder to the resin under stirring at 50°C (in the case of MA addition) - 70°C (in the case of PA addition).
- Continue stirring for 1h at 50°C – 70°C in order to completelly dissolve the anhydride.
- Leaving the liquid solution to cool until room temperature and add the sulfonium initiator (3% wt with respect to the total amount of ARALDITE).
- Cover the beaker with aluminium foils in order to prevent accidental UV-activation.
- Stirr for 30 min at room temperature (23°C) to obtain homogeneous solutions.
- Store the solutions in UV-shielded vials until use.



Figure 2.1.2 Mortar used to reduce the anhydrides to powder.

[8] Maleic anhydride's molecur weight = 98.06 g/mol.
Phthalic anhydride's molecur weight = 148.12 g/mol.

In the next table (*Table 2.1.6*), the quantities of reagents used in the formulation of *pt-ES3PA* and of *pt-ES3MA* mixtures are resumed.

DUAL-CURE FORMULATION	Araldite CY 179 BD [g]	Anhydride [g]	PI-S [g]
pt-ES3PA	10.000	1.323	0.309
pt-ES3MA	10.000	0.876	0.309

Table 2.1.6 Reagents quantities in dual-cure formulations.

2.1.2.3 Addition of plasticizers

In order to decrease the well known brittle behavior of the epoxy based material, the use of a plasticizer was taken into account. Three different materials were selected: benzyl alcohol (BA), glycerol (GLY) and epoxidized soya bean oil (ESBO).

The plasticized formulations were obtained by adding drop by drop the specific amount of liquid plasticizer, 5% wt, to the dual-cure epoxy solution, previously prepared as described in paragraph §2.1.2.2. The mixtures were then magnetically stirred for 30 minutes at room temperature. Four different formulations were prepared: three based on *pt-ES3PA* and one on *pt-ES3MA* solution.

In the table below (*Table 2.1.7*), the weighings made to prepare the four compositions are listed.

PLASTICIZED FORMULATIONS		Dual-cure mixture [g]	Plasticizer (5% wt) [g]
pt-ES3PA	BA	11.632	0.612
	ESBO		0.612
	GLY		0.612
pt-ES3MA	ESBO	11.185	0.589

Table 2.1.7 Weights of materials to prepare four different plasticized solutions.

2.1.2.4 Addition of silica

Fumed silica OX200 was used as filler in the mixtures previously described (§2.1.2.1 - §2.1.2.2), to adjust their viscosity in order to make them printable.

For each stock solution (*pt-ES, pt-ES3PA, pt-ES3MA*), four dispersions at increasing silica concentrations were prepared.

The procedure followed for dispersing fumed silica into the solution consisted in two steps: first, the desired amount of OX200, ranging from 6.5% wt to 13% wt, was slowly added to the liquid solution and manually mixed for a first homogenization; then, the obtained mixture was mechanically mixed for 5 min at 240 rpm with a Heidolph RZR 2102 Control agitator equipped with a glass spatula (*Figure 2.1.3)*.

The name of the samples will be identified by the acronym indicating the type of compound, followed by a number indicating the silica concentration as weight %; for example, *p-ES3OX200-6.5* indicates a compound made of 6.5% wt of silica in *Photocurable Epoxy* solution with *3% wt* of *Sulfonium* initiator.

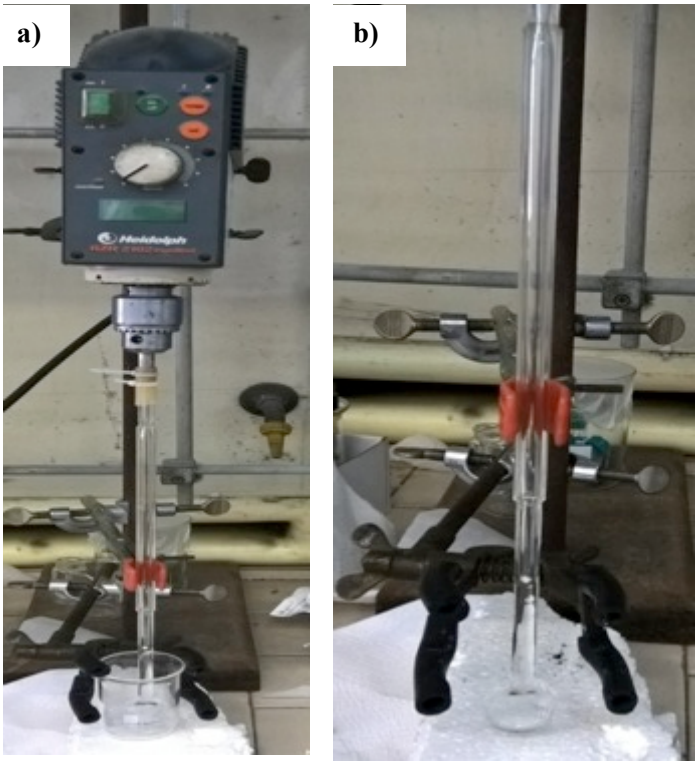

Figure 2.1.3 Instrument used to mechanically mix the silica into the liquid solution: a) Control agitator; b) Glass spatula.

In *Table 2.1.8*, the specific amount of silica OX200 added to each batch of 5g of solution in order to obtain the desired concentration by weight is reported.

Stock solution [g]	**OX200 6.5%wt [g]**	**OX200 9%wt [g]**	**OX200 11%wt [g]**	**OX200 13%wt [g]**
5.000	0.348	0.495	0.618	0.747

Table 2.1.8 Amount of fumed silica OX200 added in different concentration by weigth to 5g of unfilled system in order to modify its viscosity.

2.1.3 Fiber reinforced composites formulation

All the composites prepared during this experimental work may be collected into four groups according to the type of fibre dispersed in the polymeric matrix. As shown in paragraph *§ 2.1.1.2*, glass (FILL 100, FILL 200F) and carbon (PANEX35) fibers were used as inorganic fillers while the bamboo was tested as organic material.

The short fibers reinforced (SFR) composites, all based on pt-ES3MAOX200-11 dual-cure matrix, were obtained by adding different percentages of fibers. Every dispersion was prepared mixing manually the required amount of fibers in the matrix material, previously prepared as described in paragraph *§ 2.1.2.4*.

To try to get dispersions with the best possible homogeneity, the obtained mixtures were afterward processed using two metal spatulas, as shown in the *Figure 2.1.4.*

The name of each composite dispersion will be identified by the acronym of the type of the added fibers, followed by a number indicating its concentration as volume %; for example, *FILL100 - 10* indicates a composite containing 10% v/v of 100 μm long glass fibers.

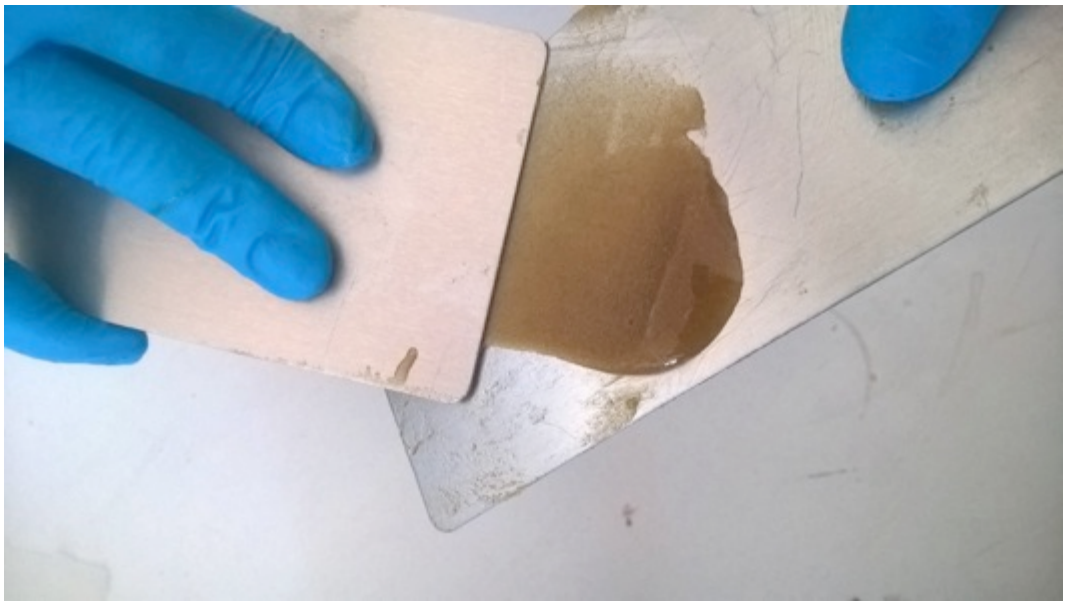

Figure 2.1.4 Homogenization of composite blend (Bamboo) by means of two metal spatulas.

In the next table (*Table2.1.9*), the amount of fibers added to the matrix material in order to obtain the desired percentage by volume, were reported. Each weighing was made considering 5g of *pt-ES3MAOX200-11* mixture, which correspond to a volume of 4 cm^3.

Type of fiber	Fiber percentage [% v/v]	Fiber volume [cm^3]	Fiber weight [g]	Composite total volum [cm^3]	Composite total weight [g]
FILL 100 ρ= 1.35 g/cm^3	10	0.44	0.60	4.44	5.60
	25	1.33	1.80	5.33	6.88
	40	2.67	3.60	6.67	8.60
	50	4.00	5.40	8	10.4
FILL 200F ρ= 0.72 g/cm^3	10	0.44	0.32	4.44	5.32
	25	1.33	0.96	5.33	5.96
	40	2.67	1.92	6.67	6.92
	50	4.00	2.88	8	7.88
PANEX35 ρ= 1.81 g/cm^3	10	0.44	0.79	4.44	5.79
BAMBOO ρ_{mean}= 1 g/cm^3	10	0.44	0.44	4.44	5.44

Table 2.1.9 Percentages (% v/v) and corresponding weighst of fibers dispersed in 5g of polymeric matrix.

2.2 UV-Assisted 3D Printing Process

2.2.1 UV-3D printer asssembly

A low-cost home-assembled 3Drag 1.2 benchop printer (Futura Elettronica, Italy) incorporating a syringe dispenser equipped with a UV-laser with emission peak at 365 nm (LC-L1V3 by Hamamatsu) was used for LDM based UV-3D printing of the novel materials presented in the previous chapter (*Figure 2.2.1*).

This machine is provided with a printing plate moving along the x and y axes and of an extrusion system moving along the z axis.

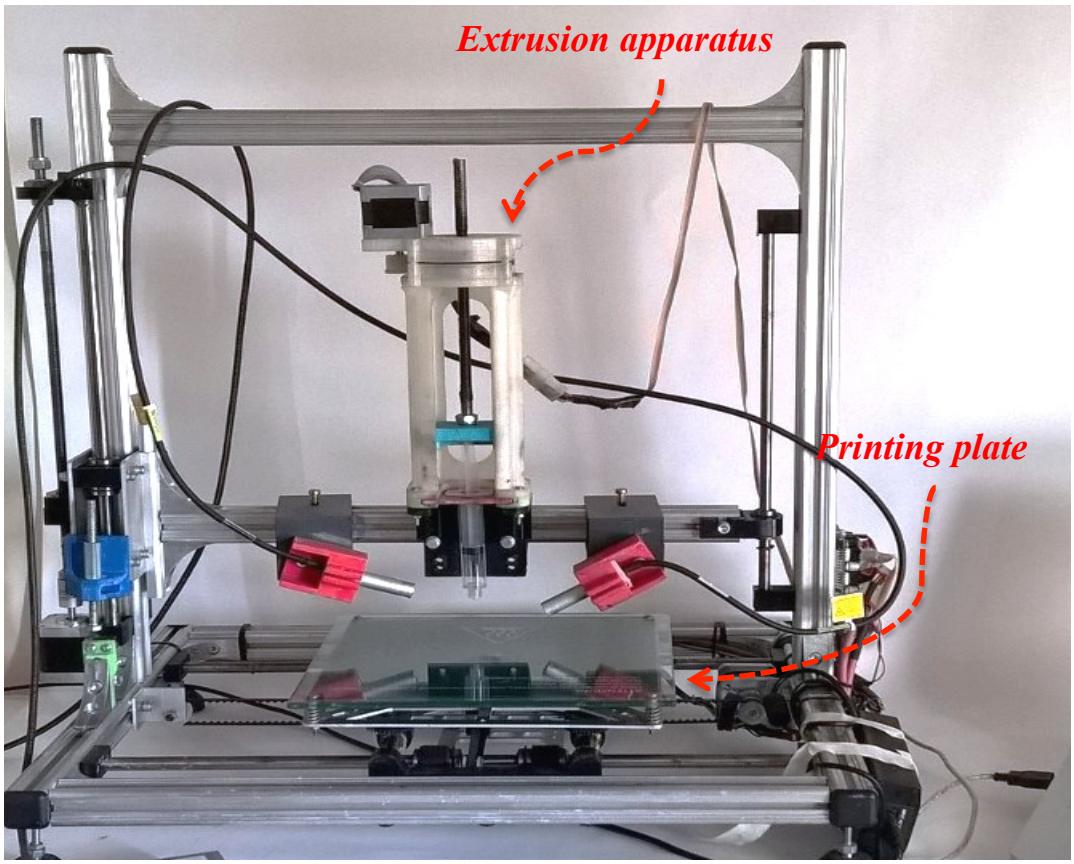

Figure 2.2.1 LDM UV-3D printer used to process the materials developed in this thesis.

2.2.1.1 Extrusion system

Originally this machine was born as a FDM version 3D printer with a standard thermally controllable extruder for solid filament melting and deposition (*Figure 2.2.2 (a)*). This standard printer was modified by Dr. Natale [29], replacing the printing head with a syringe extruder for fluid deposition (*Figure 2.2.2 (b)*), which was home fabricated using a conventional FDM 3D printer, the PowerWASP EVO by WASP (World's Advanced Saving Project srl, Italy).

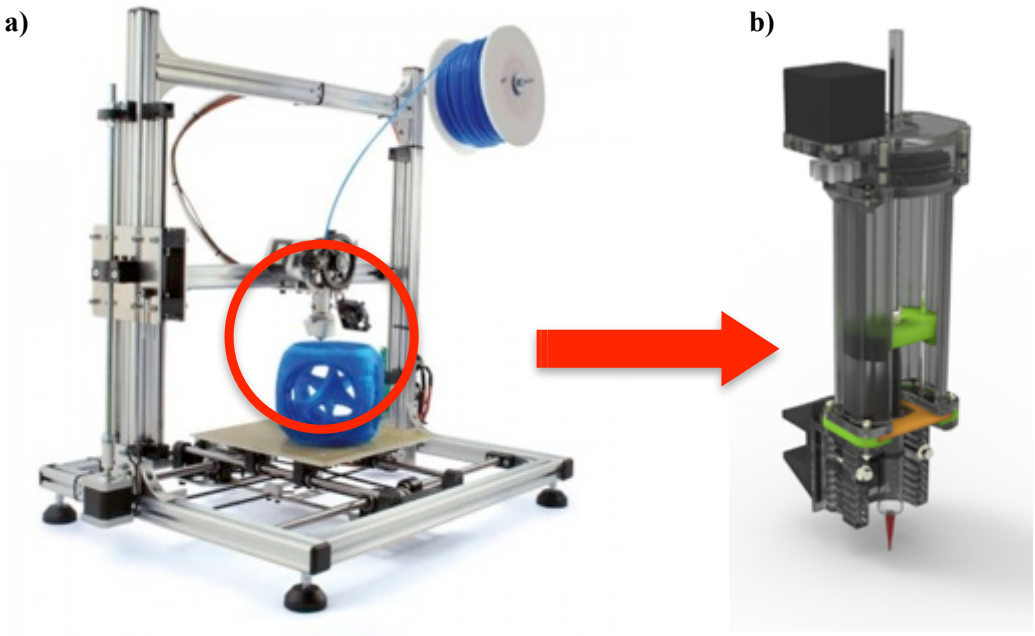

Figure 2.2.2 From FDM to LDM-printer: a) Conventional FDM 3Drag 1.2 benchop printer (Futura elettronica); b) Syringe extruder for liquid deposition designed by Natale, 2014 [29].

The entire extrusion apparatus is composed by several parts whose 3D models are shown in details in the next figure (*Figure 2.2.3*).

This is a modular model, designed to accomodate syringes of different capacity, ranging from 10 ml to 100 ml; in this experimental work, 10 ml INJLIGHT syringes were used (from RAYS S.p.A., Italy) coupled with 1.041 mm in-diameter phosphor bronze cone nozzle supplied by Techcon Systems. In particular, the conical geometry was chosen because it represents the most ideal passage for transfer of fluids, increasing the flow rate capability.

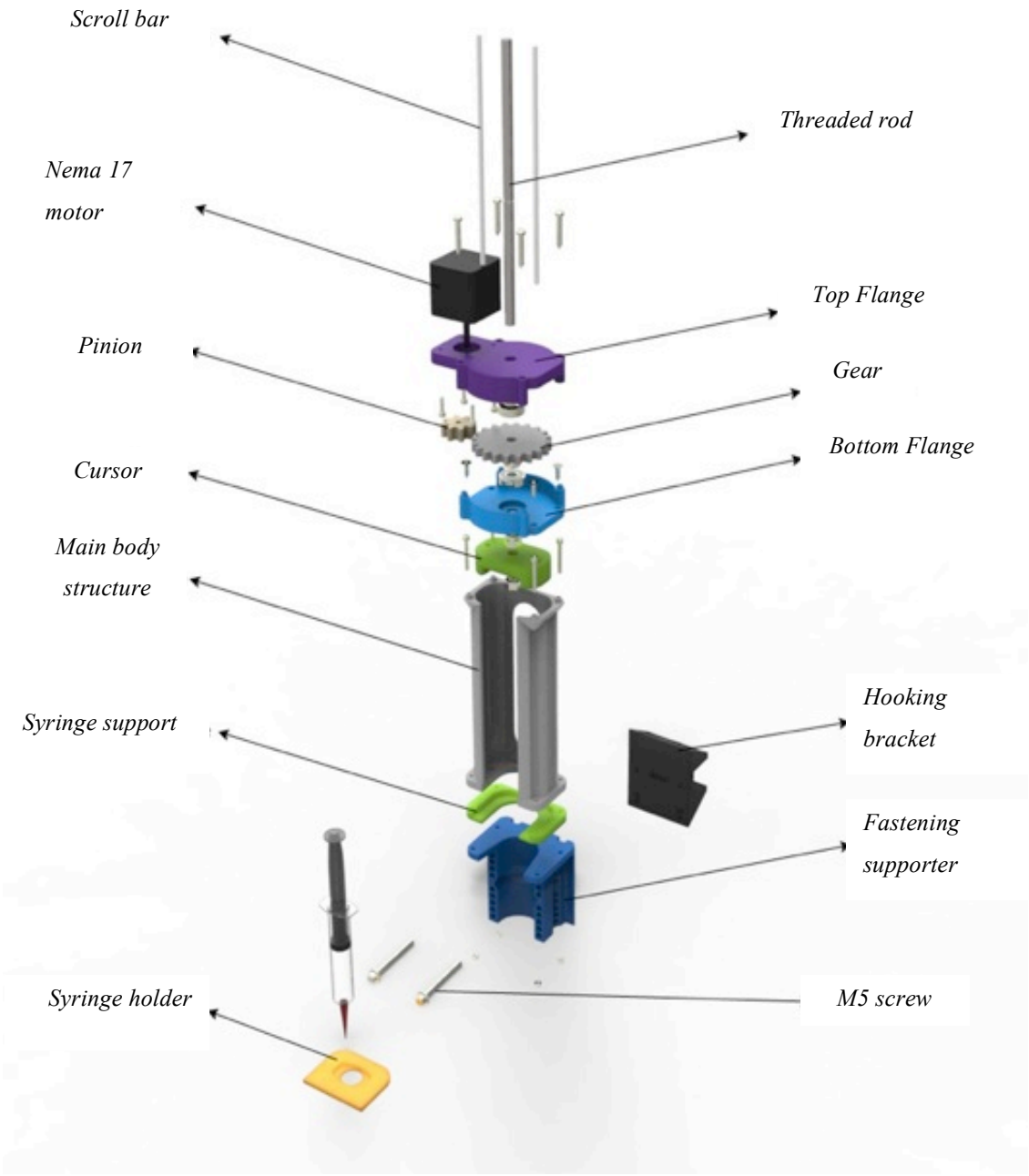

Figure 2.2.3 LDM extrusion apparatus components designed by Dr. Natale [29].

In order to obtain the desired flow at the nozzle outlet, the computer-activated NEMA 17 stepper motor controlls the gear system (pinion and gear) which allows the movement of the threaded bar to which the cursor is screwed, and then the regulation of the pressure on the syringe piston (*Figure 2.2.4*).

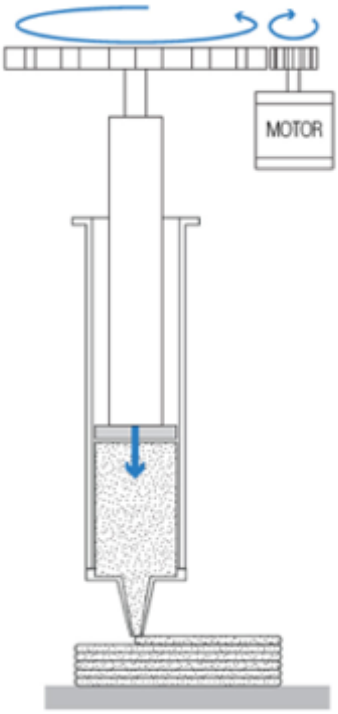

Figure 2.2.4 Exstrusion mechanism: gear system movement and pushing of the material in the syringe [29].

2.2.1.2 UV- irradiation system

In order to allow the polymerization of the dual-curable formulations *in situ* during the 3D printing, it was necessary to equip the LDM-3D printer with a UV light source. To this regard, it was chosen a UV light emitting laser peaked at 365 nm (LC-L1V3 by Hamamatsu; further details about this light source will be given later in *§ 2.3.1*). This source was provided with two optical fibers with collimating lenses to steer and focus the radiation directly on the fluid in the deposition.

In order to have a rapid curing of the material slightly after its exit from the nozzle, it was necessary that the two fibers were constantly pointed towards the nozzle, synchronously following its movements.

To this purpose, two supports were designed to fix the fibers to the transverse bar moving along z axis, near the LDM-estrusion system.

After designing the 3D model (*Figure 2.2.5*), the supports were fabricated in PLA using a conventional FDM printer, the DeltaWASP 20×40 by WASP (World's Advanced Saving Project srl, Italy).

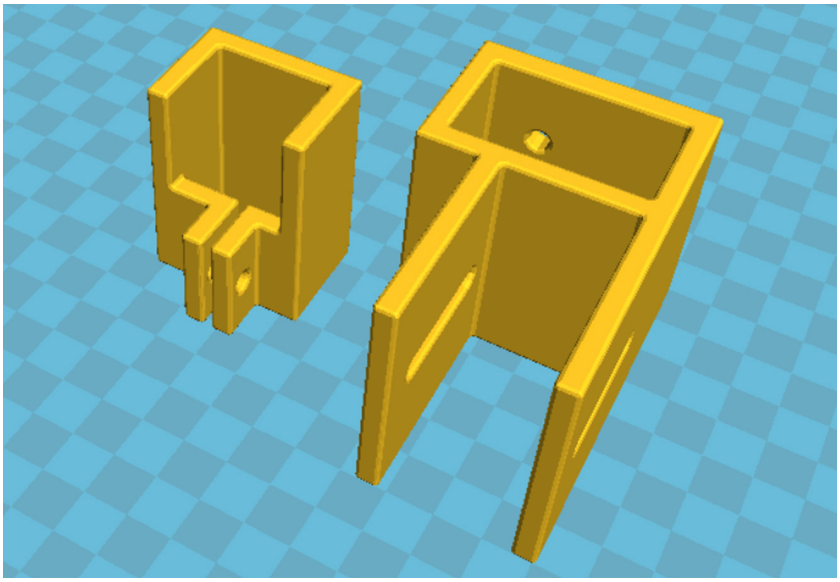

Figure 2.2.5 3D model of the supports for optical fiber.

Each support consists of two parts held together by a screw: one was fixed to the transverse bar while the other can be rotated in order to adjust the inclination of the fiber with respect to the nozzle position (*Figure 2.2.6)*.

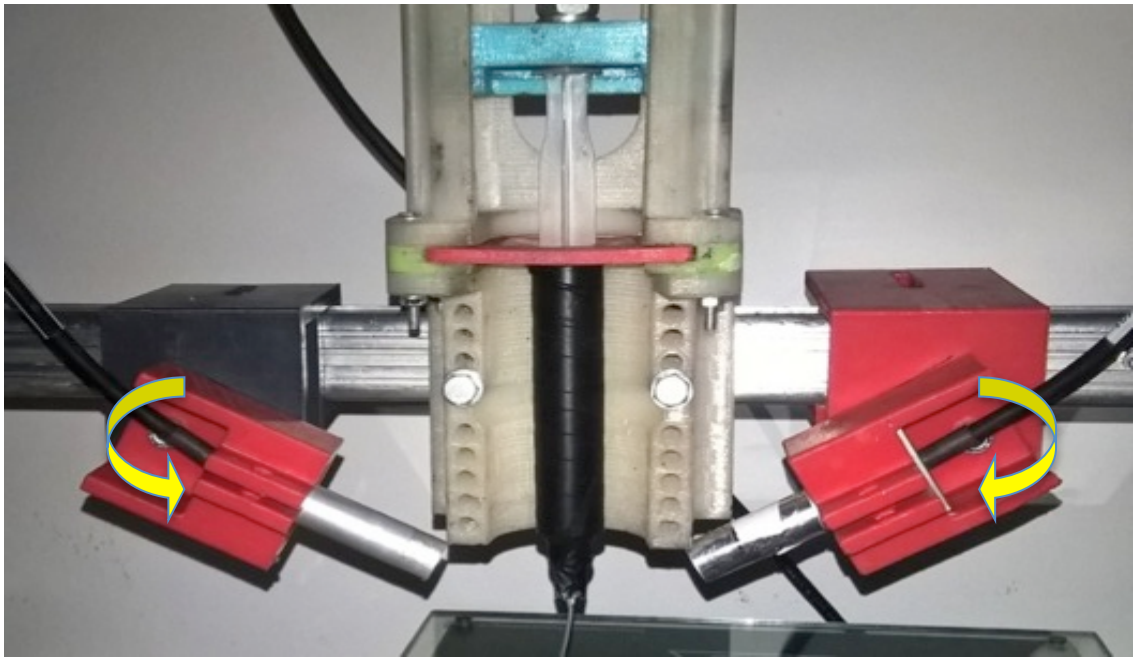

Figure 2.2.6 Supporters mounted on the transverse bar of the LDM-3D printer.

2.2.2 UV-3D printing process: from modeling to printing

The building of a 3D printed object consists of two main phases: the modeling of the object and its effective printing.

2.2.2.1 3D modeling and Gcodes generation

As already mentioned (*Section 1*), there are several software for 3D modeling; in the present work, SolidWorks (Dassault Systèmes, http://www.solidworks.com/) and Rhino's software (R. McNeel& Associates, https://www.rhino3d.com/) were used to generate the *.stl* files and the *.3dm* files, respectively. Because the printing apparatus was computer-controlled by means of *Gcode* language, the obtained *.stl* files were converted using two different software: the slicing open-source software Cura (Ultimaker, http://software.ultimaker.com/) and Grasshopper 3D software (Robert McNeel & Associates, http://grasshopper3d.com/), which permits a better control of the printing path. Examples of files generated with these two softwares will be shown in the following.

2.2.2.2 Pre-printing stages

Before starting the effective printing process, some other assembly stages were performed:

- **Syringe assembly**

The first step before printing was about the preparation and assembly of the syringe, as shown in the figures below (*Figure 2.2.7* and *Figure 2.2.8*).
First, with the aid of a metal spatula, the syringe was filled with the printable solution being careful not to create air bubbles (*Figure 2.2.7 (b)*). Then the 1.041 mm cone nozzle was screwed to the syringe (*Figure 2.2.7 (c)*), which was then wrapped with black tape to shield the contained material from light, in order to avoid the accidental activation of the photopolymerization (*Figure 2.2.7 (d)*).



Figure 2.2.7 Syringe preparation: a) Materials and instruments used; b) Filling of the syringe; c) Nozzle screwing; d) Shielding of the syringe.

After the filling and shielding, the syringe was assembled to the LDM UV-3D printer.

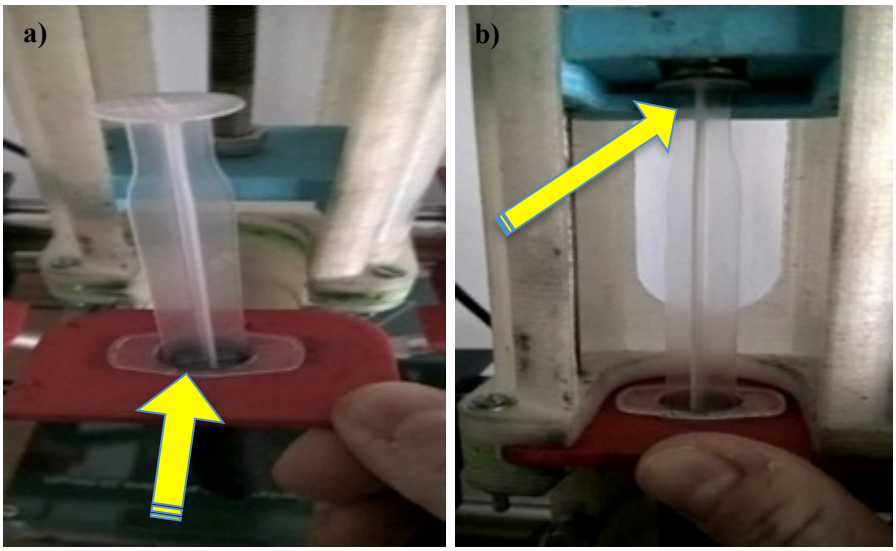

Figure 2.2.8 Syringe assembly to the LDM UV-3D printer: a) Insertion of the syringe holder; b) Piston insertion.

The syringe holder was inserted into the syringe support (*Figure 2.2.8 (a)*), and the piston was embedded into the cursor (*Figure 2.2.8 (b)*).

At this point, in order to eliminate any possible air bubble trapped in the syringe, the fluid was compressed pushing the piston slightly downwards.

During these stages, all the movements of the printer, previously USB-connected to the PC, have been handled by Repetier host software (Repetier, https://www.repetier.com/).

➢ z-Home calibration

The last step before starting the printing process was the Z-Home calibration. This passage provided for the alignment of the nozzle's tip to the printing plate.

In order to regulate the distance tip-plate, an endstop mechanism was assembled to the UV-3D printer. It is composed by a threaded bar and a small push button connected to the printers's electronics (*Figure 2.2.9 (a)*).

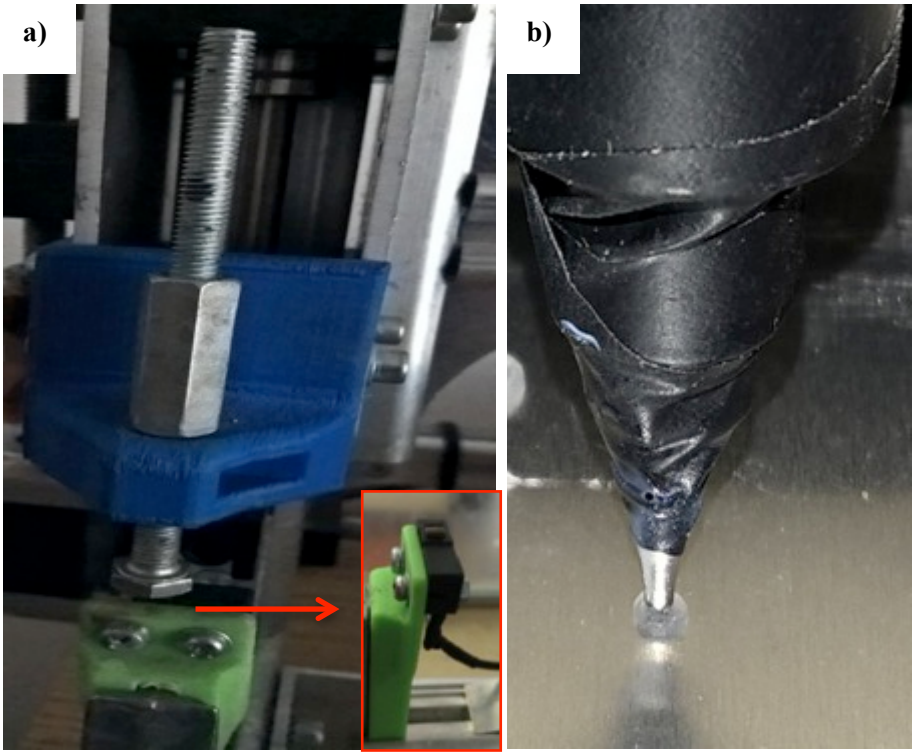

Figure 2.2.9 z-Home calibration: a) Endstop mechanism; b) Alignment of the nozzle's tip on the printing plate.

To be sure to have the correct tip-plate distance at the starting of the printing process, during the z-Home calibration phase, the nozzle's tip must touch the printing plate and the threaded bar must be in contact with the small push button (*Figure 2.2.9 (a-b)*).

After checking that everything was aligned, such z-position was acquired by the Repetier software (*z-Home* command) as the initial height for the printing.

2.2.2.3 UV-3D printing process start

After perfoming all the steps described above, the last ones were the loading on Repetier of the *.Gcode* file of the object that has to be printed, the switching on of the laser and, finally, the UV-3D printing process could be started (*Figure 2.2.10*).

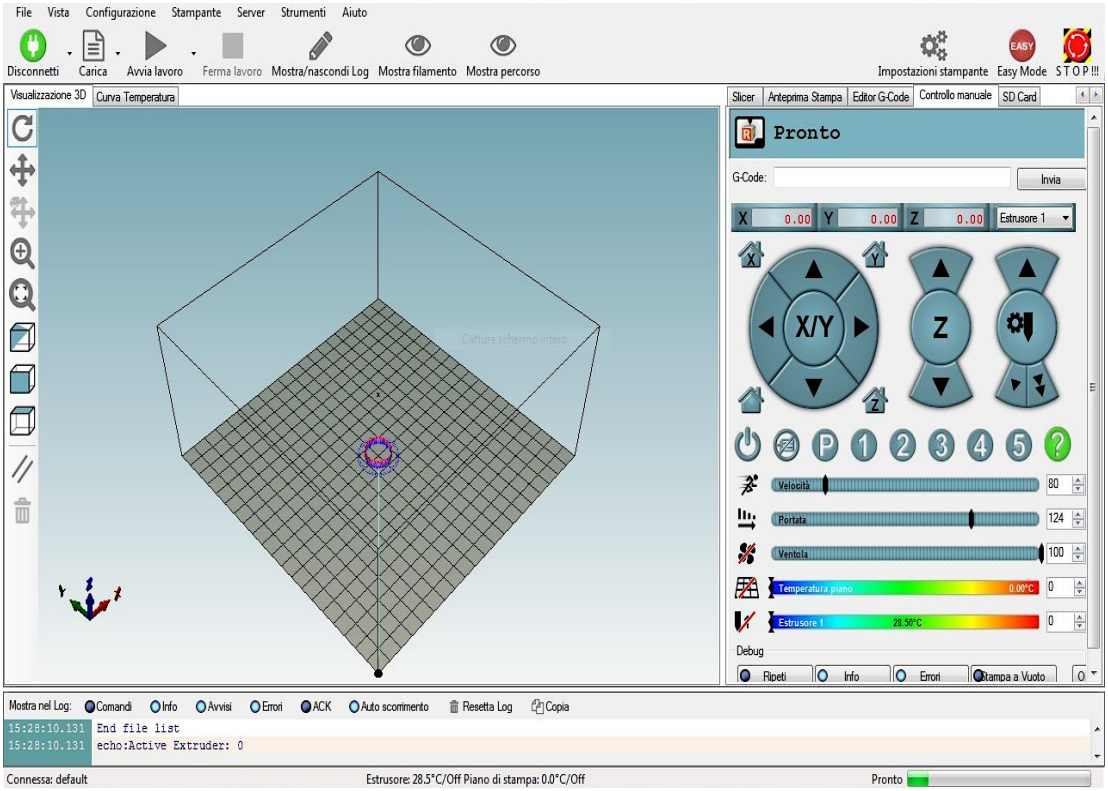

Figure 2.2.10 Repetier-Host interface: uploading and start commands.

2.2.3 Printing parameters: printability windows

In the *Gcode* generation stage, the defined slicing parameters related both to the UV-3D printer and to the imported 3D model, were the following:

- **Layer height**

It corresponds to the height of each single layer of material deposited from the nozzle (*Figure 2.2.11*).



Figure 2.2.11 Layer height [25].

By changing this parameter, different performances can be obtained: a low layer height corresponds to a more precise but slower printing, while setting a high layer height, the precision will be lower but the printing will finish in less time.

- **Shell thickness**

It represents the thickness of the external shell of the printed object (*Figure 2.2.12)*.

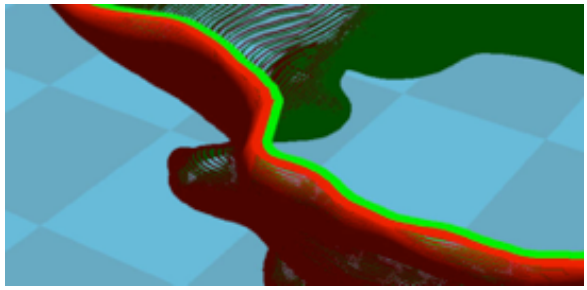

Figure 2.2.12 Shell thickness: zoom of a model whose shell thickness is set to 2. The red and green lines represent the two perimeters that will be printed with a 1 mm nozzle.

The wall thickness is defined by the number of perimeter lines for each horizontal section. It is obtained by setting a multiple nozzle size, which must correspond to the number of perimeters.

- **Fill density**

It represents the percentage of material that fills each individual layer (*Figure 2.2.13*). Setting high values of fill density, objects with greater strength can be obtained. In case of materials subjected to a strong shrinkage it is better to choice lower fill density values. When printing hollow objects with a single shell thickness, fill density is set to 0 %.

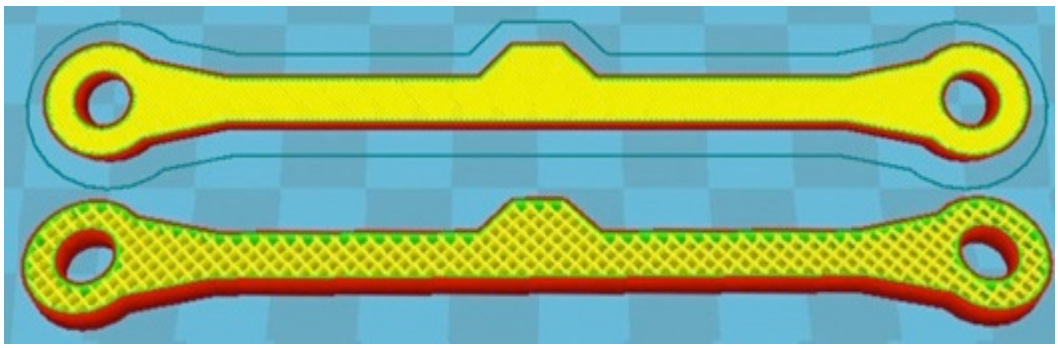

Figure 2.2.13 Example of two different fill density percentage: 75% (upper), 25% (bottom).

- **Print speed**

It is the speed of the printing plate displacement. Low quality printings are obtained with high speed values; with a low print speed the quality and the printing time increase.

- **Flow**

It represents the throughput at the nozzle tip. It is expressed as a percentage value.
In some cases it is usefull to set a flow greater than 100% in order to compensate possible shrinkage problems.

- **Nozzle size**

It is the diameter of the nozzle screwed to the syringe.

- **Filament**

In FDM printing, this parameter states for the filament diameter. In the LDM printing it refers to the diameter of the syringe mounted on the extrusion apparatus.

2.2.3.1 Spiral Cylinder Model (SCM)

In order to define the printability windows and test the ability of LDM UV-3D printing to reproduce complex geometries, it was chosen to design a cantilevered object with different inclination [51].

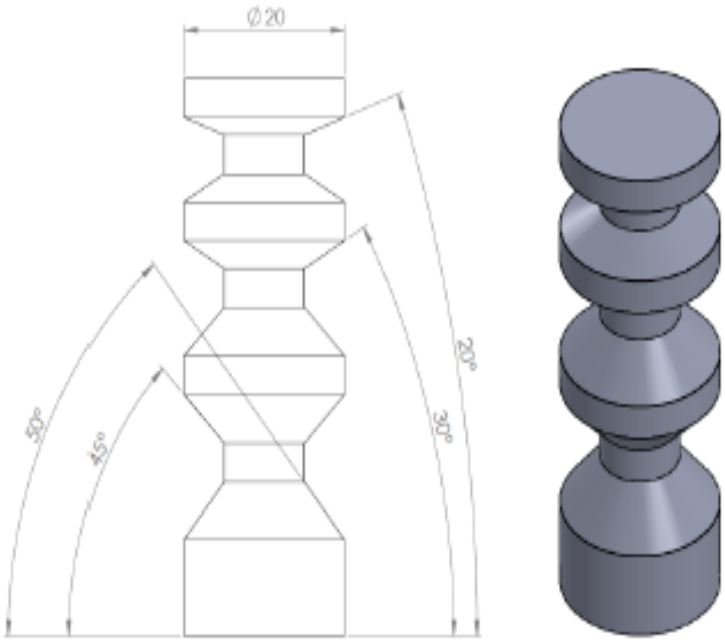

Figure 2.2.14 Model used to test the capability of LDM UV-3D printing in producing complex geometries: a) Frontal projection; b) 3D model designed with SolidWorks software [25].

As shown in the figure above (*Figure 2.2.14 (a-b)*), the selected model is made up of a vertical cylinder with overhangs inclinated at different angles ranging from 50° to 20°. Going from the bottom to the top, the smaller the inclination angle the more challenging would be the printing due to possible material sagging.

The 3D model of this particular object was designed using Solidworks software and then, the *.Gcode* file with all the instructions for the printing process was generated with Cura sofware.

For the printing of this object, the *spiral* slicing option was chosen (*Figure 2.2.15)*; this mode can be used for printing single wall thickness objects because the Z height moves continuously in a spiral fashion.

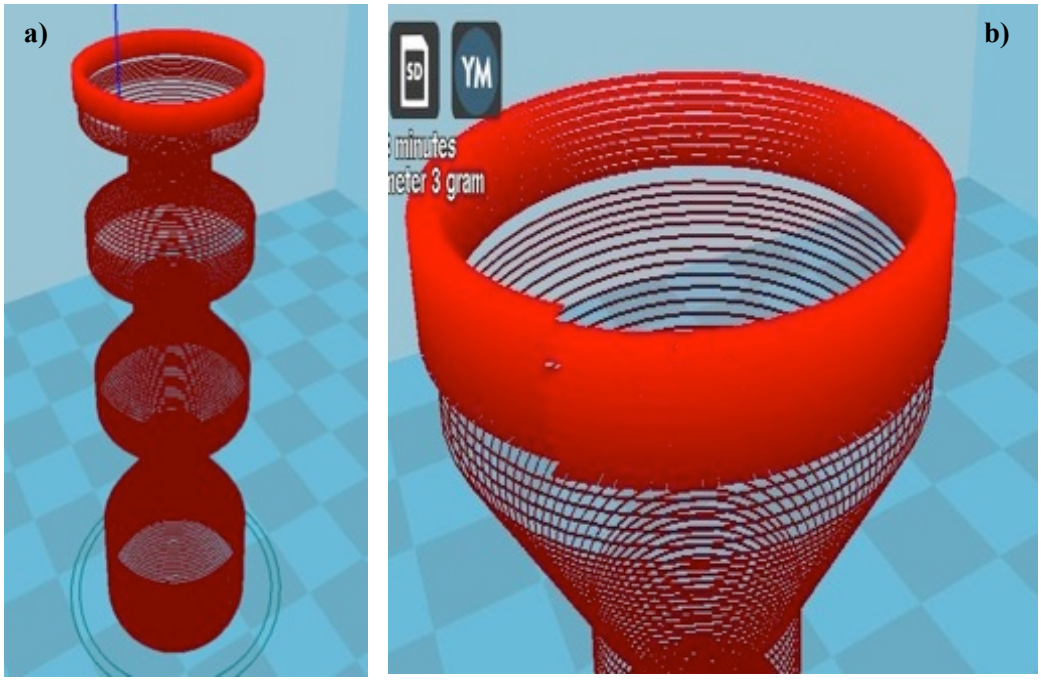

Figure 2.2.15 Spiral conical model: a) Image of the entire object; b) Close-up on some layer to show the spiral fashion.

In order to investigate the influence of the printing parameters on the ink printability different files were created varying one value each time; in the next table (*Table 2.2.1*), the ranges of the set parameters are reported.

Cura - Printing parameters	
Layer height (mm)	0.3 - 0.6
Shell thickness (mm)	1
Fill density (%)	0
Print speed (mm/s)	3 - 8
Flow (%)	90 - 130
Nozzle size (mm)	1 (conic)
Filament (mm)	14.5

Table 2.2.1 Printing parameters set in Cura software.

In some cases, the print speed and the flow have been varied also during the printing process using the special commands present in the Repetier interface.

Another important parameter, whose influence was taken into account, was the intensity of the UV-light. This parameter was varied during the printing process from 70% to 100% with respect to the total measured power density of the LC-L1V3 laser (~1300 mW/cm^2).

2.3 Characterization Techniques

2.3.1 UV-light sources

The UV- assisted process is one of the principal topic of this experimental work. For this reason, in addition to an accurate analysis of materials, a part of the research was focused on the choice of UV sources capable of providing the necessary energy for the activation of the cationic photopolymerization process.

During the work, four different devices have been used as UV sources: a UV chamber, a lamp centered at 366nm, a lamp installed on the p-DSC instrument and a laser mounted on the 3D printer. Although the three sources have different power and different emission spectrum, they are all suitable for the photopolymerization of the analyzed cationic formulations. In fact, it is known that regardless of the type of light source used, it is fundamental that that emission spectrum of the lamp overlaps at least in part the absorption spectrum of the chosen initiator.

In the following the most important characteristics of these devices are reported.

- **UV chamber**

The UV chamber is an irradiation chamber equipped with a mercury vapor lamp type Zs by Helios Italquartz (950 W/m^2), with UVA emittance from 360 nm to the visible (400-700 nm) (*Figure 2.3.1)*.



Figure 2.3.1 UV chamber: control panel and reflector [88].

➢ UV Lamp 4



UV Lamp 4 by Camag, is a lamp equipped with two tubes for irradiation (one for UV 254nm and one for UV 366 nm), each with 8 W. The desired UV wavelength can be selected through a button.

In this work we used only the emission at 366 nm.

Figure 2.3.2 Camag UV Lamp 4 [89].

➢ LC8 Lamp



The LC8 lamp is the UV source installed on the p-DSC instrument. It is a medium-pressure mercury lamp -01A type (Lightningcure LC8, 4500 mW/cm^2 at 365 nm) by Hamamatsu, equipped with two optical guides (*Figure 2.3.3*). The UV emission spectrum radiated from this lamp is in the 300-450 nm wavelength range.

Figure 2.3.3 LC8 Lamp: control panel and connected optical fiber guides [90].

➢ LC-L1V3 Laser

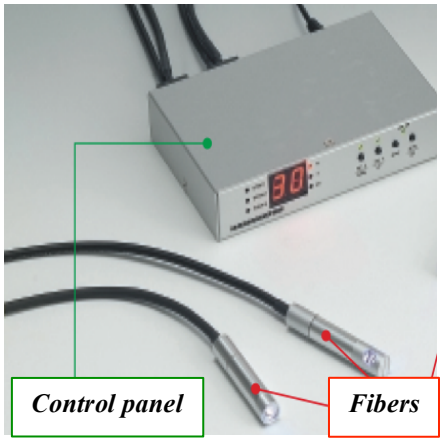

The LC-L1V3 laser (Lightningcure UV-LED spot light source) by Hamamatsu (*Figure 2.3.4*), is the UV source assembled on the 3D printer used in this thesis work. Its emission is centered at 365 nm in a band of ± 5nm, with maximum UV irradiance of 14000 mW/cm^2. The light is guided through two fibers with collimator type lenses.

Figure 2.3.4 LCL1 Laser: control panel and the two optical fibers [91].

2.3.2 Curing process investigation

The curing process was firstly studied in terms of absorption bands, kinetics and effects of dark-curing. It was evaluated by means of the UV-visible spectroscopy, the calorimetric analysis and the IR spectroscopy. The efficiency of the UV-Assisted process was also investigated, in terms of curing capability by performing two different test: the "Drop on Glass" test and the Gel Percentage measurement.

The entire study of the cationic photo-polymerization and the dual-cure kinetics of the prepared systems have been conducted in function of photoinitiator concentrations, UV intensity, temperature and exposure time.

2.3.2.1 UV-vis spectroscopy

UV-visible spectroscopy was used to evaluate the absorption bands of the different photoinitiators and plasticizers used. The analysis was performed using an Evolution 600 UV-vis spectrophotometer (*Figure 2.3.5 (a)*), and evaluated with the VISION Pro software (Thermo Scientific).

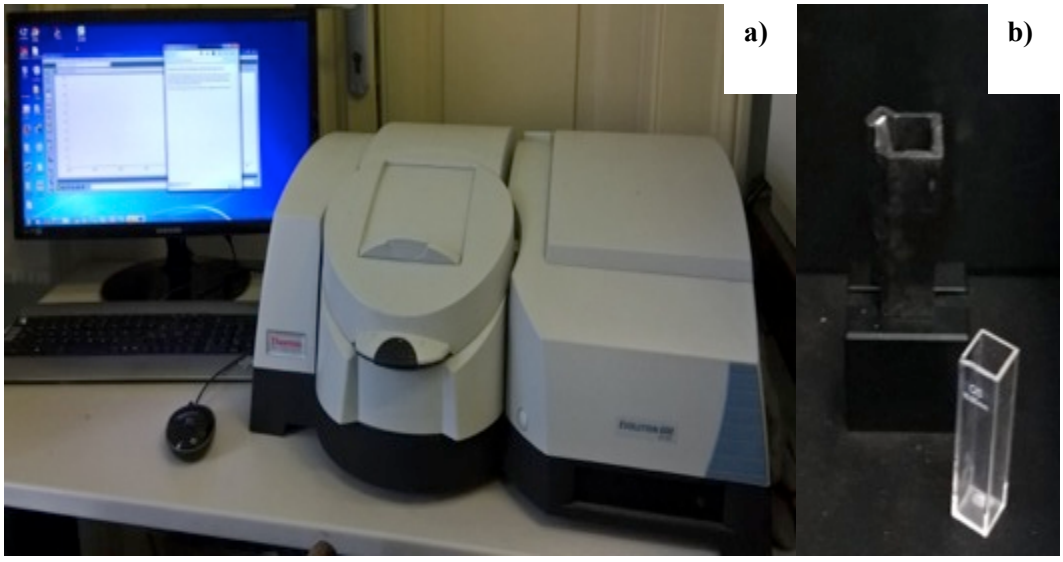

Figure 2.3.5 UV-vis spectrophotometry apparatus: a) Evolution 600 UV-vis spectrophotometer; b) Quartz cuvette and cuvette's holder.

Measurements were performed on solutions of photoinitiators and plasticizers at a concentration of 0.001% vol in acetonitrile and methanol, respectively. The solutions were poured in 10 mm quartz cuvettes (*Figure 2.3.5 (b)*) and, before starting each actual sample analysis, the baseline (spectra of

solvent only) was recorded. Multiple samples spectra were collected in absorption mode from 200 nm to 700 nm, with 120 nm/min scanning speed and 4 nm resolution.

2.3.2.2 Calorimetric analysis

Calorimetric analysis is based on the measurement of the differential heat flow rate existing between the sample and a reference. Calorimetry is usefull to investigate the occurence of chemical and physical reacions, which are connected to the generation or consumption of heat.

- **Photo-Differential Scanning Calorimetry (p-DSC)**

In this experimental work, the exothermic heat of the photo-polymerization reaction was measured isothermally at 25°C by means of a DSC/823e (Mettler-Toledo) instrument connected with two optical fibers guides, one for the sample and one for the reference, to the medium-pressure mercury lamp (Lightningcure LC8, Hamamatsu), described in paragraph *§ 2.3.1*, (*Figure 2.3.3*).

Using a Pasteur pipette, the liquid sample, stored in UV-shielded vials, was taken and open aluminium pans were filled with a droplet of 10-20 mg. The crucible was placed in the sample-pan holders (*Figure 2.3.6 (b, c)*) and the irradiation chamber was kept in a nitrogen flow (50 ml/min) during the entire UV exposure. Each UV-exposure sequence was repeated on the polymerized sample to acquire a baseline heat flow to be subtracted to the initial sequence. The heat of reaction, ΔH, was obtained by integration of the resulting exotherms.

Several experiments were carried out in order to follow the advancement of the photo-polymerization of different compositions and to evaluate the effect of irradiation intensity combined to exposure time. UV irradiation intensity was varied as follows: 100%, 80%, 50%, 10%, and 5% with respect to the maximum provided value[9] at 25° C. Samples were exposed for 3 min to UV light in the first three cases and for 10min in the last two. The sampling interval was kept constant at 1 s/pt.

[9] Total UV intensity provided by the Lightningcure LC8, Hamamatsu lamp is 4500mW/cm^2 Typ (at 365nm, -01A type). The maximum intensity that can irradiate the sample is halved due to the presence of two optical guides connected to the lamp.

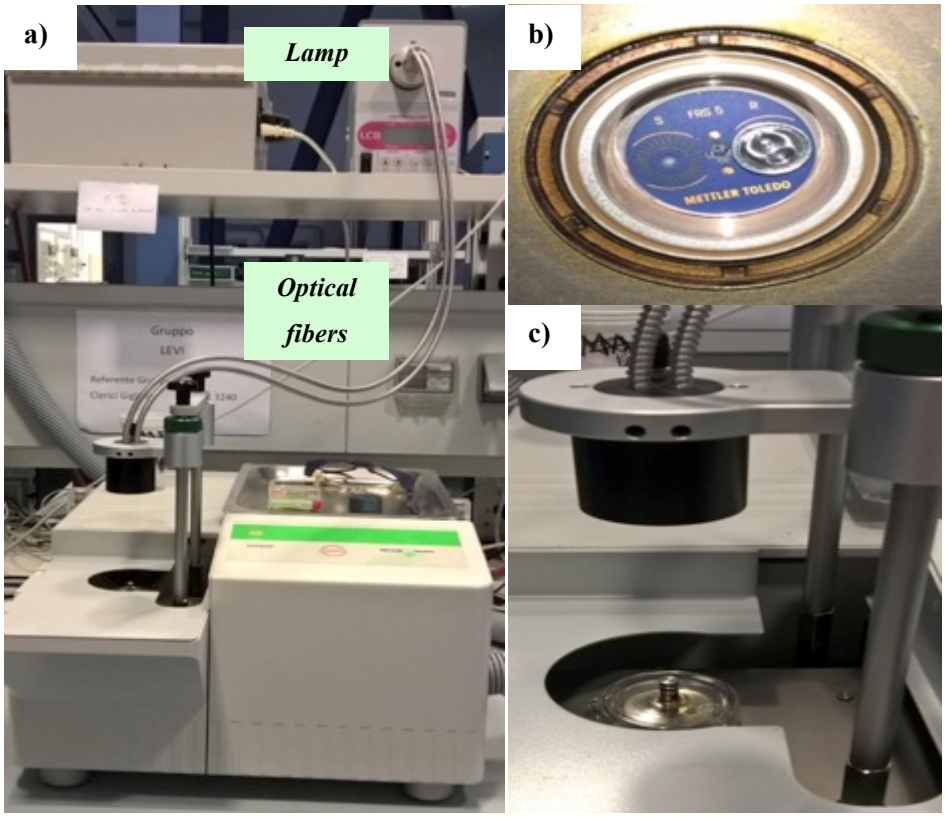

Figure 2.3.6 Apparatus for the calorimetric analysis: a) DSC/823e instrument and the mercury lamp with two optical fiber; b) Sample holder with the reference crugible; c) Chamber of the analysis.

In the specific case of the *p-ES3* solution, the p-DSC analysis was also used to study the experimental extent of conversion $\alpha_{\%}$ of the exothermic crosslinking reaction. To this end, some samples were prepared by filling an aluminium crucible with about 10 mg of liquid solution. Each one was then exposed to UV light (1300mW/cm^2) for a certain time interval and immediately immersed into liquid nitrogen for 1 min to block the curing reaction. Before performing the p-DSC analysis, the sample was further blown with a nitrogen flux.

The experimental extent of conversion was then calculated through the *Eq. 2.2,* by comparing the obtained heat of reaction ΔH_{res} of samples pre-exposed to UV-light for different time intervals to the total measured heat of reaction ΔH_{tot} of a sample not pre-irradiated.

$$\alpha_{\%} = \frac{\Delta H_{tot} - \Delta H_{res}}{\Delta H_{tot}} * 100 \qquad (2.2)$$

➢ Differential Scanning Calorimetry (DSC)

The calorimetric characterization of the dual-cure system was focused on the evaluation of the residual heat of polymerization associated to specimens previosly exposed to UV-light. The analysis, performed using the same instrument presented above (*Figure 2.3.6*), DSC/823e (Mettler-Toledo) without the coupling with the UV light source, consisted in the detection of the change in the heat flow rate difference between the sample and the reference, during a controlled non-isothermal scan.



Figure 2.3.7 Press to close the aluminium pans for DSC analysis.

The DSC-samples, made of closed aluminium crucibles (*Figure 2.3.7*), were prepared simply closing the aluminum pans previously tested in the p-DSC.

All experiments were performed under nitrogen atmosphere; the non-isothermal scan consisted of three runs: from 20° C to 250° C, from 250° C to 20° C, and from 20° C to 250° C, with a rate fixed at 20° C/min.

The final obtained plot represented the heat flow rate as a function of the temperature provided to the sample. The presence of inflections was attributed to thermal transitions occurrence; in particular the glass transition temperatures were detected looking at the plot corresponding to the third scan.

2.3.2.3 Fourier Transform Infrared Spectroscopy (*FTIR*)

In this thesis, FTIR spectroscopy was employed to evaluate the reaction conversion after UV exposure (thin film of solution were irradiated with the laser mounted on the 3D printer, Lightningcure UV-LED spot light source LC-L1V3 for1-15sec at 1300mW/ cm^2) and after a thermal post-curing treatment (180° C for 1 hour), and mainly to follow the isothermal dark-curing, characteristic of the cationic systems.

The spectra of the epoxy systems before and after UV exposure were recorded; for the evaluation of the dark-curing, the post-irradiation spectra were acquired every 5-10 min.

All the acquisitions were performed using a Thermo Nicolet Nexus 670 FTIR spectrometer (*Figure 2.3.8*), included by a Globar IR-source and by DTGS or MCT detectors. Each acquisition was made with a resolution of 4 cm^{-1} in the range of 4000 to 600 cm^{-1}. Before the acquisition of each sample's spectrum, the background was recorded, in order to be then subtracted from the real sample signal.

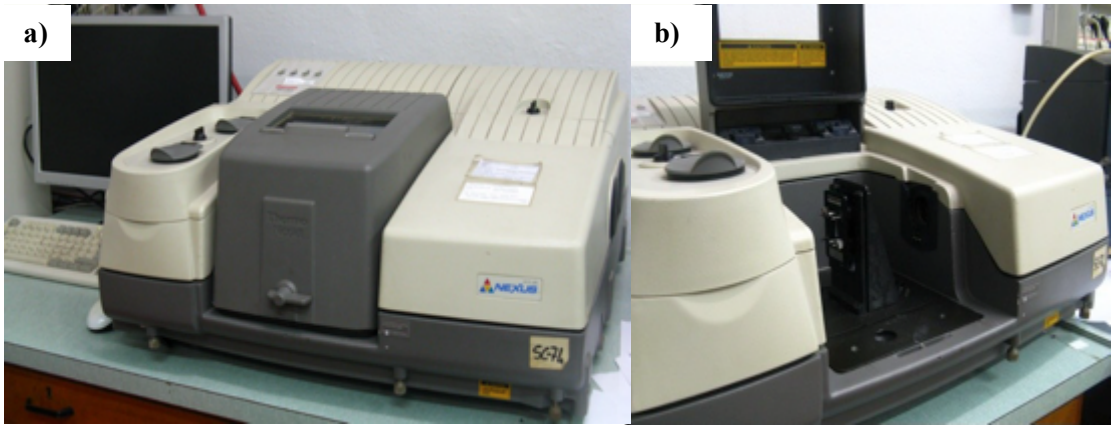

Figure 2.3.8 FTIR instrument: a) Thermo Nicolet Nexus 670 spectrometer; b) Chamber for sample analysis.

To analyze the solutions, a disk of NaCl was used as support, as NaCl crystal does not absorb in the mid-IR region. The liquid sample was taken with a Pasteur pipette from the UV-shielded vial and a drop of it was deposited on the NaCl crystal disk (*Figure 2.3.9 (a)*). With the help of another disk, the drop was spread over the entire surface in order to obtain a thin film.

Then, the sample was placed in front of the detector and the measure started.

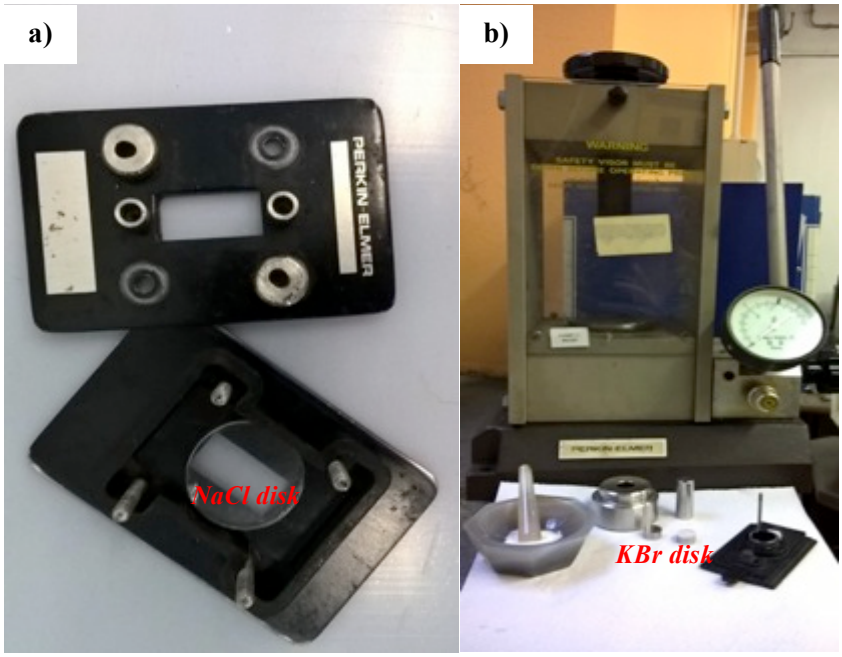

Figure 2.3.9 FTIR-sample: a) NaCl crystal disk, used as support for liquid solution, in the sample holder; b) Apparatus used to prepare the KBr disk for the analysis of powder.

In order to analyse the powders, like maleic anhydride, a disk of material dispersed in KBr was prepared using a special press (*Figure 2.3.9 (b)*). The KBr salt used for the disk fabrication was previously placed in a vacuum oven for 24 hours at 100° C, in order to avoid any possible moisture contamination. A small amount of anhydride was added to the KBr salt in such quantities as to get a signal not out of range (Absorbance <1), and in order to achieve a good dispersion a mortar was employed to crusch the two substances. The obtained powder was pressed in a disk which was directly used for the acquisition of the maleic spectrum.

The frequencies range of interest for our studies is the mid-IR, from 4000 to 600 cm^{-1}; in particular, the cure reaction was monitored by following epoxy and anhydride bands. For the dark-curing process analysis of the photocurable system, *p-ES3*, the progressive decrease of the cycloaliphatic epoxy absorption bands at 788 cm^{-1} and 746 cm^{-1} were mainly followed; for the analysis of the dual-cure systems, *pt-ES3MA*, the maleic anhydride characteristic absorption bands at 1858 cm^{-1} and 1777 cm^{-1} were also considered. Absorption was normalized with respect to the carboxylic acid bands[10].
The cure conversion α was calculated with the peak height, using the following equation (*Eq. 2.3*):

[10] Carboxylic acids exhibit a sharp band associated with vibration of the C–O vibration bond ($\nu_{C=O}$) between 1680 and 1725 cm^{-1}. A characteristic ν_{O-H} band appears as a broad peak in the 2500 to 3000 cm^{-1} region.

$$\alpha = (1 - \frac{h(t)}{h(t=0)}) * 100 \qquad (2.3)$$

where *h(t) / h(t=0)* is the ratio of the actual normalized heigth of the peak to the initial one and *h(i)* is the ratio of the height of the analysed peak to the carboxylic reference one when *t=i*.

2.3.2.4 "Drop on glass" test

The "Drop on glass" test was performed both to evaluate the response of different solutions to the UV-irradiation (wavelength above 350 nm), and select the correct position and intensity of the laser assembled on the printer, in order to have a fast curing of the materials that will be printed.
The test consisted in the deposition of a drop (≈ 50 µl) of solution on a slide (*Figure 2.3.*10), which was then positioned at a certain distance from the UV-source and irradiated for a certain time with a specific UV-light intensity.



Figure 2.3.10 Example of two drops of solution deposited on a slide to perform the "Drop on Glass" test.

Several tests were performed changing only one parameter at a time; first the intensity of the light was fixed at the maximun value varing the distance from the source (2 cm – 8 cm); then the opposite was done, maintaining the distance fixed at 4 cm on varying of the intensity (100% - 10% with respect to the maximun power density). The time of UV-exposure was varied (2 sec – 10 min) during the evaluation of the reactivity of different solutions and then, it was fixed at 2sec for the tests performed in order to select the correct parameters related to the laser assembled to the 3D printer.

2.3.2.5 Gel Percentage measurement

In order to evaluate the degree of crosslinking of bulk samples and thus the efficiency of the UV-assisted processes (UV-assisted casting and printing), the Gel Percentage measurements were performed.

The casted sample was prepared by pouring the liquid solution into a transparent mould avoiding the appearence of air bubbles and subjecting them to a successive curing cycle. Depending on the nature of the solution, the curing cycle consisted in the exposure to UV light (UV-chamber, *§ 2.3.1*) for 30 min on each side in case of UV-cure solutions and, in a subsequent thermal treatment for 1 h at 180° C -220° C, in case of dual-cure solutions.

The printed sample was instead directly UV-cured during the 3D-printing process and, only in the case of a necessary thermal cycle, it was put in the oven.

The resulting solid sample was then weighted (W_{init}) and left immersed in C_3H_6O for 24 h to remove the uncured fraction (*Figure 2.3.11 (a)*).

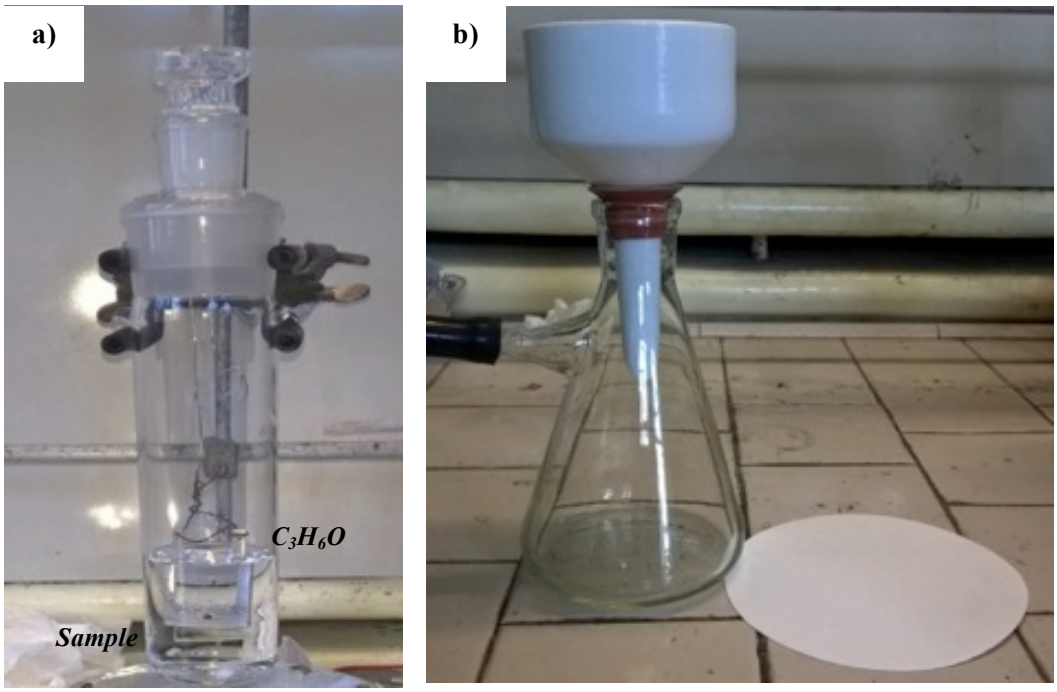

Figure 2.3.11 Apparatus for Gel Percentage measurement: a) Sample immersed in acetone; b) Instrumentation used to filter the residual solvent.

After extracting the sample from acetone bath and filtering the solvent to recover every possible sample fragment (*Figure 2.3.11 (b)*), it was weighted and put in a oven at 80°C to enhance desorption of solvent. The weight of the sample was collected at hourly intervals until it reached a constant value, which was considered as the cured fraction of the sample (W_{fin}).

The degree of crosslinking (*DC*) was thus obtained by the following formula:

$$Degree\ of\ crosslinking = \frac{W_{fin}}{W_{init}} * 100 \qquad (2.4)$$

In the case of values lower than 100%, filtered residual solvent was concentrated using a rotavapour (Ika HB10) and the obtained solution was analyzed by FTIR spectroscopy in order to verify the presence of the characteristic peaks of the basic monomers of the processed materials.

2.3.3 Rheological investigation

The rheological characterization of the unloaded epoxy matrix and SFR-composites was performed using two different instruments: a Bohlin CVO 120 high resolution rheometer with a 20 mm plate-plate configuration at 25° C (*Figure 2.3.12 (a)*) and a Rheometrics DSR200 rheometer with a 25 mm plate-plate configuration at 25° C (*Figure 2.3.12 (b)*), respectively.

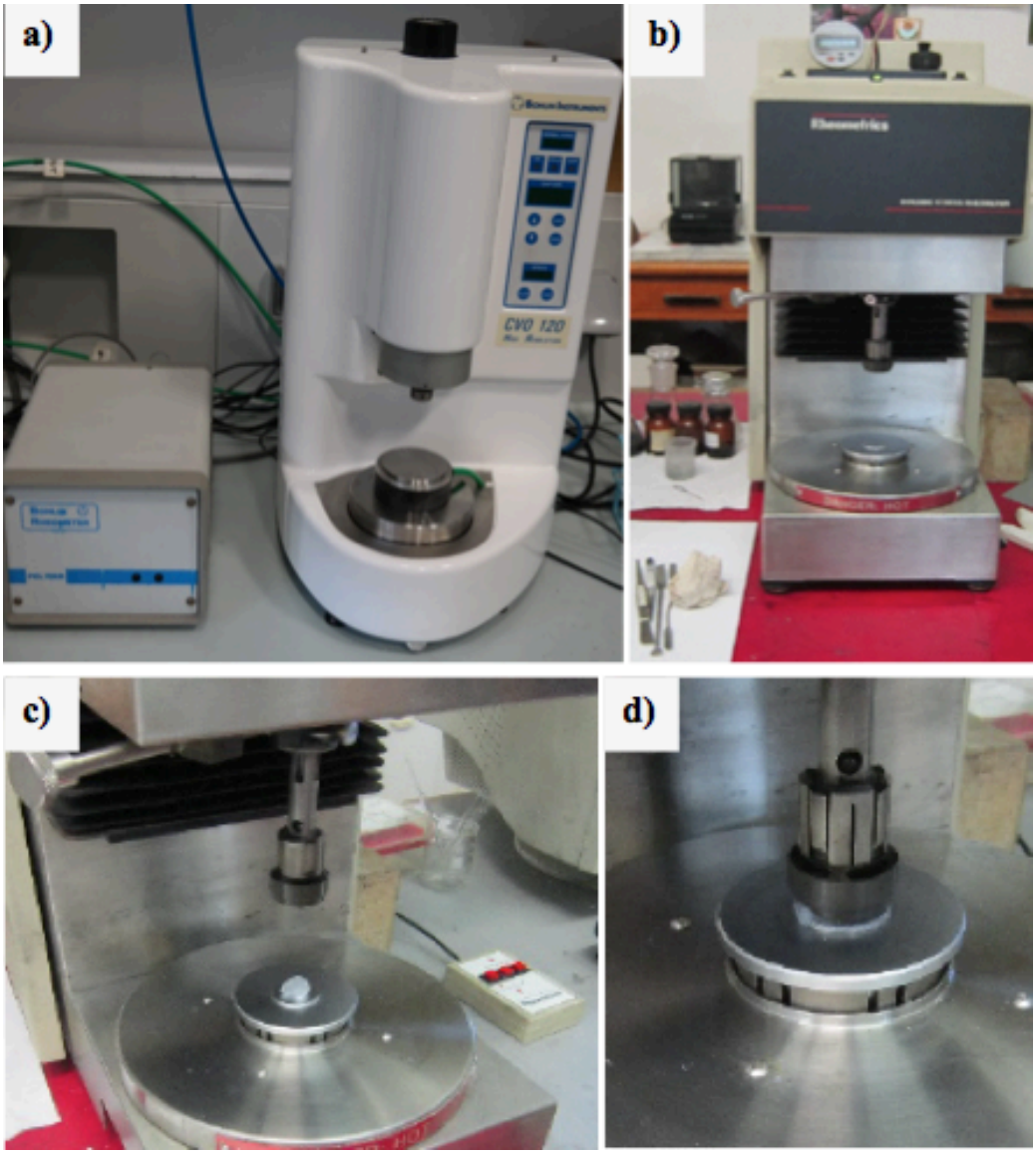

Figure 2.3.12 a) Bohlin rheometer used for the characterization of the epoxy matrix. b) Rheometrics rheometer employed in the composite dispersions characterization. c) Deposition of the mixture on the bottom plate. d) Sandwiching of the material between the plates.

All the samples prepared as described in the previous paragraphs *(§ 2.1.2* unloaded systems, and *§ 2.1.3* loaded systems), were analysed in 15 min after preparation in order to avoid any possible modification of their real rheological behavior.

As shown in the following figure, (*Figure 2.3.12 (c)*), using a spatula, a small amount of mixture is deposited on the bottom plate. Then the upper plate was lowered until contact with the sample, setting an average gap (plate-plate) to 0.8 mm (*Figure 2.3.12 (d)*). Before starting the actual measure, each sample was subjected to a pre-shear for 10 sec in the 0-10 Pa range in the case of newtonian unfilled systems, and in the 0-300 Pa range for the loaded ones. After that, steady shear tests were performed for 5 min in the 0-100 Pa range on Newtonian resins, and in the 0-6000 Pa on the filled ones.

2.3.4 Mechanical properties investigation

In order to investigate the mechanical properties of the polymeric matrix and of the fiber reinforced composites developed in this experimental work, two different methods were adopted: the dynamic mechanical analysis (DMA) and the tensile test.

2.3.4.1 Dynamic Mechanical Analysis (*DMA*)

Dynamic mechanical analysis is useful for the investigation of the response of a material when subjected to a sinusoidal input.

Since polymeric materials are characterized by a viscoelastic behavior, sum of an elastic (spring-like) as well as a viscous (dashpot-like) behavior, the sinusoidal output shows a phase difference with respect to the applied input. This difference can be quantified by the angle δ. As a consequence of this phase mismatch, the amplitude of the material response to a sinusoidal sollecitation, can be splitted into two parts: an *in phase* component and an *out of phase* one. Following this approach, also the modulus of the material (that is the ratio between output and input) can be splitted into two terms: the *loss modulus*, related to the viscous component; the *storage modulus*, related to the elastic response. The ratio between the two components is the *tan δ factor,* which gives an indication of the energy dissipation during molecular rearrangement.

In this experimental work, DMA analyses were performed both to evaluate the storage modulus of the polymeric materials (E') at room temperature and to understand the temperature range where they exhibits a rubbery-like behavior: that is the glass transition temperature (T_g), related to the tan δ factor.

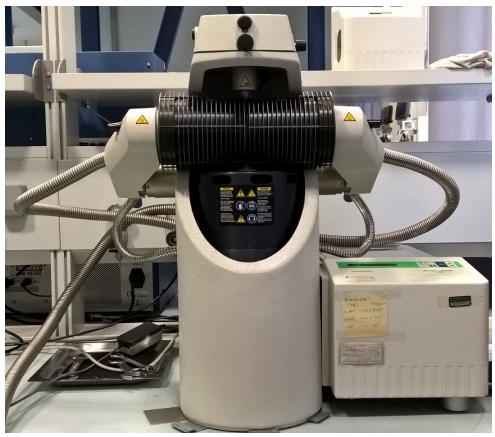

Figure 2.3.13 DMA/SDTA861 instrument used for the Dynamic Mechanical Analysis of cast and 3D printed rectangular samples.

The analyses were carried out in three-point bending mode on a Mettler Toledo DMA/SDTA861 instrument (*Figure 2.3.13)*.

Isothermal tests in strain sweep (0.1-200 μm) were performed at 25° C. The frequency was kept constant at 1 Hz. The analyses in dynamic scan were performed applying the sinusoidal strain (amplitude 2 μm) at 1 Hz and the resultant stress was measured with a temperature ramp of 3° C/min in the range - 20° C and 250° C.

The samples for DMA were 80 × 10 × 4 mm^3 rectangular beams.

To evaluate and compare the bulk mechanical properties of the material subjected to different fabrication processes (casting and 3D printing), the samples were prepared both by pouring the liquid solution in a mould containing the negative impression of the desired model (*Figure2.3.14 (a)),* and directly by printing the 3D model. In this last case, the sample digital model was previously drawn with Rhino-Grasshopper (*Figure2.3.14 (b))*, and then it was UV-3D printed at print speed ranged between 4–12 mm/s, with layer height set to 0.25 mm, and using a 1mm diameter nozzle. The formulations are printed onto glass slides covered with baking paper to prevent adhesion.

The casted samples were cured 30 min on each side using the UV chamber, described in *§ 2.3.1*; the UV-3D printed ones were cured directly during the printing process (15 min).

For what concern the analysis of dual-cure materials, the above procedure continued with a thermal treatment at 180° C (220° C in case of formulation containing PA) for 1 h. In order to avoid warping effects during the thermal cycle, a heavy metal plate was placed over the samples.

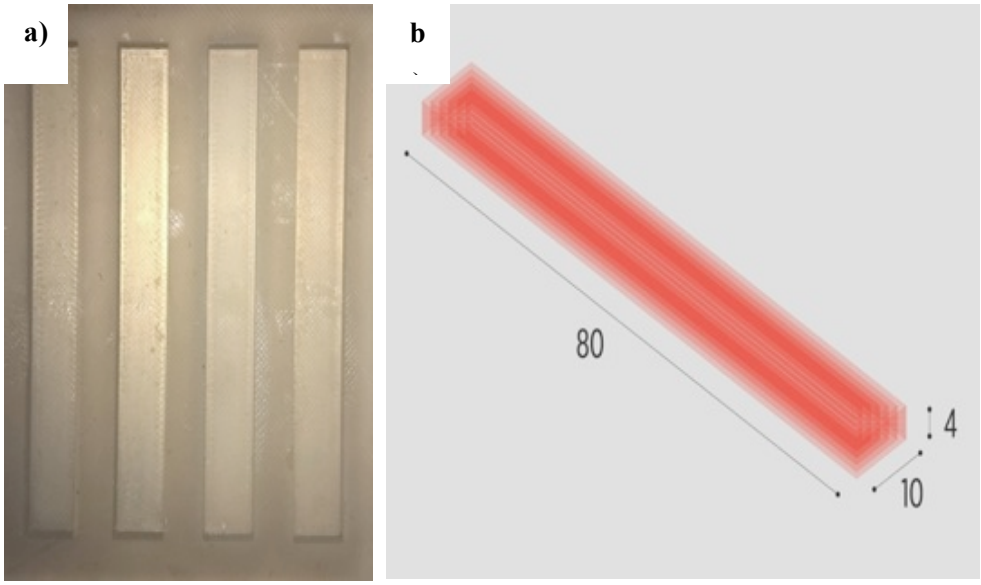

Figure 2.3.14 a) Mould for the preparation of DMA casted sample; b) 3D model (generated with Grasshopper software) for the printing of the DMA sample.

2.3.4.2 Tensile test

Uniaxial tensile test was adopted for a further investigation of the mechanical behavior of the novel materials: the dual-cure polymer matrix and the corresponding fiber-reinforced composites.
The tests were performed at room temperature at 1mm/min testing speed and 2N of pre-load on a Zwick-Roell Z010 (Zwick Roell, Italy) (*Figure 2.3.15 (a)*) with a 10 kN load cell and a longstroke extensometer[11] (*Figure 2.3.15 (b)*).

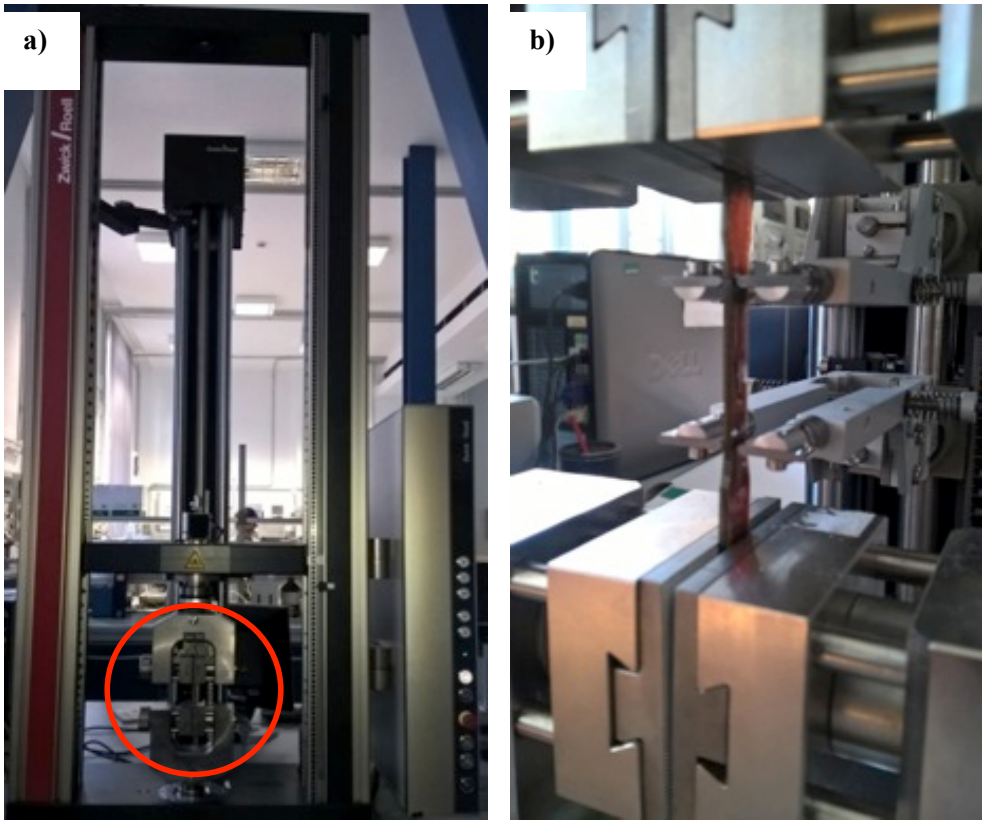

Figure 2.3.15 Apparatus for tensile test: a) Zwick-Roell Z010 instrument; b) Longstroke extensometer closed on a sample.

The tensile tests to estimate the Young's modulus (E), stress (σ_r) and strain (ε_r) at break of the dual-cured matrix have been carried out both on cast and on UV-3D printed dumbbell specimens following the ASTM D638 standard test method. The Type I specimen was selected and, in order to shorter the time of printing process, its dimensions were down-scaled obtaining a narrow section of 35 × 8 × 2 mm^3.

[11] During the fiber-reinforced composites testing the extensometers has been removed because they were malfunctioning.

The cast specimens were obtained by casting the liquid material (*pt-ES3MA* and *pt-ES3MAOX200-11*) in the silicon mould (*Figure 2.3.16 (a)*) avoiding the formation of air bubbles and proceding with the dual-curing cycle (UV-irradiation in the UV-chamber and thermal cycle 180° C for 1h).

For the UV-printed specimens production, the 3D model was first drawn with SolidWorks software, then the .Gcode file was produced with Cura software (*Figure 2.3.16 (b)*) and, at the end, the *pt-ES3MAOX200-11* mixture was UV-printed (100% infill, layer height set to 0.25 mm) operating te 3D printer at 15mm/s with a 1 mm nozzle. After the UV-printing process (≈10 min/sample), the samples were subjected to the thermal cycle at 180° C for 1 h in the oven.

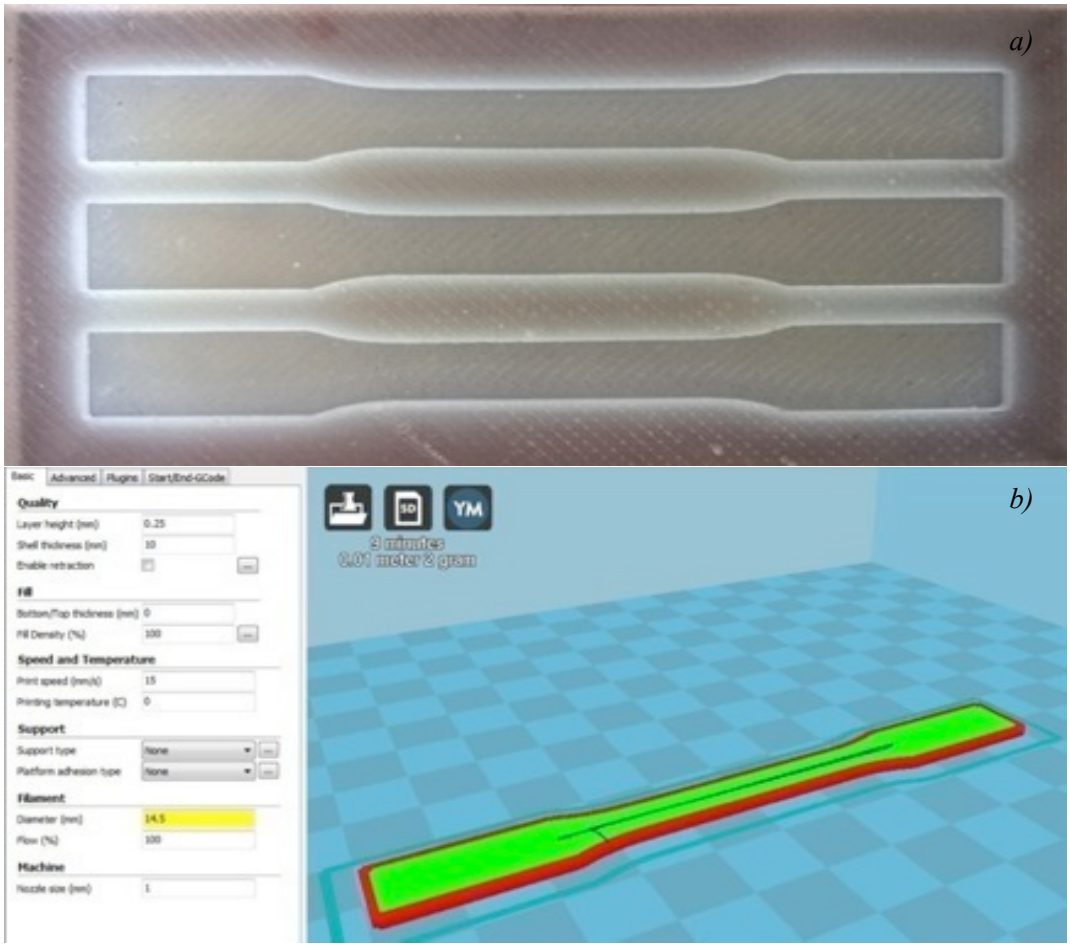

Figure 2.3.16 Tensile test specmen preparation: a) Mould used to cast the dumbbell specimen; b) 3D model in Cura.

The mechanical properties of the fiber-reinforced dual-cure polymer composites were tested only on UV-printed specimens, following the D3039/3039M standard test methods. The *random-discontinuous fiber orientation* (*RDFO*) type specimen was selected and its dimensions were down-scaled obtaining a 90 × 10 × 2.5 mm^3 rectangular beam.

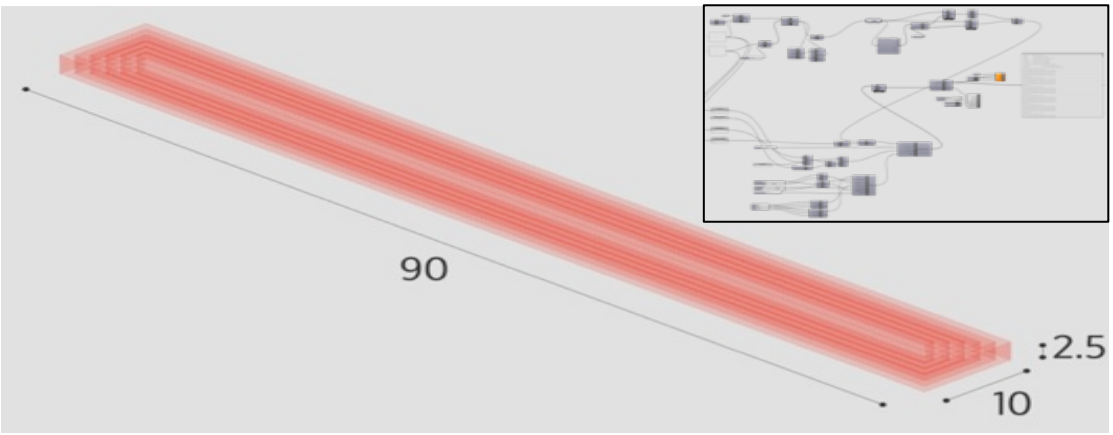

Figure 2.3.17 3D model of the RDFO specimen. In the upper right the diagram designed with Grasshopper.

Before printing, the 3D model was produced using Rhino-Grasshopper softwares (*Figure 2.3.17*) and then the specimens were UV-printed with a 100% infill, a layer height set to 0.25 mm at print speed ranged between 4-12 mm/s with a 1mm nozzle.

After the UV exposure during the printing process (*Figure 2.3.18*) (≈ 15-45 min/sample, depending on the composite formulation), the dual-curing cycle was completed in the oven at 180° C for 1h.

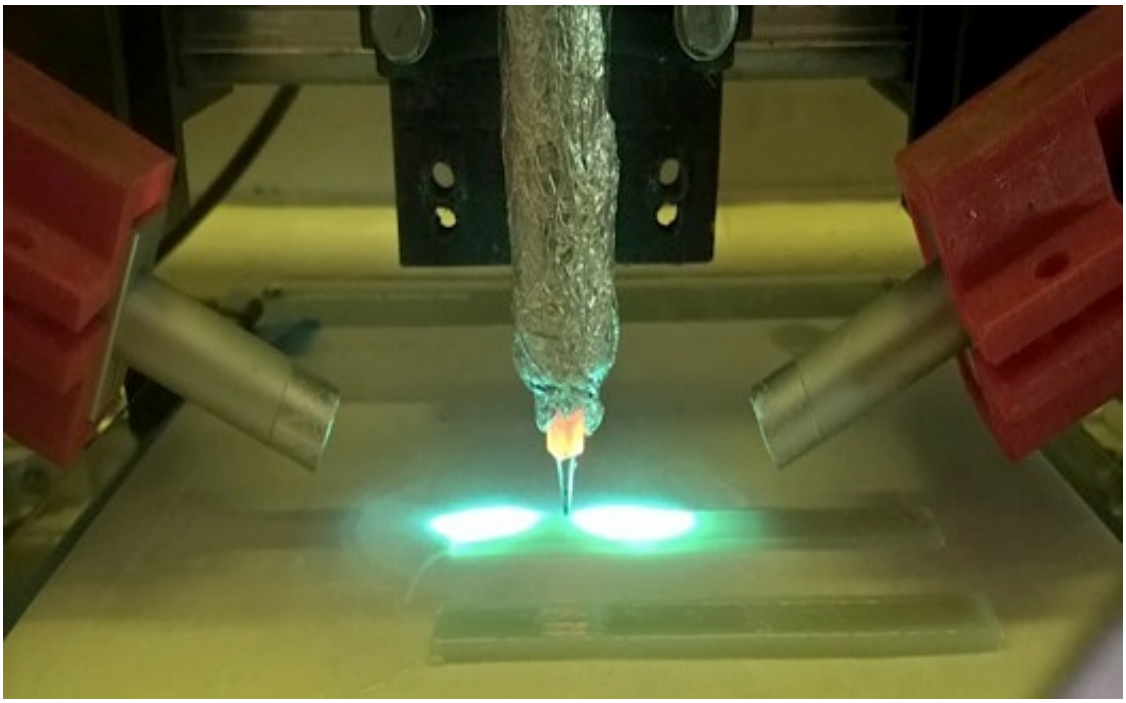

Figure 2.3.18 UV-3D printing process: printing of a glass fiber-reinforced RDFO sample. In the foreground an already printed sample.

Since it is known that the mechanical properties of materials depend on the geometry of the objects, to make a correct evaluation of the composites properties compared to those of the starting matrix, a series of *RDFO* type specimens was also prepared with the dual-cure matrix material, *pt-ES3MAOX200-11*.

However, in order to evaluate the effect of the filament printing direction and demonstrate the potential of UV-3D printing in processing complex geometry, a different type of UV-3D printed specimen for tensile analysis was prepared. This type of specimen was realized with composite inks, following a cellular arbitrary patterns (infill<100%), taking inspiration from the natural world, as J. Lewis has done in her works [48]. The corresponding 3D model was designed using Grasshopper software (*Figure 2.3.*18) and then the specimens were fabricated by operating the UV-3D printer at 7 mm/s, setting a layer height of 0.25 mm, and adopting a 1 mm cone nozzle.

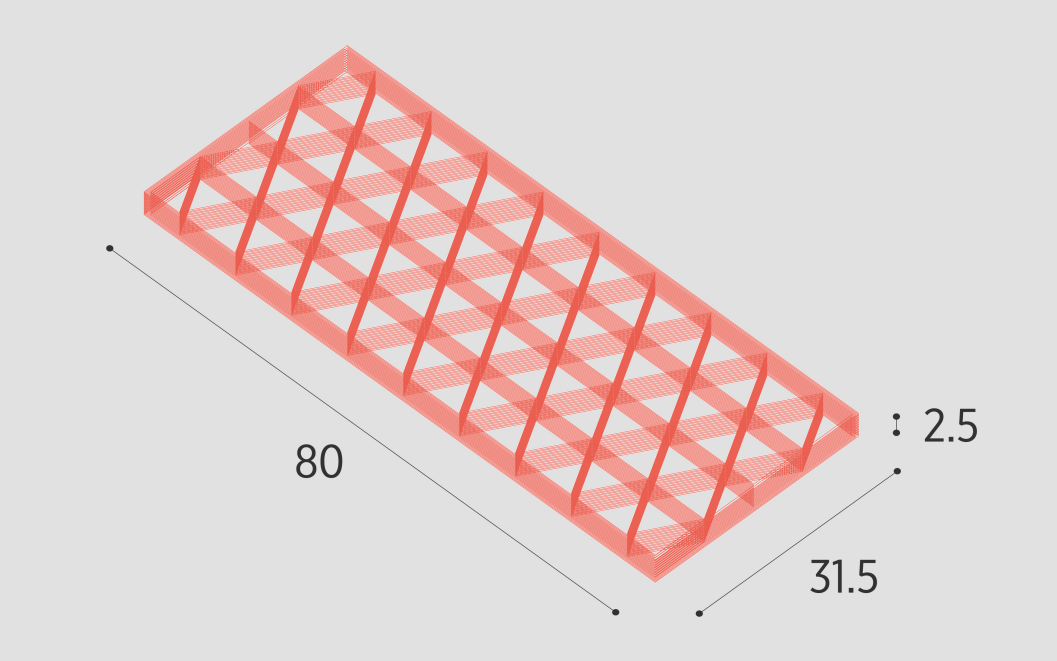

Figure 2.3.19 3D model of the lightweight cellular specimen.

After the UV exposure during the printing process (≈ 30 min/sample), the thermal curing was provided in the same way used previously.

The actual thickness and width of the section (narrowest area for the dumbbell specimens) of the samples were measured with a caliber. For each specimen, the measurements were taken at three different points: at the center and at the ends of the narrow area; then the values were averaged. Moreover, in order to facilitate the mounting of the specimens on the testing machine, the gripping

and gauge lengths were marked on each specimen, as shown in the following image (*Figure 2.3.20)*, where all the prepared samples (casted and UV-printed) were shown.

For each RDFO type, at least five specimens were tested; in case of cellular specimens three.

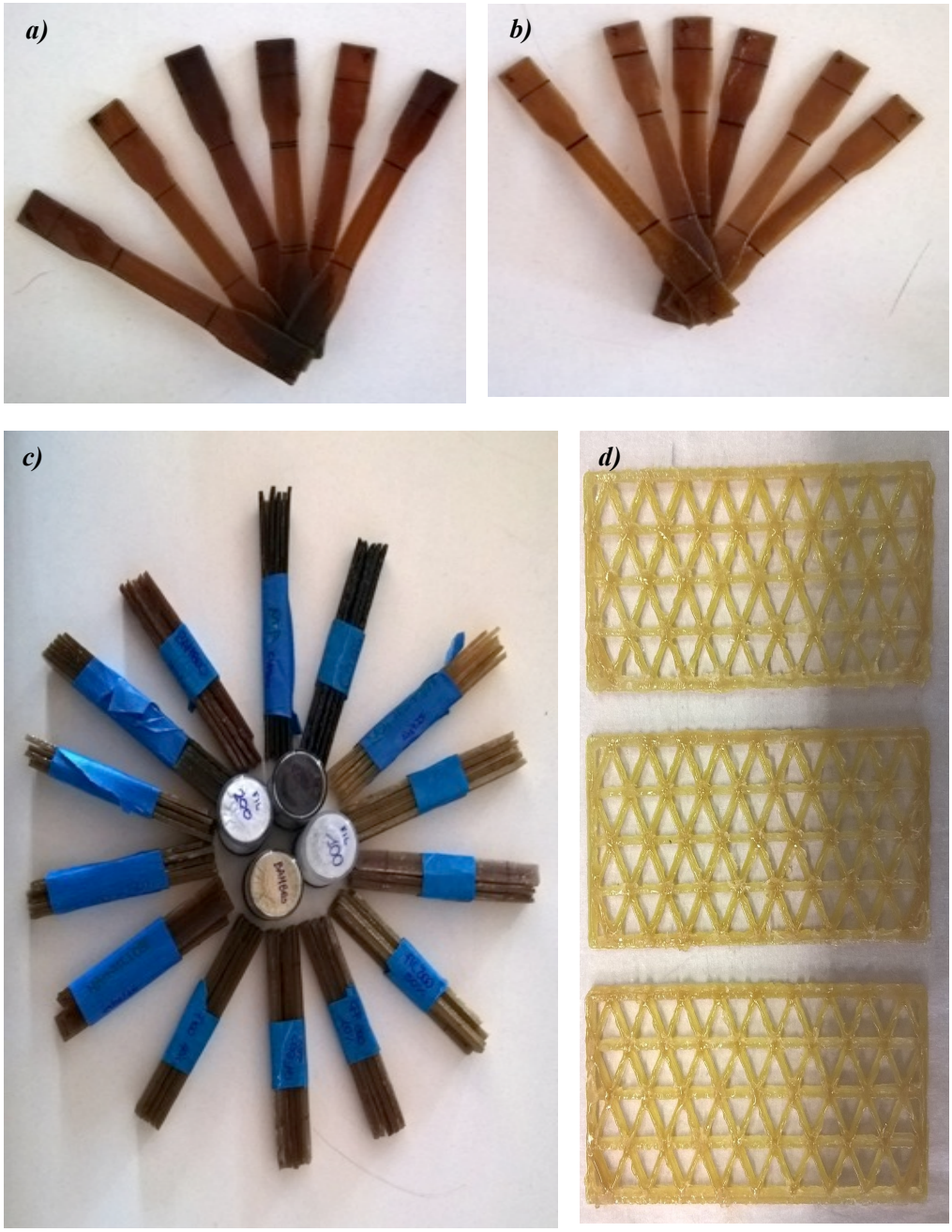

Figure 2.3.20 Specimens prepared for tensile test: a) casted pt-ES3MA dumbbell samples; b) casted pt-ES3MAOX200-11 dumbbell samples; c) RDFO (100% infill) UV-3D printed sample made of pt-ES3MAOX200-11 and SFR-composites; d) Lightweight cellular UV-3D printed samples made of FILL100-25 composite ink.

2.3.5 Morphology investigation

Optical microscopy (OM) was employed to analyze the morphological features of the SFR-composites filaments outgoing from the syringe and of the fractured surfaces of the tensile tested samples with the aim of investigate the effects of shear-induced filler alignment.

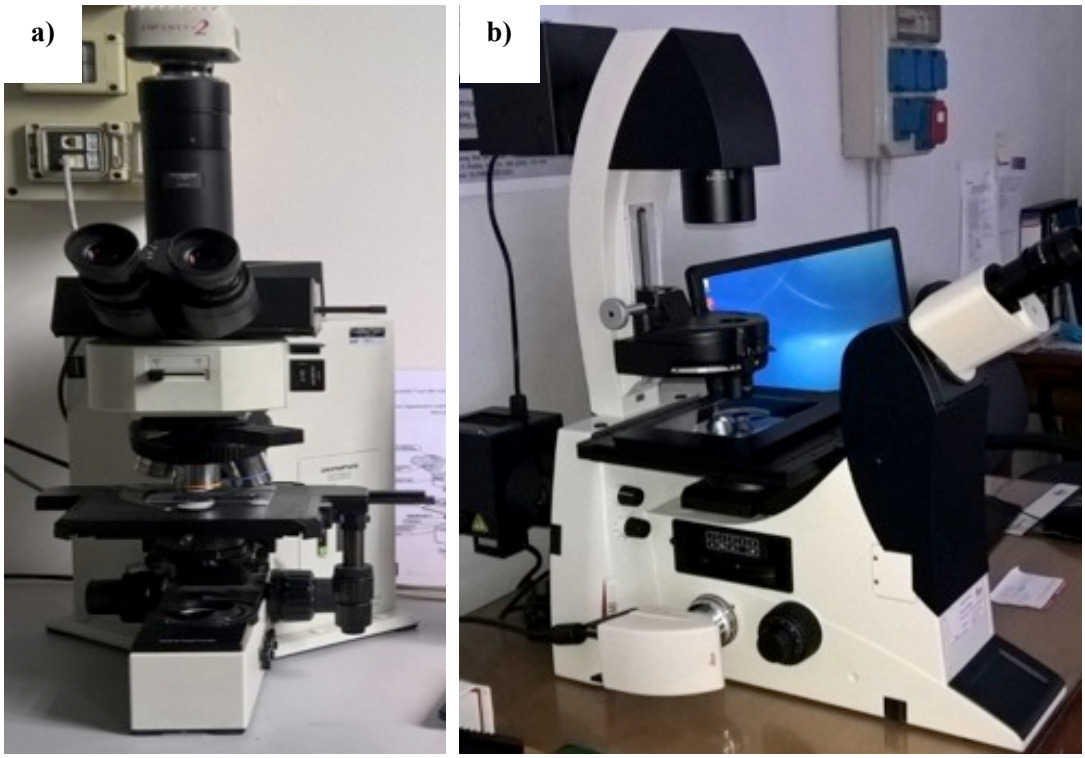

Figure 2.3.21 Optical microscope used for the morphological investigation: a) Olympus BX-60 microscope; b) Leica DMI 3000

Two instruments were used for the analyses: an Olympus BX-60 reflected-light optical microscope (*Figure 2.3.21 (a)*) with dark-fiel and bright-field imaging equipped with an Infinity 2 digital camera for the acquisition of the images, and a Leica DMI 3000 optical microscope (*Figure 2.3.21 (b)*).

In order to capture the finest details, samples were observed at different magnifications: 50x, 100x, 200x, 500x, 1000x.

Section 3. RESULTS AND DISCUSSION

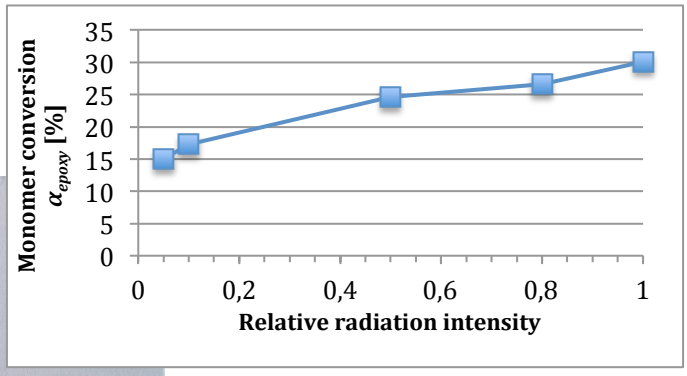

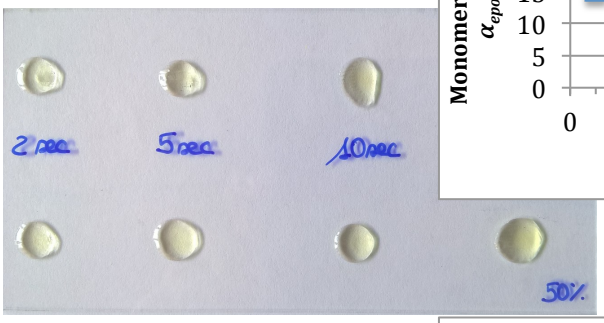





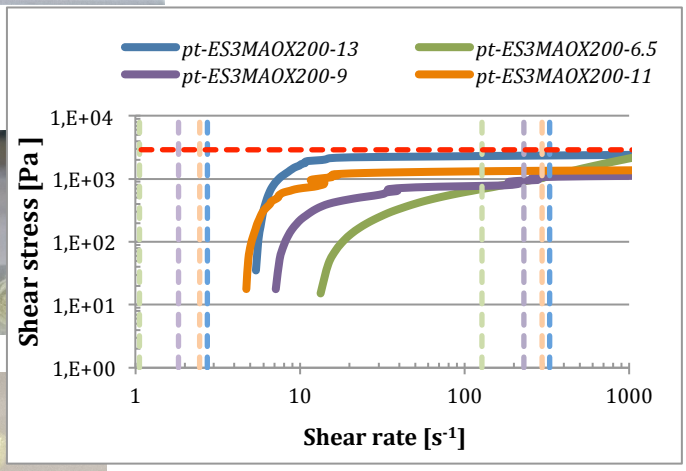



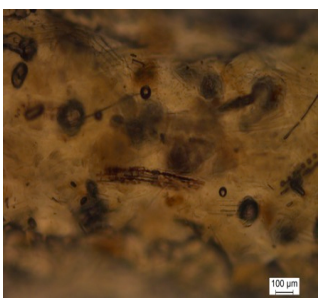

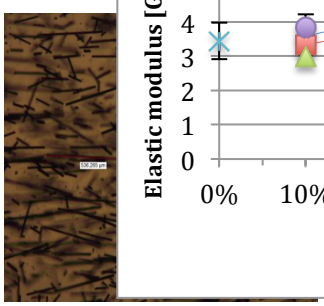

3.1 Polymer Composites Formulation

3.1.1 Polymer for UV-curing

It is known that cycloaliphatic diepoxides and divinyl ethers based systems have a rapid polymerization in presence of strong cationic initiators, such as the onium salts, which have been developed as the most reactive photoinitiators that undergo photolysis in presence of UV light to form efficient cationic species.

Since in most manufacturing processes the conversion rate is one of the most important features as it strongly affects the efficiency and productivity, several photopolymerization studies for vinyl ethers and cycloepoxides have been conducted [78]–[80], [92]–[95].

Although the nature of the UV process allows by itself the cure to occur very fast, the nature of the materials in terms of chemical reactive groups and the curing conditions such as initiator concentration, UV intensity and exposure time are not less important as well. For this purpose, in this experimental work, several analyses were performed to study the effects of different conditions on UV-curable cationic epoxy and divinyl ether based formulations. As explained in the previous section (*Section 2, § 2.1.2.1*), different cationic formulations were prepared with two resins (*ARALDITE CY 179 BD* and *TEGDVE*) and onium salts (*PI-I* and *PI-S*).

In order to evaluate the effects of the chemical structure of the monomers and those of the nature and concentration of the photoinitiator, different methods were adopted.

In the following paragraphs the collected results are reported and discussed.

3.1.1.1 Curing process investigation

First of all the photo-reactivity of the cationic formulations was evaluated.

It is known that the rate and extent of polymerization are strongly dependent on the reactivity of the monomer species but mainly on the photolysis reaction efficiency of the onium salts and then, on their absorption capability at a specific range of wavelength. In general, onium photoinitiators are characterized by a more high initiating efficiency for wavelength ranges between 210 and 350 nm. In

this work, in order to check the possibility of absorpion also at longer wavelengths (where the adopted UV sources emit), the UV-vis spectroscopy analysis was performed.

➢ UV-vis spectroscopy

Absorption spectra for the PI-I and PI-S (0.001% vol in acetonitrile) were acquired and shown in the graph below (*Graph 3.1.1*)

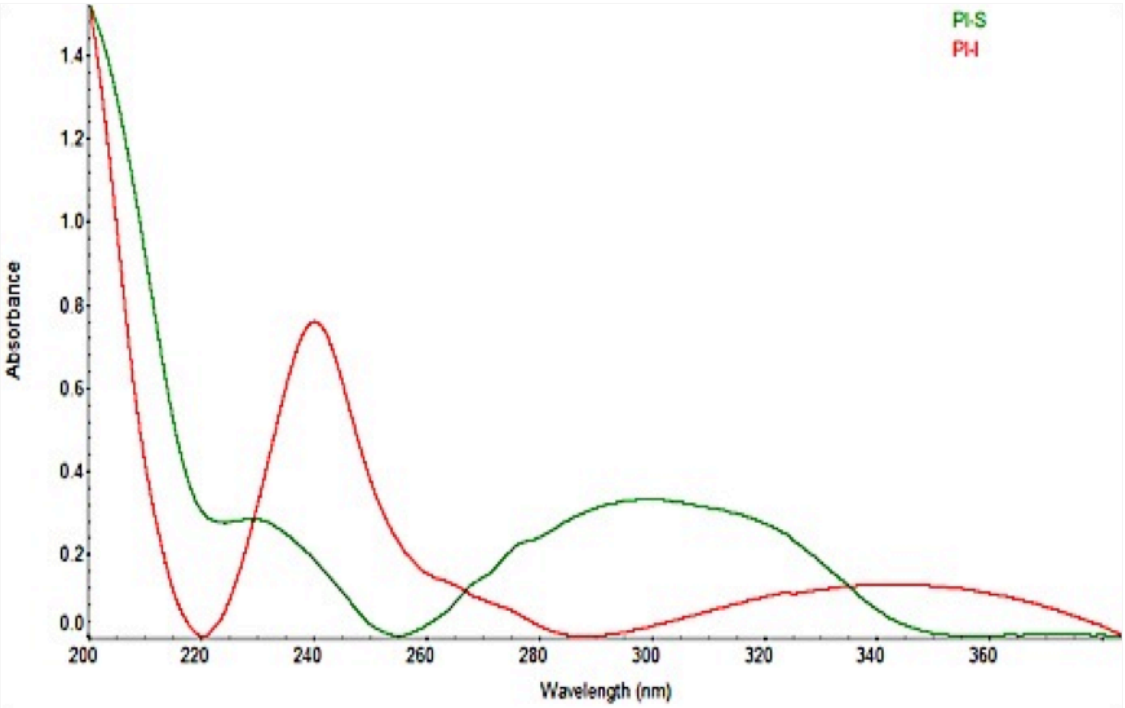

Graph 3.1.1 UV-vis absorption spectra of the photoinitiators used for the cationic UV-curing formulations: sulfonium salt (PI-S) and iodonium salt (PI-I).

PI-I absorbs in the range 200-360 nm region with a maximun around 240 nm, but not above 360 nm, while PI-S absorbs strongly below 350 nm and it exhibits no absorption above this wavelength, in the tail of the spectrum.

As previously explained, in order to have an effective photolysis of the initiators, it is required that the emission spectrum of the light source overlaps at least in part the absorption spectrum of the selected initiator.

Knowing that the available mercury lamps (*§ 2.3.1*) emit much of their radiation above 350 nm, none of the two initiators seemed to be suitable for the formulation of an efficient photocurable compound.

To overcome this problem of poor absorption at the characteristic emmision band of the available mercury lamps, the literature suggest the use of photo-sensitizers to expand the spectral region of the onium salts over longer wavelengths [80], [95].
However, this option has not been taken into consideration because the use of photo-sensitizers in photo-induced polymerization could have the disadvantage of making the formulation carcinogenic, due to the presence of paired benzene rings, characteristics of the chemical structures of the sensitizers.
For this reason, it was decided to continue to develope photocurable compounds using only photoinitiators, trying to exploit even only a small overlap of the absorption-emmision bands above 350 nm.

- **"Drop on glass" test**

For a first qualitative evaluation of the real reactivity of the formulations based on both the epoxy and vinyl ether resin, the "drop on glass" test was performed. Taking inspiration from the literature [79], four solutions with 3% wt of photoinitiator were initially formulated and tested: *p-EI3, p-ES3, p-DVEI3, p-DVES3*.
As previously described (*§ 2.3.2.*4), some drops of liquid solution were deposited on glass slides and irradiated with UV light from the UV Lamp 4, for increasing time intervals.
The evaluation of the solution photo-reactivity was carried out by touching the drop with a metal tip to feel its consistency: the start of the polymerization was identified with the appearance of the first semisolid drop.
The resulting images of the drops are collected in the following table, (*Table 3.1.1*).

p-EI3	p-ES3	p-DVEI3	p-DVES3
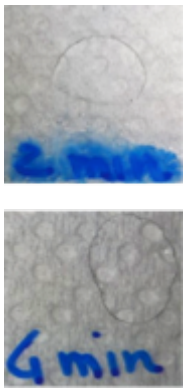	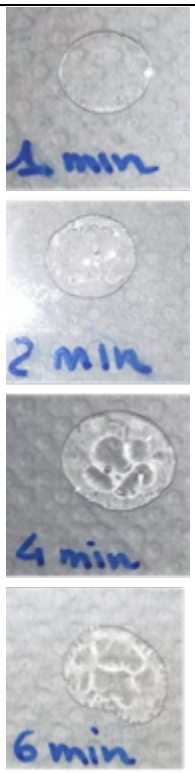	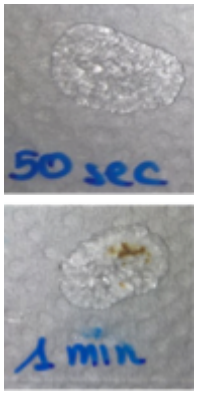	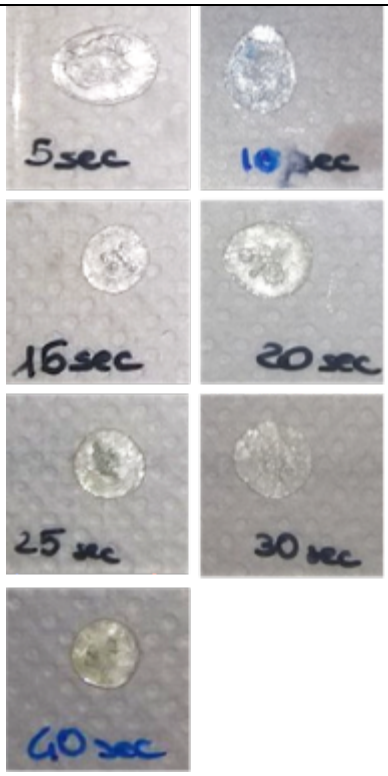

Table 3.1.1 Drops resulting from the "drop on glass" test. Each drop was irradiated with UV-light using theUV Lamp 4.

Looking at the drops, it's clear that for both resins, the formulations containing sulfonium initiator began to harden in a shorter time than those with iodonium. Such behavior was in agreement with the UV-vis spectra above (*Graph 3.1.1*), where the iodonium showed a greater absorption band at much lower wavelengths than those of the emission of the lamp. It is also evident that the two resins responded to the light stimulus at different times: the epoxy system, which started to polymerize only after a couple of minutes of exposure, resulted to have a lower photo-reactivity compared to the divinyl ether one which began to harden for exposure times smaller than one minute.

In particular, the *p-DVEI3* system showed a strange behavior: the polymerization did not start before 50 min of exposure but, once the process had begun, it turn out to be very fast that it took only 10 seconds longer to see the first burned spots.

On the basis of these results it was decided to further investigate the efficiency of the two different monomers by carrying out the photo-calorimetric analysis in order to quantitatively determine the heat of reaction for each composition.

➢ Photo-DSC analysis

The graph below (*Graph 3.1.2)* represents the photo-DSC exotherms for photo-polymeriation of the four formulations.

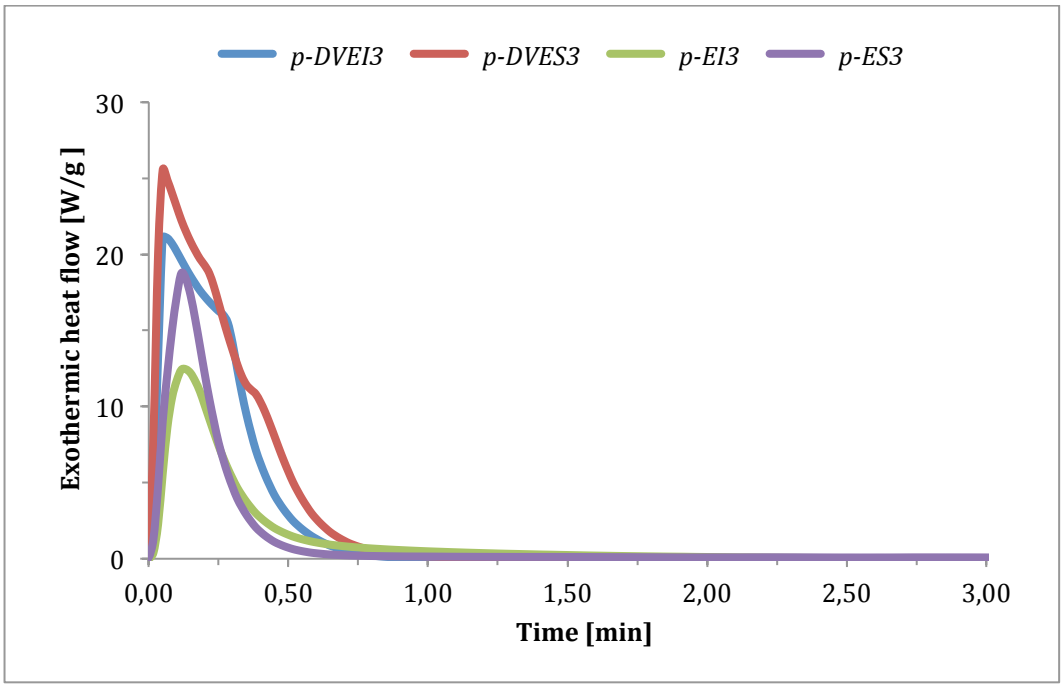

Graph 3.1.2 Photo-DSC exotherms for the photo-polymerization of p-EI3, p-ES3, p-DVEI3 and p-DVES3 solutions at 25°C. time of exposure 3 min, light intensity percentage 100%.

For all the solutions, curing seems to start immediately upon exposure to UV light (UV source: LC8 lamp), resulting in a peak followed by a drop. The process appeared to be completed within 50 sec.

	Maximun peak [s]	***ΔH_{exo} [J/g]***
p-DVEI3	3	405.17
p-DVES3	3	498.27
p-EI3	8	209.51
p-ES3	5	225.81

Table 3.1.2 p-DSC analysis results for the photopolymeriation of the p-EI3, p-ES3, p-DVEI3 and p-DVES3 solution. The data derive from the elaboration of the exotherm curves shown in the graph 3.1.2.

As seen from the "drop on glass" test results, even DSC analysis confirmed that the mixtures based on TEGDVE was more reactive than the epoxy one. Indeed, in the graph above, the growth towards the peak of *p-DVEI3* and *p-DVES3* (blue and red lines, respectively) is much more rapid compared to that of *p-EI3* and *p-ES3* (green and purple lines, respectively).
The time necessary to reach the maximun peak and the amount of heat of polymerization ΔH_{exo}, derived from the integration of the area under the heat flow curve, are reported in the table above (*Table 3.1.2)*.

Assuming that the heat produced by the polymerization is proportional to the number of monomer units reacted, the values of ΔH in the above table give further proof of the higher conversion efficiency in the case of TEGDVE based mixtures.

In order to deeper analyze the TEGDVE based systems and try to assess the cause of the appearance of burned spots in the particular case of *p-DVEI* solution, a more detailed analysis was performed. Several photo-DSC were carried out to evaluate at first the effects of the reduction of the photoinitiator concentration and then the influence of radiation intensity and time of UV-exposure.
In the following graphs and tables, all the collected results are reported: the graph and table *3.1.3* represent the results related to the solutions with variable concentration of sulfonium initiator while, the graph and table *3.1.4* are about the variation of iodonium initiator concentrations.

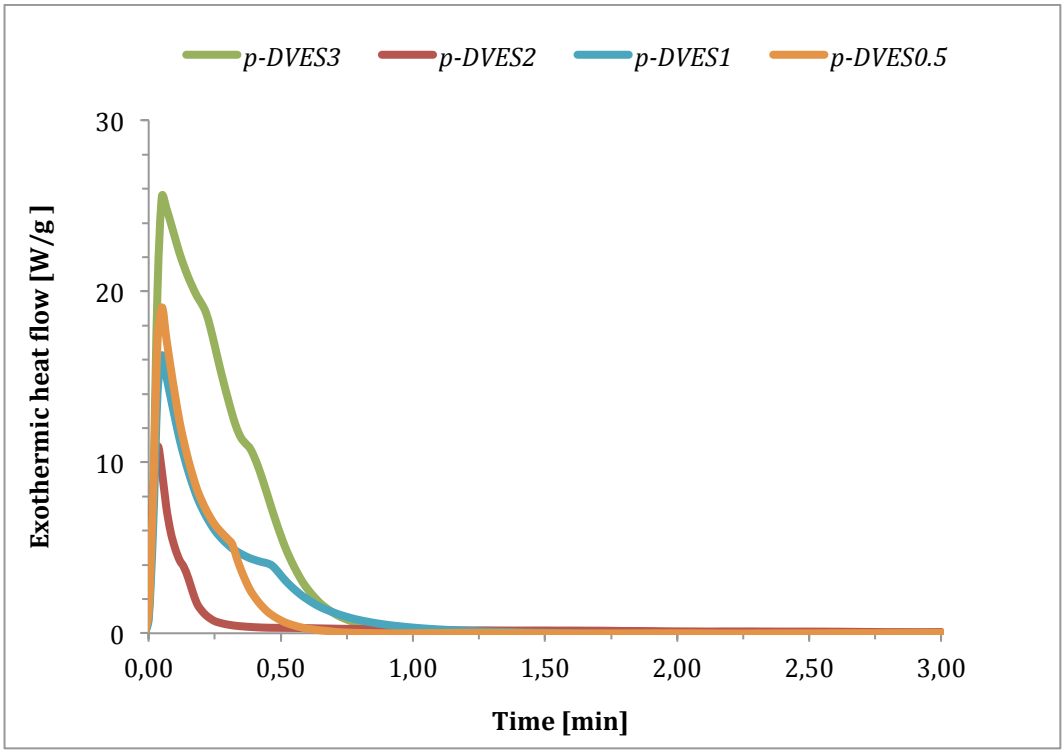

Graph 3.1.3 Photo-DSC exotherms for the photo-polymerization of p-DVES solutions at 3, 2, 1, 0.5% wt of sulfonium initiator. Test conditions: temperature 25°C, time of exposure 3 min, light intensity percentage 100%.

	Maximun peak [s]	***ΔH_{exo} [J/g]***
p-DVES3	3	498.27
p-DVES2	3	75.46
p-DVES1	3	259.66
p-DVES0.5	3	221.48

Table 3.1.3 p-DSC analysis results for the photopolymeriation of the p-DVES solutions at different initiator concentrations: 3, 2, 1, 0.5% wt. The data derive from the elaboration of the exotherms shown in the graph 3.1.3.

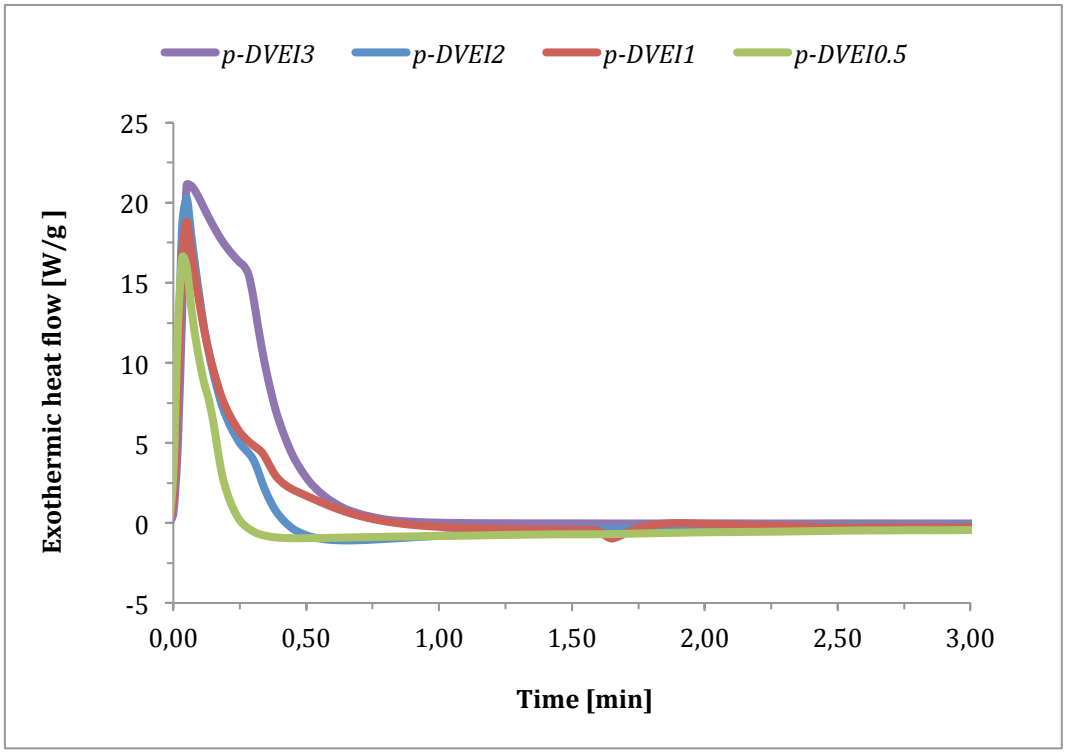

Graph 3.1.4 Photo-DSC exotherms for the photo-polymerization of p-DVEI solutions at 3, 2, 1, 0.5% wt of iodonium initiator. Test conditions: temperature 25°C, time of exposure 3 min, light intensity percentage 100%.

	Maximun peak [s]	***ΔH_{exo} [J/g]***
p-DVEI3	3	405.17
p-DVEI2	3	207.33
p-DVEI1	3	235.30
p-DVEI0.5	2	125.87

Table 3.1.4 p-DSC analysis results for the photopolymeriation of the p-DVEI solutions at different initiator concentrations: 3, 2, 1, 0.5% wt. The data derive from the elaboration of the exotherms shown in the graph 3.1.4.

The results collected from the analysis of both *p-DVES* and *p-DVEI* solutions, whose PI concentrations ranged from 0.5% to 3% by weight, show a reactivity decrease going from higher concentration to lower ones. The specific case of the formulations with 2% wt of photoinitiator had a singular behavior; the heat of reation ΔH of these solutions was lower then that of solutions with both higher (3% wt) and lower (1% wt) initiator concentration. This behavior was very evident mainly in

the case of sulfonium-contained solution, *p-DVES2*, whose ΔH_{exo} (75.46 J/g) resulted the lowest of all the obtained values.

For the *p-DVES* formulations, a thorough p-DSC analysis was then conducted varying test conditions, such as the relative irradiation intensity (from 1 to 0.5) and the time of UV-exposure (from 3 min to 1 min). In order to have a comparison with the behavior of other compositions, the same analysis was performed also on the *p-DVES3* and *p-DVEI1* solution. The obtained results are reported below (*Tables 3.1.5 – 3.1.6*).

	ΔH$_{exo}$ at 100% - 3min [J/g]	***ΔH$_{exo}$ at 100% - 1min [J/g]***
p-DVES3	498.27	373.11
p-DVES2	75.46	495.9
p-DVEI1	235.30	271.59

Table 3.1.5 ΔHexo values resulting from the p-DSC analysis performed at 100% irradiation intensity and varying the time of exposure from 3 to 1 min.

	ΔH$_{exo}$ at 50% - 3min [J/g]	***ΔH$_{exo}$ at 50% - 1min [J/g]***
p-DVES3	492.57	520.69
p-DVES2	509.6	523.98
p-DVEI1	383.91	412.29

Table 3.1.6 ΔHexo values resulting from the p-DSC analysis performed at 50% irradiation intensity and varying the time of exposure from 3 to 1 min.

Also this time, the collected results show a strange trend. In fact, the heat flows, which generally decreases with lower incident light intensity [80], tended to higher values at halved intensity. Moreover, the time to reach the maximum peak heat flow remained constant to 3 seconds instead of increasing, as it would be expected.

In order to try to explain the strange behavior of these formulations, the crucibles containing the analyzed solutions have been also subjected to a visual inspection. As it can be seen in the figure below (*Figure 3.1.1*), the samples had become very dark, symptom that something had happened

during the photo-polymerization process. In fact, before the p-DSC analysis, the solutions appeared as colorless liquids.

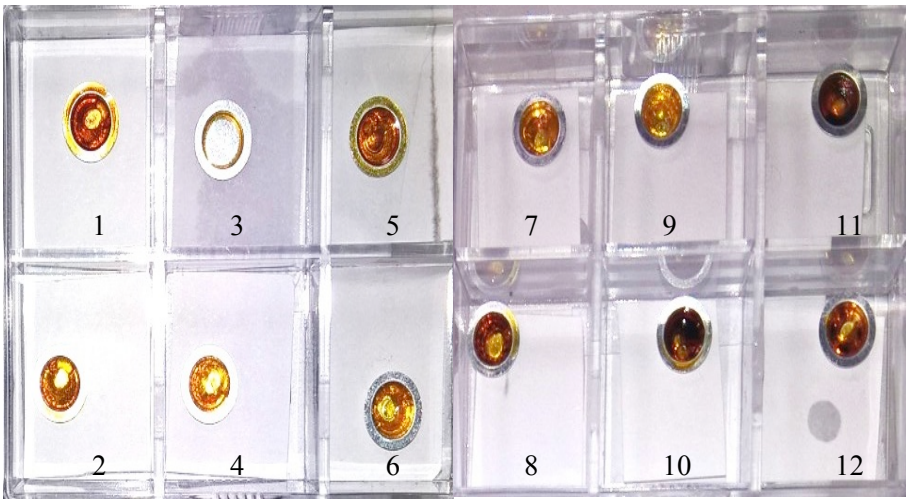

Figure 3.1.1 Aluminium crucible containing the samples, post p-DSC analysis: p-DVES3 solutions (1,4,5,7); p-DVES2 solutions (2,3,6,9); p-DVEI1 solutions (8,10-12). Samples UV-exposed for 3 min at 100% irradiation intensity: 1,3,11. SamplesUV- exposed for 1 min at 100% irradiation intensity: 2,5,8. SamplesUV- exposed for 3 min at 50% irradiation intensity: 4,6,10. SamplesUV- exposed for 1 min at 50% irradiation intensity: 7,9,12.

Further confirmation of the strange behavior stemmed from the fact that all the TEGDVE-based solutions stored (about 48 hours) in the UV-shielded vials, had reacted even without being activated by the UV light. The in-vail contained material seemed to be burnt, as shown in the following figure (*Figure 3.1.2*).



Figure 3.1.2 UV-shielding vial with the reacted materials. In particular this picture shows the p-DVEI solutions with 1% wt and 0,5% wt of photoinitiator.

This fact and the data shown in the tables above were sufficient to adfirm that the TEGDVE based solutions, with an uncontrollable photo-polymerization process, were too unstable to be adopted as basic material for the development of UV-3D printable fiber-composite dispersions.

Following these results, therefore, all further experiments were performed using the epoxy-based solutions (ARALDITE). In particular the study was focused on the use of the sulfonium initiator, which showed the best results (*Graph* and *Table 3.1.2*), at a concentration of 3% wt.

Moreover for this formulation, *p-ES3,* the effect of the variation of the incident light intensity on the extent of polymerization was studied; the p-DSC analyses were perfomed varying the relative intensity from 1 to 0.05.

The collected results are presented in the following graph and table (*Graph 3.1.5, Table 3.1.7*).

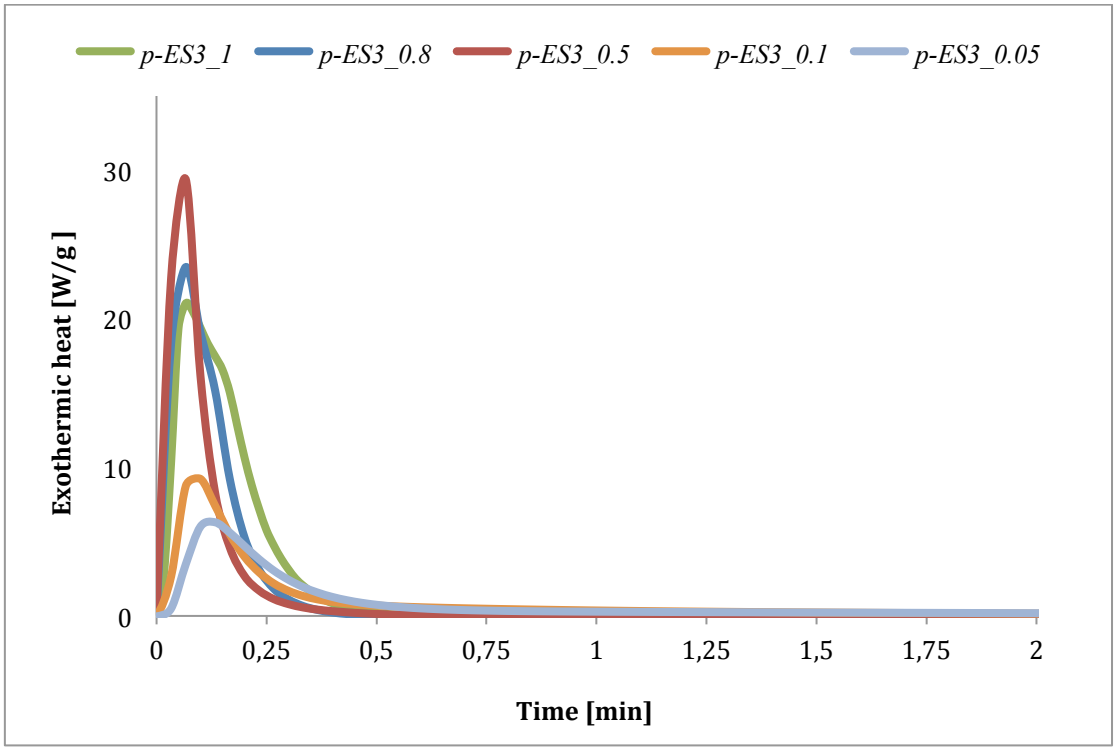

Graph 3.1.5 Photo-DSC exotherms for the photo-polymerization of p-EI3 solution at 25°C at varying relative light intensity from 1 to 0.05.

	Maximun peak [s]	***ΔH_{exo} [J/g]***
p-ES3_1	5	225.81
p-ES3_0.8	4	199.81
p-ES3_0.5	4	184.88
p-ES3_0.1	8	129.43
p-ES3_0.05	8	112.6

Table 3.1.7 p-DSC analysis results for the photopolymeriation of the p-ES3 at varying UV light intensity. The data derive from the elaboration of the exotherm curves shown in the graph 3.15.

Assuming that the monomer conversion of the polymerization reaction, i.e. the extent of polymerization, can be evaluated by the *Eq. 3.1*, the experimental conversion relative to each light intensity was calculated.

$$\alpha_{epoxy} = \frac{\Delta Hexo}{\Delta Ht} * 100 \qquad (3.1)$$

where ΔH_{exo} is the experimental exothermic enthalpy of reaction (J/g) and ΔH_t is the theoretical enthalpy (J/g), taken as reference and calculated using the following relationship, *Eq. 3.2*:

$$\Delta H_t = \frac{\Delta H_{tfunc}}{M} * f \qquad (3.2)$$

in which $\Delta H_{t\,func}$ is the theoretical enthalpy of one reacted function group (J/mol); f is the functionality of the monomer considered and M is its molar mass (g).
For the reaction of the epoxy function group, the $\Delta H_{t\,func}$= 94.47 kJ/mol [4]. Considering f = 2 and M = 252 g, a ΔH_t of 749.76 J/g was obtained.

The next graph (*Graph 3.1.6)* presents the experimental monomer conversion in *p-ES3* compound against relative light intensity.

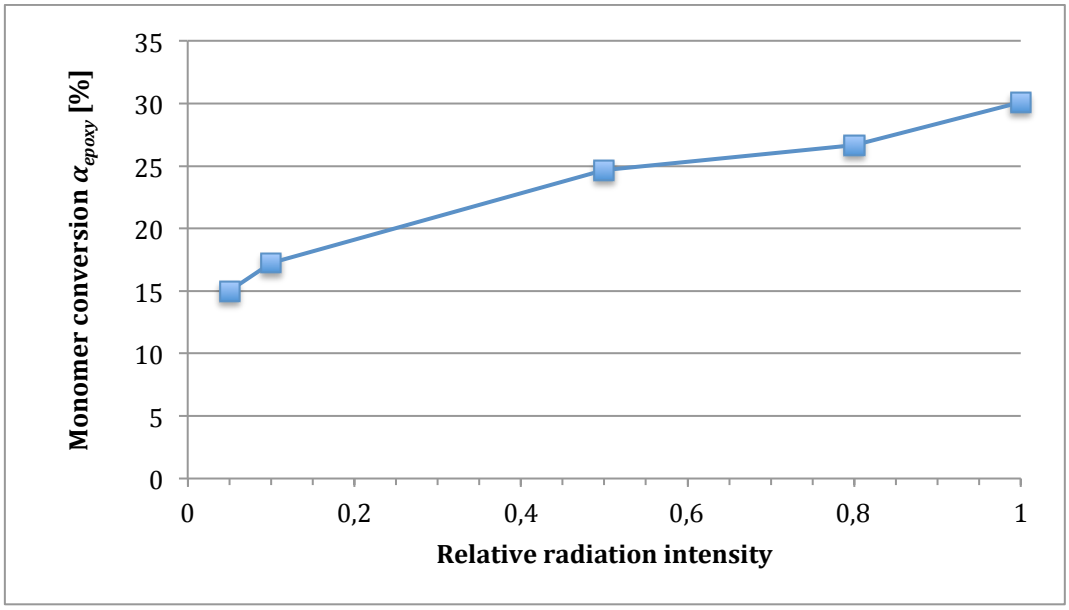

Graph 3.1.6 Epoxy monomer conversion of p-ES3 solution photocured at 25°C with various relative intensities. The corresponding ΔHexo are listed in Table 3.1.7.

From *Graph 3.1.6,* it can be seen that, higher it is the relative intensity greater is the degree of epoxy monomer conversion, up to a maximum of 30% (for intensity of UV-radiation set at the maximum available).

The *p-ES3* curing process investigation continued with the evaluation of the experimental crosslinking conversion, $\alpha_{\%}$, against the time of UV-exposure.
As explained in the previous section (§ *2.2.3.2*), it was determinated using the p-DSC, through *Eq. 2.2*, by comparing the residual heat of reaction ΔH_{res} of samples pre-exposed to 80% UV-light intensity (LC8 lamp at 1300 mW/cm^2), for different time intervals, to the total measured heat of reaction ΔH_{tot}.
The obtained results are plotted in the *Graph 3.1.7,* where it is possible to see that the *p-ES3* system approached the maximun possible crosslinking conversion in a very short time interval; only 1 second of exposure was sufficient to reach 90% of crosslinking process, which was completed within 5 seconds.

.

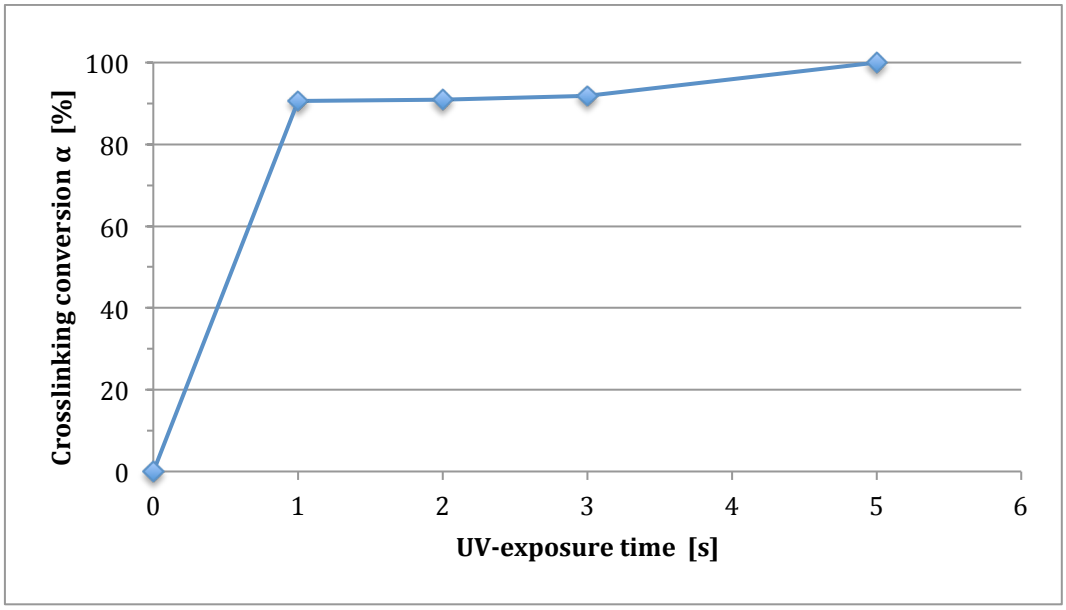

Graph 3.1.7 Crosslinking conversion percentage against time of UV exposure. The samples used for the photocalorimetric analysis were irradiated at light intensity of 1300mW/cm^2.

On the basis of the results obtained so far, a UV source capable to provide at least the same energy of that generated by the p-DSC lamp at 80% (about 1300 mW/cm^2), was chosen to be assembled on the UV-3D printer (see § *2.2.1.2*). This UV source was also used in the irradiation phase of the samples prepared for the FTIR analysis.

➢ FTIR spectroscopy

FTIR spectroscopy was performed in order to evaluate the instantaneous response of *p-ES3* solution to the specific UV-light, at which it would be subjected during the 3D printing process, and to study the dark-curing reaction, a distinctive feature of the cationic formulations, whose photopolymerization can continue also after the end of irradiation time.

The mechanism of the epoxides cationic photo-polymerization is schematically shown in *Figure 3.1.3*. The reaction starts with the UV-initiation step in which the photoinitiator, (*PI-S* in our case), after photolysis reaction, induces a polarization of the oxirane group making the oxygen atom of the epoxy group on the monomer susceptible to nucleophilic attack from another protonated monomer.

The ionic polymerization is thus UV-initiated and the homopolymerization reaction of the cycloaliphatic epoxy can continue also after UV-irradiation because the two propagating polymer cations cannot interact to undergo coupling or disproportionation, as generally occur for the radical acrylate systems.

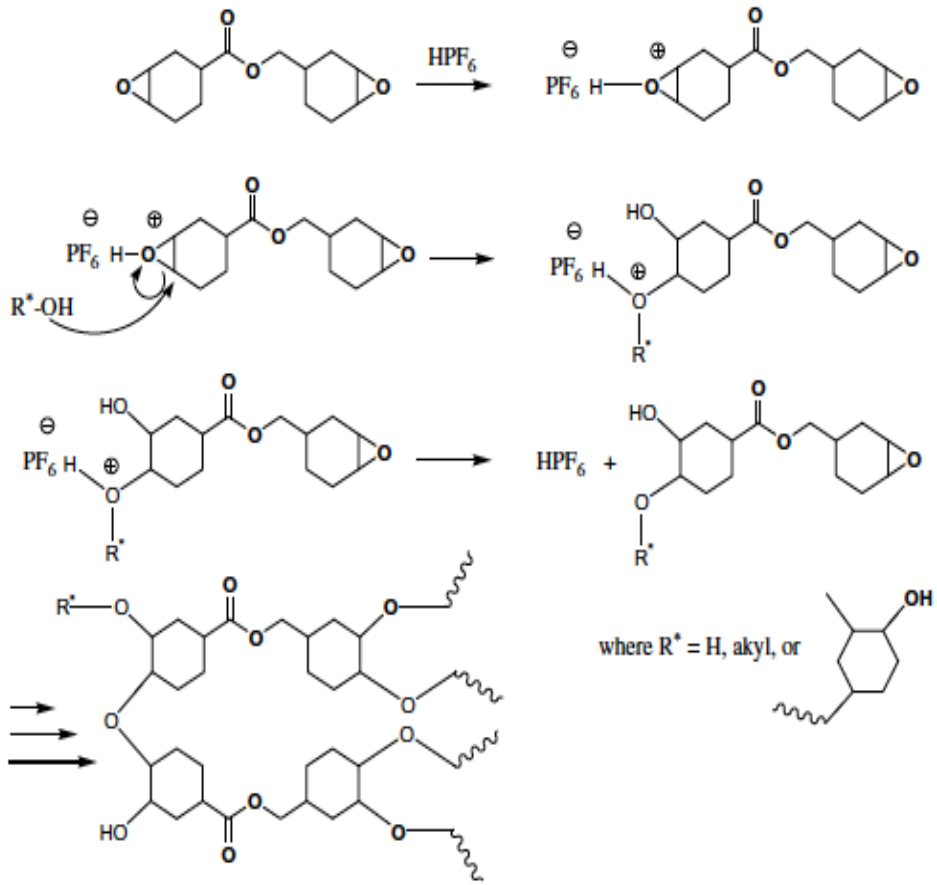

Figure 3.1.3 Photolytically initiated crosslinking reaction of the cycloaliphatic diepoxide [79].

Thus, the "living" epoxy polymer chain will continue to grow in the dark until termination occurs by transfer reaction or bimolecular interaction with another species present in the mixture, e.g other component of the polymer chain or water (moisture is the worst enemy for cationic formulations). The occurrence of this dark-curing phenomenum can be monitored by following the progressive decrease of the cycloaliphatic epoxy absorption bands.

For this purpose, several spectra of samples irradiated for different time intervals (1 sec and 15 sec) were acquired in dark. In particular, for the 15sec UV-cured sample, spectra after a thermal treatment at 180° C for 2 hours were also collected.

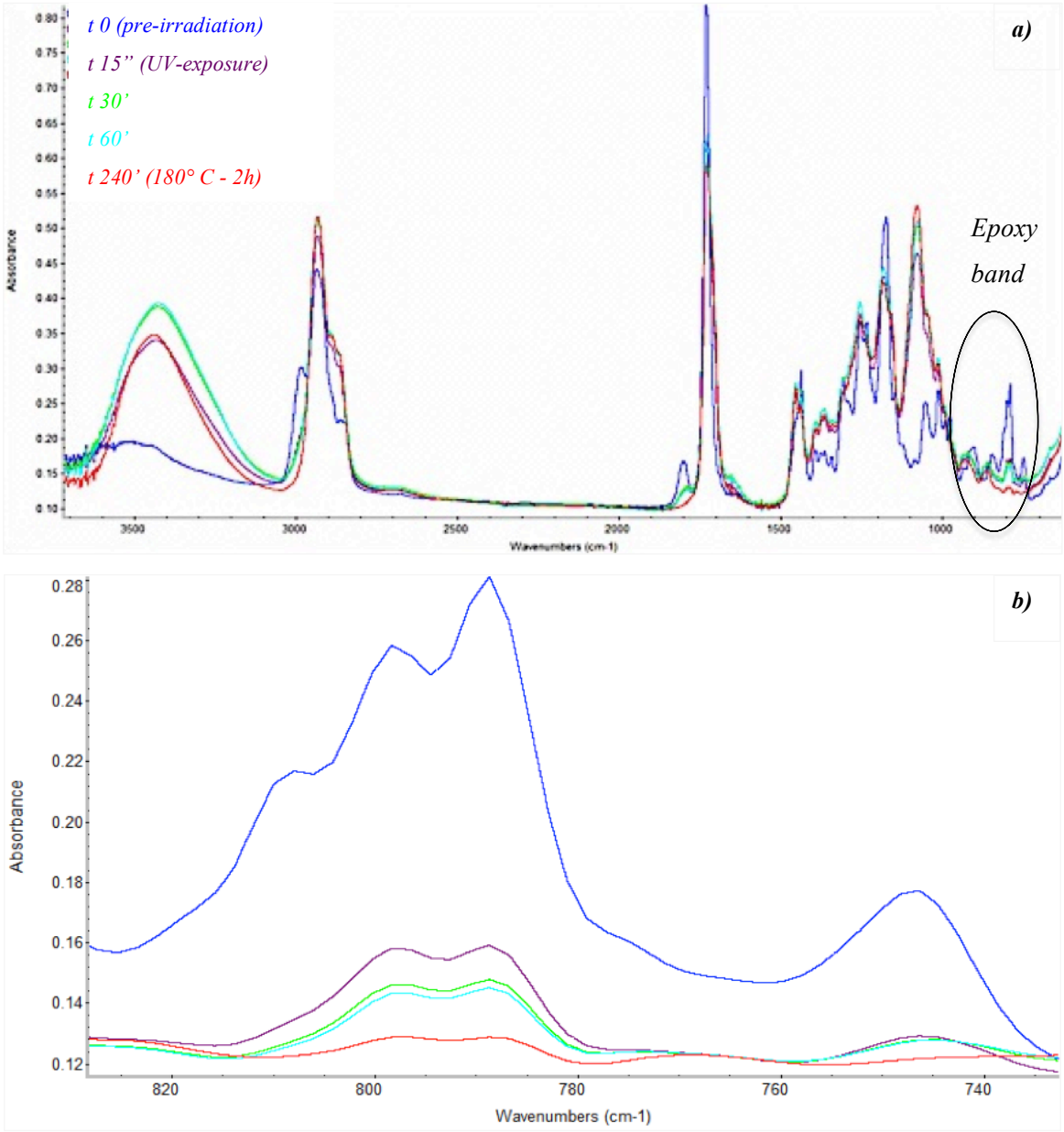

Graph 3.1.8 FTIR analysis: a) Sspectra of p-ES3 pre-irradiation (blue), after UV exposure for 15 sec (purple) and in dark (green and light blue). The spectrum after a thermal treatment is also reported (red). b) Magnification of the epoxy band.

Graph *3.1.8* compares the FTIR spectra of the *p-ES3* compound before (blue spectrum) and after 15 sec UV-irradiaton (purple spectrum), presenting also the spectra acquired in dark (light blue and green spectrum). The red spectrum in the above graph was acquired after the thermal treatment.

As the photo-polymerization of the cycloaliphatic epoxy proceeds, the intensity of the characteristic absorption bands for the epoxy ring at 788 cm^{-1} and 746 cm^{-1} decreases while the characteristic band in the region of 1150 – 1000 cm^{-1} increases from the polymerized polyether structure (see polymerization

scheme in *Figure 3.1.3*). An increase of the intencity of the band around 3450 cm^{-1} (from the stretch of the hydroxyl groups formed during the ring-opening reaction) is also noticeable.
The most evident change can be noted between the FTIR spectra of the uncured solution and post-irradiation (UV-curing); changes between the spectra acquired in the dark-curing period are relatively small, but it can be easily seen, in the particular of the graph above, that the absorption band at 788 cm^{-1} decreases while the band of C−O group around 1080 cm^{-1} increases with reaction time.

In order to quantify the dark-curing and thermal treatment effects, the epoxy conversion was calculated according to the *Eq. 2.3,* by monitoring the progressive decrease of the cycloaliphatic epoxy absorption bands at 788 cm^{-1}.

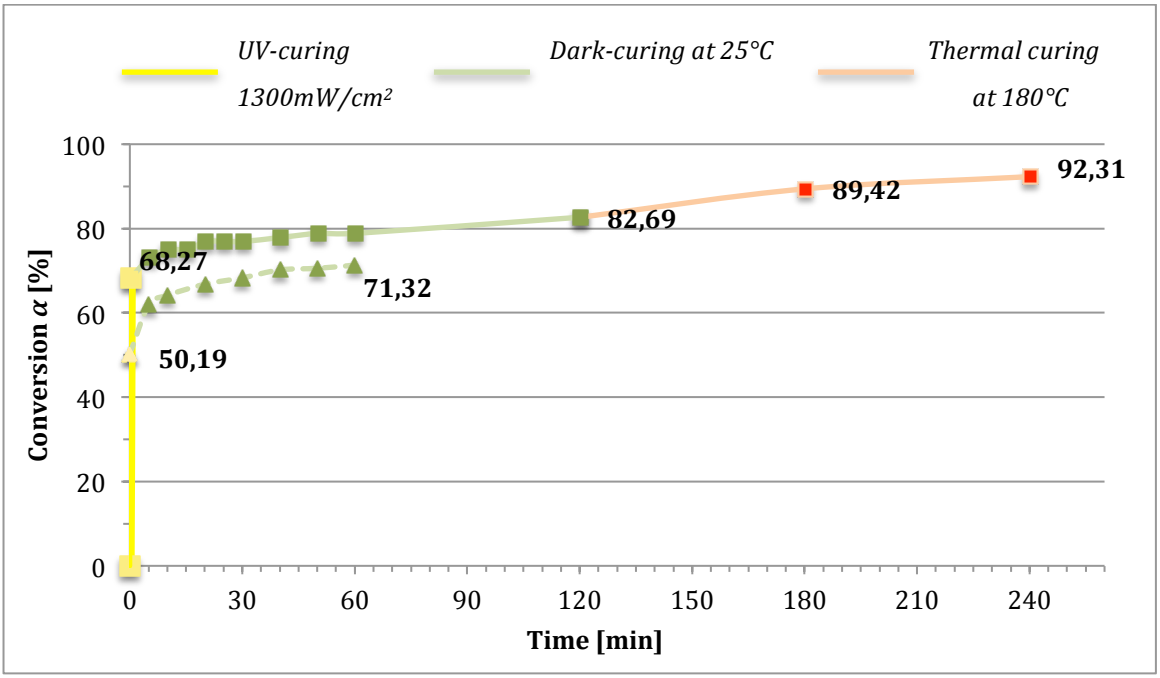

Graph 3.1.9 Conversion determined by the evaluation of the FTIR spectra. Squares-continuous line: irradiation for 15 sec (yellow), dark curing for 2h (green), thermal treatment for 2h (orange). Triangles-dashed line: irradiation for 1 sec (yellow), dark curing for 1h (green).

Graph *3.1.9* showes the conversion percentage versus time for the epoxy monomer during the three stages of polymerization: UV-curing (LC-L1V3 laser at 1300 mW/cm^2), dark-curing (at 25° C), thermal-curing (180° C in a ventilated oven).
It can be noted that the UV-curing stage was the most efficient: more than half of the monomers were converted; in fact, $\alpha_{\%}$ reached values higher than 50%. The dark-curing effect was also important, increasing the conversion up to ~70% and ~80% in the case of shorter and longer pre-irradiation,

respectively. Also the thermal treatment resulted efficient in increasing the conversion that, after 2 hours treatment, was stabilized around 90%.

The curing process investigation for *p-ES3* finished with the evaluation of its crosslinking efficiency in case of which it would be used for the preparation of thicker and more realistic pieces. In fact, all the conversion studies presented above, were performed on thin sample with thickness ranging from hundreds of micrometers (thin film for FTIR analyses) up to a few mm (p-DSC samples and drops on glass) but, knowing that the greater efficiency of radiation-material interaction was only in the first layers of material due to an attenuation effect going from outside to inside and, remembering that the ultimate goal of the work was the printing of pieces ranging in size from small to large, the assessment of how much the shielding effect could affect the curing of thick pieces was necessary. For this purpose, the gel percentage measurements on bulk samples were performed.

➢ Gel percentage test

Samples of *p-ES3* were casted using a silicon mould with rectangular shape (80 × 10 × 4 mm^3) and crosslinked under UV-A ligth for 30 min each side. As previously explained (*§ 2.3.2.5*), after being weighed, the crosslinked samples were immersed in acetone for 24 hours and then dried in the oven at 80° C, measuring the weight at regular time intervals, until a final constant value was reached. At this point, by means of the *Eq. 2.4,* the degree of crosslinking, e.g. the gel percentage, was calculated as the ratio between the final weight and that of the crosslinked sample before the immersion.

p-ES3 sample	***W_{in} [g]***	***W_{fin} [g]***	***Gel percentage [%]***
1	1.400	1.046	74.7
2	1.380	1.124	81.4

Table 3.1.8 Gel percentage test results: the initial and final weight of p-ES3 samples are reported with the corresponding calculated gel percentage.

According to the results listed in *Table 3.1.8*, the bulk *p-ES3* had a mean gel fraction of *ca.* 80%. This means that *ca*. 20% of the epoxy monomer remained unreacted, as already found from the FTIR analysis presented above in the *Graph 3.1.9.*

Further confirmation of the incomplete crosslinking conversion was also given by the visual inspection of the samples after the test and by the FTIR analysis of the residual solvent.

As shown in the *Figure 3.1.4*, the sample after the test appeared to be open at the centre; this also confirmed the difficulty of the UV-radiation to activate the inner regions of a thick geometry, as expected.

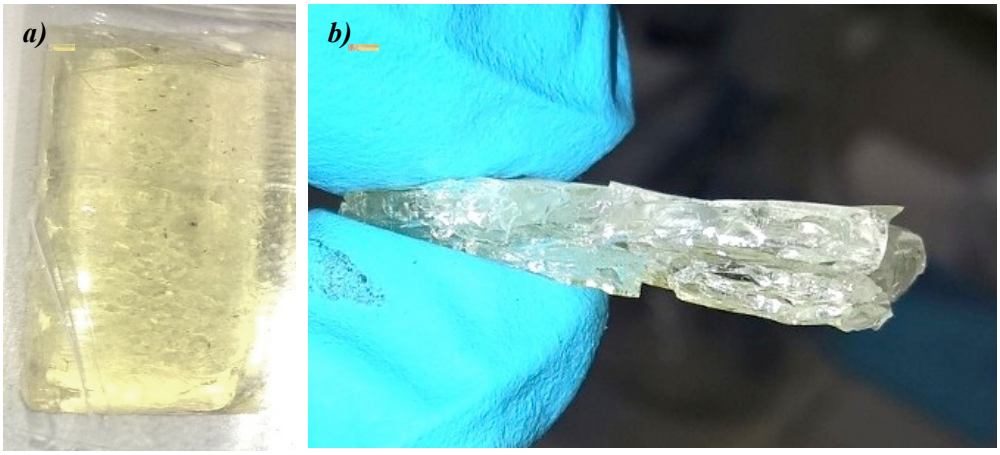

Figure 3.1.4 Particular of a p-ES3 casted sample: a) piece of sample before the gel percentage test; b) sample after the immersion in acetone.

FTIR spectrum of the residual acetone (sample 1), where the characteristic epoxy bands at 788 cm^{-1} and 746 cm^{-1} were easily visible, is shown in the graph below (*Graph 3.1.10*).

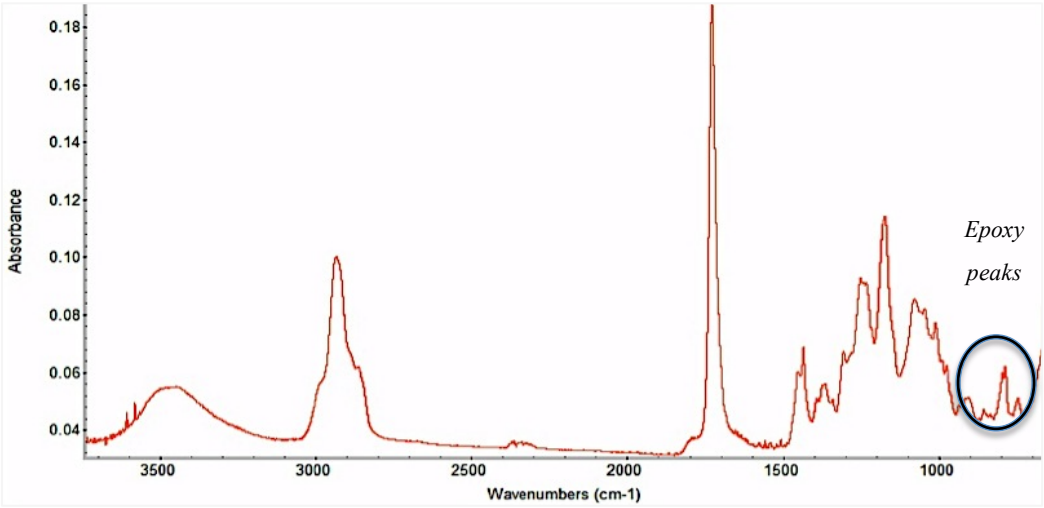

Graph 3.1.10 FTIR spectrum of the residual acetone used for the immersion of p-ES3 casted samples (1) in the gel percentage test.

The evident peaks in the characteristic epoxy regions, confirmed the presence of unreacted epoxy monomer, dissolved in acetone.

This last gel percentage evaluation, allowed to conclude that the complete curing of thick cationic UV-curable object, would be difficult. This inefficiency could be overcome by a post-curing thermal treatment; in fact, as previously seen (*Graph 3.1.9*), an efficient way to increase the monomer conversion has been the thermal treatment at 180°C.

This result and the support of the literature [96]–[102], have led to improve the cationic UV-curable formulation by adding some hardeners in order to complete the polymerization performing a dual-curing. As will be shown in the following paragraphs (*§ 3.1.2*) the dual-curing technique, involving two steps such as UV-irradiation-induced cationic generation followed by thermal-induced polymerization, improved the crosslinking of both the surface and the inner regions.

Before developing the dual-curable formulation, the *p-ES3* UV-curable solution was still processed with the UV-3D printer in order to verify the possibility of producing thick but completely crosslinked objects only by exploiting the layer by layer photo-curing, special feature of the UV-assisted 3D printing process. To this end, the *p-E*S3 solution had to be more viscous (in order to make it printable) and so a rheological investigation was performed.

3.1.1.2 Rheology investigation

Since *p-ES3* formulation presented a too low viscosity to be deposited from the syringe dispenser of the UV-3D printer, a flow viscosity modifying admixture agent was added to the liquid solution.

As explained in the previous section (*§ 2.1.2.4*), four compounds with an amount of fumed silica OX200 ranging from 6.5 % to 13 % by weight were prepared.

In order to investigate the viscosity trend at variable concentrations of fumed silica, a rheological study became necessary. The viscosity of each compound was determined by isothermal plate-plate rheological measurements.

The viscosity results, plotted as a function of shear-rate, are shown in the next graph (*Graph 3.1.11)*, in which also the plot for the unmodified *p-ES3* solution is presented.

This last showed a typical Newtonian behavior, with a constant viscosity for increasing shear-rate: $\eta \approx 0.48$ Pa s in the $1\text{-}2 \cdot 10^2$ s^{-1} shear-rate interval. Instead, all the silica dispersions exhibited a considerable increased viscosity and a typical shear-thinning behavior: the high viscosity decreased with increasing the shear-rate. This increase in viscosity for the silica-incorporated mixtures might be due to a weak network formation due to hydrogen bonds provided by the silica, which caused a gel-

like rheological behavior to the mixture at rest. These networks could be then destroyed under moderate shear force resulting in the reduction of the viscosity.

As shown in the graph below, all the viscosity curves were well fitted with a power-law relationship (black line) according to the following equation, *Eq. 3.3:*

$$\eta = K\dot{\gamma}^{n-1} \qquad (3.3)$$

where *K* is the consistency index and *n* the power-law index.

The first coefficient is useful to give an indication of the viscosity of the formulations at shear-rate of 1 s^{-1}, while the second, related to the slope of the viscosity curves, provides an indication of the shear-thinning character conferred to the pristine resin by the interaction with the filler.

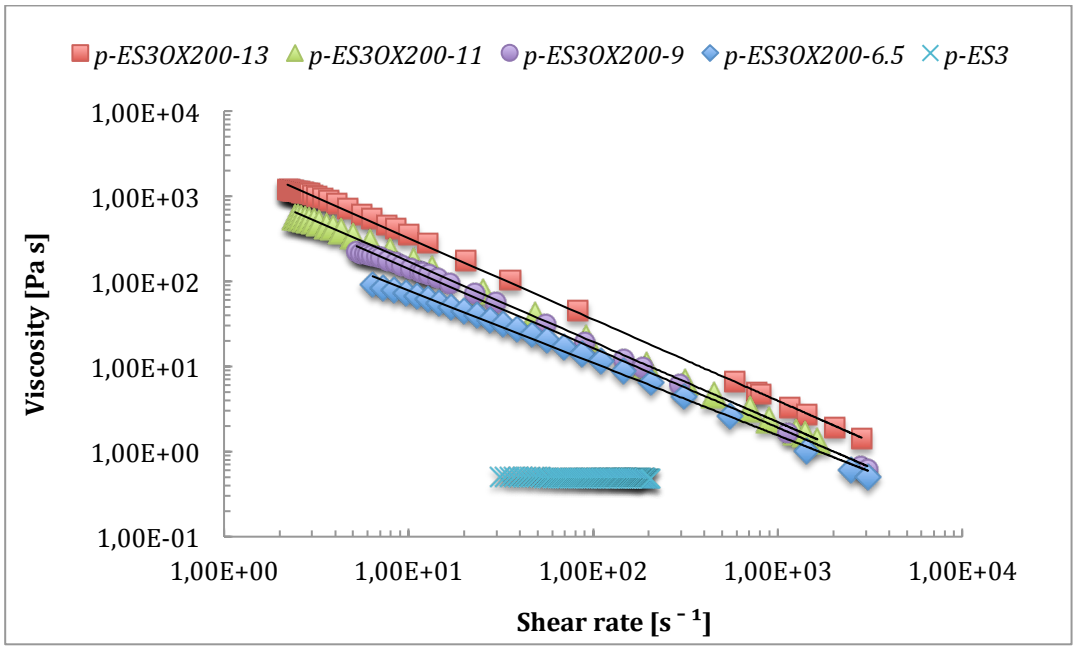

Graph 3.1.11 Viscosity curves of p-ES3OX200 formulations at increasing filler concentrations.

Confirming the shear-thinning behavior, the four formulations presented power-law index n<1. As it can be seen from the values reported in the *Table 3.1.9, n* index tended to increase going from higher to lower filler concentration. This trend can be explained by a weaker resin-silica interaction in less filled systems.

The consistency index *K* shown a strong dependence on the filler concentration; according to the values reported in *Table 3.1.9,* an increase in concentration gave rise to an increase of *K* value. In

particular, a significant increase in K was found when the OX200 concentration increased from 11% wt to 13% wt: adding only a further low amount of silica, the K value was more than doubled.

OX200 concentration wt [%]	***Power-law index n***	***Consistency index K [Pa s^n]***
13	0.044	2915.1
11	0.057	1490.2
9	0.067	1204.9
6.5	0.149	555.13

Table 3.1.9 Power-law index n and consistency index K, relative to the p-ES3OX200 formulations at different silica concentration.

As it will be explained later (*§ 3.2.2*), exactly in this range of concentration, the optimal formulation choice for UV-3D printing was found.

3.1.2 Polymer for Dual-curing

As mentioned above, in order to overcome the problems of incomplete photo-polymerization, the dual-cure technique was adopted. Dual-curable systems were obtained by simply adding a hardener to the stock *p-ES3* solution; the phthalic anhydride and the maleic one were used to prepare the *pt-ES3PA* and the *pt-ES3MA* solutions, respectively.

The amount of anhydride added to the pristine solution has been evaluated on the basis of the results obtained from the gel percentage test (*Table 3.1.8*). In order to be sure to reach a complete monomer conversion, it was decided to add an amount of anhydride such that the 25% by weight of epoxy resin (ARALDITE that before, only with UV-curing, remained uncured), could be thermally polymerized, reacting with the anhydride itself. The exact amount was calculated through the *Eq. 2.1*, as explained in the previous section (*§ 2.1.2.2*).

Also in this case, the photo-thermal response and the rheological behavior of the obtained solutions were investigated. The study began with the analysis of *pt-ES3PA* solution and it continued focusing only on the formulation *pt-ES3MA*, when the first turned out to be unsuitable to work at room temperature, due to the re-precipitation of the phthalic anhydride. In fact, if the vial containing the solution was left at room temperature for more than a couple of hours, on the bottom of it a white precipitate was easily visible. An example is shown in the *Figure 3.1.5*.



Figure 3.1.5 Vial containing the pt-ES3PA solution. The white PA precipitate can be easily seen after leading the solution at room temperature for a couple of hours.

In the paragraphs below only the results about the maleic-containing formulation are reported, while the all the data relative to phthalic-containing solution are provided in the Appendix.

3.1.2.1 Curing process investigation

As in the case of polymers for UV-curing, the reactivity of the dual-cure solution was first investigated by means of the "drop on glass" test and then a more accurate analysis was performed by means of p-DSC/ DSC and FTIR spectroscopy. At the end, in order to verify the real ability of the dual-curing method to bring the monomer conversion to completion, the gel percentage measurements were performed.

- **"Drop on glass" test**

A first qualitative investigation of the photo-reactivity of the dual-cure solution was performed by means of the "drop on glass" test. Some drops of *pt-ES3MA* solution were drop cast on a slide and irradiated with the LC-L1V3 laser at relative intensity of 1 and 0.5, for increasing time intervals: 2 sec, 5 sec, 10 sec, 1 min.

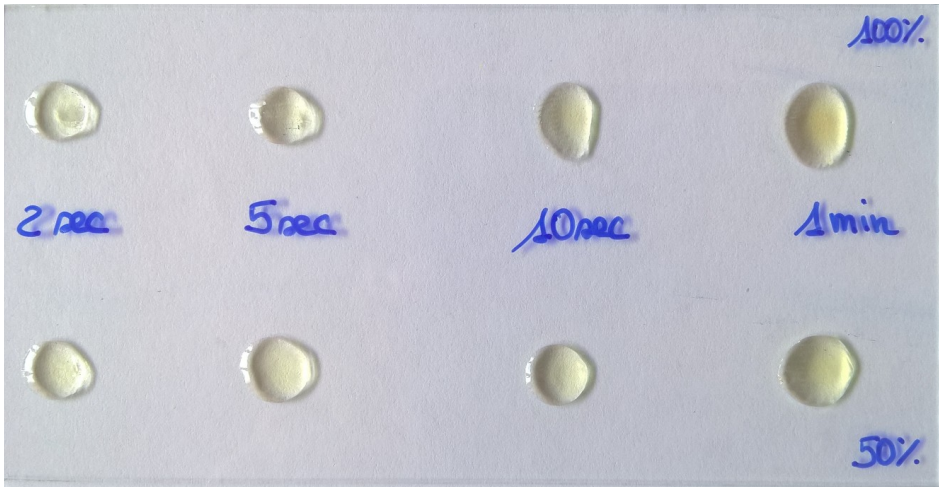

Figure 3.1.6 Drops irradiated with LC-L1V3 laser (relative intensity 1-0.5%) for increasing time intervals.

After irradiation the slide with the drops was put in the oven at 180°C for 1h.
The first qualitative evaluation of the dual-cure process efficiency was obtained by touching each drop with a metal tip before and after the thermal treatment. On the basis of the increase of solidity for all the drops subjected to the post-thermal treatment, it was possible to confirm that the dual-curing was usefull to enhance the conversion efficiency.

➢ Calorimetric analysis: photo-DSC / DSC

A more quantitative characterization of the dual-curing process was performed by measuring the heat of polymerization produced during a first photo-curing and during a post-thermal-curing. In detail, the liquid *pt-ES3MA* solution was subjected to a first isothermal photo-DSC mesaurement (1300mW/cm^2 light intensity, 3min at 25° C) and then, the resulted solid sample was analysed by non-isothermal DSC (-20° C ÷ 250° C, 20° C/min). From both the two scans, exotherms were obtained; the values resulting from their integration, i.e. the heat of polymerization, are reported in the following table (*Table 3.1.10*). This also shown the data related to the dual-cure solution containing 5% wt of ESBO oil plasticizer which, as already explained (*§ 2.1.2.3*), had been added to the *pt-ES3MA* formulation in order to try to decrease its known brittle behavior.

	ΔH_{UV} [J/g]	ΔH_T [J/g]	ΔH_{tot} [J/g]	UV-cure [%]	Thermal-cure [%]	T_g [° C]
pt-ES3MA	116.51	15.8	132.31	88.06	11.94	177.39
pt-ES3MA-ESBO5	106.19	22.69	128.88	82.39	17.61	175.89

Table 3.1.10 Photo-DSC/DSC analysis results of dual-cure solutions: pt-ES3MA, pt-ES3MA-ESBO5.

On the basis of the proportions adopted in the preparation of the mixture, it was expected that only 75% of the polymerization was UV-activated and the remaining 25% would have to react during the thermal cycle. For both formulations, the deviation from what it is expected can be explained by a pre-activation of the thermal process due to a possible heating of the material during the UV-curing step, for the presence of the very energetic UV source. In fact, a temperature increase was registered during the irradiation time and this could be enough to initiate the thermal-polymerization that, for both the solutions (*pt-ES3MA* and *pt-ES3MA*-ESBO5), resulted to start at around 50° C.

DSC analyses were also carried out to identify the glass transition temperature of these formulated materials. The comparison between the T_g of the two materials is particularly important to verify the real effectiveness of the plasticizer in reducing the well-known brittleness of the cationic-epoxy-material. In fact, if the addition of plasticizer to the dual-cure solution had introduced an effective plastic behavior, the T_g of the material would have to decrease. From the data reported in the last column of the previous table (*Table 3.1.10*), the addition of 5% wt of ESBO oil to the pt-ES3MA

solution provide only a slightly decrease in T_g. This, as even confirmed by mechanical tests (results are reported in *Appendix*), means that no plasticizing effect had taken place. For this reason it was decided to abandon the idea of adding a plasticizer and the experimental study has been continued with the dual-cure solution as such.

➢ FTIR spectroscopy

The evaluation of the extent of reaction by means of the FTIR analysis was performed also on the *pt-ES3MA* formulation.

First, in order to identify the characteristic bands of the maleic anhydride, its spectrum was acquired. As shown in the *Graph 3.1.12,* the characteristic peaks of a conjugated five-membered ring anhydride were present: 3310 cm^{-1} (=C−H stretch), 1858 cm^{-1} (C=O in-phase stretch), 1777 cm^{-1} (C=O out-of-phase stretch), 1595 cm^{-1} (C=C stretch), 1060 cm^{-1} (C−O antisymmetric stretch), 899 cm^{-1} (C−O symmetric stretch) and 835 cm^{-1} (H−C=C−H out-of-plane bend).

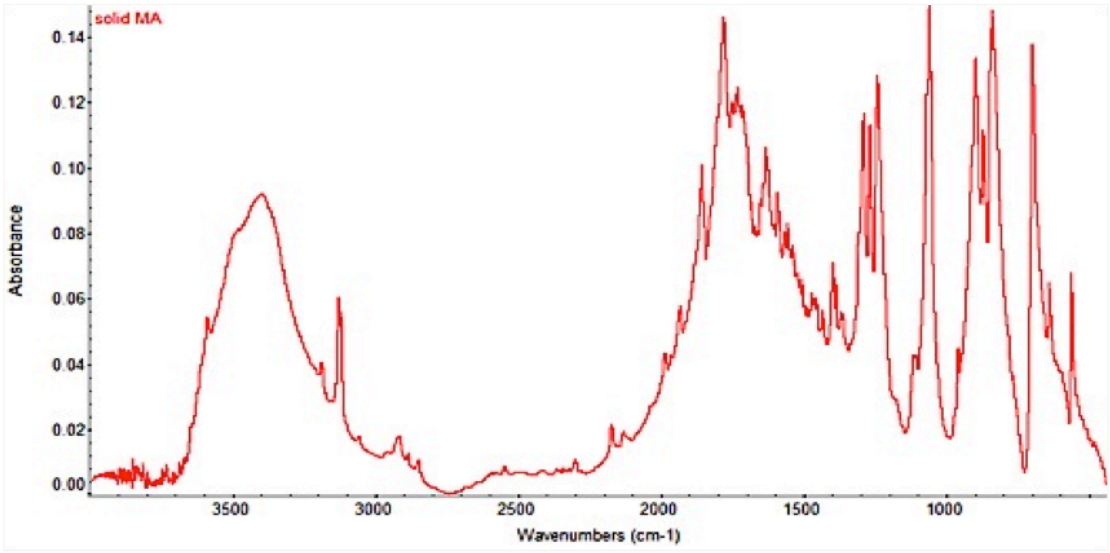

Graph 3.1.12 FTIR spectrum of maleic anhydride.

All the above listed peaks remained well visible also in the *pt-ES3MA* liquid solution spectrum presented in the graph below (*Graph 3.1.13)*, which also reports the spectra acquired during an entire dual-curing cycle: i.e, after the UV-irradiation at 1300mW/cm^2 for 15sec, during the dark-curing at 25° C for 1h and after the final thermal treatment at 180° C for 1h.

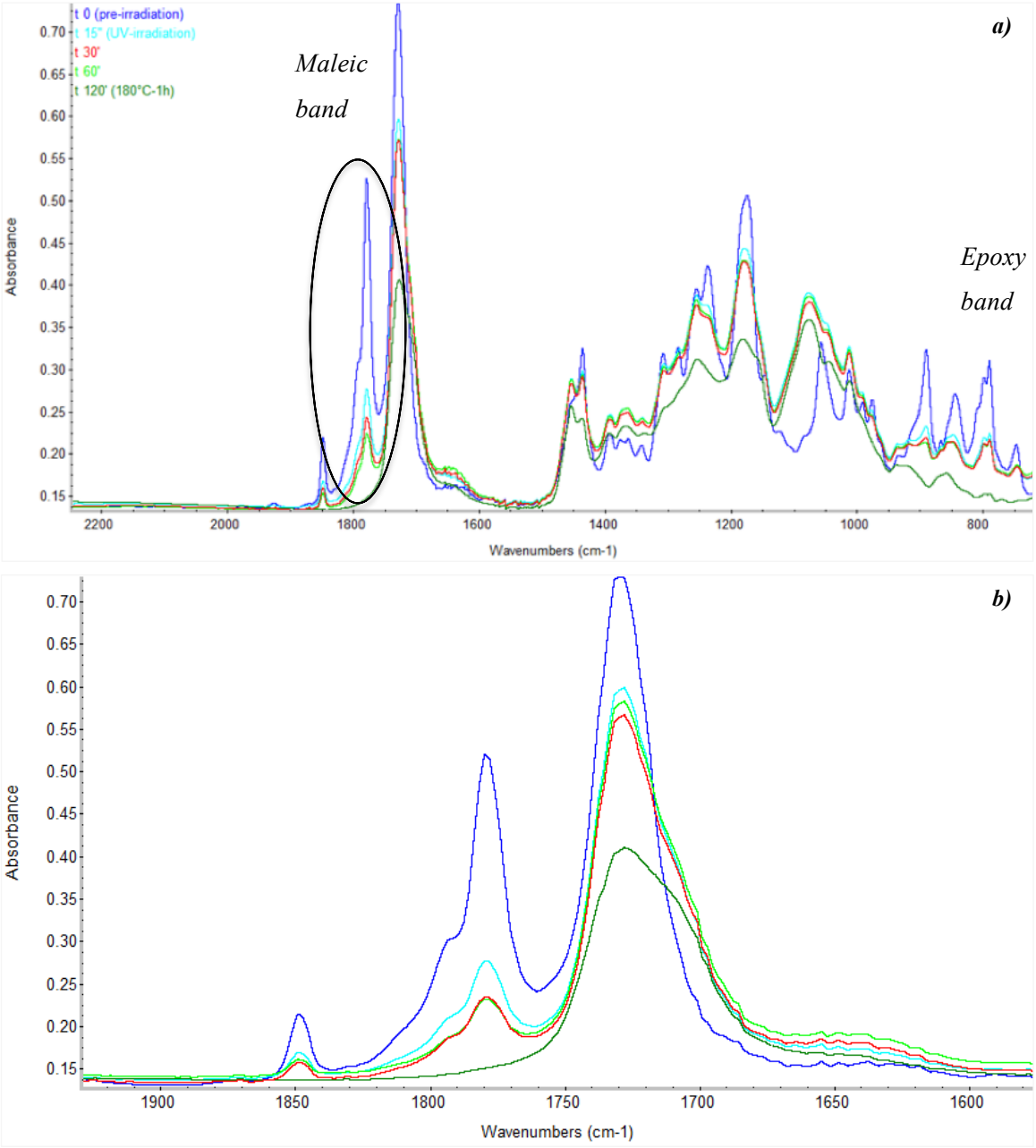

Graph 3.1.13 FTIR analysis: a) Sspectra of pt-ES3MA pre-irradiation (blue), after UV exposure for 15 sec (light blue) and in dark (red and light green). The spectrum after a thermal treatment is also reported (dark green). b) Magnification of the maleic band.

In order to follow the crosslinking reaction, whose thermally activated step is schematically presented in the *Figure 3.1.7*, the characteristic bands of MA at 1858 cm^{-1} and 1777 $cm^{-}1$, together with the epoxy characteristic band at 788 cm^{-1} were mainly considered. As it can be easily see in the graph, during the progressive advance of the reaction, the height of these peaks tended to decrease until the almost complete disappearence.

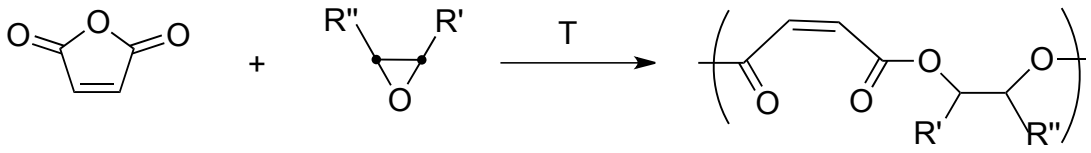

Figure 3.1.7 Scheme of the thermally activated reaction.

The conversion percentage was then calculated by means of the *Eq. 2.3*; the obtained results have been plotted as function of time, as shown below (*Graph 3.1.14*).

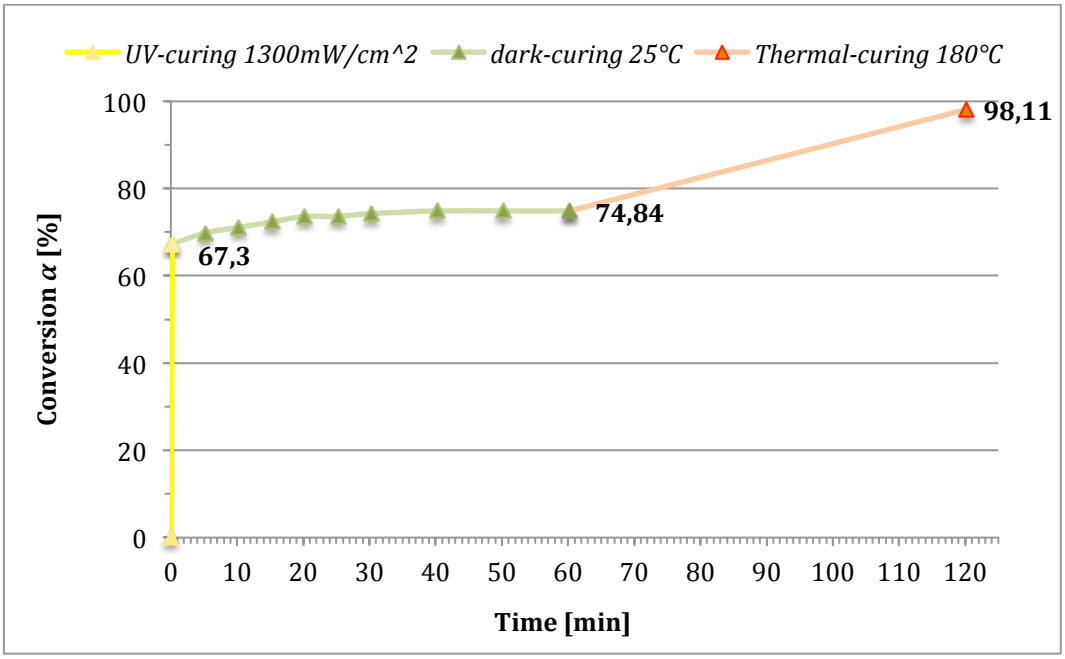

Graph 3.1.14 Conversion determined by the evaluation of the FTIR spectra of the p-ES3MA dual-curable solution. Conversion associated to three curing stages are shown: irradiation for 15 sec (yellow line), dark curing for 1h (green line), and thermal treatment for 1h (orange line).

It can be noted that the *pt-ES3MA* responded to UV- and dark- curing in the same way as it was found for the *p-ES3*: the conversion values obtained after the two curing stages were very similar for both formulations ($UV_{p\text{-}ES3} \approx 67\%$, $UV_{pt\text{-}ES3MA} \approx 68\%$, $dark_{p\text{-}ES3} \approx 79\%$, $dark_{pt\text{-}ES3MA} \approx 75\%$). In particular, the greater efficiency of the *pt-ES3MA* formulation was shown only in the last phase of the curing cycle, i.e. after the thermal treatment, when the conversion reached a value of 98.11% with respect to 89.4% obtained after keeping the *p-ES3* solution for one hour at 180° C.

➢ Gel percentage test

In the same way adopted for the analysis of UV-curing process, in order to verify the efficiency of the dual-cure technique in bringing to completion the polymerization of different pieces (including the thicker ones), the gel percentage tests were performed.
In this case, the tests were conducted on casted samples made of the same material (*pt-ES3MA*) but subjected to different curing cycle in order to select the optimal curing conditions in terms of temperature and time. A series of samples was UV-cured by exposing the cast material for 20 min on each side under UV-A light while the other series of samples was maintained 10 min more under the source. Both were then subjected to a thermal treatment for 1h but for the first the temperature was set at 150° C while for the second at 180° C.

As in the previous analyses, the samples weight before and after the drying cycle were registered and, by means of the *Eq. 2.4,* their gel percentage values are calculated. The results (average of two samples for each series), together with the images of post-test samples, are reported in the table below (*Table 3.1.11*).

Curing cycle	***Gel percentage [%]***	***Post-test sample appearence***
UV-A 20min 150°C 1h	86.67 ± 0.90	
UV-A 30min 180°C 1h	99.90 ± 0.02	

Table 3.1.11 Gel percentage test results: mean and standars deviation values are reported. The images represent the samples appearence after the test with also the residual concentrated solvent stored in vials.

According to the above results, the optimal curing conditions were found to be those adopted for the second series of samples: longer time under the UV-A and thermal treatment at 180 ° C for 1h. In fact, these conditions have led to an almost complete monomer conversion, as also confirmed by the spectra of the residual solvent presented in the *Graph 3.1.15*.

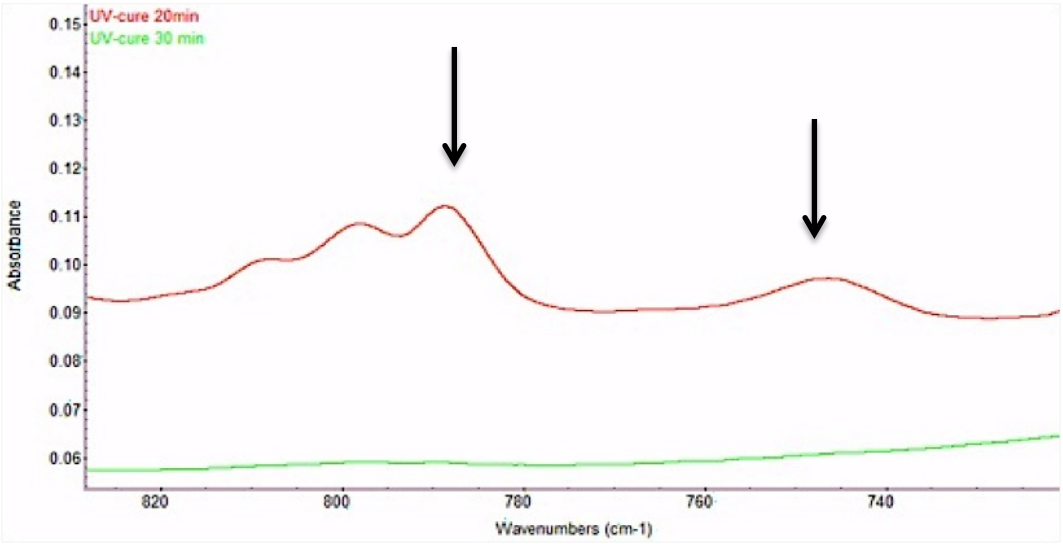

Graph 3.1.15 FTIR spectra of the residual solvent used for the immersion of the samples in the gel percentage measurement. Green line represents the spectrum of the solvent in which the most cured sample was immersed; red line is about the residual of the less cured sample.

As it might be expected from the different color of the solutions, in the spectrum of the solvent used for the immersion of the most cured sample, the epoxy characteristic bands (peaks at 746 cm^{-1} and at 788 cm^{-1}) are not detectable, while they are well visible in the spectrum of the solvent in which the less cured sample had been immersed.

3.1.2.2 Rheology investigation

The pt-ES3MA solution was too liquid to be printed as such thus, as done for the UV solution, it was made more viscous by the addition of fumed silica. Four blends with an increasing content of filler (from 6.5% wt up to 13% wt) have been prepared and then subjected to rheological analysis. The obtained rheological curves are presented in the *Graph 3.1.16,* where the plot of the liquid unfilled *pt-ES3MA* solution is also reported.

The dual-cure unfilled solution showed a Newtonian behavior, with constant viscosity value lower than that found for the UV-curable solution. The constant viscosity for increasing shear-rate was $\eta \approx$

0.34 Pa s in the 1-2 · 10^2 s^{-1} shear-rate interval. The silica dispersions showed the typical shear-thinning behavior with the viscosity decreasing with increasing shear-rate, as expected.

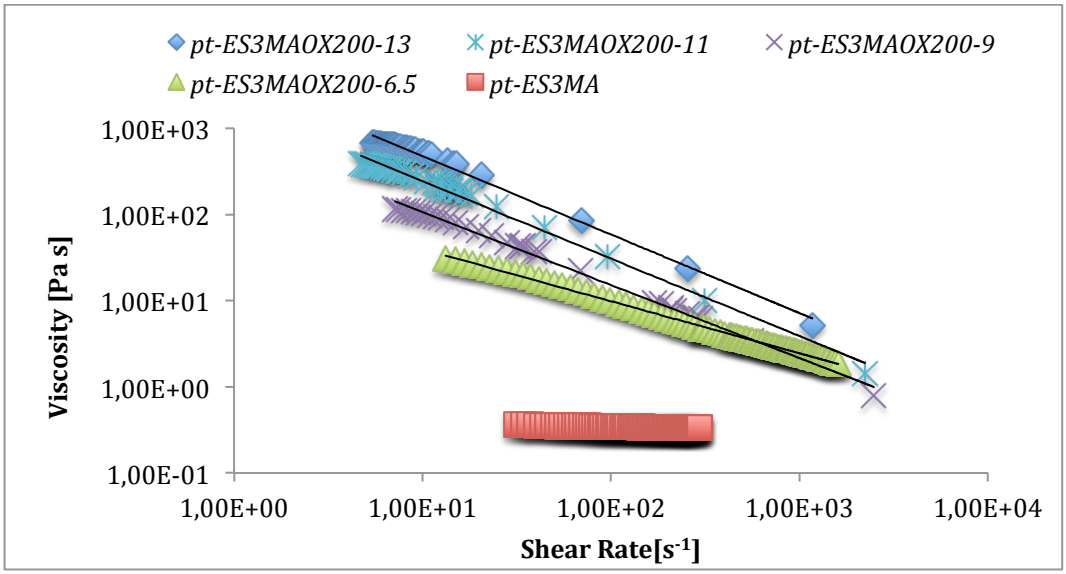

Graph 3.1.16 Viscosity curves of pt-ES3MAOX200 formulations at increasing filler concentrations.

As already explained for the previous rheological study *(§ 3.1.1.2)*, the viscosity curve could be well fitted by a power-law relationship (black line); the power-law index and the consistency one for each blend are listed in the table below (*Table 3.1.12*). As expected, the four loaded formulation presented power-law index n<1 that increased going from higher to lower silica content. The consistency K values were low for the mixtures containing up to 9% wt of silica while they showed higher values for the mixtures with a greater amount of fillers.

OX200 concentration wt [%]	***Power-law index n***	***Consistency index K [Pa s^n]***
13	0.089	3880.1
11	0.102	1920.5
9	0.153	751.18
6.5	0.396	158.79

Table 3.1.12 Power-law index n and consistency index K, relative to the tp-ES3MAOX200 formulations at different silica concentration.

3.1.3 Short fiber reinforced composites

The short fiber reinforced (SFR) composites were all obtained by adding different volume percentages of fibers to the *pt-ES3MAOX200-11* dual-cure material. Several blends were prepared by adding different types of short fibers: glass (FILL 100, FILL 200F) and carbon (PANEX35) fibers were used as inorganic fillers while the bamboo was tested as organic reinforcement.
Starting from small quantities of fibers, i.e. 10% v/v, the work is proceeded preparing composites with an increasing fiber content, up to 50% v/v. The maximum amount of fiber that could be added to the matrix was evaluated with a simple hand-compression test, to simulate the extrusion phase; this is necessary because the composite ink has to pass through a noozle and the quantity of fibers can obstruct this passage. This test consisted in filling a syringe with the compound to be tested, and then in the manual compression of the plunger so as to obtain the output of material from the nozzle. Mixtures with increasing amount of fibers were prepared as long as it was possible to extrude a wire of them without applying a too high compression. At 50% v/v it was found that this concentration was the maximum acceptable as the subsequent blend with a greater amount of fibers was impossible to extrude even by applying a high force. At the end, ten different blends (FILL100-10, FILL100-25, FILL100-40, FILL100-50, FILL200-10, FILL200-25, FILL200-40, FILL200-50, PX35-10, BAMBOO-10) were prepared and analyzed. The obtained results were presented in the following paragraphs.

3.1.3.1 Curing process investigation

In order to investigate the effect of fibers addition on the reactivity of the previously analyzed dual-cure formulation, adopted as matrix material for the SFR composites, both qualitative and quantitative analyses were carried. A first qualitative evaluation of the response time to UV light was given by the "drop on glass" test. The p-DSC analyses were usefull to obtain quantitative results.

- **"Drop on glass" test**

A drop for each composites formulation was cast on a slide and irradiated with the LC-L1V3 laser (1300mW/cm^2) until it resulted solidified.

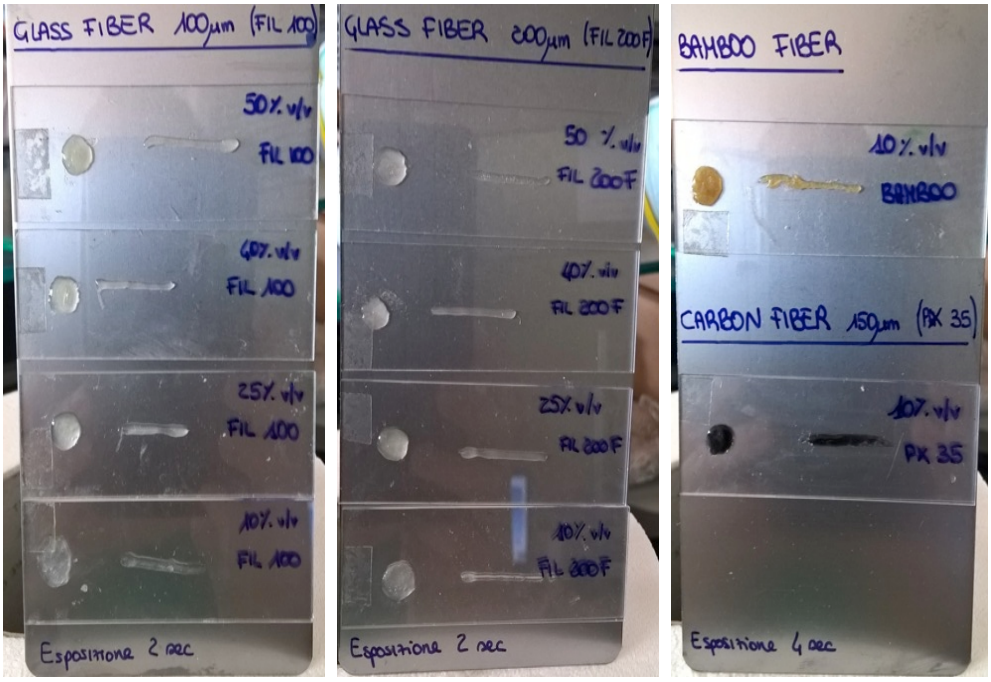

Figure 3.1.8 SFR composites drops: the drops containing glass fiber were exposed to UV light for 2 sec while those with carbon and bamboo fibers for 4sec in order to make them solid.

As it can be seen in *Figure 3.1.8*, glass fibers, being white-transparent, did not affect the photo-reactivity of the matrix while carbon and bamboo, being more dark, absorbed most of the UV-light hampering the possibility for light to be absorbed by the PIS photoinitiator. The explanation to the low efficiency of polymerization found for the materials containing these last types of fibers, is also in their chemical structure: the PX35, made of sheets of carbon in sp^2 hybridization, presents benzene structures which absorb in the UV; the same happens in the case of bamboo, composed of cellulose and lignin. This absorption leads to a reduction of the energy supplied to the epoxy resin and, consequently the polymerization is affected. As a consequence, all the drops of glass fiber reinforced composites became solid only after 2 sec of irradiation (as for the *pt-ES3MA* matrix solution), while for the hardening of carbon and bamboo drops a double irradiation time, 4 sec, was required. Moreover, while the entire volume of the transparent white drops appeared solid, dark drops tended to remain semi-liquid inside; indeed the strong shielding effect induced to a polymerization gradient going from the surface towards the inside of the drop.

On the basis of this result, during UV-3D printing of the thick samples of composites material, it has been tried to solve the problem of lower conversion in the inner region by reducing both the layer thickness and the printing speed so as to allow the radiation to penetrate the entire thickness of the printing-filament. In fact, as explained in detail later, different printing parameters were set during the printing of composite thick samples, such as those prepared for the mechanical tests.

➢ Photo-DSC analysis

In order to characterize the photopolymerization process of the SFR-composite inks and to evaluate the effect of the presence of different fibers on the thermodynamics of the curing process, photo-DSC measurements (0.8 relative intensity, 5 min UV-irradiation) were carried out on the compositions containing the lowest and the highest fiber volume fraction (10% v/v and 50% v/v).

The measured heat of polymerization for each ink has been corrected considering the exact fiber/matrix weight fraction present in every compound during the photocalorimetric scan. The obtained data are presented in the following table and graph

as a function of filler type and concentration.

	Maximun peak [s]	***ΔH_{exo} [J/g]***
pt-ES3MAOX200-11	4	168.10
FILL 100-10	4	145.52
FILL 100-50	6	166.51
FILL 200-10	4	157.64
FILL 200-50	4	151.63
BAMBOO-10	10	126.70
PX35-10	8	32.26

Table 3.1.13 p-DSC analysis results for the photopolymeriation of different SFR-composites inks. The data about the polymeric matrix are also reported for comparison.

As it can be noted from the *Table 3.1.13 and Graph 3.1.17 (a)–(b),* the presence of glass fibers not affects so much the heat of polymerization of the composites inks, as in all glass composites an enthalpy value ΔH_{exo} very close to that found for the unfilled polymeric matrix *pt-ES3MAOX200-11* was measured (see *Graph 3.1.17 (b)*). Only slightly lower value was recorded for the FILL 100-10 ink.

Very different behavior was found in the case of inks with bamboo and carbon fibers, which have greatly influenced the polymerization of the compounds. Lower exotherms were indeed recorded for these formulations; the conversion of the UV-curing reaction, calculated as the ratio between the enthalpy of reaction for the SFR-composite ink and the enthalpy for the unloaded matrix, resulted of 75 % and 19 % for the BAMBOO-10 and PX35-10 inks, respectively. In the graph below (*Graph*

3.1.17 (a)), it can be also noted as these formulations with a shielding chemical structure, compared to those containing white transparent glass fibers, presented slower kinetics: the time to reach the maximum exothermic peak of polymerization was found to be doubled in case of bamboo and carbon fibers reinforced inks.

All of these results are in agreement with what is already seen in the test previous "drop on glass" test.

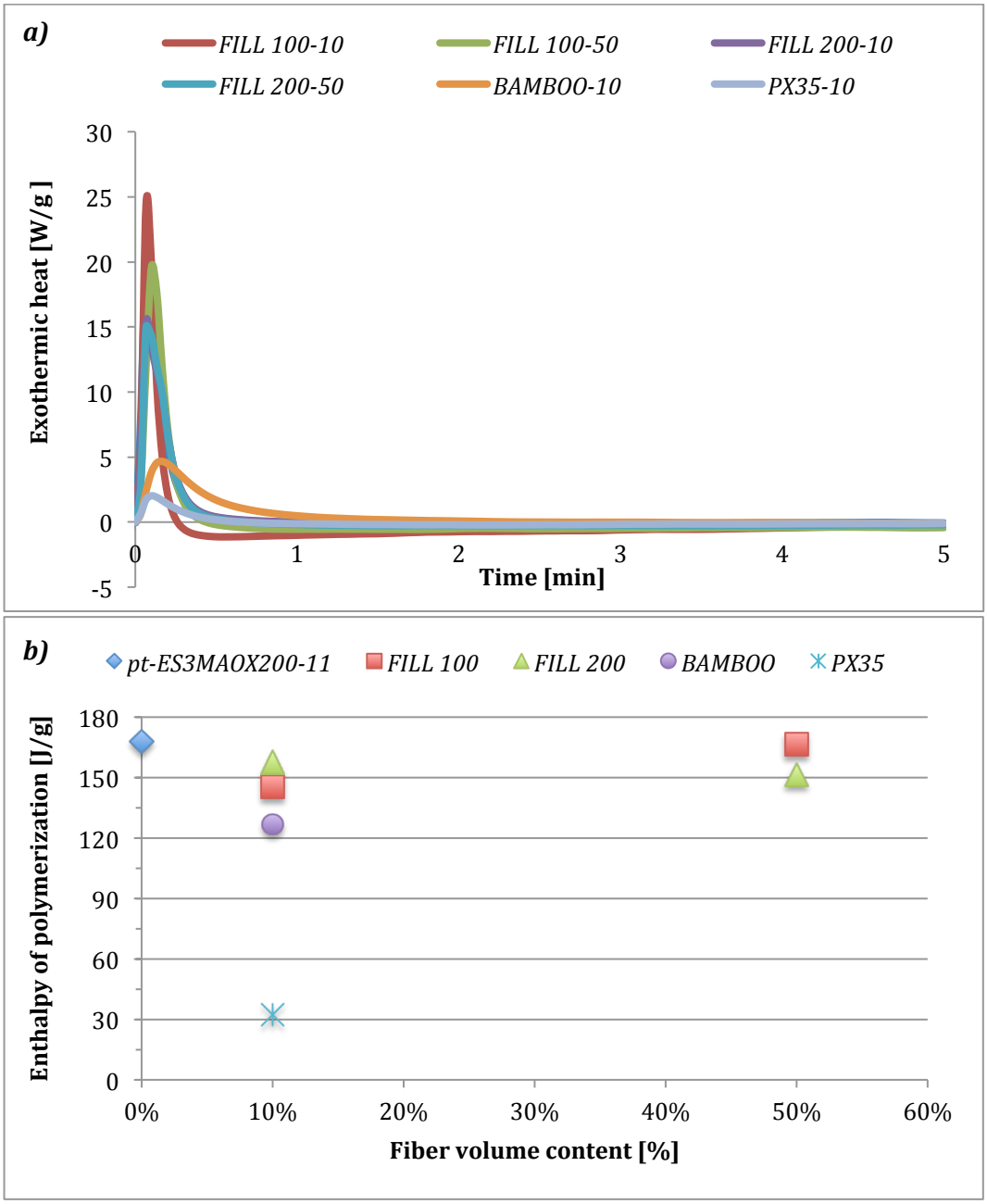

Graph 3.1.17 Photo-DSC results for SFR-composites inks: a) Exothermic curves; b) Enthalpy values.

3.1.3.2 Rheology investigation

In addition to the effects produced by the addition of fibers on the curing process, also the rheological behaviors were investigated. The viscosity curves of the SFR-composites, as function of the shear-rate, are reported on the graphs below (*Graph 3.1.18 (a)-(b)* and *Graph 3.1.19*).

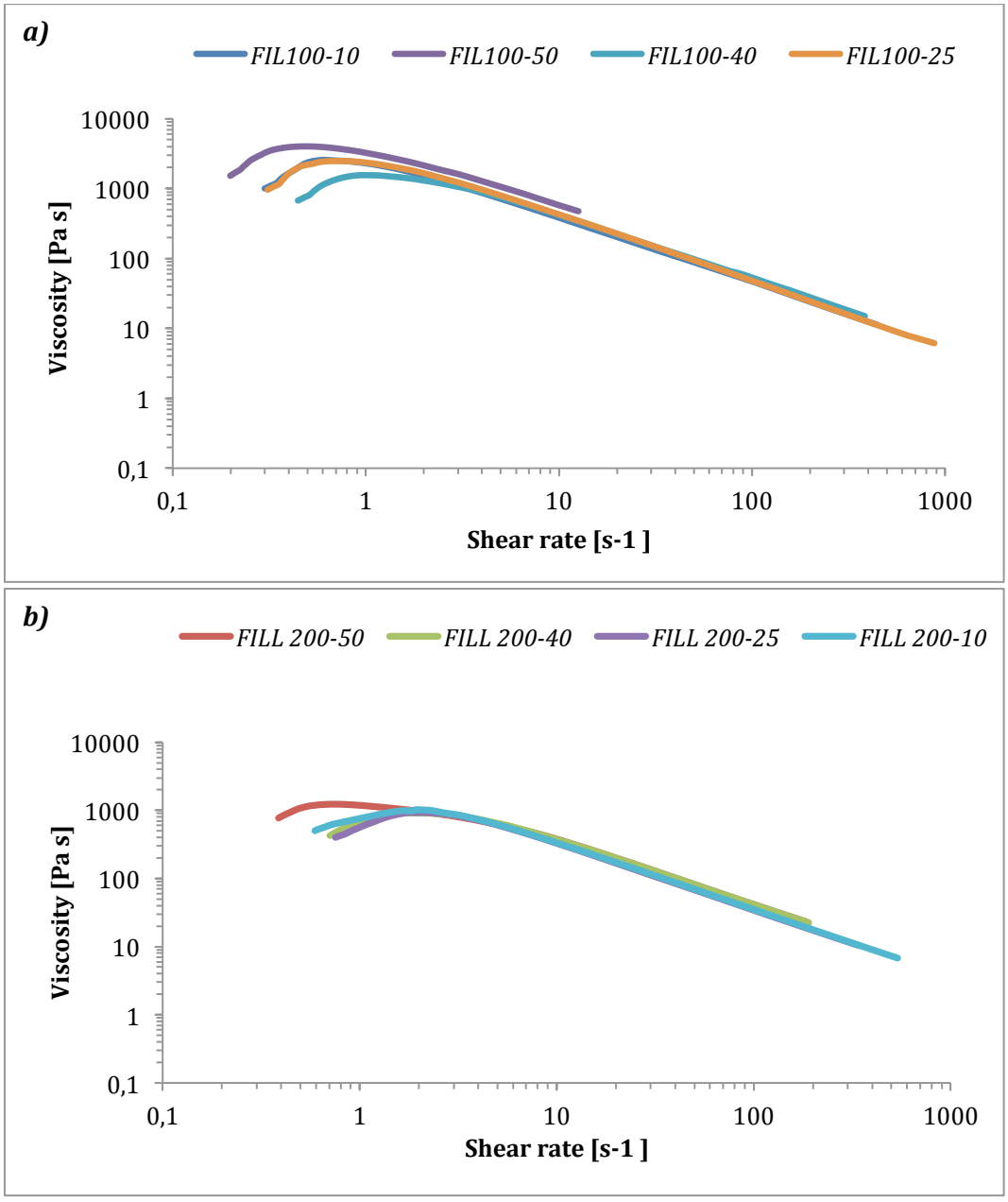

Graph 3.1.18 Viscosity curves of SFR composite formulations at increasing fibers volume fraction: a) FILL 100; b) FILL 200.

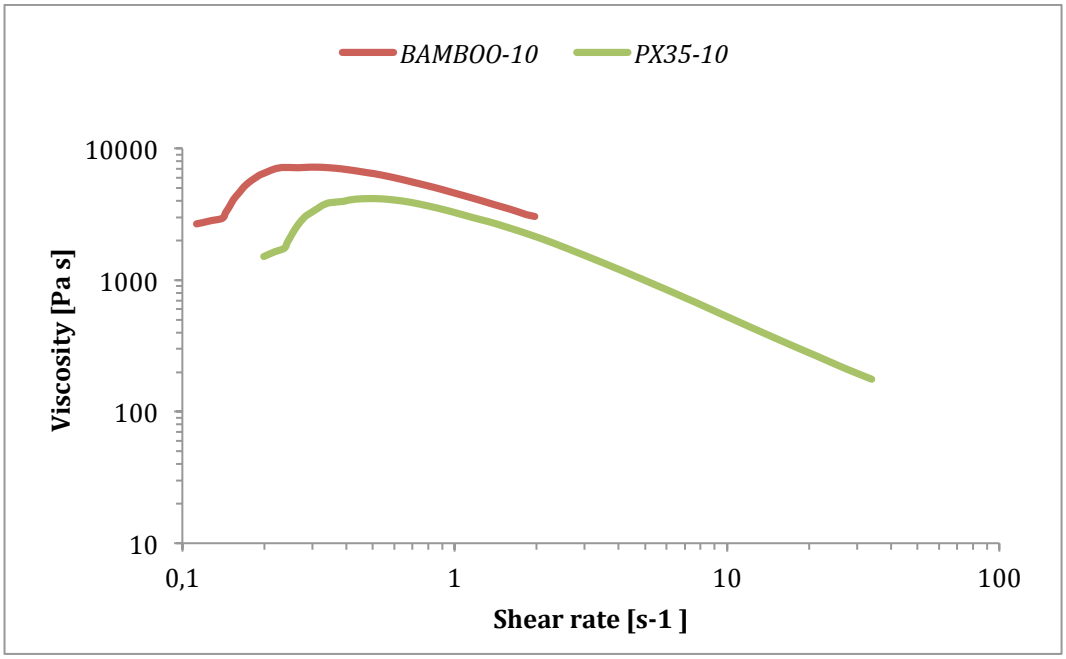

Graph 3.1.19 Viscosity curves of carbon (PX35) and bamboo (BAMBOO) SFR-composites.

The shear thinning behavior of the SFR-composites is shown in the above graphs. In particular, focusing on *Graphs 3.1.18 (a)* and *(b),* relative to SFR- composites with the FILL100 and FILL200, respectively, an increase in viscosity with increased fiber loading can be noted only at low shear rates while, at high deformation rates, the viscosity variation resulted negligible. This trend was strange compared to the curves found for the matrix; but, in agreement with the literature [103], it was found to be a typical behavior for fiber-filled polymers.

According to the power law approximation (*Eq. 3.3*), the values of consistency index, *K,* and power-law index, *n,* of all the SFR-composites inks were calculated. The obtained values are listed in the *Table 3.1.14*.

Comfirming the shear-thinning behavior, all the inks presented n<1. From the data reported in the table, there seems to be not a great variation neither of K nor of n, varying the amount of fiber added to the polymer matrix. This confirms what has been said above.

Moreover, the shorter glass fibers (FILL 100), allowing a better dispersion, presented slightly higher viscosity (higher K values) compared to the longer ones (FILL 200). Altought BAMBOO and PX35 inks contained the same volume percentage (10% v/v), the first resulted more viscous at low shear rates.

SFR-composites	*Power-law index n*	*Consistency index K [Pa s^n]*
FILL 100-10	0.119	2725.9
FILL 100-25	0.082	3228.7
FILL 100-40	0.107	3249.7
FILL 100-50	0.270	3368.1
FILL 200-10	0.116	2163
FILL 200-25	0.135	2030.2
FILL 200-40	0.167	2219
FILL 200-50	0.185	2111.8
BAMBOO-10	0.473	4492.8
PX35-10	0.186	3410.4

Table 3.1.14 Power-law index n and consistency index K, relative to the SFR-composite formulations.

According to the data in the table, all the composite formulations might be suitable for LDM process. This will be verified later.

3.2 UV-Assisted 3D Printing process

3.2.1 First approch to UV-3D printer: UV system optimization

Photopolymer conversion rate is a very important parameter that should be taken into account in the development of a UV-3D printing process. Indeed, as already seen, it depends on both the intrinsic properties of the material, such as type of monomer and concentration of photoinitiator, and on the processing-related parameters, such as intensity of UV-light source, distance between source and extrusion point and UV-exposure time (in order to obtain an accurate UV-3D printed fabrication, high photopolymer conversion should occur within seconds).

According to this, the first approach to the UV-3D printer used in this work consisted in the assembly and optimization of the UV-light providing system, both in terms of correct optical fibers position (angle and distance from the nozzle), and light intensity. As previously explained (*§ 2.2.1.2*), two supports, specially manufactured for the attachment of the two optical fibers to the printer, were designed in such a way that they could be rotated in order to adjust the correct position of the fibers with respect to the extrusion system.

The "drop on glass" test was adopted for the evaluation of the correct fiber-nozzle distance in relation with the UV-irradiation intensity, conditions at which the maximum curing efficiency should be obtained.

Drops (≈ 50 µl) of UV-curable formulations with and without fumed silica were deposited on slides. Four series of drops (three of *p-ES3,* and one of *p-ES3OX200*-13) were prepared and, for the curing of each one, different irradiation parameters were set.

The first two series, prepared to define the correct UV-source position, were irradiated varying for each one only the fiber-slide distance of 2 cm at time.

The last two, prepared to evaluate the effect of the UV-intensity variation, were irradiated varying only the light intensity of 10% at a time.

The first set was irradiated for 2 sec, at the maximum available UV-radiation intensity, placing each drop at an increased distance from the UV-source (from 2 cm up to 8 cm). For the second set the same procedure was followed but, this time, the relative UV-irradiation intensity was set to 50%.

The figure below presents the drops obtained by irradiating the *p-ES3* material according to the conditions described above: on the left the drops of the first set are presented while on the right those belonging to the second series are shown (*Figure 3.2.1*).

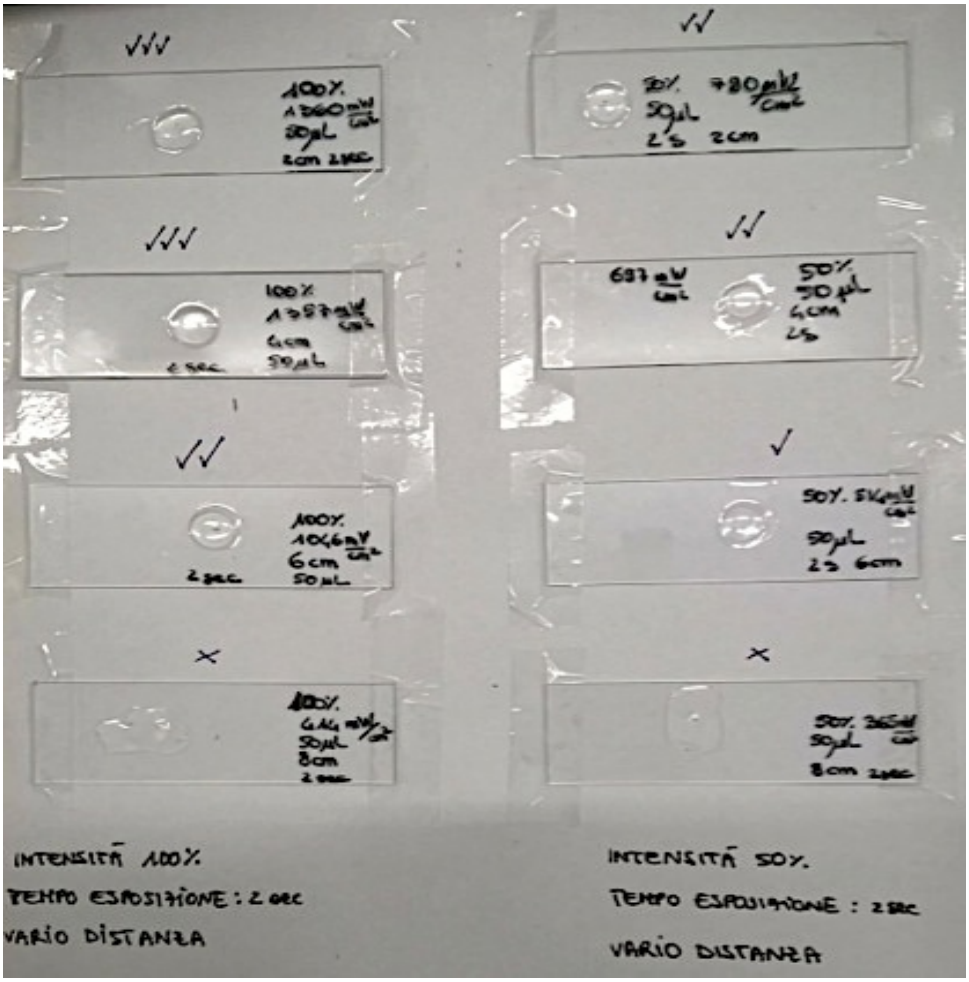

Figure 3.2.1 Results of the "drop on glass" test (p-ES3 solution): on the left, the drops irradiated at the maximun intensity (100%) for 2 sec, varying the distance UV-source-drop from 2 cm up to 8 cm. On the right, the drops irradiated at halved intensity (50%) for 2 sec, varying the distance UV-source-drop from 2 cm up to 8 cm.

In both cases, only the drops placed at distances equal to or lower than 4 cm were able to complete their polymerization in 2 sec.

According to the above result, the last two series were tested positioning the slides exactly at 4 cm from the source. As before, the exposure time was maintained at 2sec, but the UV-intensity was decreased from its maximum to lower relative values. For the third set the drops are prepared using the *p-ES3* solution (*Figure 3.2.2*), while for the fourth, the *p-ES3OX200-13* formulation was employed (*Figure 3.2.3*).

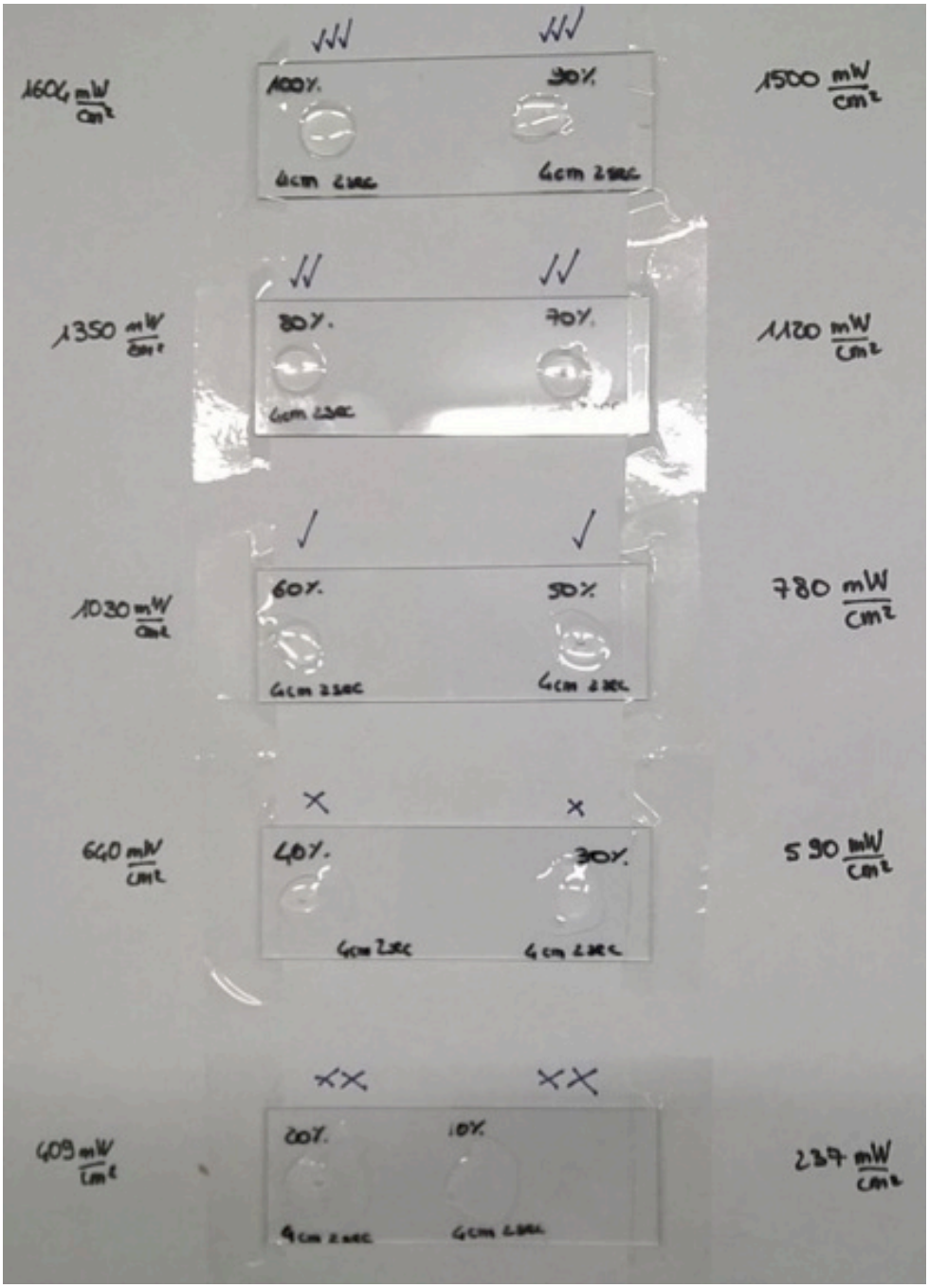

Figure 3.2.2 Results of the "drop on glass" test (p-ES3 solution). Irradiation conditions: 2sec at a constant distance of 4 cm from the UV-source, varying the light intensity from 100% to 10%.

The UV-curable *p-ES3 drops* could be completely polymerized in 2 sec only by setting a UV-intensity value equal or greater than 70% of the maximun available.

At lower intensity, the drops tended to remain semiliquid and, in the extreme cases of 0.2 and 0.1 relative intensity values, they were liquid.

The same result was found for the material containing fumed silica. As shown below, solid drops were obtained only in the case of high intensity irradiation; the efficiency of photo-polymerization decreased with the UV-intensity decrease.

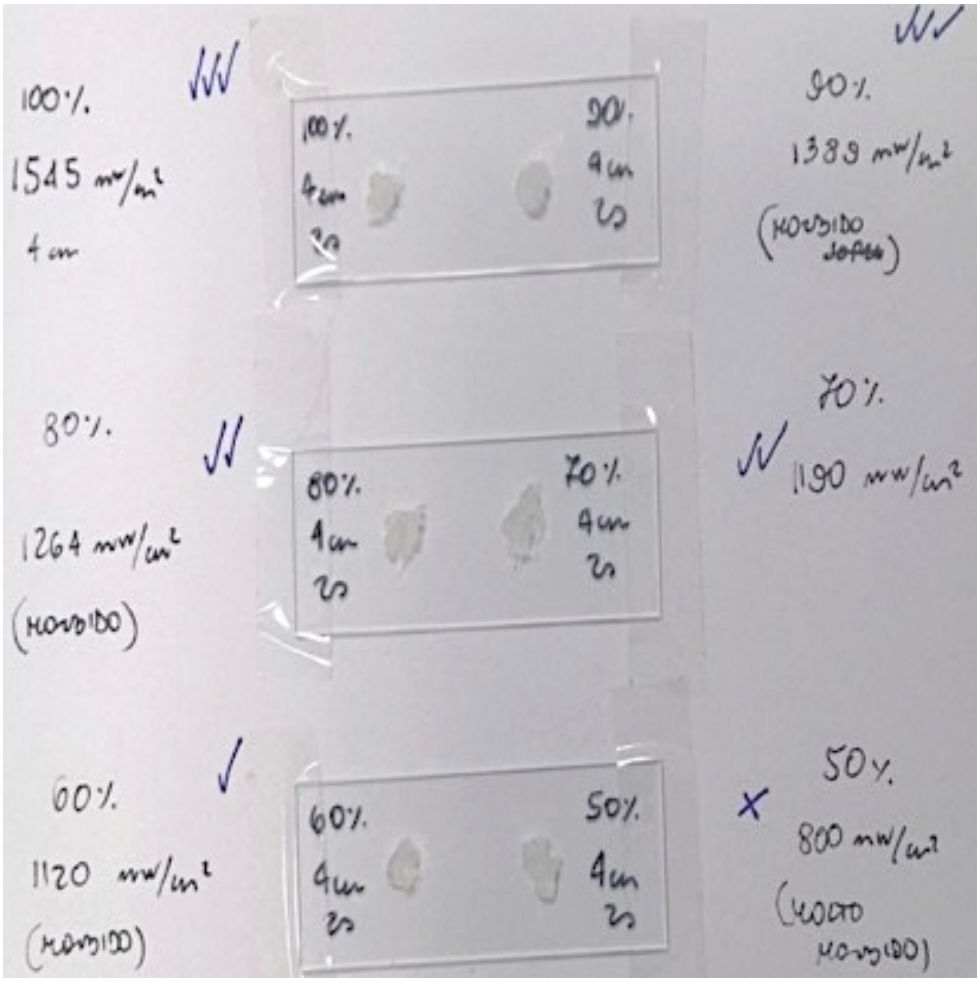

Figure 3.2.3 Results of the "drop on glass" test (p-ES3OX200-13 solution). Irradiation conditions: 2sec at a constant distance of 4 cm from the UV-source, varying the light intensity from 100% to 10%.

On the basis of these results, it was possible to assembly the UV-system on the 3D-printer in order to guarantee the highest UV-3D-printing process efficiency. The fibers supports were mounted on the transverse bar of the printer, at a position such that the distance between the end of the fibers and the nozzle was less than 4 cm. Instead, as will be shown in the following paragraphs, the relative intensity of the laser was varied during the printing of different inks but, it was always set at a value greater than 0.7.

3.2.2 Printability windows

Normally, in the micro-extrusion process (including the LDM-based UV-3D printing), an ink with tailored viscoelastic behavior and optimized deposition process parameters are required to successfully obtain 3D micro- and macrostructures. In order to optimize the resulting shape of the objects, the ink must have two important characteristics: its rheological profile during the extrusion must allow the ink to flow easily through a fine printing nozzle and it must be characterized by self-supporting ability, once deposited.

As already shown in previous paragraphs (*§ 3.1.1.2*, *§ 3.1.2.2, §3.1.3.2),* all the inks formulated during this experimental work (*p-ES3OX200, pt-ES3MAOX200, SFR-composites*), exhibited a rheological response highly desirable in the context of LDM-based processes. Indeed, they showed a typical shear-thinning behavior which, being characterized by decreasing viscosity with increasing shear-rate, generally lead to the enhancement of the ink processability through the capillary nozzle under the high shear-rate typical of the extrusion processes.

In this paragraph, a further characterization of the rheological properties of the above inks, in relation to extrusion process, is presented.

Based on the values of the power-law index *n* and the consistency index *k* derived from the power-law approximation, *Eq. 3.3,* the UV-3D printing process-related wall shear-rate and wall shear-stress were predicted using the capillary flow model [104]–[106] and thus printability windows for each material could be determined.

At first, the apparent Newtonian shear-rate $\dot{\gamma}_{app}$ of an ink inside the capillary was determined by means of the *Hagen-Poiseuille* equation (*Eq. 3.4*):

$$\dot{\gamma}_{app} = \frac{4Q}{\pi R^3} \qquad (3.4)$$

where Q is the volumetric flow rate and R is the inner radius of the capillary.

According to the *Mooney-Rabinowitch* correction for the non-Newtonian fluids, the actual shear-rate $\dot{\gamma}$ could be estimated using the following relation (*Eq. 3.5*):

$$\dot{\gamma} = \dot{\gamma}_{app} \left(\frac{3n+1}{4n}\right) \qquad (3.5)$$

with n being the power-law index.

Since Q could be calculated from the linear printing speed through the cross-section area[12] of the printing nozzle and, having adopted a 3D printer whose optimal printing speed was ranging from 0,1 mm/s to 12mm/s, an allowable process-related shear-rate interval for each particular material was estimated as a function of the printing speed settings.

Instead, the process-related wall shear-stress τ could be obtained using the following equation (*Eq. 3.6*):

$$\tau = \frac{P_{max} - P_a}{2\left(L/R\right)} \qquad (3.6)$$

where P_{max} is the maximum applicable pressure, P_a the atmospheric pressure, and L the length of the capillary. Since the maximun pressure attainable by the stepper motor controlling the movement of the piston of the syringe dispenser could originate a maximum working pressure value of 0.8 MPa, the shear-stress upper limit provided by the UV-3D printer was τ_{max} = 2900 Pa. This value was obtained by neglecting the *Bagley* correction, $2\left(L/R\right)$, being larger than 50[13] [105].

According to the above calculations, the material/process-related printability windows were determined. Below, the plots of the process-related shear stress as function of the process-related shear-rate for the different printable formulations are presented, together with the corresponding printability windows.

As evident from the *Graph 3.2.1* and *Graph 3.2.2*, the rheological curves of all the unloaded systems, i.e. *p-ES3OX200* and *pt-ES3MAOX200* at increasing weight fraction of OX200 silica, are inside their printability window. This means that the viscosity of such inks were all compatible with the adopted printing apparatus.

In particular, the rheological curve of *p-ES3OX200-13* ink is found to be at the limit of the acceptable conditions, but as will be shown later, even this formulation was printed successfully.

Completely different results were obtain for the SFR-composite systems. In fact, as it can be noted from the Graph *3.2.3 (a)-(c)*, the rheological curves of such systems are almost completely outside the corresponding printability windows, especially for the higher shear-rates.

[12] In this experimental work a conic nozzle was adopted; the considered cross-section area is that related to its inner smaller diameter measuring 1.041 mm.

[13] The material was extruded through a nozzle with length 18mm and inner diameter 1.041mm. The calculated Bagley correction 2(L/R) is ≈69 >50.

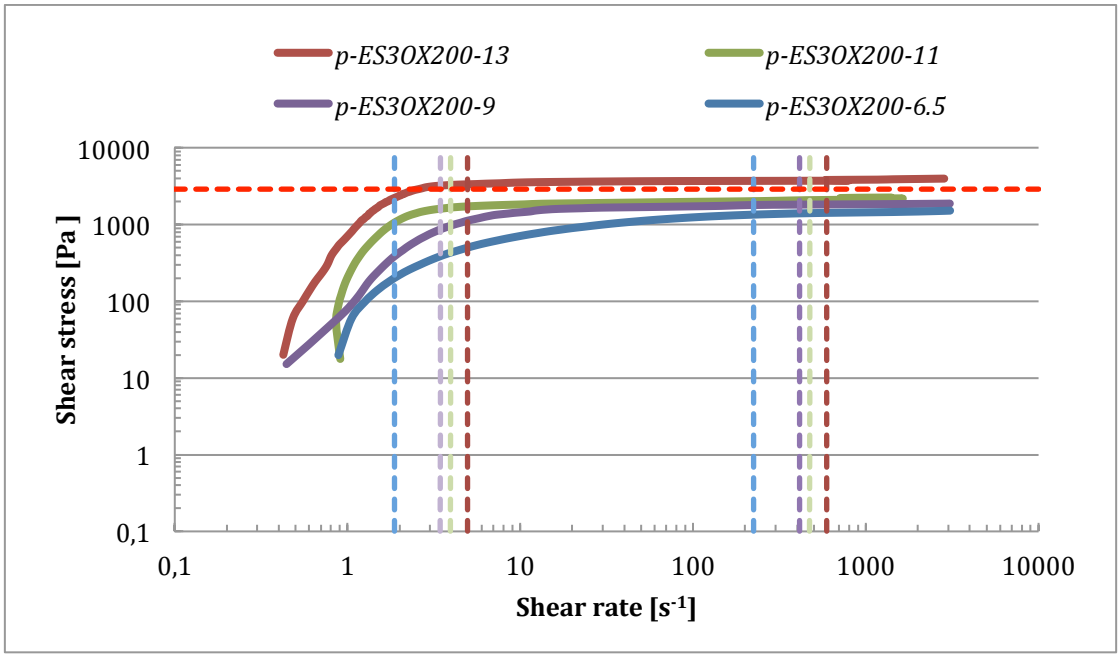

Graph 3.2.1 Shear stress as function of shear rate for UV-curable inks at increasing silica content. The corresponding printability windows are also presented as the region within the dashed lines (the window related to a partcilar material is identified with the same color used for its rheological curve).

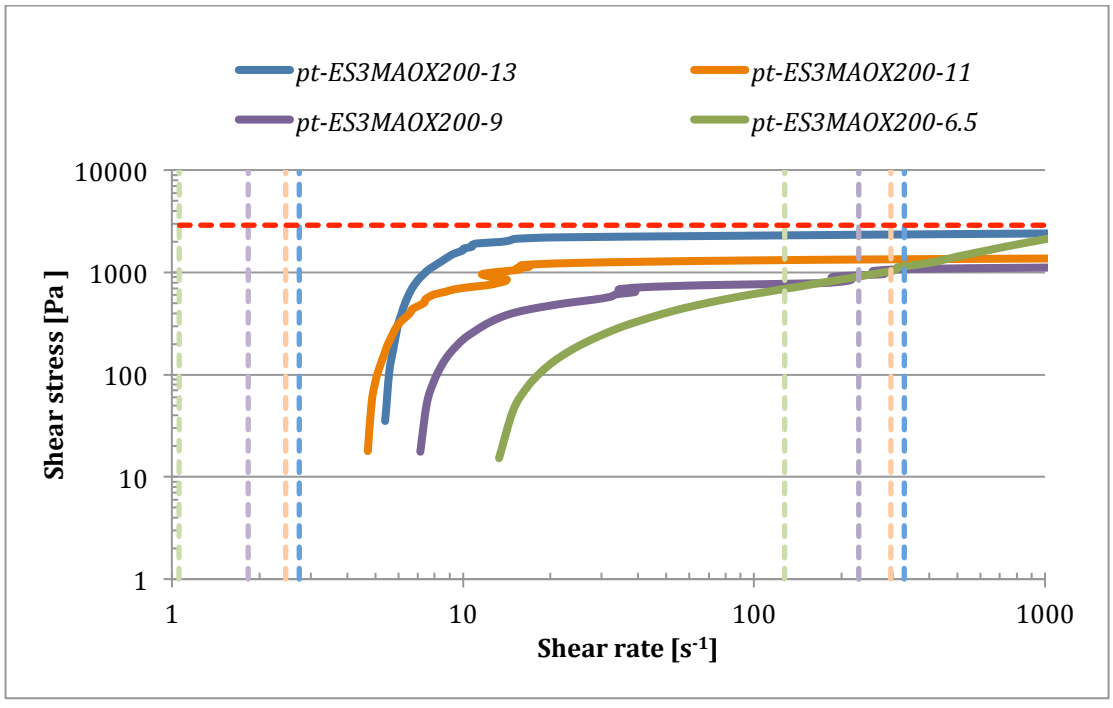

Graph 3.2.2 Shear stress as function of shear rate for dual-curable inks at increasing silica content. The correspondind printability windows are also presented as the region within the dashed lines (the window related to a partcilar material is identified with the same color used for its rheological curve).

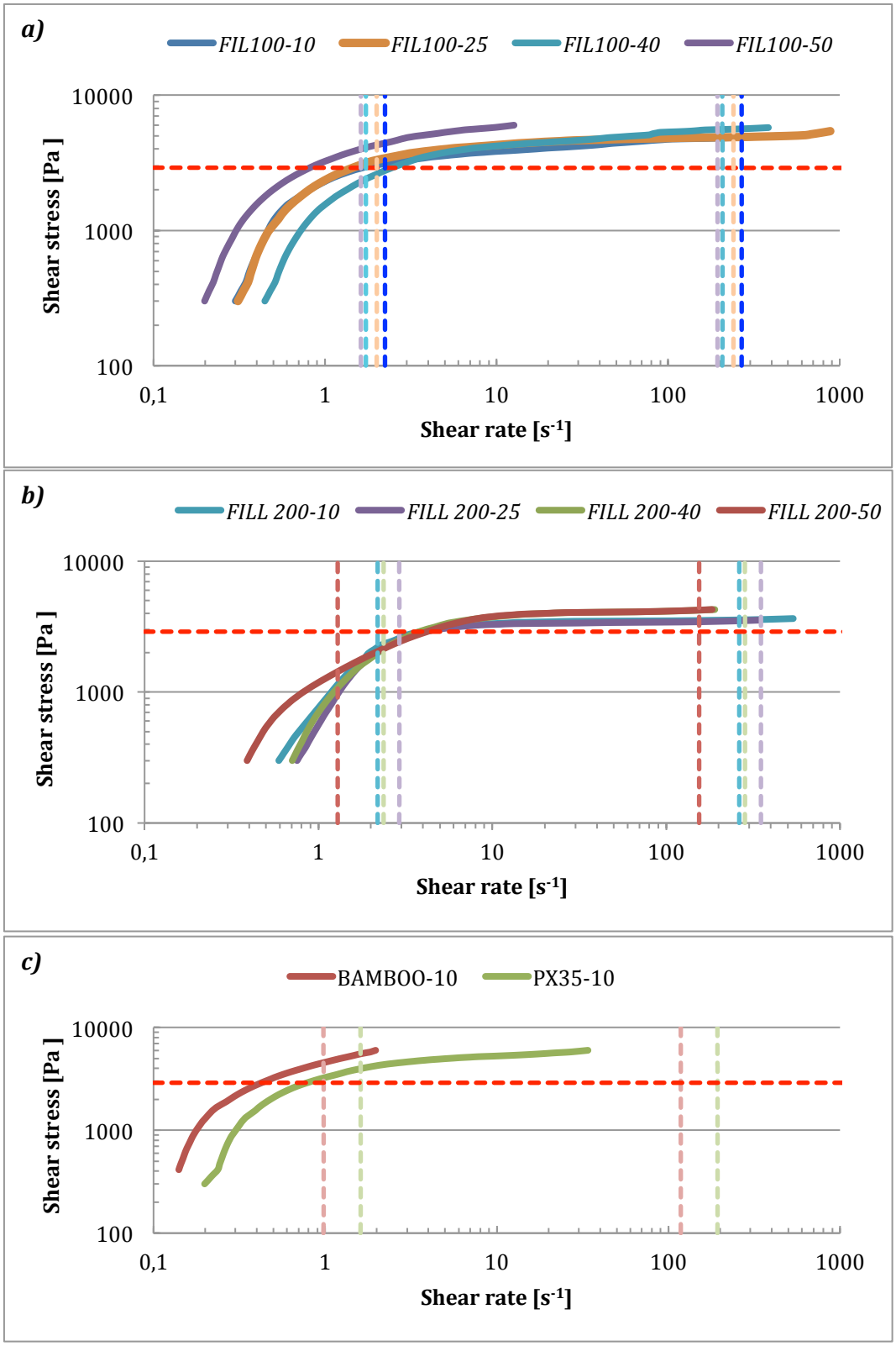

Graph 3.2.3 Shear stress as function of shear rate for SFR-composites at increasing fiber volume content. The correspondind printability windows are also presented as the region within the dashed lines (the window related to a partcilar material is identified with the same color used for its rheological curve). a) FILL 100; b) FILL200; c) BAMBOO and PX35

According to the previous graph, it seemed that a minimum extruding pressure, i.e. minimum applied shear-stress, higher than the maximum pressure reached by the 3D printer (τ_{max} = 2900 Pa) was necessary to process such systems. However, this does not correspond to what actually occurred. In fact, as shown in the following paragraphs, all formulations were able to get out of the nozzle during printing.

The explanation for this apparent discrepancy between the rheological results and the real possibility of estrusion can be found in the fact that during the printing process, the fibers tended to align along the direction of extrusion (see *Figure 3.2.7 – Figure 3.2.9*).

Such fibers alignment may have led to a reduction of the resistance at the nozzle outlet and so the inks could be extruded easily.

3.2.2.1 SCM printing: material selection

The printability of all the formulated inks was also practically tested by printing the SCM model (*§ 2.2.3.1*), specially designed to verify if the material has good printing properties, i.e. that the extruded filament was self-supported immediately after the deposition, prior to UV irradiation, and it was able to guarantee the best print resolution. As already explained, this particular geometry was also suitable to verify the possibility of developing complex designes.

Despite all the unloaded formulations previously analyzed (UV-curable and dual-curable materials at increasing silica concentrations) could be extruded through the 1.041 mm diameter nozzle (in agreement with theoretical data calculated above), only some of these actually exhibited good printing properties.

In order to prove this fact, the SCM models printed with inks at increasing concentrations of fumed silica in the case of UV-curable and dual-curable formulations are shown in the *Figure 3.2.4* and *Figure 3.2.5,* respectively.

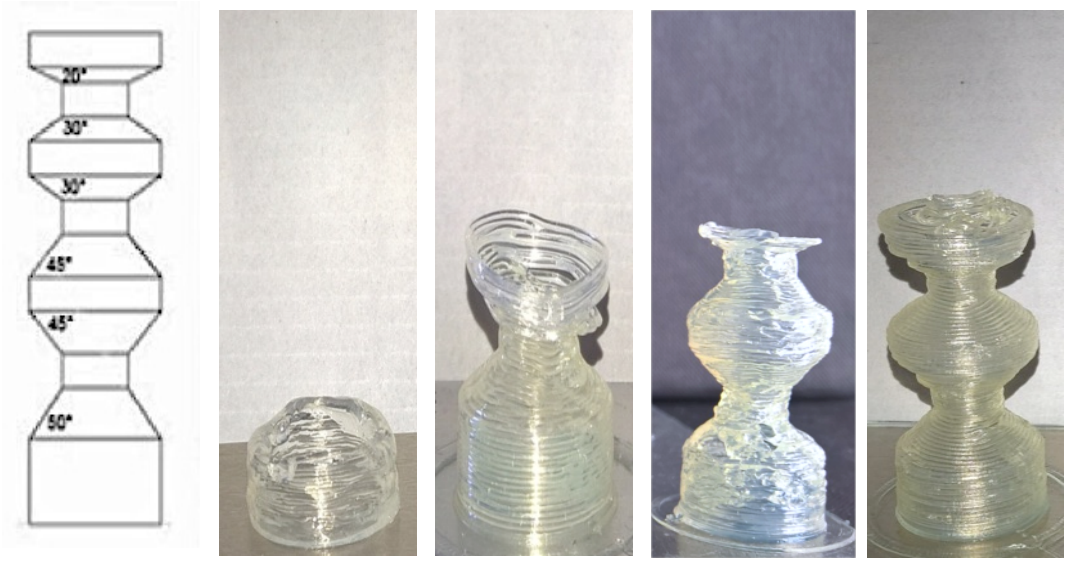

Figure 3.2.4 SCM printed with p-ES3OX200 at increasing OX200 weight concentration. On the left the 3D model is presented. Formulations with the silica content less than 9 %wt are not good to be UV-3D printed. The two with higher filler concentration are instead correct to be printed. All the presented samples are printed setting the UV-laser at the maximun available intensity.



Figure 3.2.5 SCM printed with pt-ES3MAOX200 at increasing OX200 weight concentration. On the left the 3D model is presented. Formulations with the silica content less than 9 %wt are not good to be UV-3D printed. The two with higher filler concentration are instead correct to be printed. All the presented samples are printed setting the UV-laser at the maximun available intensity but they are not yet thermal-treated.

All the SCMs shown in the two figures above have been printed using a conical nozzle of 1.041 mm diameter and setting constant printing parameters, that is: layer height 0.5 mm, print speed 5 for the UV-cure ink and 7 mm/s for the dual-cure inks, flow 100%.

According to all the experimental SCM-printing tests it was clear that, only the inks with sufficiently high fumed silica content could be used to fabricate well defined structures. As evident in the figure aboves, both the UV curable and the dual-curable inks exhibited better printability properties if their silica content was equal or greater than 11% wt. In particular, in the last figure it can be noted that increasing the silica content and therefore the printability of the dual-cure *pt-ES3MAOX200* material, also the color of the samples tended to darken. This phenomenon was not accidental but rather, it was related to the duration of the UV-3D printing process. In fact, the inks with greater printability ability allowed to achieve higher printed SCM sample which, in consequence, remained for more time under the UV-radiation. This caused a slight heating of the material that, as seen above, was enough to start the thermal-polymerization which gave the material a more dark color.
Considering the experimental printing results, on the basis of the consistency index value *K* which is known to be an indication of the viscosity of a particular formulation, it was possible to establish an experimental printability lower limit. This limit, graphically represented in the graph below (*Graph 3.2.4*), where all the *K* values of the printed solutions are reported, has been set to K = 1500 Pa s^n.

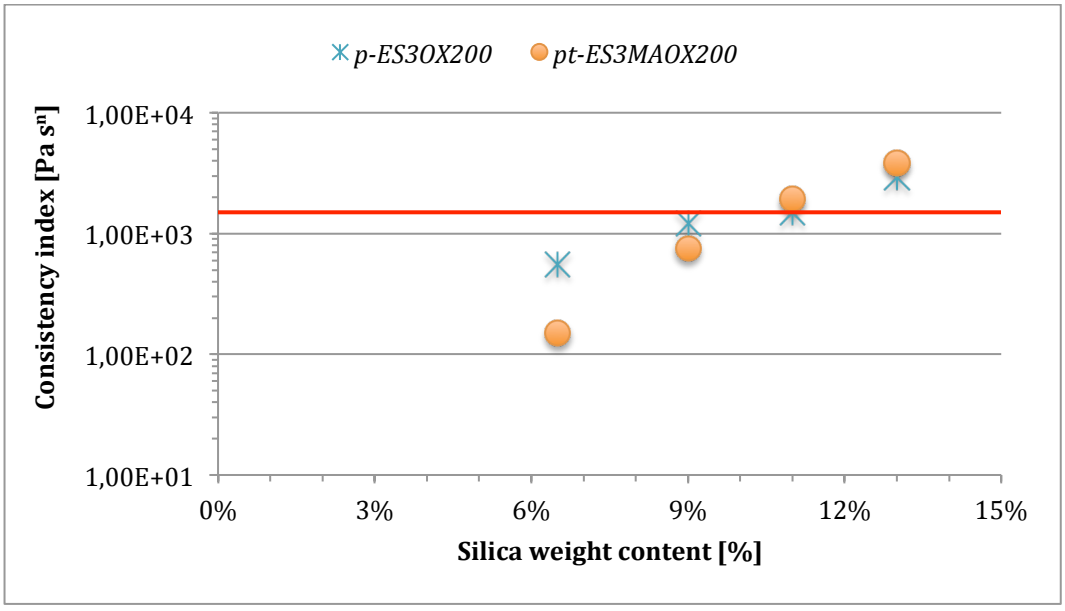

Graph 3.2.4 Consistency indexes K as function of filler OX200 concentration; the values are obtained by the power-law approximation for the viscosity curves shown in the Graph 3.1.11 for the p-ES3OX200 and in the Graph 3.1.16 for the pt-ES3MAOX200. The lower limit K value was reported as red line.

The experimental SCM-printing test was then also performed using the SFR-composites formulations. In particular, in the case of glass-reinforced composites only the FILL 100 inks with the lowest (10% v/v) and the highest (50% v/v) fiber volume concentrationwere tested.

All the composites SCMs have been printed using a conical nozzle of 1.041 mm diameter and setting constant printing parameters, that is: layer height 0.25 mm, print speed 5 mm/s, flow 100%.

As it can be noted in the next figure (*Figure 3.2.6*), that represents all the printed spiral-cylinders, the composite material which ensured a better printing resolution was that containing the white-transparent glass fibers.

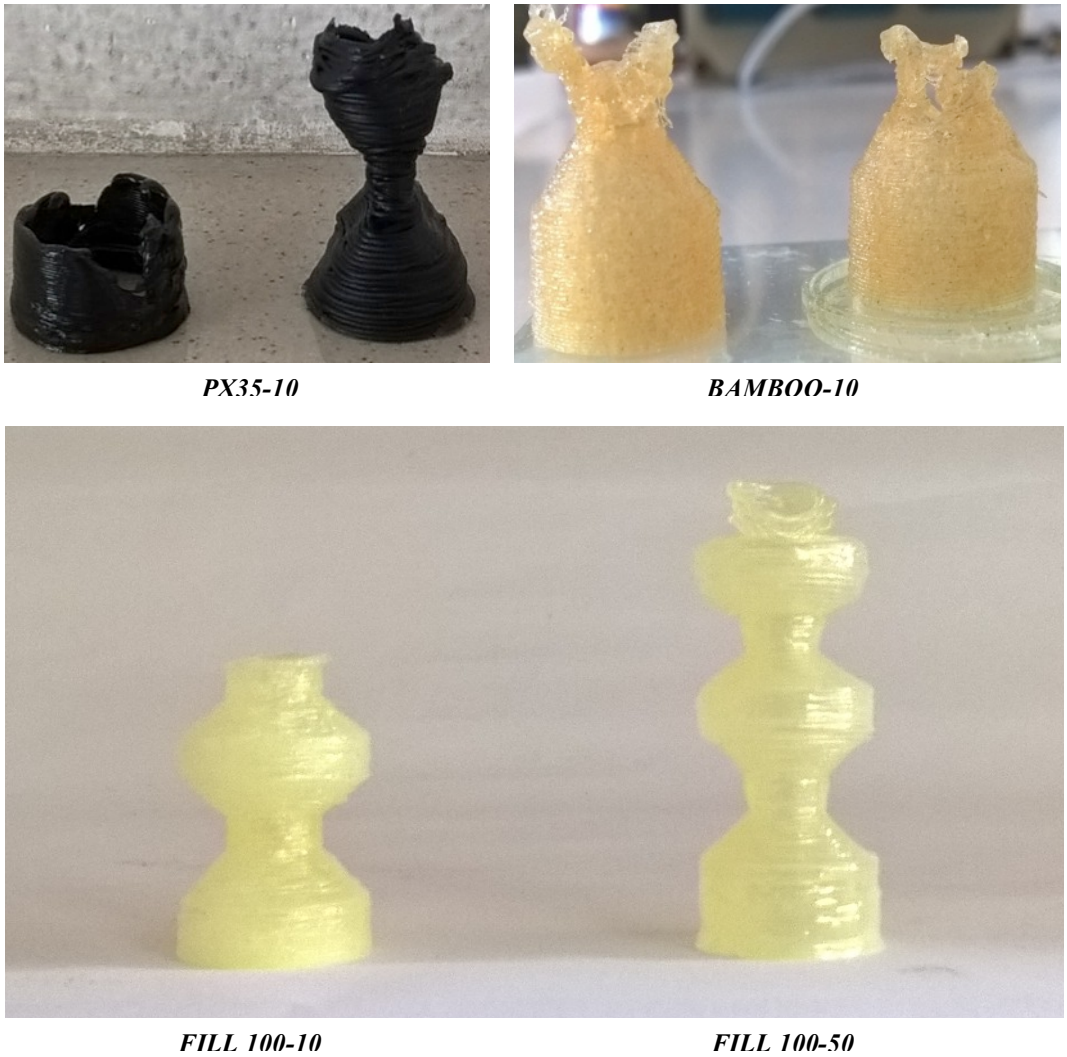

Figure 3.2.6 SCM printed with SFR-composites inks: PX35-10, BAMBOO-10, FILL100-10, FILL100-50. Only the last two formulations are suitable to fabricate the SCM. The first two remain to soft during the UV-3D printing process. All the presented samples are not thermal-treated.

Despite all composite formulations showed high viscosity with *K* values greater than the set *K* limit (1500 Pa s^n), as shown in the *Graph 3.2.5,* those containing the carbon and bamboo fibers appeared not to be suitable for the printing of overhanging geometries which, in order to grow in height, required the instantaneous layer by layer solidification. In fact, these inks did not allow to obtain a complete print of SCM object, since the already printed layers, remaining soft, could not provide a solid support for the subsequent layers; the structures tended to collapse due to a low polymerization efficiency, result already found in the previous "drop on glass" test and in photo-DSC analysis.

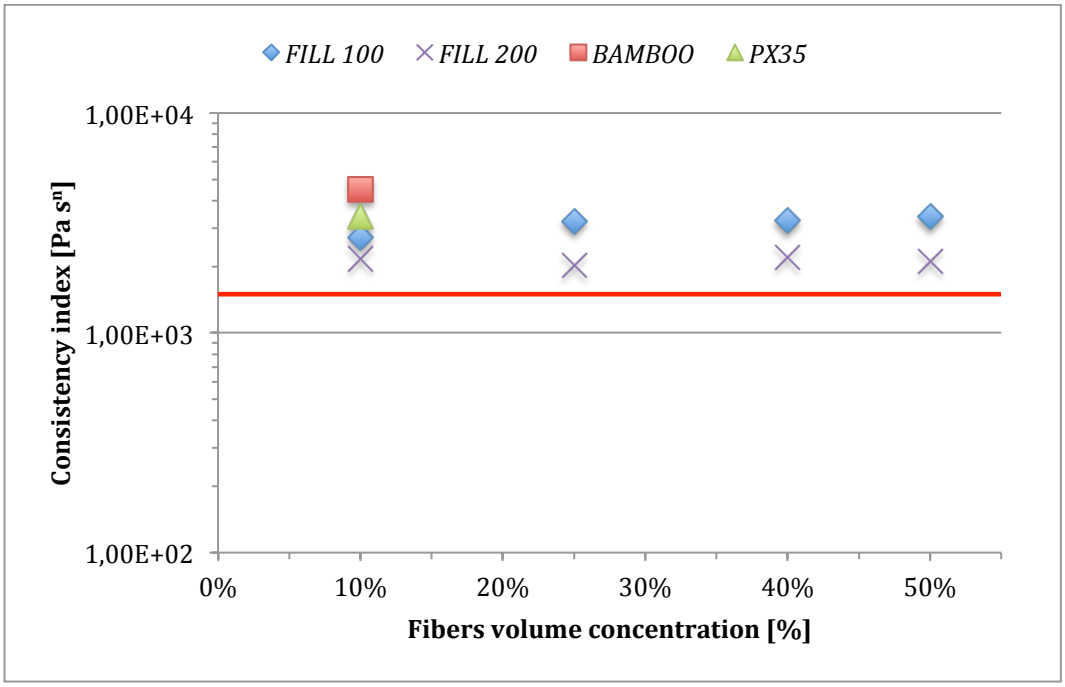

Graph 3.2.5 Consistency indexes K as function of fiber (glass, carbon and bamboo) concentration; the values are obtained by the power-law approximation for the SFR-composites viscosity curves shown in the Graph 3.1.17. The lower limit K value was reported as red line.

3.2.2.2 SCM printing: process parameters optimization

Besides the selection of a material with a suitable viscosity, to obtain good printability results it is also important to set the correct UV-3D-printing process parameters. As already mentioned, since every material responds differently to the UV-assisted process, for each one the appropriate parameters must be selected.

In particular, this work was mainly focused on the optimization of the UV-3D-printing process parameters of a single material selected from those presented in the previous section. This is the UV-

curable ink with 13% wt of fumed silica (*p-ES3OX200-13),* that, in the previous tests, allowed to print the highest SCM sample. Below, the most significative results obtained from the SCM-printing tests at varying the parameters are presented. The different values were set during the .*Gcode* formulation with *Cura* software or directly during the printing process by means of special commands present on the *Repetier*'s interface.

CURA		***SCM_1***
Layer height (mm)	0.6	
Shell thickness	1	
Print speed (mm/s)	3	
Flow (%)	130	
Nozzle size (mm)	1	
REPETIER		
Speed (%)	270	
Flow (%)	124	
LASER		
Relative UV- intensity	1	

Table 3.2.1 UV-3D-printing parameters set to print the SCM_1 shown in the figure on the right.

Looking at the picture on the right in the *Table 3.2.1*, some imperfections can be noted. These were caused by an excess of material exiting from the nozzle (too abundant flow) and by a too high UV-intensity. In some moments during the printing these two factors prevented the proper deposition of the filament, as the ink tended to polymerize at the tip of the nozzle. In the worst cases, this rapid polymerization could even lead to clogging of the nozzle therefore, interrupting the material flow, some holes appeared in the piece. In order to overcome these problems, with *Repetier*'s commands the flow was reduced and also the relative UV-intensity was lowered from 1 to 0.8. The resulting sample is shown below.

CURA		*SCM_2*
Layer height (mm)	0.6	
Shell thickness	1	
Print speed (mm/s)	3	
Flow (%)	130	
Nozzle size (mm)	1	
REPETIER		
Speed (%)	270	
Flow (%)	80	
LASER		
Relative UV- intensity	0.8	

Table 3.2.2 UV-3D-printing parameters set to print the SCM_2 shown in the figure on the right.

It can be noted (*Table 3.2.2*), as reducing the flow parameter an the intensity of the laser, the previous imperfections were no longer produced. But the object was not yet perfectly printed becuase, in some points, the still soft layers tended to collapse.

With the aim to increase the irradiation time of a layer, so that it could completely polymerize, it was tried to slightly decrease the printing speed in *Repetier from 270% to 200%,* and the relative UV-intensity was set to 0.9. The spiral cylinder fabricated with these set parameters is presented in the next picture (*Table 3.2.3*).

CURA		*SCM_3*
Layer height (mm)	0.6	
Shell thickness	1	
Print speed (mm/s)	3	
Flow (%)	130	
Nozzle size (mm)	1	
REPETIER		
Speed (%)	200	
Flow (%)	80	
LASER		
Relative UV- intensity	0.9	

Table 3.2.3 UV-3D-printing parameters set to print the SCM_3 shown in the figure on the right.

Also in this case the structure tended to collapse but it was noted that this phenomenon was mainly pronounced in the inward overhangs. To try to solve this problem, it is thought that a more stable structure could be obtained by decreasing the layer height. In this way, in fact, the overhang was completed with a larger number of thin layers which, being therefore more overlapping each other, conferred greater stability to the piece.

Moreover, another strategy adopted to try to print even at the most difficult angles, such as those at 20°, consisted in varying the print speed during the process. As shown in the SCM_4 relative table (*Table 3.2.4*), during the print of the last two overhangs, the print speed was reducing in order to have a slower and more controlled material deposition.

CURA		*SCM_4*
Layer height (mm)	0.5	
Shell thickness	1	
Print speed (mm/s)	5	
Flow (%)	100	
Nozzle size (mm)	1	
REPETIER		
Speed (%)	200-120	
Flow (%)	100	
LASER		
Relative UV- intensity	0.9	

Table 3.2.4 UV-3D-printing parameters set to print the SCM_4 shown in the figure on the right.

As it can be noted, the reduction of the layer height of only 0.1 mm (from 0.6 to 0.5) was very usefull to improve the printing of the overhangs; the collapse problems were almost disappeared. The speed reduction during the printing of the last part of the sample did not allow to print perfectly the overhangs at 20° but the more slowly deposition avoided that the latest layers fell on the previous printed ones as happened in the print of the SCM_3.

At the end, the last spiral cylinder, SCM_5, was obtained by still reducing speed, setting the maximum available UV-intensity and reducing a bit the material flow. Looking at the picture of the cylinder printed with these new parameters (*Table 3.2.5*), it is possible to adfirm that it turns out to be the best among all those previously presented.
In fact, even if the last inward overhang (20°) was not correctly printed, in general the entire structure resulted very precise with high resolution.

CURA		*SCM_5*
Layer height (mm)	0.5	
Shell thickness	1	
Print speed (mm/s)	5	
Flow (%)	100	
Nozzle size (mm)	1	
REPETIER		
Speed (%)	100	
Flow (%)	95	
LASER		
Relative UV- intensity	1	

Table 3.2.5 UV-3D-printing parameters set to print the SCM_5 shown in the figure on the right.

According to the obtained results, the optimal UV-3D-printing parameters windows for the print of *p-ES3OX200-13* ink are: layer height 0.5 mm, print speed ranging from 5 to 7 mm/sec, flow 95-100% and relative UV-intensity ranging from 0.9 to 1. Setting the higher print speed, it is recommended to reduce the value during the printing of the very overhanging regions.

3.2.3 Efficiency of the UV-3D printing process

The efficiency of the UV-3D-printing process was evaluated both in terms of ability to bring the photo-polymerization to completeness and in terms of orientation conferred to the fibers during the printing of the SFR-composite formulations.
The first aspect was evaluated by performing the gel percentage tests on thick UV-3D-printed samples while for the investigation of a possible fiber orientation, optical microscopy analysis of extruded filaments was carried out.

➢ Gel percentage test

In order to evaluate the efficiency of the UV-3D printing process in terms of photo-polymerization, the degree of crosslinking of printed samples was measured. The test procedure was the same followed for the analysis of casted samples (*§ 3.1.1.1* and *§ 3.1.2.1 "Gel percentage test"*) but in this case the samples have been prepared and cured directly by UV-3D printing the rectangular (80 × 10 × 4 mm^3) 3D model. Only in the case of dual-cure material, the samples were also subjected to a post thermal-treatment (180° C, 1h).
In order to obtain the evaluation of the process efficiency, also in relation with the type of printable inks, gel percentage tests on different materials were performed. At least two samples for each material type were prepared.

First, samples made of UV-curable material were tested. In particular, the UV-curable *p-ES3OX200-13* ink and the dual-curable *pt-ES3MAOX200-11* ink were chosen. For the print of the rectangular models, a 1.041 mm conic nozzle was used and, the following printing parameters were set: layer height 0.4 mm, flow 100%, print speed 12 mm/s and 15mm/s for the UV-curable and the dual-curable materials, respectively. In both cases the laser's relative intensity was set to 0.9 and each sample was subjected to UV-light for about 15 min, i.e. the duration of the entire printing process.
The collected gel percentage values were averaged; the results are reported in the next table (*Table 3.2.6*), where, for a comparison, the data obtained for the cast samples made of the same material but without silica, are also reported.

Material type	*Gel percentage Print [%]*	*Gel percentage Cast [%]*
UV-curable	74.06 ± 5.02	78.05 ± 4.73
Dual-curable	100.00 ± 0.00	99.90 ± 0.02

Table 3.2.6 Gel percentage results (mean and standars deviation values are reported) obtained by performing the test on printed samples. In the last column, the data previously obtained for cast samples are reported.

The gel percentage values obtained for the printed samples showed what already found for the cast samples: the dual-cure technique appeared once again to be the most efficient. The hypothesis of being able to obtain a complete monomer conversion for bulk UV-curable material only by exploiting the UV-induced layer by layer polymerization was not confirmed. Indeed, about 25% wt of material still remained uncrosslinked; the resulting loss of epoxides in acetone, solvent used for the sample immersion, was confirmed by the FTIR analysis conducted on the solvent residual solutions. In the FTIR spectrum reported below (*Graph 3.2.6*), the characteristic epoxy-peaks at 788 cm^{-1} and 746 cm^{-1} are clearly visible.

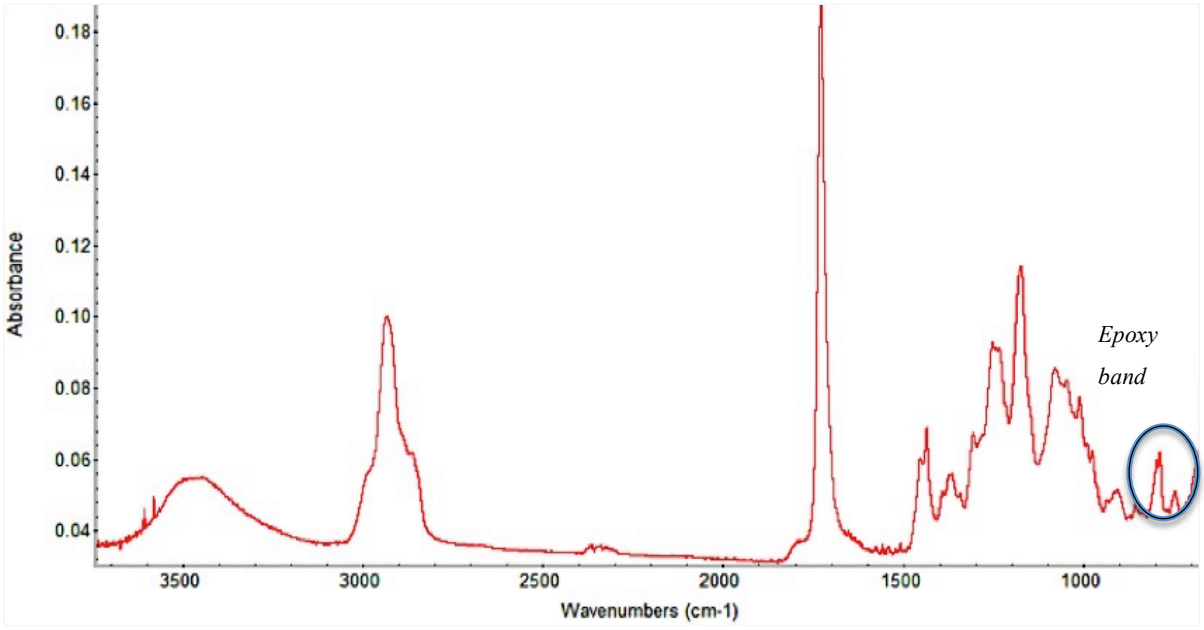

Graph 3.2.6 FTIR spectrun of residual acetone, used in the gel percentage test.

Instead, as expected, the double curing-treatment of the dual-cure formulation enabled an effective polymerization of the residual epoxy, leading to a 100% gel percentage.

After the analysis of the matrix materials, the SFR-composites were also tested. In particular, for what concern the glass-composites, only the formulations with the lowest (10% v/v) and the highest (50% v/v) fibers content were considered. For the print of the rectangular models, a 1.041 mm conic nozzle was used and, the following printing parameters were set: layer height 0.25 mm, flow 100%, print speed 12.5 mm/s for the glass-composites and 5 mm/s for the bamboo and the carbon-composites, and the maximun available UV-intensity was set. The glass-composites prints lasted around 25 min for each sample, while the prints of the composites containing the carbon and bamboo fibers lasted more than 45 min.

As before, the calculated gel percentage values were averaged and the results are reported in the following table (*Table 3.2.7*).

Material type	***Gel percentage Print [%]***
FILL100-10	100.00 ± 0.00
FILL100-50	100.00 ± 0.00
FILL200-10	100.00 ± 0.00
FILL200-50	100.00 ± 0.00
BAMBOO-10	82.00 ± 2.30
PX35-10	77.50 ± 3.06

Table 3.2.7 Gel percentage results (mean and standars deviation values are reported) obtained by performing the test on SFR-composites printed samples.

Analyzing these results, it was possible to confirm what already found with the "drops on glass" test and photo-DSC analysis (*§ 3.1.3.1*). The presence of white-transparent fillers, such as glass fibers (FILL 100, FILL 200), did not alter the curing speed of the dual-cure polymer-based SFR-composites, thus enabling an effective UV-3D-printing process, thanks to which completely crosslinked samples could be obtained. Instead, with shielding fibers, such carbon and bamboo, the effectiveness of the UV-3D-printing process resulted reduced; as confirmed by the lower gel percentage values, the PX35-10 and the BAMBOO-10 samples were not completely crosslinked.

➢ Optical microscopy inspection

In the attempt to investigate the effect produced by the 3D-printing process on fibers orientation, some wet filaments of SFR-composites were deposited on slides and they have been observed with the optical microscope.

Below, the magnifications of the SFR-composites filaments with a fiber content of 50% v/v (only in the case of glass-composites) and 10% v/v are shown.

The optical microscopy analysis showed that the fibers embedded in the polymeric matrix tended to be partially oriented in the direction of extrusion (*Figure 3.2.7 - 3.2.9*).

As it can be seen by comparing the images shown below, this orientation appeared more pronounced in the inks with higher fiber content. This behavior could be explained by the possibility for these formulations of a greater packing of the fibers due to a lower amount of matrix between them.

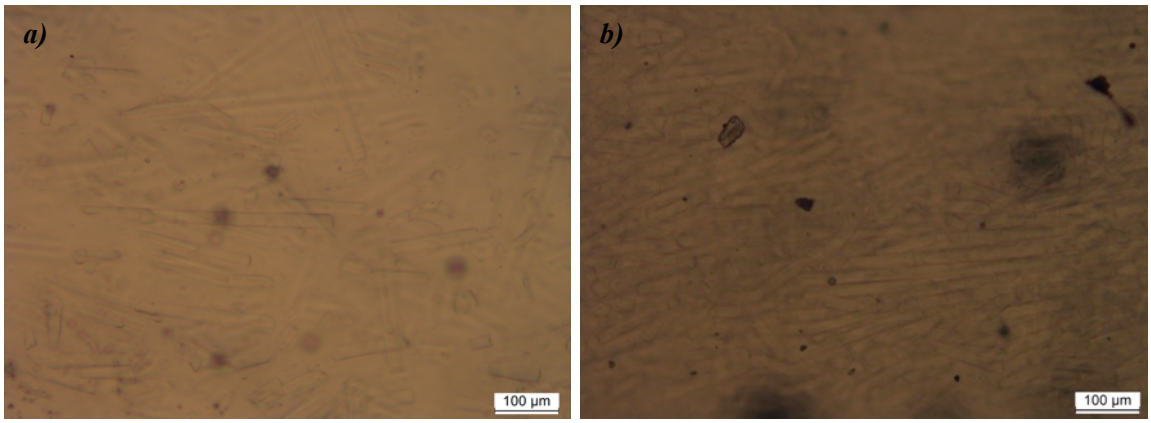

Figure 3.2.7 Optical microscopic images (20x magnification) of a) FILL100-10; b) FILL100-50.

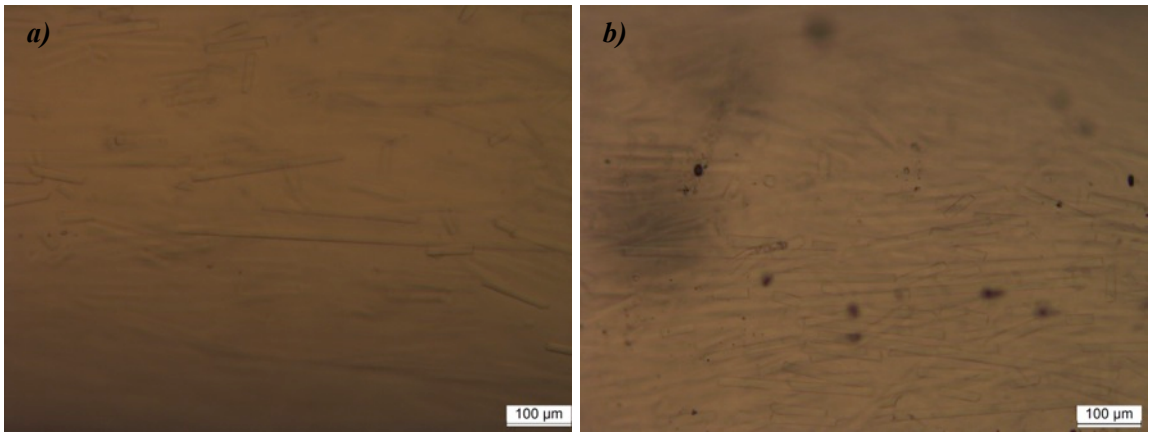

Figure 3.2.8 Optical microscopic images (20x magnification) of a) FILL200-10; b) FILL200-50.

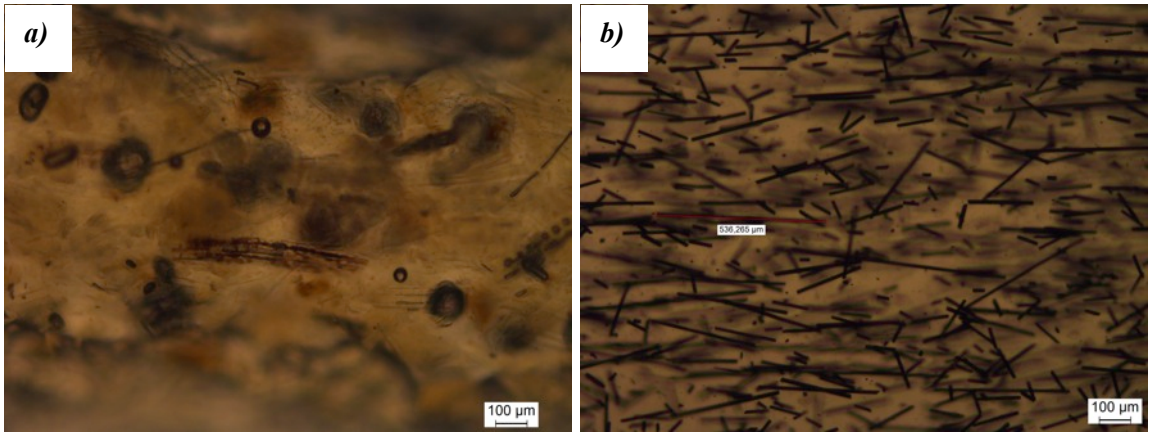

Figure 3.2.9 Optical microscopic images of a) BAMBOO-10 (20x); b) PX35-10 (10x).

As it can be noted from the images shown above, all the fibers were characterized by a regular cylindrical geometry except the bamboo ones that presented irregular shape with different sections. This irregularity was also reflected in a lower fibers orientation.

3.3 Mechanical response

3.3.1 Dual-curable matrix

Generally, polymeric composite materials exhibit naturally viscoelastic behaviour; this means that they show a combination of both elastic and viscous attitude.
The characterization of these materials should include both static mechanical properties like tensile, and dynamic mechanical properties such as storage modulus, loss modulus and loss factor.
In this experimental work, whose last goal is the mechanical characterization of UV-3D printed SFR-composite materials, the analysis was first focused on the study of the dynamic and static mechanical properties of the dual-cure epoxy system, specially formulated to be used as matrix for the fabrication of SFR-composites.
In order to assess the mechanical response of the material in relation to the type of process to which it is subjected and thus, the effect produced by the silica added to make the material printable, the analyses were carried out both on samples prepared by casting that on UV-3D printed ones. The obtained results are presented in the following paragraphs.

3.3.1.1 DMA analysis

The mechanical behavior and thermal trasitions of the dual-cure epoxy material were preliminarily investigated by means of DMA analysis. Cast (*pt-ES3MA cast)* and UV-3D-printed samples (*pt-ES3MAOX20011 print*) were prepared as explained in the paragraph *§ 2.3.4.1*.
The resulting experimental values for the storage modulus E' at room temperature and the temperature at which the *tan(δ)*, ratio between loss and storage modulus of the material, presented the maximun peak, are summarized in the next table (*Table 3.3.1*), where the glass transition temperature T_g, measured with DSC method, is also reported.

	E' at T_{room} [GPa]	Max tan(δ)	$T_{g,DSC}$
pt-ES3MA cast	3.71 ± 1.03	160	-
pt-ES3MAOX20011 print	5.21 ± 0.08	150	140

Table 3.3.1 Storage modulus E' and temperature at the tan(δ) peak as obtained from DMA, and T_g as measured via DSC of crosslinked dual-cure epoxy resin processed by casting and by UV-3D-printing.

From these results, it can be deduced that the UV-3D printing process was more efficient to confer greater desirable mechanical properties to the processed material. This higher efficiency can be due to the "*layer by layer photopolymerization*" and the introduction of silica, filler which must be necessarily added to the liquid formulation in order to make it printable. In fact, despite the amorphous and highly-crosslinked epoxy systems are known to have many useful properties for structural engineering applications, such as high modulus and failure strength, and good performance at elevated temperatures, their are also characterized by highly undesirable brittle behavior, which can be controlled by the incorporation of some second microphases [52], [107], [108]. This is exactly what it was done with the addition of silica OX200 in the dual-cure material in order to swicth from casting to 3D-printing process. As it can be noted from the values in the table, the silica-containing printable ink, presented an increased modulus. The slightly lower glass transition temperatures (max tan(δ) value) for the printed material may be related to the different type of process to which the material has been subjected, and not to the presence of the silica.

The mechanical investigation of the matrix dual-cure material continued with the analysis of the static tensile properties.

3.3.1.2 Uniaxial tensile test

In order to investigate the tensile response of the epoxy dual-cure system, several specimens were prepared. Also this time, the two fabrication processes have been employed. Two series of dumbbell specimens, one made of liquid dual cure *pt-ES3MA* solution and the other made of silica-added *pt-ES3MAOX200-11* material, were obtained by casting the material in a silicone mould. Other samples were prepared by depositing the *pt-ES3MAOX200-11* material layer by layer using the UV-3D-printer. In particular, the 3D printed specimens were produced according to two different geometries: the dumbbell and the rectangular one. This last, is exactly the same adopted for testing the mechanical properties of the SFR-composite inks (*§ 2.3.4.2*, *RDFO* type specimens). Indeed, the choice to adopt

such a geometry also to test the matrix material, usually tested only with dumbbell geometry, is derived precisely from the necessity to make a correct analysis of the variation of the mechanical response of the epoxy system to the addition of fibers, without having the influence of a different geometry.

Representative stress-strain curves for the tested samples are plotted in the following graph (*Graph 3.3.1)*

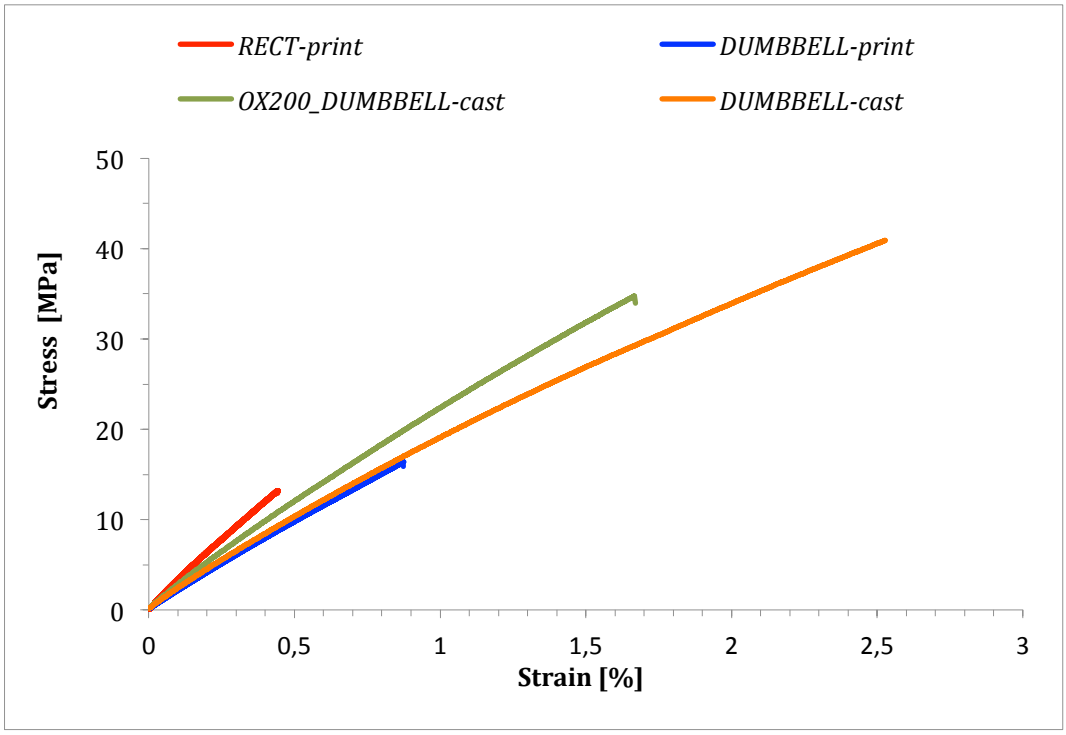

Graph 3.3.1 Representative stress-strain curves of UV-3D printed and cast samples made of dual-cure material.

As it can be noted from the graph, the dual-cure polymeric matrix presented a pronounced linear elastic behavior with brittle fracture.

The average values ef elastic modulus (tangent modulus at 0.05% of deformation), ultimate tensile strength and deformation at break obtained from the tensile tests are presented in the next graph (*Graph 3.3.2 (a)-(c)*).

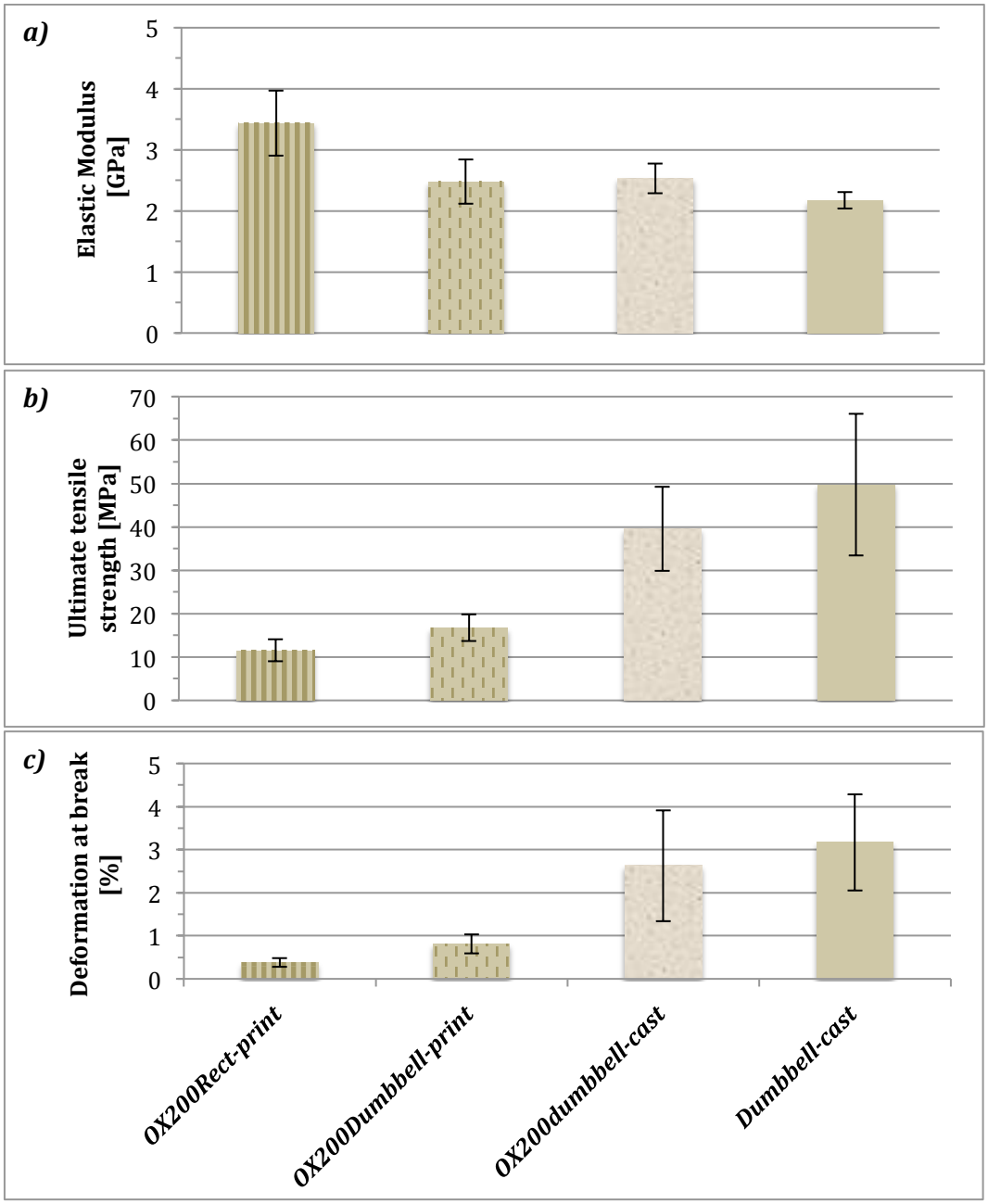

Graph 3.3.2 Average values of a) elastic modulus, b) ultimate tensile strength and c) deformation at break.

As evident from the previous graph (*Graph3.3.2*), the sample geometry affected a lot the mechanical response of the dual-cure material. Indeed, focusing the attention on the results obtained from tests performed on printed samples, it can be noted that the rectangular sample presented the best performance in terms of elastic modulus (3.44 GPa) but worst values for ultimate strength and deformation were obtained with this geometry. Instead, for the dumbbell geometry, lower elastic

modulus was found but better results in terms of ultimate strength and deformation at break were collected.

By comparing the results obtained for the UV-3D printed dumbell specimens and for those prepared by casting the *pt-ES3MAOX200-11* material, it is possible to see that, despite the elastic modulus of the printed ones was comparable with that found for the corresponding cast, which lied in the range of 2.5 GPa, the first showed lower tensile strength (16.8 MPa vs 39.5 MPa) and deformation at break (0.8% vs 2.6%). Such behavior could be caused by the presence inside the UV-3D printed samples of small imperfections, such as micro-voids procured by small air bubbles probably trapped in extruded filament.

Moreover, looking at the elastic modulus results for the cast dumbbell with and without silica content, it can be noted that, as already found with the DMA analysis, the presence of silica tended to slightly increase the elastic modulus of the unfilled material (*Graph 3.3.2 (a)*). Unfortunately, this improvement did not appeared neither for the tensile strength nor for the strain at break. Indeed, the presence of silica in the material seemed to give lower values of deformation and ultime strength, although this may not be statistically significant given the large standard deviations registered for these values (*Graph 3.3.2 (b),(c)*).

All these results suggest that in general, the UV-3D printing process allows to obtain properties which, although lower than those obtainable with a cast process, however, are good for a material that will be used as matrix for the development of SFR-composite structures [47], [48], [51], [52], [69].

3.3.2 Fiber reinforced composites

Composite materials, due to their multiphase composition, have peculiar characteristics that distinguish them from the traditional structural engineering materials. Although some of their features may be seen as a variation of the conventional materials behavior, others are completely new. Therefore, new proper analytical models are required for the description of structural behavior of composites materials. To this end, it has been developed a wide range of models able to predict the elastic properties of the fiber-reinforced composites as a function of the properties of the constituents materials and the fiber-reinforcement geometry. An approach of this type is generally denoted by the term '*micromechanics*'.

In this thesis work, the Halpin-Tsai model for nearly random and discontinuous fiber-reinforced polymers was adopted to compare the experimental results with the theoretical prediction of the elastic modulus of the developed SFR-composite systems.

The Halpin-Tsai model is a simplified analytical form of Hill's generalized self-consistent model[14] with engineering approximations to make it suitable for the designing of composite materials [109]. Halpin and Tsai rearranged the formulae resulting from exact theory of elasticity to conform to a generalized equation, that is:

$$E_c = E_m \frac{1 + \eta\zeta v_f}{1 - \eta v_f} \qquad (3.7)$$

where E_c, E_f, E_m are the elastic modulus of the composite, of the fibers and of the matrix, respectively. The v_f is the fibers volume fraction, and η and ζ are two parameters that introduce the features of both matrix and fibers.

The first, η, can be expressed as:

$$\eta = \frac{E_f/E_m - 1}{E_f/E_m + \zeta} \qquad (3.8)$$

The second, ζ, depends on the geometry and boundary conditions of the reinforcing phase. For a composites reinforced with short and aligned fibers, at a low volume fraction ($v_f < 0.7$), this parameter can be expressed as:

[14] Hill assumed a composite cylinder model in which the embedded phase consisted of continuous and perfectly aligned cylindrical fibers. Both materials were assumed to be homogeneous and elastically transversely isotropic about the fiber direction [109].

$$\zeta = 2\left(l/d\right) \qquad (3.9)$$

where *l* and *d* are the length and the diameter of the reinforcing fiber, respectively.

As done for the dual-cure polymeric matrix, the characterization of the mechanical response of the developed SFR-composites materials was performed by DMA analysis and by uniaxial tensile tests. The collected experimental data are presented in the following paragraphs together with the theoretical prediction obtained through the above Halpin-Tsai equations.

3.3.2.1 DMA analysis

The dynamic mechanical behavior and the thermal transitions of the SFR-composite dispersions were investigated by performing DMA analyses on rectangular samples. In this case, only UV-3D printed samples were analyzed because the thick cast specimens could not be produced due to incomplete polymerization of such samples. In fact, as already explained, specially in case of larger samples containing carboon or bamboo fibers, the UV-curing reaction was difficult due to the UV-shielding effect of these fibers that partially hampers UV light from being absorbed by the sulfonium photoinitiator, thus preventing the liquid ink from being efficiently UV-cured.
For each composite material, the UV-3D printed samples were prepared as descibed in the paragraph *§ 2.3.4.1*. The experimental results of storage modulus E' at room temperature and those of temperature at *tan(δ)* peak are summarized in the table and graph below (*Table 3.3.2, Graph 3.3.3*).

	E'_{exp} *at* T_{room} *[GPa]*	*Max tan(δ) [°C]*
pt-ES3MAOX20011 print	5.21 ± 0.08	150
FILL 100-10	6.67 ± 0.13	153
FILL 100-25	7.45 ± 0.50	135
FILL 100-40	9.83 - 25.56 (T_{room})[15]	162
FILL 100-50	12.94 ± 1.54	158
FILL 200-10	5.58 ± 0.41	152

[15] In case of FILL100-40 the storage modulus values obtained by isothermal DMA (T room) and DMA in temperature scan (from -20°C to 250°C) resulted very different: 25.56 GPa and 9.83 GPa were obtained, respectively.

FILL 200-25	7.17 ± 0.28	154
FILL 200-40	9.75 ± 0.72	150
FILL 200-50	4.65 - 12.36 (T_{room})[16]	147
BAMBOO-10	4.84 ± 1.39	130
PX35-10	6.86 ± 1.00	100

Table 3.3.2 Storage modulus E' and temperature at the tan(δ) peak as obtained from DMA analyses performed on UV-3D printed samples of SFR-composites.

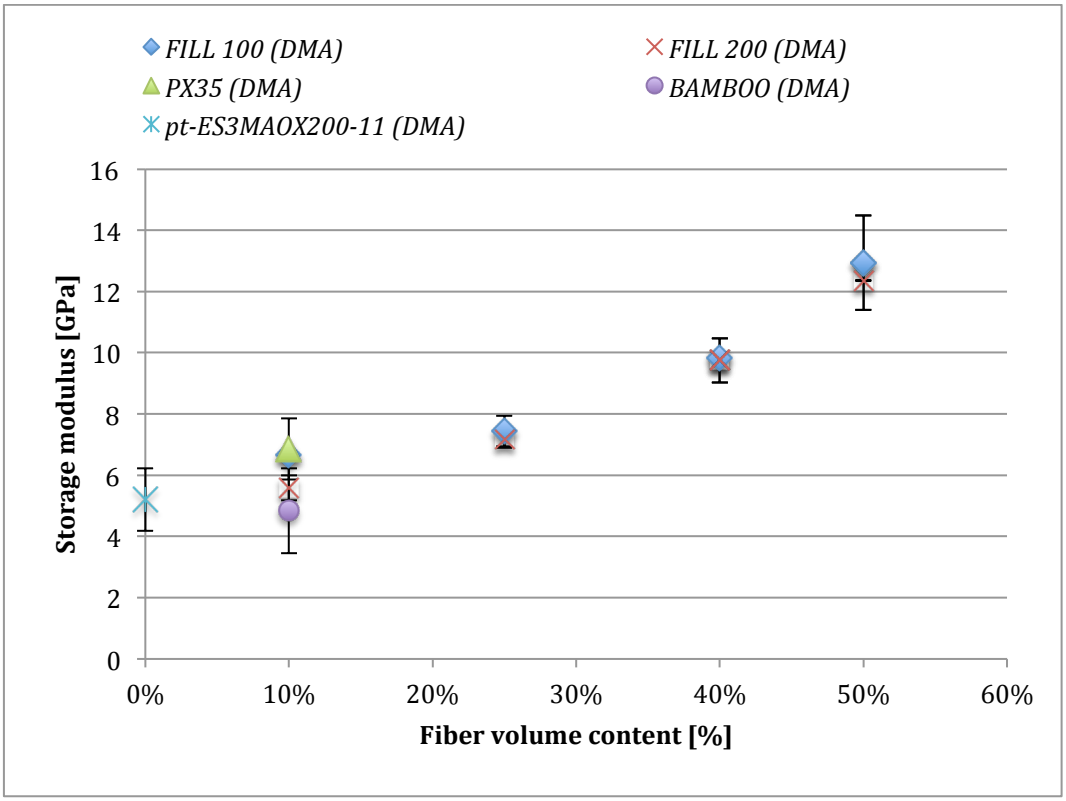

Graph 3.3.3 Storage modulus obtain by DMA analysis. The value of 25.56 GPa and 4.65 GPa, related to FILL 100-40 and Fill 200-50, respectively, are strange results. As they not follow the incresing trend, they will be not considered as valid data and are not reported in this graph .

According to the obtained results, it can be possible to affirm that the addition of fibers to the dual-cure polymer material conferred enhanced mechanical properties to the printed parts if the content of

[16] In case of FILL200-50 the storage modulus values obtained by isothermal DMA (T room) and DMA in temperature scan (from -20°C to 250°C) resulted very different: 12.36 GPa and 4.65 GPa were obtained, respectively.

fibers is greater than 10%v/v. A slightly increase in the storage modulus can be noted at lower fiber volume fractions (10%v/v) only in case of FILL 100 and PX35. Indeed, from an average value of 5.21 GPa for the *pt-ES3MAOX20011* material matrix, the storage modulus passed to 6.67 GPa and 6.86 GPa in case of composites reinforced with 10% v/v of FILL100 and PX35, respectively. Only for the bamboo-reinforced composite material, a slight decrease of storage modulus was found. This could be due to a lower UV-light curing of the sample, as confirmed by gel percentage analysis (*Table 3.2.7*) or due to the inhomogeneity of such fibers (see *Figure 3.2.9 (a)*).

As shown in the *Graph 3.3.3*, a gradual increase of the storage modulus was registered for mixtures with higher glass-fiber volume fractions.
Strange results were obtained in case of FILL 100-50 and FILL 200-40; in fact, the data obtained by isothermal DMA analysis and those resulting from DMA in temperature scan were very different between them. This could due to a measurement error. Unfortunaly, for the DMA analysis only two specimens were prepared thus the measurements could not be repeated. The value 25.56 GPa and 4.65 GPa, could not be considered as valid results.
On the basis of the average values and considering also the standard deviation for each one, it can be affirmed that the best result for inks reinforced with shorter glass-fiber was obtained at a fiber volume fraction of 50% v/v, with a mean storage modulus of 12.94 GPa in case of FILL 100, and a measured value of 12.36 GPa in case of FILL 200.

Although the mechanical properties of the dual-cure polymeric material resulted improved by the fibers content, no significant variation of T_g (temperature at the *tan(δ)* peak) was recorded during the DMA analysis of SFR-composite samples.This could be an indication of the fact that the polymeric matrix (pt-Es3MAOX200-11) was not altered in any way. In fact, if for the matrix was obtained a T_g value of 150° C, the values recorded for SFR-composites were only a few degrees or a maximum of ten degrees higher. Moreover, no particular trend could be noted at varying the concentration of fiber in the materials.
As found for the storage modulus, also in this case, the values of T_g of the composites reinforced with carbon and bamboo fibers resulted much lower than those obtained for the glass fibers and, even smaller than 150° C. This fact further confirmed the partial photopolymerization of those samples.

A further investigation of the mechanical properties of the developed SFR-composites was obtained by performing uniaxial tensile tests on UV-3D printed specimens. In the following paragraph the tensile response of the composites will be presented.

3.3.2.2 Uniaxial tensile test

A further investigation of the mechanical properties of the developed SFR-composites was possible by performing uniaxial tensile tests on UV-3D printed specimens.
In order to evaluate the effect of the filament printing direction and to demonstrate the potential of UV-3D printing in processing complex geometry, two different UV-3D printed samples for tensile test were prepared (*§ 2.3.4.2*).
The 100% infill RDFO type specimens were produced for all the developed SFR-composites inks, i.e. FILL 100, FILL 200, BAMBOO and PX35 at increasing the volume fraction of fibers. Instead the cellular (triangular lattice) type samples were UV-3D printed only with FILL 100-40[17] ink. Each sample was tested at a tensile speed of 1 mm/sec with a pre-load of 2N.

- **100% infill RDFO specimens**

The measured values of elastic modulus (tangent modulus at stress-strain curve in the point corresponding to 0.05% of deformation), the maximun tensile strength and deformation at break for each type of SFR-composite material were averaged and the obtained results, with the standard deviations, are plotted in order to compare the behavior conferred to the dual-cure materials by different type of fibers and also to evaluate the mechanical response of composites reinforced with the same type of fiber increasing their volume fraction.
However, a theoretical prediction of the mechanical response of such composite materials was obtained by following the Halpin-Tsai model, previously described. In order to calcultate the theoretical elastic modulus for the SFR-composites the Halpin-Tsai equation, *Eq. 3.7,* was fitted setting for the matrix elastic modulus the value measured in the case of rectangular UV-3D printed specimens, that is E_m = 3.44 GPa (see *Graph 3.3.2 (a)*). For the variables related to the fiber features, such as modulus, dimensions, and thus the parameters ζ and η, the used values are reported in the next table (*Table 3.3.3*).
In particular, the data related to the dimensions of the carbon and glass fibers were taken from the data sheets provided by their suppliers. Instead, as regards the bamboo, the average values of length and diameter were obtained from measurements carried out by the optical microscope analysis of some samples of BAMBOO-10 ink (*Figure 3.3.1*).

[17] This particular ink is chosen for printing cellular geometry because it shown the best results in terms of strength and elongation at break, during the tensile tests of rectangular 100% infill specimens.

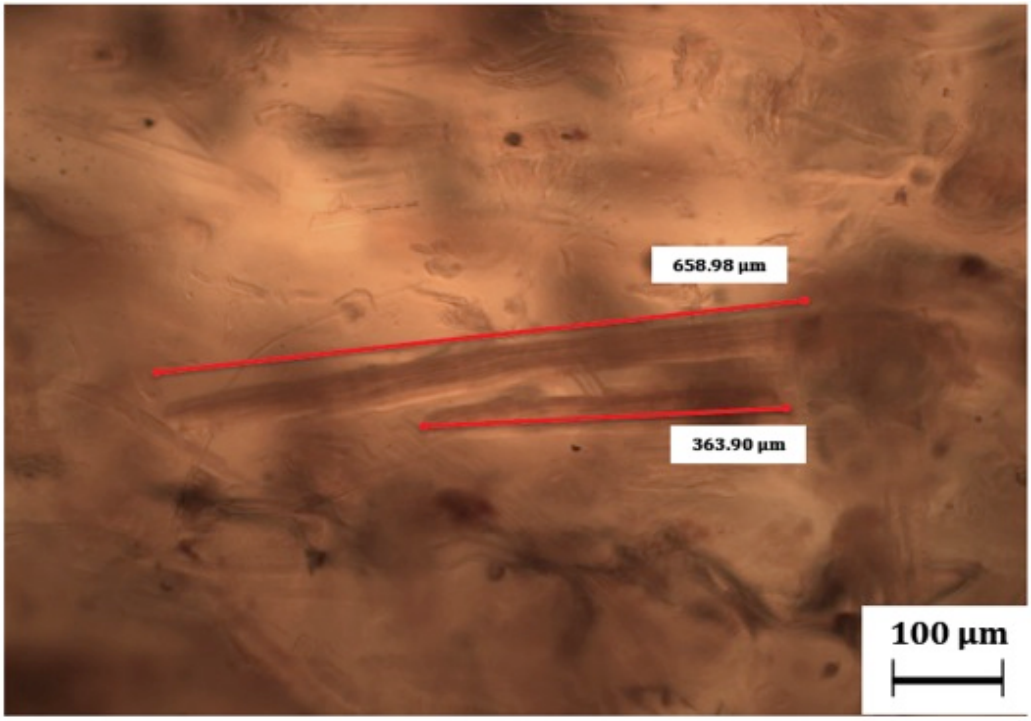

Figure 3.3.1 Microscopic image (100x magnification) of banboo fibers embedded in the duel-cure polymeric matrix.

	E_f [GPa]	l [µm]	d [µm]	ζ	η
FILL 100	75	100	13	15.38	0.56
FILL 200	75	200	13	30.77	0.40
BAMBOO	20	500	60	16.67	0.21
PX35	200	150	7.2	41.67	0.57

Table 3.3.3 Values of parameters used for fitting the Halpin-Tsai equation.

Below, representative stress-strain curves for the RDFO type tested samples (only the curves related to samples containing 10% v/v of fibers are here plotted) are shown (*Graph 3.3.4)*.

Just from this graph it can be noticed that even the SFR-composites presented a brittle behavior. It is possible to see that only in case of glass fibers the mechanical response of the dual-curable polymeric material seems to be improved in terms of increased tensile strength and elongation at break. The elastic modulus seems to be very similar to the one of the matrix.

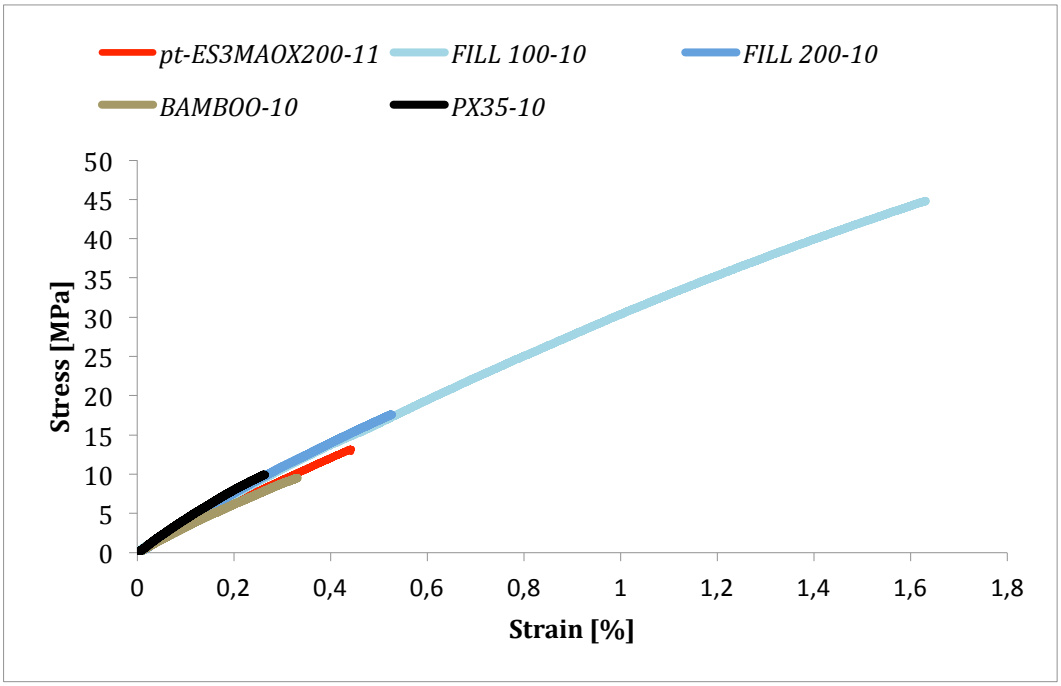

Graph 3.3.4 Representative stress-strain curves of RDFO-type UV-3D printed sample made of SFR-composites (10% v/v of fibers) The red line refers to sample made of dual-cure polymeric matrix.

More detailed results are shown in the next graphs, where it is possible to observe how fibers of different nature and size modify the mechanical response of a composite material. In fact, the results obtained for the inks reinforced with short glass fibers (FILL 100, FILL200), the short carbon fibers (PX35) and the bamboo ones (BAMBOO), showed differences in terms of elastic modulus and mostly in strength and deformation.

However, from these graphs it is evident that the fiber volume fraction is an important parameter in the determination of the mechanical response of the SFR-composite materials.

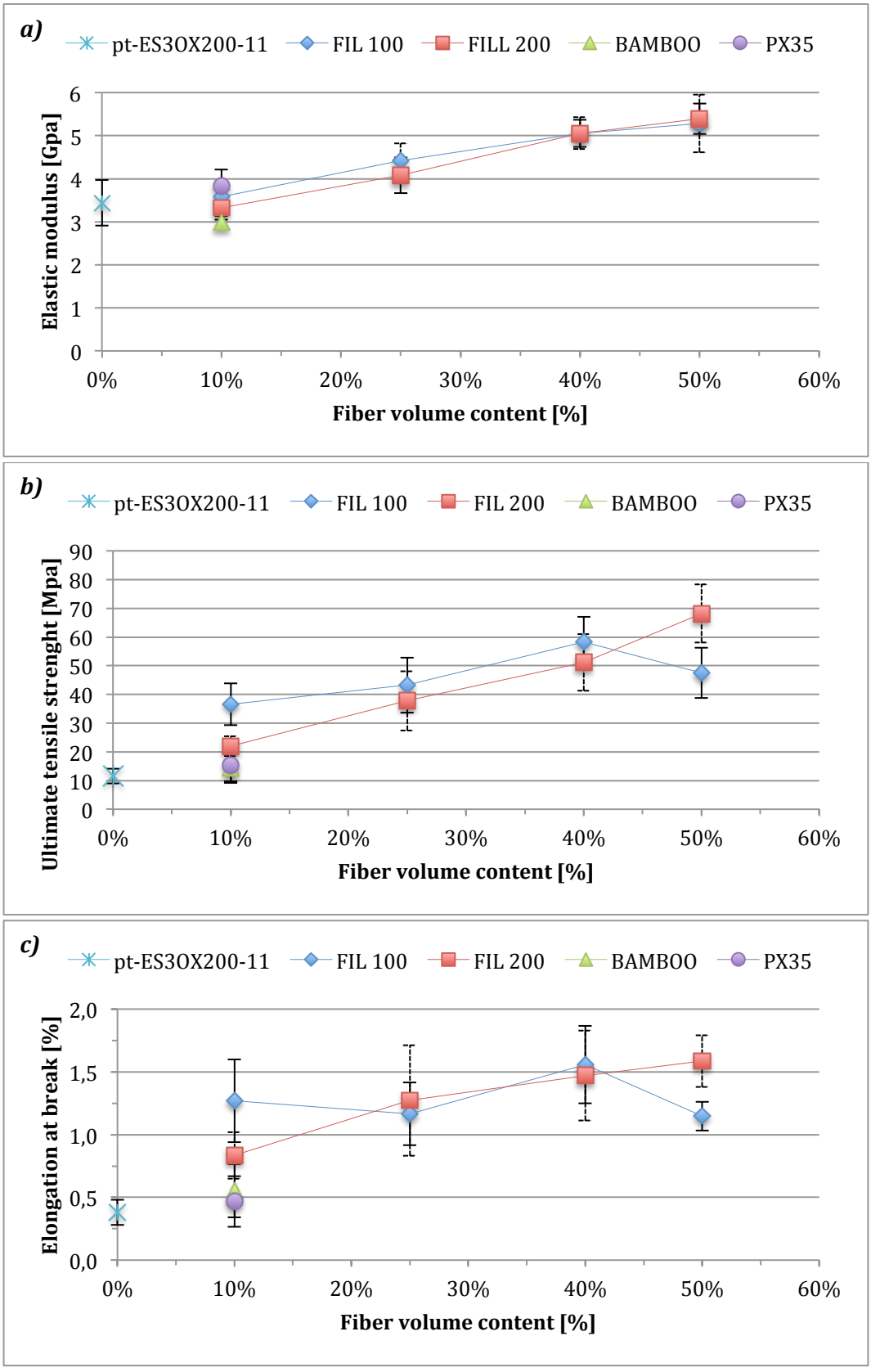

Graph 3.3.5 Average values of a) elastic modulus, b) ultimate tensile strength and c) deformation at break for composite specimens.

Focusing the attention on the group of inks with 10% v/v of fiber content, it can be seen that, although the values of the elastic modulus did not seem to vary a lot from fiber to fiber, in fact all of them lay in the range 3-4 GPa, a significant difference in the ultimate tensile strength and deformation is shown specially for the FILL 100 with respect to the other composite formulations. In general, best results were obtained for the glass-reinforced composites that resisted up to 36.6 MPa, in the case of FILL 100, and up to 22 MPa, in case of FILL 200, deforming also almost double compared to composites reinforced with bamboo and carbon, respectively. The lower efficiency of the latter two could be explained by the fact that, as previously shown, the inks reinforced with such fibers appeared to be not completely photopolymerize due to the UV-shielding effect.

Another usual composites behavior can be observed in the previous graphs. Indeed, focusing the attention on the results obtained for all the glass-fiber reinforced inks, the FILL 100 and the FILL 200, it can be observed that the increase in fiber content, from 10% v/v up to 50% v/v, led to a general increase of the mechanical properties of the materials. Such trend, more pronounced in the case of the FILL 200, was demonstrated in increased modulus from 3.3 GPa to 5.4 GPa going from the lowest concentrations to the highest one. The ultimate tensile strength values rised from 22 MPa to 68.2MPa and, finally, the deformation at break resulted doubled going from 0.8% to 1.6%. In general, looking at the error bars reported in the graphs above, it is possible to note that, for each of these quantities, only a gradual increase was recorded.
In the case of FILL 100 inks, a gradual increase with increasing fiber volume fraction was found for both the elastic modulus and the ultimate strength while the strain at break did not show a specific trend. In fact, the modulus increased from 3.6 GPa of the FILL 100-10 ink to 5.3 GPa of the FILL 100-50; the maximun tensile strength rised from the value of 36.6 MPa for the less loaded ink to 58.2 MPa of the FILL 100-40. An unexpected lower value was observed for the ink reinforced with 50% v/v of fiber, whose strength went down to 47.5MPa. The deformation at break for the FILL 100 inks tended to lie at values close to 1.2% for all fiber content. Only in the case of the 40% v/v, the elongation seemed to reach an higher value but its large standard deviation confirmed the costant value around 1.2%.

According to the analytical model developed to design the fiber-reinforced composites, the mechanical properties of such materials generally increase with the increasing of fiber length [109]. What we can see from the above graphs is not in agreement with the usual behavior of composites. In fact, the fibers with double length, FILL 200, showed lower or equal mechanical properties with respect to the FILL 100. This behavior, also showed during the DMA analysis (*§ 3.3.2.1*), can be explained by the fibers break that could take place during the processing of the inks. This phenomenum can generally result

from fiber-polymer interaction, fiber-fiber interaction, and fiber contact with surfaces of processing equipment [66]. This last case could be what happened to the 200 μm glass fibers during extrusion of the corresponding composite inks through the conic metal nozzle. In fact, as already shown in the microscopic images of an extruded filament (see *Figure 3.2.8*), some fibers were broken and therefore the shorter fiber length reduced the fiber reinforcing efficiency.

At the end, a comparison between the values of elastic modulus experimentally obtained and those computed by the Halpin-Tsai equation is reported. The values for each type of developed ink are listed in the *Table 3.3.4*.

	E_{exp} [GPa]	$E_{Halpin\text{-}Tsai}$ [GPa]
pt-ES3MAOX20011 print (rect)	3.44 ± 0.53	-
FILL 100-10	3.58 ± 0.28	6.78
FILL 100-25	4.42 ± 0.40	12.60
FILL 100-40	5.06 ± 0.37	19.69
FILL 100-50	5.28 ± 0.67	25.33
FILL 200-10	3.32 ± 0.27	7.94
FILL 200-25	4.08 ± 0.41	15.44
FILL 200-40	5.06 ± 0.32	23.99
FILL 200-50	5.40± 0.36	30.40
BAMBOO-10	2.98 ± 0.15	4.77
PX35-10	3.83 ± 0.39	12.35

Table 3.3.4 Elastic modulus of SFR-composites: the measured values and the predicted ones are reported for comparison.

Measured moduli for composites were found to be systematically lower than the limiting theoretical values. Also in this case, a possible explanation for such discrepancies may be given by the fibers breakage during the extrusion. This brings to an overestimation of the fiber aspect ratio *l/d* in the actual sample. Moreover, the lower measured mechanical properties could be due to a less strong chemical interaction between fiber and matrix: indeed the fibers were not chemically treated before their addition in the dul-curable material.

Nevertheless, the experimental values found for the SFR-composites systems investigated in this work are in good agreements with experimental results reported in the literature about composites system reinforced with the same type of fibers [48], [51], [52], [66], [69].

In conclusion, the mechanical analyses, both the dynamic and the static one, suggested that the glass-fibers, and in particular the FILL 100, are the best candidate for the development of composites to be processed with a UV-assisted 3D printing process. Below, in the *Graph 3.3.6,* the mean values of elastic modulus obtained by both the DMA and the tensile tests are shown for comparison.

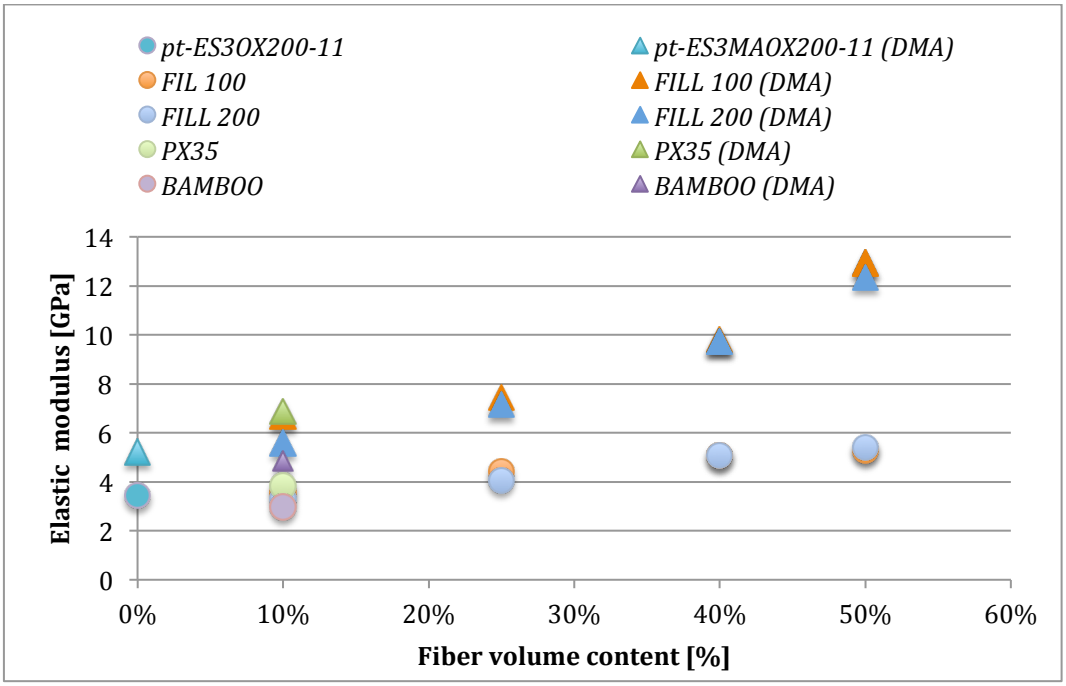

Graph 3.3.6 Elastic modulus obtain by performing tensile tests (points) and DMA analysis (triangle) on SFR-composites. The data about the matrix are also reported for comparison. In this graph the error bars are not reported for a better visualization of the data. The exact standard variation from the mean values are already shown in the Grapgh 3.3.3 and Graph 3.3.5 (a) for DMA and tensile test, respectively.

From this graph it is possible to note that there is differences in the values of elastic modulus measured by the two techniques. In the case of DMA analysis, the results showed an evident increasing trend as the fiber volume fraction increases while the moduli values collected by performing tensile test were lower and little different from each other.
This results are not conflicting: indeed the DMA works in micrometric deformations, while zwick instrument subjects the sample to loads that are closer to those that the material should support in real applications.

➢ Triangular unit cell specimens

Uniaxial tensile tests were also performed on the samples which present a triangular unit cell type infill, prepared as described in paragraph *§ 2.3.4.2*. The collected results are reported below.
In particular, in the *Graph 3.3.7,* the obtained stress-strain curve is presented. In *Table 3.3.5*, the mean values with the corresponding standard deviations of the elastic modulus (tangent at stress-strain curve in the point corresponding to 0.05% of deformation), maximun tensile strength and deformation at break obtained experimentally by tensile tests and those theoretically predicted are resumed.

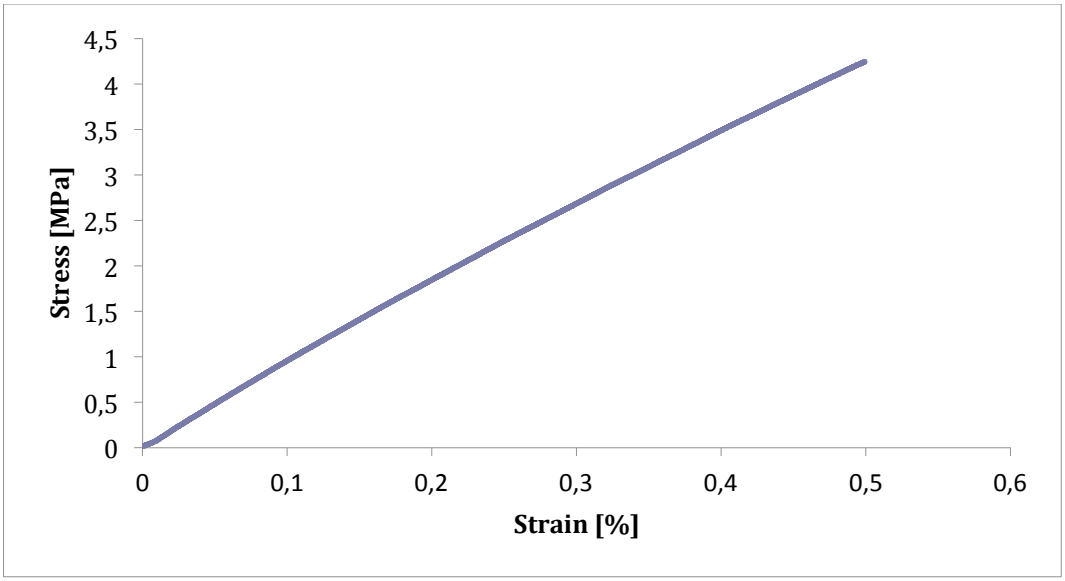

Graph 3.3.7 Stress-strain curve resulting from the tensile test of a FILL 100-40 sample with triangular infill.

In order to predict the mechanical properties of the cellular material, the scaling laws governing the elastic modulus and strength of triangular honeycombs have been adopted.
The elastic modulus was calculated according to the *Eq. 3.10* while for the strength the *Eq. 3.11* was used.

$$E_c = E_s B \left(\frac{\rho}{\rho_s}\right)^b \qquad (3.10)$$

$$\sigma_c = \sigma_s C \left(\frac{\rho}{\rho_s}\right)^c \qquad (3.11)$$

where E_s, σ_s, ρ_s are the elastic modulus, tensile strength, and density of the base solid material (infill 100%), respectively. For a triangular lattice, B=C=1/3 and b=1. The value of c depends on the nature

of failure in the material; for the calculation reported in the following table, c=1 as the cell walls fail in uniaxial tension.

	Elastic Modulus [GPa]	Ultimate tensile strength [MPa]	Elongation at break [%]
Experimental results	1 ± 0.08	4.16 ± 0.42	0.61 ± 0,17
Theoretical results	0.66	7.62	-

Table 3.3.5 Mechanical properties of FILL 100-40 (triangular infill): the measured values and the predicted ones are reported for comparison.

From the data shown in the table above, it is possible to conclude that the cellular structures are somewhat weaker than the predictions based on scaling laws. The discepancy between the measured and predicted values can be attributed, in part, to geometric imperfections in the structures, such as micro voids and nodal misalignment [48].

Furthermore, by comparing the elastic modulus reported above with that obtained for the 100% filled RDFO samples, it can be affirmed the ability of UV-3D printing technology to control the mechanical response of a material simply by depositing it according to different infills. In fact, in case of completely filled FILL 100-40 sample (100% infill) the measured elastic modulus was the 25% of the predicted one (E_{test}= 5.06 GPa vs $E_{Halpin\text{-}Tsai}$=19.69 GPa); while the measured value for the sample with of triangular unit cell results to be the 66% of the theoretical one.

3.3.2.3 Fractured surface inspection

Trying to verify fibers' alignment conferred by the 3D-printing process during the extrusion of composites inks, the fractures surfaces of the SFR-composites tensile tested samples (100% infill RDFO specimens) were observed with an optical microscopy.

Below, the magnifications of some fractured surfaces are shown (*Figure 3.3.2 - 3.3.4*).

On the basis of the acquired images, it is possible to confirm what already seen during the inspection of wet extruded filaments (see *Figure 3.2.7 - 3.2.9*): the simple extrusion process appeared to be sufficient to confer a great orientation of the short fibers. Indeed, a clear alignment of the fibers in the proximity of the fracture can be noted.

Moreover, the presence of the matrix material on the fibers, particularly visible in *Figure 3.3.2 (b),* is a proof of the existing interaction between the matrix and the fibers themselves.

In *Figure 3.3.3 (b)*, two different sample's layers are shown. This can be seen as a sort of delamination of the printed layers during the tensile test.

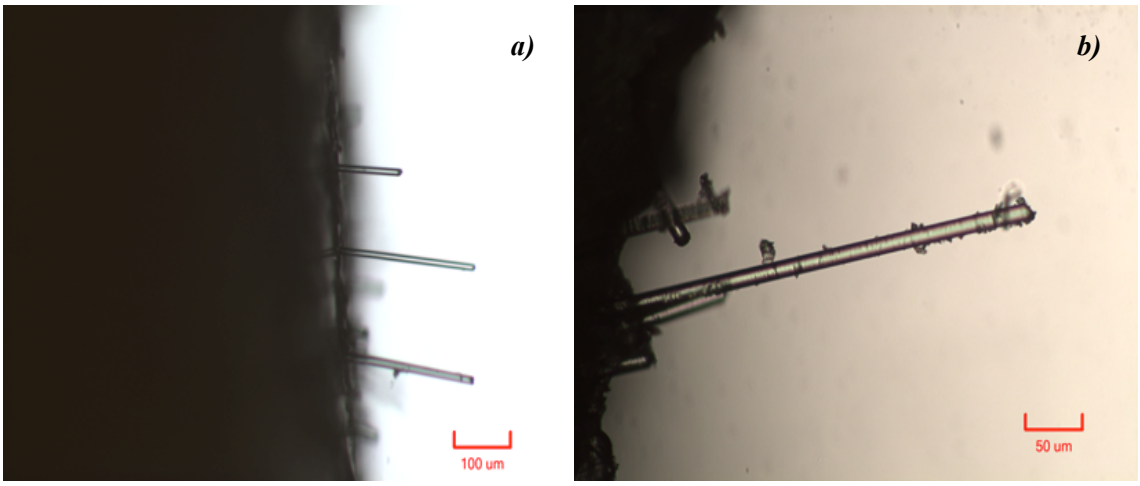

Figure 3.3.2 Microscopic images of fractured surfaces: a) FILL 100-10 (magnification 100x), b)) FILL 100-50 (magnification 200x).

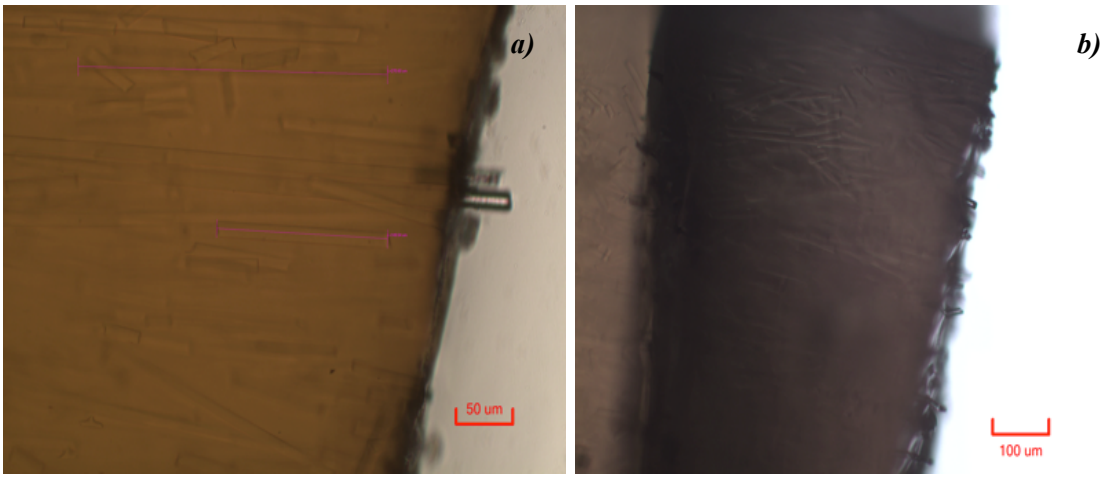

Figure 3.3.3 Microscopic images of fractured surfaces: a) FILL 200-10 (magnification 200x), b) FILL 200-10 (magnification 100x).

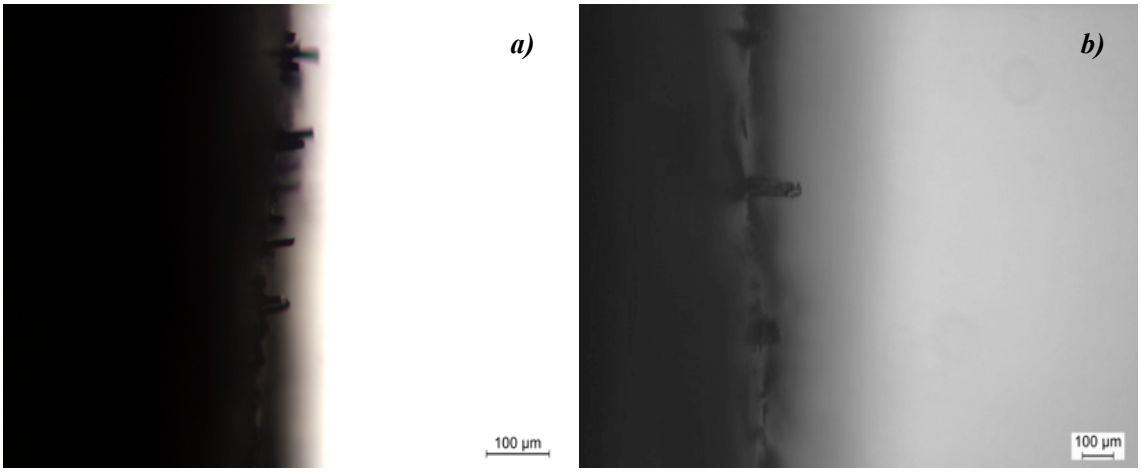

Figure 3.3.4 Microscopic images of fractured surfaces: a) PX35-10 (magnification 20x), b) BAMBOO-10 (magnification 10x).

CONCLUSIONS AND OUTLOOKS

Conclusion

Through the present experimental work, whose purpose was to develope photopolymer-based composite materials for use in UV-3D printing applications, it was possible to take note of the advantages and disadvantages of the LDM additive manufacturing methods.

The whole experimental work can be divided into three macro parts: formulation and characterization of photopolymer-based systems, specially optimized to be printed according to the LDM UV-3D printing technology; investigation of the effective LDM process capabilities by means of several printing trials; study of the mechanical response of printed specimens.

At the beginning, the experimental work was dedicated to the development of photopolymeric cationic systems to use as matrix material in SFR composites: an UV-curable epoxy system, the p-ES3, was primarily developed but, because its photopolymerization efficiency resulted too low, a new formulation based on dual-cure technique (the *pt-ES3MA*) was adopted. FTIR-spectroscopy, calorimetric and gel percentage analyses demonstrated that the highest efficiency could be achieved with this system subjected to a double sequential curing cycle consisting in a first UV-irradiation and a thermal treatment at 180° C for 1h.
In order to increase the viscosity of this Newtonian formulation and make it printable, an inorganic filler (fumed silica) was added at increasing concentrations. The rheological caracterization of these dispersions was performed and optimal extrusion and printability windows were identified calculating the shear-rate of the materials at the nozzle by applying the power-law relationships and the capillary flow model. The best solution adopted as matrix material was the one with a silica content equal to 11% by weight. Indeed this showed all the necessary requirements to be an optimal UV-3D printable ink: non-Newtonian shear thinning behavior with sufficiently high viscosity, rapid photopolymeization kinetics and high conversion efficiency. Based on this compound, glass (FILL 100 and FILL 200), carbon (PX35), and bamboo reinforced composites, at increasing fiber volume fraction, were developed.
Drop on glass and photocalorimetric measurements of the SFR-composite formulations demonstrated that a rapid curing reaction could be maintained only in case of inks reinforced with white-transparent

glass fibers. In contrast, the addition of the darker bamboo and carbon fibers, due to shielding effects (resulting from their chemical nature), negatively affected the thermodynamics and kinetics of the UV-curing process of the polymeric dual-cure matrix.

After the optimization of the printable materials, the work continued with the assembly of the UV-3D printer: a UV laser equipped with two optical fiber was assembled on the transversal bar of an already existing LDM low cost machine present at +LAB.
The best position of the optical fibers in respect to the extruded material, together with the optimal relative UV-light intensity to have a rapid photopolymerization of the inks were selected by performing drop on glass tests. It resulted that a distance equal or lower than 4 cm and relative UV-intensity grater than 0.7 were required to have rapid hardening (2 sec) of the deposited materials.
At this point, the research of the optimal printing parameters (layer height, print speed, flow percentage, etc) for the developed inks was conducted. In order to evaluate possibility of printing even complex geometries, a specific model with overhanging parts, the spiral cylinder model, was adopted and printability windows was determined: layer height 0.5 mm, print speed ranging from 5 to 7 mm/sec, flow 95-100% and relative UV-intensity ranging from 0.9 to 1.

In addition to the optimization of the material and process-related parameters, the final part of this thesis work was dedicated to the investigation of the mechanical properties of different samples fabricated via UV-assisted LDM. The mechanical analysis (DMA and tensile tests) of 3D printed specimens demonstrated that for some application, the LDM technology is still far from replacing the traditional production techniques. Indeed, despite the optimization of the parameters that generally affect the mechanical properties of 3D printed materials, such as print direction, layer height, degree of filling, orientation and amount of fibers, the properties of the composite samples obtained by LDM resulted lower with respect to the predicted values, which are normally reached in components fabricated with traditional technology.
All the sample showed brittle behavior and elastic modulus not much higher than that of the base matrix. Only the ultimate tensile strength and the deformation at break seemed to be improved. Among the four types of fibers selected for the SFR-composite inks formulation, the FILL 100 at a concentration of 40% v/v showed the best results.
However, the mechanical properties of the samples fabricated in this thesis experience are consistent with those found in other experimental works about the UV-3D printing of composite materials. In addition, the mechanical results obtained for the triangular unit cell composites demonstrate the possibility offered by the UV-3D printing to contol the mechanical response by simply varying the infill percentage and design of the structures.

In conclusion, this thesis represent the proof that the main advantages of the LDM 3D printing tecnology remain its lower cost, its ability to fabricate even very complex geometries and the possibility to print a wide range of materials, also reinforced with a lot of type of fibers, inorganic and organic. These characteristics represent the stepping-stone towards the possibility of becoming the technology of the future. If mechanical properties of the components obtained by 3D printing can be improved, this technology could become more than an alternative to traditional manufacturing processes.

Outlooks

During the development of the experimental work some difficulties have been appeared. In particular, the main problems were about the incomplete photopolymerization of some formulations, the presence of micro bubbles in the printable inks, the break of the fibers during the mixing step and their poor adhesion with the matrix and the excessive brittle behavior of the composites.

In order to improve the conversion efficiency of the UV-curable systems, a photosensitizer may be added to the basic mixture (monomer + initiator). As known from the literature, such molecules allow to shift the absorption of the material at the wavelength nearest to those of emission of the commercial UV lamps. For example, a small percentage of CPTXO could be added to the *p-ES3* system so as to increase its absorption efficiency at 365 nm.
In the case of the darker composite inks, the shielding effect which lead to low conversion, may be offser by increasing the weight concentration of sulfonium photoinitiator added to the epoxy resin.

To ensure a higher quality of the composite mixtures avoiding the formation of micro-bubbles, which tend to decrease the mechanical properties of the printed samples, one solution might be the adoption of a mechanical homogenization technique instead of the manual one used in this work. This could also be a good way to avoid the chopping of the fibers.

Another way to improve the mechanical response of the composite materials could be the use of a sizing treatment on the short fibers. This treatments are generally used to improved the fiber/matrix interfacial adhesion and thus the mechanical resistance of the material.

In order to decrease the brittleness of the composite material, it could be useful to think about the addition of a plasticizer. Perhaps a more detailed study on the various available types of plasticizers should be conducted and, probably, an appropriate content of such material may improve the fracture behavior of composites.

APPENDIX

Characterization of pt-ES3PA dual-cure system



Figure 2A Drops on glass of pt-ES3PA irradiated with laser at 365nm for different time intervals.

Curing cycle for pt-ES3PA	**$T_{g\ DSC}$**
UV 10 sec – 1h 180°C	90.77
UV 20 sec – 1h 180°C	127.05

Table 1A Glass transition temperature related to the drops shown on the Figure 1.

Characterization of pt-ES3PA dual-cure system

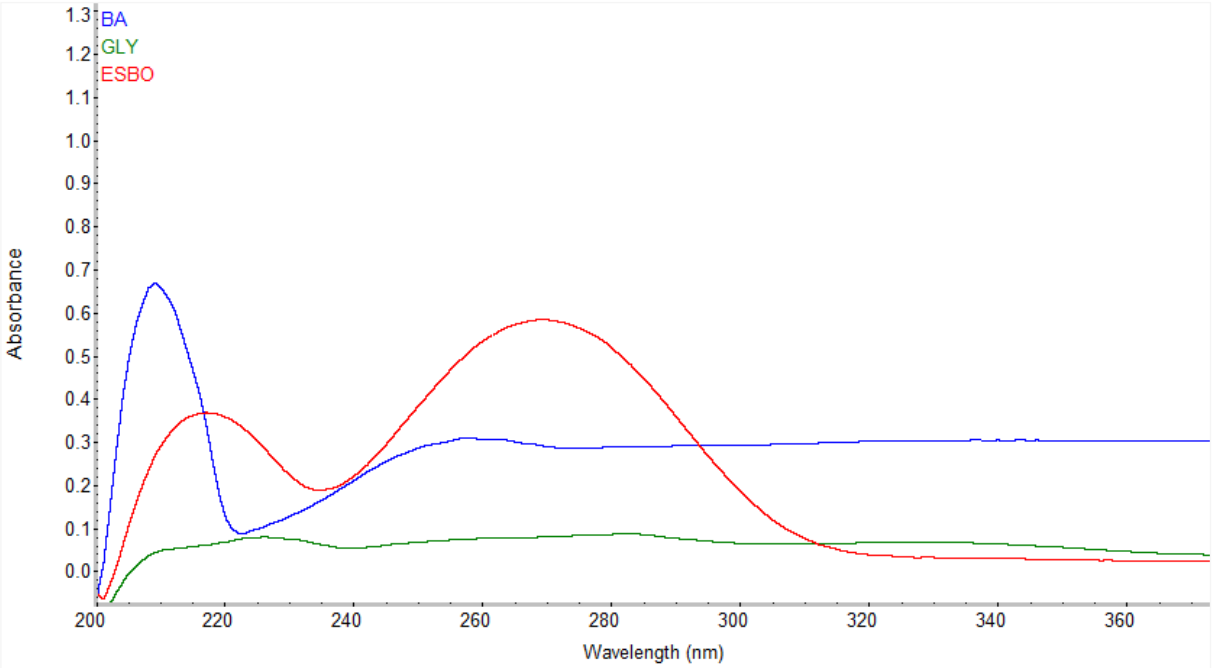

Graph 1A UV-vis spectra of solution of BA, GLY, ESBO plasticizers diluted (0.001%) in methanol.

pt-ES3PA+ Plasticizer 5% wt	$T_{g\ DSC}$
GLY	26.73
ESBO	26.52

Table 2A Glass transition temperature of dual-cure mixture with plasticizer at 5%wt.

Mechanical response of pt-ES3MA with and without ESBO plasticizer

Cast dumbbell sample	Elastic Modulus [GPa]	Ultimate tensile strength [MPa]	Elongation at break [%]
pt-ES3MA	3.03 ± 0.23	51.73 ± 6.57	3.24 ± 0.89
pt-ES3MA+ 5%wt	2.81 ± 0.17	52.12 ± 2.18	2.88 ± 0.30

Table 3 Mechanical properties of dual-cure formulation containing the maleic anhydride. The results obtained for the material with and without the addition of ESBO plasticizer are reported. The uniaxial tensile tests are performed on both sample at a speed of 0.3 mm/s with a pre-load of 3N.

BIBLIOGRAPHY

[1] "3D Printing Basics." [Online]. Available: http://3dprintingindustry.com/3d-printing-basics-free-beginners-guide/. [Accessed: 26-Aug-2016].

[2] "What is 3D printing?" [Online]. Available: https://www.3dhubs.com/what-is-3d-printing#/additive-manufacturing-infographic. [Accessed: 25-Aug-2016].

[3] "Additive Manufacturing." [Online]. Available: http://additivemanufacturing.com/basics/. [Accessed: 18-Jun-2016].

[4] GAO, "3D Printing.," 2013.

[5] I. Gibson, D. W. Rosen, and B. Stucke, *Additive Manufacturing Technologies: Rapid Prototyping to Direct Digital Manufacturing.* 2010.

[6] "3D Hubs." [Online]. Available: https://www.3dhubs.com. [Accessed: 20-Aug-2016].

[7] B. Berman, "3-D printing: The new industrial revolution," *Bus. Horiz.*, vol. 55, no. 2, pp. 155–162, 2012.

[8] S. M. C. H. H. S. H. Voswinckel, "Geometric Complexity Analysis in an Integrative Technology Evaluation," vol. 23, no. July, pp. 97–105, 2012.

[9] H. Charles, "Apparatus for production of three-dimensional objects by stereolithography," 1984.

[10] "3D Systems." [Online]. Available: http://www.3dsystems.com. [Accessed: 20-Aug-2016].

[11] C. R. Deckard, J. J. Beaman, and J. F. Darrah, "Method for Selective Laser Sintering with layerwise cross-scanning," 1992.

[12] "stratasys Inc." .

[13] S. S. Crump, "apparatus and method for creating three-dimensional objects," 5,121,329, 1992.

[14] “EOS.” [Online]. Available: http://www.eos.info. [Accessed: 29-Aug-2016].

[15] “3D Printing industry.” [Online]. Available: http://3dprintingindustry.com. [Accessed: 20-Aug-2016].

[16] “RepRap project.” [Online]. Available: https://it.wikipedia.org/wiki/Progetto_RepRap. [Accessed: 20-Aug-2016].

[17] W. Oropallo and L. A. Piegl, “Ten challenges in 3D printing,” *Eng. Comput.*, vol. 32, no. 1, pp. 135–148, 2016.

[18] “Guida ai software per la stampa 3D.” [Online]. Available: http://www.stampa3d-forum.it/guida-software-stampa-3d/. [Accessed: 25-Aug-2016].

[19] “Standford Bunny 3D model.” [Online]. Available: http://www.thingiverse.com/thing:3731/#files. [Accessed: 25-Aug-2016].

[20] W. H. Wah, “introduction to STL format.” 1999.

[21] A. Armillotta, “Assessment of surface quality on textured FDM prototypes,” *Rapid Prototyp. J.*, vol. 12, pp. 35–41, 2006.

[22] Pandey, Pulak, V. Reddy, and Dhande, “Slicing procedures in layered manufacturing: a review.,” *Rapid Prototyp. J.*, vol. 9, no. 5, pp. 274–288, 2003.

[23] “Online 3D printing service.” [Online]. Available: http://www.stampa-3d.com/762/i-6-migliori-servizi-di-stampa-3d-online/. [Accessed: 27-Aug-2016].

[24] F. Riva, “‘Superficie in attesa: processi di finitura superficiale per stampa 3d FDM,’” Politecnico di Milano, 2013.

[25] “+Lab, Politecnico di Milano.” [Online]. Available: http://www.piulab.it.

[26] ASTM International, “F2792-12a - Standard Terminology for Additive Manufacturing Technologies,” *Rapid Manuf. Assoc.*, pp. 10–12, 2013.

[27] C. Chua and K. Leong, “Rapid prototyping: principles and applications in manufacturing.,” *Wiley*, 1998.

[28] D. T. Pham and S. Gault, R, “A comparison of rapid prototyping technologies.pdf,” *Int. J.*

Mach. tools Manuf., vol. 38, pp. 1257–1287, 1998.

[29] G. Natale, "3D Composites Extrusion Project," Politecnico di Milano, 2014.

[30] "Material Jetting." [Online]. Available: http://www.slideshare.net/amanthapar18/advanced-manufacturing-38876256. [Accessed: 25-Aug-2016].

[31] "Markforg3D." [Online]. Available: https://markforged.com. [Accessed: 26-Aug-2016].

[32] M. Levi, *Make or make not. There is no try. What to Print in 3D and Why*, First. Milano, 2016.

[33] "Pascal's law." [Online]. Available: https://it.wikipedia.org/wiki/Legge_di_Pascal.

[34] "Periodic Table of 3D Printable Thermoplastics." [Online]. Available: http://consulting.stratasys.com/2015/12/materials-in-additive-manufacturing-polymers/. [Accessed: 28-Aug-2016].

[35] "Tangram Technology." [Online]. Available: http://www.tangram.co.uk/TI-Polymer-Periodic Table.html. [Accessed: 28-Aug-2016].

[36] "PLA." [Online]. Available: http://reprap.org/wiki/PLA. [Accessed: 30-Aug-2016].

[37] "3D printer filament." [Online]. Available: http://www.filamentostampanti3d.it. [Accessed: 30-Aug-2016].

[38] "No Title." [Online]. Available: http://www.stampa-3d.com/325/le-3-plastiche-piu-utilizzate-nelle-stampanti-3d/. [Accessed: 30-Aug-2016].

[39] F. Ning, W. Cong, J. Qiu, J. Wei, and S. Wang, "Additive manufacturing of carbon fiber reinforced thermoplastic composites using fused deposition modeling," *Compos. Part B Eng.*, vol. 80, pp. 369–378, 2015.

[40] M. Nikzad, S. H. Masood, and I. Sbarski, "Thermo-mechanical properties of a highly filled polymeric composites for Fused Deposition Modeling," *Mater. Des.*, vol. 32, no. 6, pp. 3448–3456, 2011.

[41] Wasp and F. Pacelli, "Ceramic Art and 3D printing." [Online]. Available: http://www.wasproject.it/w/en/ceramic-art-and-3d-printing/.

[42] J. A. Lewis, J. E. Smay, J. Stuecker, and J. Cesarano, "Direct ink writing of three-dimensional

ceramic structures," *J. Am. Ceram. Soc.*, vol. 89, no. 12, pp. 3599–3609, 2006.

[43] "Big Delta." [Online]. Available: http://www.wasproject.it/w/en/il-muro-di-terra-e-paglia-alle-soglie-dei-3-metri/. [Accessed: 30-Aug-2016].

[44] J. W. Stansbury and M. J. Idacavage, "3D printing with polymers: Challenges among expanding options and opportunities," *Dent. Mater.*, vol. 32, no. 1, pp. 54–64, 2016.

[45] G. Postiglione, G. Natale, G. Griffini, M. Levi, and S. Turri, "Conductive 3D microstructures by direct 3D printing of polymer/carbon nanotube nanocomposites via liquid deposition modeling," *Compos. Part A Appl. Sci. Manuf.*, vol. 76, pp. 110–114, 2015.

[46] D. Işin, N. Kayaman-Apohan, and A. Güngör, "Preparation and characterization of UV-curable epoxy/silica nanocomposite coatings," *Prog. Org. Coatings*, vol. 65, no. 4, pp. 477–483, 2009.

[47] C. C. Spackman, C. R. Frank, K. C. Picha, and J. Samuel, "3D printing of fiber-reinforced soft composites: Process study and material characterization," *J. Manuf. Process.*, 2015.

[48] B. G. Compton and J. A. Lewis, "3D-printing of lightweight cellular composites," *Adv. Mater.*, vol. 26, no. 34, pp. 5930–5935, 2014.

[49] R. D. Farahani, L. L. Lebel, and D. Therriault, "Processing parameters investigation for the fabrication of self-supported and freeform polymeric microstructures using ultraviolet-assisted three-dimensional printing," *J. Micromechanics Microengineering*, vol. 24, p. 055020, 2014.

[50] L. L. Lebel, B. Aissa, M. A. El Khakani, and D. Therriault, "Ultraviolet-assisted direct-write fabrication of carbon nanotube/polymer nanocomposite microcoils," *Adv. Mater.*, vol. 22, no. 5, pp. 592–596, 2010.

[51] G. Griffini, M. Invernizzi, M. Levi, G. Natale, G. Postiglione, and S. Turri, "3D-printable CFR polymer composites with dual-cure sequential IPNs," *Polymer (Guildf).*, vol. 91, pp. 174–179, 2016.

[52] M. Invernizzi, G. Natale, M. Levi, S. Turri, and G. Griffini, "UV-Assisted 3D Printing of Glass and Carbon Fiber-Reinforced Dual-Cure Polymer Composites," *Materials (Basel).*, vol. 9, no. 7, p. 583, 2016.

[53] M. A. Skylar-Scott, S. Gunasekaran, and J. A. Lewis, "Laser-assisted direct ink writing of planar and 3D metal architectures," *Proc. Natl. Acad. Sci.*, p. 201525131, 2016.

[54] J. A. Lewis and G. M. Gratson, “Direct writing in three dimensions,” *Mater. Today*, vol. 7, no. 7, pp. 32–39, 2004.

[55] T. J. Ober, D. Foresti, and J. A. Lewis, “Active mixing of complex fluids at the microscale,” *Proc. Natl. Acad. Sci.*, vol. 112, no. 40, pp. 2–7, 2015.

[56] B. Y. Ahn, S. B. Walker, S. C. Slimmer, A. Russo, A. Gupta, E. B. Duoss, T. F. Malkowski, and J. A. Lewis, “Planar and Three-Dimensional Printing of Conductive Inks,” *J. Vis. Exp.*, vol. 58, no. e3189, pp. 1–8, 2011.

[57] B. Y. Ahn, D. J. Lorang, and J. a Lewis, “Transparent conductive grids via direct writing of silver nanoparticle inks.,” *Nanoscale*, vol. 3, no. 7, pp. 2700–2702, 2011.

[58] J. O. Hardin, T. J. Ober, A. D. Valentine, and J. A. Lewis, “Microfluidic Printheads for Multimaterial 3D Printing of Viscoelastic Inks,” *Adv. Mater.*, pp. 3279–3284, 2015.

[59] J. A. Lewis, “Direct ink writing of 3D functional materials,” *Adv. Funct. Mater.*, vol. 16, no. 17, pp. 2193–2204, 2006.

[60] R. Frassine, *Materiali compositi XXI Secolo*. Treccani, 2010.

[61] “Assocompositi.” [Online]. Available: http://www.assocompositi.it/1/cosa_sono_i_compositi_316238.html. [Accessed: 30-Aug-2016].

[62] R. Frassine, “TECNOLOGIE E PROPRIETA ’.”

[63] S. a. Joseph, a.; Sreekala, M.S.; Oomen, Z.; Koshy, P.; Thomas, “A comparison of the mechanical properties of phenol formaldehyde composites reinforced with banana fibre and glass fibres,” *Compos. Sci. Technol.*, vol. 62, pp. 1857–1868, 2002.

[64] M. R. Sanjay, G. R. Arpitha, and B. Yogesha, “Study on Mechanical Properties of Natural - Glass Fibre Reinforced Polymer Hybrid Composites: A Review,” *Mater. Today Proc.*, vol. 2, no. 4–5, pp. 2959–2967, 2015.

[65] R. Murugan, R. Ramesh, and K. Padmanabhan, “Investigation on static and dynamic mechanical properties of epoxy based woven fabric glass/carbon hybrid composite laminates,” *Procedia Eng.*, vol. 97, pp. 459–468, 2014.

[66] S.-Y. Fu, B. Lauke, E. Mäder, C.-Y. Yue, and X. Hu, “Tensile properties of short-glass-fiber- and short-carbon-fiber-reinforced polypropylene composites,” *Compos. Part A Appl. Sci. Manuf.*, vol. 31, no. 10, pp. 1117–1125, 2000.

[67] N. M. Barkoula, B. Alcock, N. O. Cabrera, and T. Peijs, “Fatigue properties of highly oriented polypropylene tapes and all-polypropylene composites,” *Polym. Polym. Compos.*, vol. 16, no. 2, pp. 101–113, 2008.

[68] W. Zhong, F. Li, Z. Zhang, L. Song, and Z. Li, “Short fiber reinforced composites for fused deposition modeling,” vol. 301, pp. 125–130, 2001.

[69] H. Zhang, Z. Zhang, and C. Breidt, “Comparison of short carbon fibre surface treatments on epoxy composites I. Enhancement of the mechanical properties,” *Compos. Sci. Technol.*, vol. 64, no. 13–14, pp. 2021–2029, 2004.

[70] M. Martin-Gallego, M. Hern??ndez, V. Lorenzo, R. Verdejo, M. A. Lopez-Manchado, and M. Sangermano, “Cationic photocured epoxy nanocomposites filled with different carbon fillers,” *Polymer (Guildf).*, vol. 53, no. 9, pp. 1831–1838, 2012.

[71] P. Tsotra and K. Friedrich, “Electrical and mechanical properties of functionally graded epoxy-resin / carbon fibre composites,” vol. 34, pp. 75–82, 2003.

[72] H. L. Tekinalp, V. Kunc, G. M. Velez-Garcia, C. E. Duty, L. J. Love, A. K. Naskar, C. A. Blue, and S. Ozcan, “Highly oriented carbon fiber-polymer composites via additive manufacturing,” *Compos. Sci. Technol.*, vol. 105, pp. 144–150, 2014.

[73] M. Vatani, E. D. Engeberg, and J. W. Choi, “Force and slip detection with direct-write compliant tactile sensors using multi-walled carbon nanotube/polymer composites,” *Sensors Actuators, A Phys.*, vol. 195, pp. 90–97, 2013.

[74] C. Santulli, R. La, I. Chimica, and M. Ambiente, “Compositi in fibra naturale.”

[75] K. Okubo, T. Fujii, and Y. Yamamoto, “Development of bamboo-based polymer composites and their mechanical properties,” *Compos. Part A Appl. Sci. Manuf.*, vol. 35, no. 3, pp. 377–383, 2004.

[76] M. M. Thwe and K. Liao, “Effects of environmental aging on the mechanical properties of bamboo-glass fiber reinforced polymer matrix hybrid composites,” *Compos. Part A*, vol. 33, no. 1, pp. 43–52, 2002.

[77] Y. Yagci, S. Jockusch, and N. J. Turro, “Photoinitiated polymerization: Advances, challenges, and opportunities,” *Macromolecules*, vol. 43, no. 15, pp. 6245–6260, 2010.

[78] J. Ortyl and R. Popielarz, “New photoinitiators for cationic polymerization,” *Polimery/Polymers*, vol. 57, no. 7–8, pp. 510–517, 2012.

[79] V. Y. Voytekunas, F. L. Ng, and M. J. M. Abadie, “Kinetics study of the UV-initiated cationic polymerization of cycloaliphatic diepoxide resins,” *Eur. Polym. J.*, vol. 44, no. 11, pp. 3640–3649, 2008.

[80] S. Chen, W. D. Cook, and F. Chen, “Photopolymerization of vinyl ether networks using an iodonium initiator: Effect of radiation intensity and iodonium concentration,” *Macromolecules*, vol. 42, no. 16, pp. 5965–5975, 2009.

[81] S. Schl??gl, M. Reischl, V. Ribitsch, and W. Kern, “UV induced microcellular foaming - A new approach towards the production of 3D structures in offset printing techniques,” *Prog. Org. Coatings*, vol. 73, no. 1, pp. 54–61, 2012.

[82] “Free radical mechanism.” [Online]. Available: http://america.pink/radical-polymerization_3657298.html. [Accessed: 30-Aug-2016].

[83] J. V. Crivello and E. Reichmanis, “Photopolymer materials and processes for advanced technologies,” *Chem. Mater.*, vol. 26, no. 1, pp. 533–548, 2014.

[84] P. D. E. L. Prodotto, “F i l 1 0 0,” pp. 1–2.

[85] P. D. E. L. Prodotto, “F i l 2 0 0 f,” pp. 1–2.

[86] “Technical Datasheet ZOLTEK ^{TM} PX35 Milled Carbon Fibers,” p. 63044.

[87] T. D. SUNDSTRAND and B. Fibers, “No Title.” [Online]. Available: http://www.sunstrands.com/sunstrand-biomaterials-industrial-technical-applications/materials/bamboo/.

[88] “Data sheet UV chamber.” .

[89] “CAMAG UV Lamp 4.” pp. 8–9.

[90] “LC8 Hamamatsu lamp.” .

[91] “Data sheet LC-L1 Hamamatsu.” .

[92] J. V Crivello, “The Discovery and Development of Onium Salt Cationic Photoinitiators,” *J. Polym. Sci. Part A Polym. Chem.*, vol. 37, no. August, pp. 4241–4254, 1999.

[93] U. Bulut and J. V. Crivello, “Reactivity of oxetane monomers in photoinitiated cationic polymerization,” *J. Polym. Sci. Part A Polym. Chem.*, vol. 43, no. 15, pp. 3205–3220, 2005.

[94] Y. M. Kim, L. K. Kostanski, and J. F. MacGregor, “Photopolymerization of 3,4-epoxycyclohexylmethyl-3’,4'-epoxycyclohexane carboxylate and tri (ethylene glycol) methyl vinyl ether,” *Polymer (Guildf).*, vol. 44, no. 18, pp. 5103–5109, 2003.

[95] J. D. Cho and J. W. Hong, “Photo-curing kinetics for the UV-initiated cationic polymerization of a cycloaliphatic diepoxide system photosensitized by thioxanthone,” *Eur. Polym. J.*, vol. 41, no. 2, pp. 367–374, 2005.

[96] J. D. Cho, H. K. Kim, Y. S. Kim, and J. W. Hong, “Dual curing of cationic UV-curable clear and pigmented coating systems photosensitized by thioxanthone and anthracene,” *Polym. Test.*, vol. 22, no. 6, pp. 633–645, 2003.

[97] J. Rocks, “Characterization of Novel Co-Anhydride cured Epoxy Resins,” *Technology*, p. 190, 2004.

[98] M. Harsch, J. Karger-Kocsis, and M. Holst, “Influence of fillers and additives on the cure kinetics of an epoxy/anhydride resin,” *Eur. Polym. J.*, vol. 43, no. 4, pp. 1168–1178, 2007.

[99] G. C. Huang and J. K. Lee, “Isothermal cure characterization of fumed silica/epoxy nanocomposites: The glass transition temperature and conversion,” *Compos. Part A Appl. Sci. Manuf.*, vol. 41, no. 4, pp. 473–479, 2010.

[100] J. Parameswaranpillai, A. George, J. Pionteck, and S. Thomas, “Investigation of Cure Reaction , Rheology , Volume Shrinkage and Thermomechanical Properties of Nano-TiO 2 Filled Epoxy / DDS Composites,” *Polymers (Basel).*, vol. 2013, pp. 1–17, 2013.

[101] P. Vol and P. Chem, “Cure Reaction and Kinetic Analysis,” vol. 48, no. March 2007.

[102] X. Fernàndez-Francos, S. G. Kazarian, X. Ramis, and A. Serraa, “Simultaneous monitoring of curing shrinkage and degree of cure of thermosets by attenuated total reflection fourier transform infrared (ATR FT-IR) spectroscopy,” *Appl. Spectrosc.*, vol. 67, no. 12, pp. 1427–

1436, 2013.

[103] M. . Becraft and A. B. Metzner, “The rheology, fiber orientation, and processing behavior of fiber-filled fluids,” *J. Rheol. (New*, pp. 143–174, 1991.

[104] H. A. Barnes, J. F. Hutton, and K. Walters, *An Introduction to Rheology*. Elsevier, 1989.

[105] S. G. Hatzikiriakos and K. B. Migler, *Polymer Processing Instabilities: Understanding And Control*. Marcel Dekker, 2005.

[106] J. Bruneaux, D. Therriault, and M.-C. Heuzey, “Micro-extrusion of organic inks for direct-write assembly,” *J. Micromechanics Microengineering*, vol. 18, no. 11, p. 115020, 2008.

[107] B. B. Johnsen, A. J. Kinloch, R. D. Mohammed, A. C. Taylor, and S. Sprenger, “Toughening mechanisms of nanoparticle-modified epoxy polymers,” *Polymer (Guildf).*, vol. 48, no. 2, pp. 530–541, 2007.

[108] M. Sangermano, M. Naguib, and M. Messori, “Fracture Toughness Enhancement of UV-Cured Epoxy Coatings Containing Al 2 O 3 Nanoparticles,” *Macromol. Mater. Eng.*, vol. 298, no. 11, pp. 1184–1189, 2013.

[109] J. C. Halpin and J. L. Kardos, “The Halpin-Tsai equations: A review,” *Polym. Eng. Sci.*, vol. 16, no. 5, pp. 344–352, 1976.

ACKNOWLEDGEMENTS

Il mio primo ringraziamento va alla professoressa M.Levi, per avermi insegnato che la ricerca richiede impegno, sacrificio, determinazione e soprattutto carattere. La ringrazio per avermi aperto le porte del +LAB, dove ho avuto la possibilità di incontrare fantastici amici. Ragazzi e ragazze speciali che, tra una battuta e l'altra, mi hanno sempre aiutato a superare le difficoltà incontrate durante il lavoro in laboratorio. Grazie al professor S. Turri, per la diponibilità e i suoi preziosi suggerimenti. Mi scuso con entrambi per le continue 'incursioni' in ufficio!

Grazie ad ogni membro del ChipLab, per la disponibilità e il supporto dimostratomi. Un particolare ringraziamento a Gilly che ha sempre pazientemente ascoltato le mie richieste, aiutandomi ogni qualvolta ne avessi la necessità.

Ringrazio tutti i miei amici per avermi fatto sorridere nei momenti più difficili, sempre pronti a sopportare i miei sfoghi.

Ringrazio la mia famiglia che ha sempre dimostrato di credere in me, supportandomi in ogni mia scelta.

Last but not least ringrazio Sandro che, seppur distante, è sempre stato al mio fianco. Lo ringrazio per avermi supportato e sopportato nei momenti più critici della mia esperienza universitaria.

Un ringraziamento generale va a tutte le persone che mi sono state vicine in questo ultimo anno. Alla mia prima famiglia e a quella acquisita…..

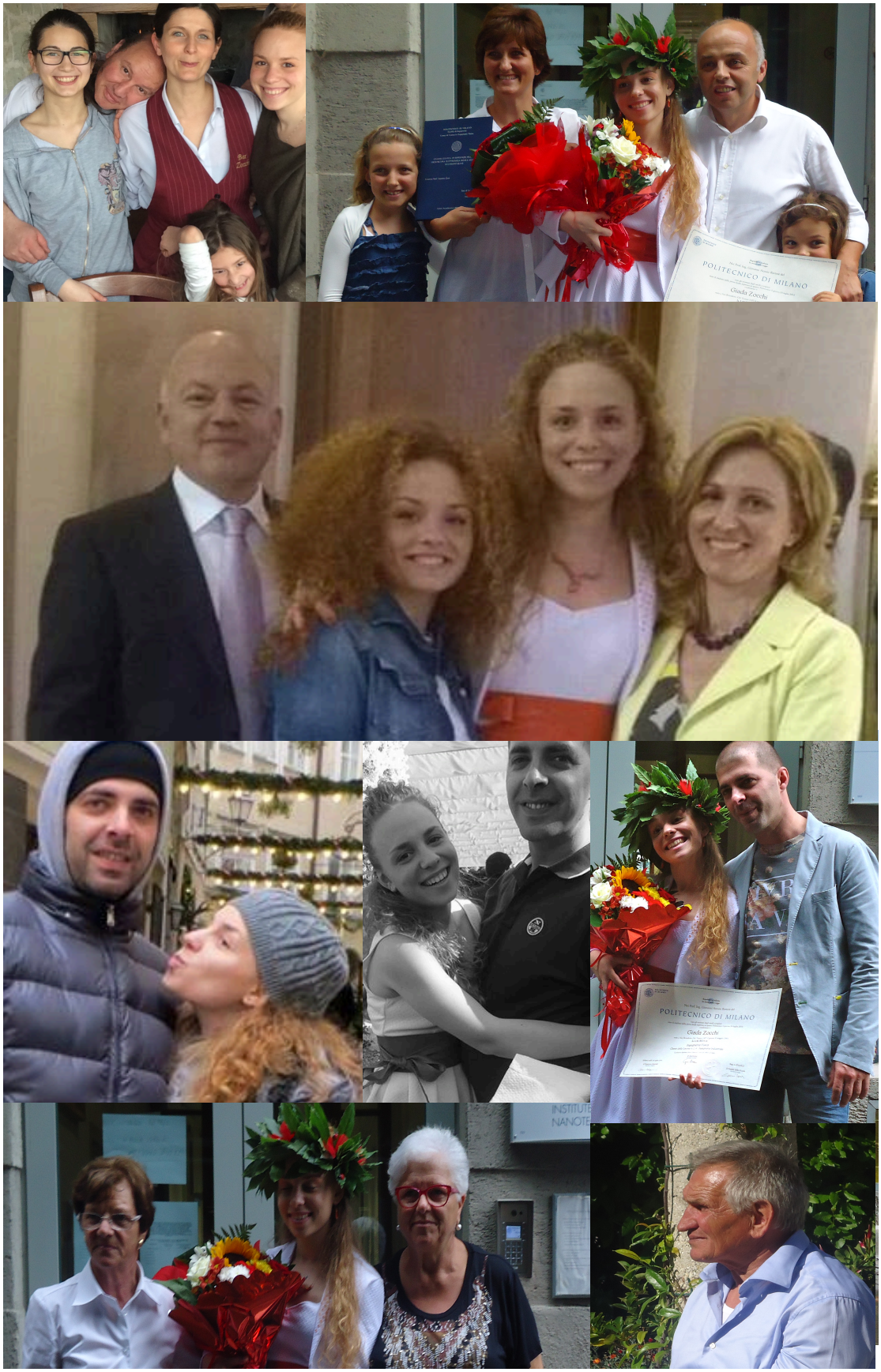
POLITECNICO DI MILANO
Giada Zocchi
POLITECNICO DI MILANO
Giada Zocchi


+LAB
+LAB